Czech Technical University
in Prague

Faculty of Nuclear Sciences and Physical
Engineering

Department of Physics

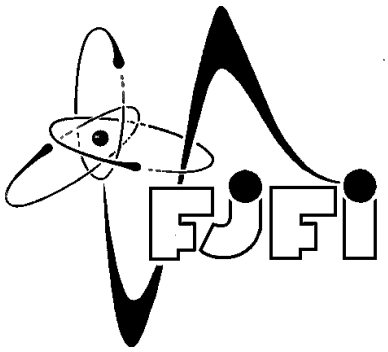

Ph.D. THESIS

Interactions of Hadrons in Few-Body Systems

Ing. Martin Schäfer

Prague, 2020

Supervisor: RNDr. Jiří Mareš, CSc.

České vysoké učení technické
v Praze

Fakulta jaderná a fyzikálně inženýrská

Katedra fyziky

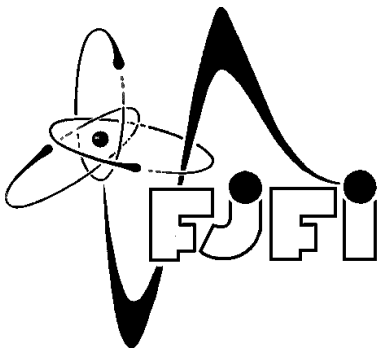

DIZERTAČNÍ PRÁCE

Interakce hadronů v máločásticových systémech

Ing. Martin Schäfer

Praha, 2020

Školitel: RNDr. Jiří Mareš, CSc.

Bibliographic entry

Author:	Ing. Martin Schäfer Czech Technical University in Prague Faculty of Nuclear Sciences and Physical Engineering Department of Physics
Thesis title:	Interactions of Hadrons in Few-Body Systems
Kind of thesis:	Ph.D. thesis
Degree program	Application of Natural Sciences
Branch of study:	Nuclear Engineering
Supervisor:	RNDr. Jiří Mareš, CSc. Nuclear Physics Institute of the CAS Department of Theoretical Physics
Academic year:	2019/2020
Number of pages:	196
Keywords:	few-body systems, hadron, hypernuclei, interaction, mesic nuclei, resonances

Bibliografický záznam

Autor:	Ing. Martin Schäfer České vysoké učení technické v Praze Fakulta jaderná a fyzikálně inženýrská Katedra fyziky
Název práce:	Interakce hadronů v máločásticových systémech
Druh práce:	dizertační práce
Studijní program:	Aplikace přírodních věd
Obor studia:	Jaderné inženýrství
Školitel:	RNDr. Jiří Mareš, CSc. Ústav jaderné fyziky AV ČR, v. v. i. Oddělení teoretické fyziky
Akademický rok:	2019/2020
Počet stran:	196
Klíčová slova:	máločásticové systémy, hadron, hyperjádra, interakce, mezonová jádra, rezonance

Abstract

This thesis concerns the study of interactions of hadrons in selected few-body systems, namely, η-nuclei, Λ^*-systems ($\Lambda^* \equiv \Lambda(1405)$), single-$\Lambda$ and double-Λ hypernuclei. While calculations of few-body bound states were performed within the Stochastic Variational Method with a correlated Gaussian basis, the few-body continuum was explored using two independent approaches - Inverse Analytic Continuation in the Coupling Constant and Complex Scaling Method. We studied the onset of η-nuclear binding by performing self-consistent calculations of η^3He, η^4He, and η^6Li systems taking into account the effect of η absorption. In the case of Λ^*-systems, we refuted Akaishi-Yamazaki conjecture of stable Λ^*-matter. We demonstrated that with increasing number of Λ^* constituents the binding energy per Λ^* saturates thus leaving these systems susceptible to strong decay. We performed detailed calculations of the Λnn ($J^\pi = 1/2^+, I = 1$) and ${}^{3}_{\Lambda}\mathrm{H}^*$ ($J^\pi = 3/2^+, I = 0$) states, and light $\Lambda\Lambda$-hypernuclei within the LO $\not\pi$EFT . The Λnn was found to be a near-threshold resonance and the ${}^{3}_{\Lambda}\mathrm{H}^*$ was robustly predicted as a virtual state. Concerning the strangeness $\mathcal{S} = -2$ hypernuclei, we revealed firm binding of ${}^{5}_{\Lambda\Lambda}\mathrm{H}$, while particle stability of the ${}^{4}_{\Lambda\Lambda}\mathrm{H}$ system requires large $\Lambda\Lambda$ scattering length, which seems unlikely. The neutral $\Lambda\Lambda n$ and $\Lambda\Lambda nn$ systems were obtained unbound by a wide margin. The applicability of LO the $\not\pi$EFT in p-shell systems faces certain difficulties which are explored in the final part of this work. Consequently, this topic remains an open and highly important question which should be addressed in future studies.

Abstrakt

Tato dizertační práce se zabývá interakcemi hadronů v máločásticových systémech, konkrétně η-jádry, Λ^*-systémy ($\Lambda^* \equiv \Lambda(1405)$) a hyperjádry s jedním a dvěmi Λ hyperony. Máločásticové výpočty vázaných stavů jsou provedeny prostřednictvím stochastické variační metody v bázi korelovaných Gaussových funkcí. Máločásticové kontinuum je zkoumáno dvěma nezávislými přístupy - inverzním analytickým rozšířením ve vazbové konstantě (Inverse Analytical Continuation in the Coupling Constant) a metodou komplexní rotace (Complex Scaling Method). Provedli jsme selfkonzistentní výpočty η-jader η^3He, η^4He a η^6Li a studovali jsme vliv absorpce η mezonu na vznik vázaných stavů v nejlehčích η-jádrech. V případě Λ^*-systémů jsme vyvrátili hypotézu Akaishiho a Yamazakiho o stabilní Λ^*-materii. Ukázali jsme, že se zvyšujícím se počtem Λ^* částic vazebná energie na Λ^* saturuje, takže tyto systémy podléhají silnému rozpadu. Provedli jsme podrobné výpočty stavů Λnn ($J^\pi = 1/2^+, I = 1$) a ${}^3_\Lambda\mathrm{H}^*$ ($J^\pi = 3/2^+, I = 0$) a lehkých $\Lambda\Lambda$-hyperjader v LO $\not\pi$EFT . Bylo zjištěno, že Λnn existuje ve formě rezonance blízko prahu a ${}^3_\Lambda\mathrm{H}^*$ byl jednoznačně předpovězen jako virtuální stav. Co se týče $\mathcal{S} = -2$ hyperjader, předpověděli jsme, že ${}^5_{\Lambda\Lambda}$H systém je vázaný, zatímco stabilita ${}^4_{\Lambda\Lambda}$H vyžaduje poměrně velkou $\Lambda\Lambda$ rozptylovou délku - je tedy nepravděpodobné, že by bylo toto hyperjádro vázané. Nenašli jsme žádný vázaný stav v neutrálních systémech $\Lambda\Lambda n$ and $\Lambda\Lambda nn$. Použitelnost LO $\not\pi$EFT pro popis jader p-slupky čelí určitým obtížím, kterým je věnována závěrečná část práce. Toto téma zůstává otevřenou a velmi důležitou otázkou, která by měla být dále zkoumána.

Prohlášení

Prohlašuji, že jsem svou dizertační práci vypracoval samostatně a použil jsem pouze podklady (literaturu, projekty, SW atd.) uvedené v přiloženém seznamu. Tato práce obsahuje výsledky výzkumu uskutečněného v Ústavu jaderné fyziky Akademie věd České republiky v.v.i. Pokud není uvedena explicitně reference, je dizertace založena pouze na originálních článcích autora.

Nemám závažný důvod proti použití tohoto školského díla ve smyslu zákona §60 Zákon č.121/2000 Sb., o právu autorském a právech souvisejících s právem autorským a o změně některých zákonů (autorský zákon).

Declaration

I declare that I wrote my Ph.D. thesis independently and exclusively within the use of cited bibliography. This thesis contains results of research conducted at Nuclear Physics Institute of the Czech Academy of Sciences. Unless an explicit reference is given, the thesis is based solely on the published papers of the author.

I agree with the usage of this thesis in the purport of the Act 121/2000 (Copyright Act).

V Praze dne .....

.....

Martin Schäfer

Acknowledgment

Foremost, I would like to express my deepest gratitude to my supervisor, Dr. Jiří Mareš, for his professional and personal support, invaluable advice, and inspiring discussions throughout my Ph.D. study. My thanks also belong to Prof. Nir Barnea for his hospitality and guidance during my stay at Hebrew University. In particular, I would like to thank for introducing me into the Stochastic Variational Method and pionless effective field theory. I thank my collaborators Dr. Betzalel Bazak, Dr. Lorenzo Contessi, Prof. Avraham Gal, and Dr. Johannes Kirscher for countless enriching discussions. Last but not least, my personal words of thanks belong to my parents, my family, for their unconditional love, support, and patience during the time of my university studies.

Contents

Preface

This thesis deals with interactions of hadrons in few-body systems. These systems play an essential role in the modern hadronic physics as they provide a direct link between their observed properties and underlying interaction models. In a current situation when most models of hadronic interactions quite differ in their predictions and experimental scattering data are scarce and not precise enough, unlike the NN data, each measured property of a few-body system represents highly valuable and stringent constraint on hadronic interactions. Moreover, rather topical issue of in-medium effects, such as the role of three-body force might be studied only in systems of more then two particles. Current theoretical endeavor attempts not only to confront existing models of interactions with already measured few-body data but also to direct experimental efforts towards hadronic systems which still could be observed in principle. However, these systems do not exist only in a form of bound states but they are quite often particle unstable or they decay through the strong interaction to energetically more favorable channels. It is thus crucial to study consistently both bound and continuum regions which might reveal characteristics of such hadronic states or exclude their existence. The study of few-body hadronic systems considered in this work ($\eta(548)$- nuclei, $\Lambda(1405)$-systems, single-$\Lambda(1116)$ and double-$\Lambda(1116)$ hypernuclei) is highly up-to-date. It has been one of the main topics in multiple international conferences (e.g. MESON2018, HYP2018, HADRON2019) or a subject of ongoing, approved or planned experiments in the J-Lab (USA) and J-PARC (Japan) facilities.

The thesis is structured as follows: An introduction to the topic is given in Chapter 1. Here, we outline the main motivation of our work together with an overview of both theoretical and experimental current status of ηN as well as ΛN and $\Lambda\Lambda$ interactions and their connection with studied few-body η-nucler as well as Λ- and $\Lambda\Lambda$- hypernuclear systems, respectively. Hypothetical Λ^*-aggregates ($\Lambda^* \equiv \Lambda(1405)$) are closely related to the properties of few-body K^-- nuclei. Taking into account that the topic of kaonic systems is certainly broad and, moreover, they are not ex-

plicitly studied in this thesis we include just necessary amount of information which led to the hypothesis of stable Λ^* matter. In Chapter 2, we present hadronic interactions considered in this study. Methods and means of few-body calculations are given in Chapter 3. We start with a description of correlated Gaussian basis functions. Next, we briefly introduce the Stochastic Variational Method applied in few-body bound state calculations and two methods employed in the study of few-body continuum - the Inverse Analytic Continuation in the Coupling Constant and Complex Scaling Method. General concept of the evaluation of matrix elements in a correlated Gaussian basis for several operators is then outlined in Appendix A. In addition, we summarize the main properties of two-body S-matrix poles in Appendix B, which we believe provides the reader with more complete explication of both applied few-body continuum techniques. Since all calculations have been performed by employing a new few-body code which was developed as a part of this thesis, we present an indispensable benchmark study in Appendix C. In Chapter 4, we highlight selected results of our work. First, we present results of self-consistent calculations of η-nuclear quasi-bound states - η^3He, η^4He, and η^6Li for two ηN interaction models. The effect of imaginary part of the ηN potential on the onset of η-nuclear binding is evaluated as well. Next, we discuss the stability of hypothetical Λ^*-matter. Using both Stochastic Variational Method (few-body) and Relativistic Mean-Field approach (many-body) we study the binding energy per particle as a function of mass number A in a systems composed solely of Λ^*. The major part of this chapter is devoted to our study of few-body s-shell hypernuclei within the leading-order pionless effective field theory (LO $\not\pi$EFT) representation of nuclear and hypernuclear interactions. First, we present our results concerning the continuum spectrum of three-body Λ-hypernuclear systems and we explore the nature of the $\Lambda nn(J^\pi = 1/2^+, I = 1)$ and ${}^3_\Lambda\mathrm{H}^*(J^\pi = 3/2^+, I = 0)$ states. Second, we construct the LO $\not\pi$EFT representation of the $\Lambda\Lambda$ interaction and we address the onset of $\Lambda\Lambda$ hypernuclear binding. The last section is devoted to possible insufficiency of the nuclear $\not\pi$EFT at LO which emerges once the theory is applied to the description of p-shell nuclear systems. Chapter 4 presents only the main and the most important accomplishments of our work; further results together with a more detailed discussion can be found in our selected articles enclosed in Appendix D. Finally, main conclusions together with future prospects are summarized in Chapter 5.

Chapter 1

Introduction

It is basic human nature to strive to discover the world around us and a tremendous amount of effort has been put into understanding its laws throughout history. One of the essential questions concerns properties of the visible matter in the Universe. Here, the physics of hadrons, strongly interacting particles, plays an important role. The strong interactions are currently described by Quantum Chromodynamics (QCD). At low energies QCD gives rise to mesons and baryons which then manifest themselves in various phenomena such as the existence of atomic nuclei or compact astrophysical objects (neutron stars). However, QCD in this energy regime is highly difficult to solve. There are basically two main approaches which aim to overcome this obstacle: The first one, *the lattice QCD*, employs extensive numerical simulations (for review see [1]). Although lattice calculations have undergone considerable progress in recent few years, the full description of hadronic interactions or even hadronic systems at physical quark masses is still a subject of ongoing research. The second option involves application of effective field theories (EFTs) that implement symmetries and dynamics of QCD. Nowadays, the state-of-the-art low energy EFTs are based on approximate chiral symmetry of QCD, which is full in the limit of zero quark masses. Free parameters of these theories, so called low energy constants, have to be fixed by experimental input. At this point the significance of few-body hadronic systems becomes apparent - applying highly precise few-body techniques one can make direct link between models of hadronic interactions and their predictions for few-body hadronic systems, test or constrain these models using experimental data, or even predict new, so far not experimentally observed systems.

This chapter presents a short overview of the interactions of hadrons in few-body systems – η-nuclei, K^--nuclei, and single- and double-Λ hypernuclei studied

in this work. The hypernuclear systems provide important information on interactions among constituents of the ground state baryonic octet. They allow us to study the strangeness $\mathcal{S} = 0$ (nuclear) and $\mathcal{S} = -1,\ -2$ baryonic interactions within the broader perspective of the broken flavor SU(3) symmetry. The study of η- and K^--nuclear systems provides deeper insight into a more general concept of meson-baryon interactions between the pseudoscalar meson octet (π, K, η) and the ground state baryonic octet. In addition, properties of (pseudoscalar) mesons inside the strongly interacting medium have been of great interest recently. According to several scenarios [2–5], the meson masses are subject to in-medium modifications which lead to partial restoration of chiral symmetry at high nuclear densities. Moreover, it was proposed that kaons can appear in dense nuclear matter [6,7], e.g. in the inner core of neutron stars [8].

η-nuclear systems

The first prediction concerning the nature of the ηN interaction was made in 1985 by Bhalerao and Liu [9] who performed coupled-channel analysis of πN phase shifts [10] together with $\pi^- + p \to \eta + n$ cross-section data [11]. They found that due to the presence of the $N^*(1535)$ hadronic resonance just ≈ 50 MeV above the ηN threshold the s-wave ηN interaction is attractive with $|\mathrm{Re}(a_{\eta N})| \approx 0.28$ fm and $\mathrm{Im}(a_{\eta N}) \approx 0.2$ fm. In the following works [12], Haider and Liu illustrated that attraction of this magnitude may be sufficient to allow formation of a strongly-bound system of η and nucleus (the so called *η-mesic nucleus*) starting with ^{12}C. They further stressed that exploring these systems could compensate for the lack of η beams and could thus provide a natural laboratory for testing the ηN interaction.

Since the pioneering work of Haider and Liu numerous experiments studying η-mesic nuclei (briefly η-nuclei) with the nuclear core mass number $A > 10$ reported negative or inconclusive results [13–17]. The only candidate for such a system was announced by the COSY@GEM collaboration [16] which observed a peak in the missing mass spectrum of the proton induced reaction $p +^{27}\mathrm{Al} \to \eta^{25}\mathrm{Mg} + {}^3\mathrm{He} \to \pi^- + p + X + {}^3\mathrm{He}$ with the decay of the η ^{25}Mg mesic state due to $\eta + n \to \pi^- + p$. The measured η separation energy and width were $B_\eta^{\mathrm{exp}}(\eta^{25}\mathrm{Mg}) = 13.1 \pm 1.6$ MeV and $\Gamma^{\mathrm{exp}}(\eta^{25}\mathrm{Mg}) = 10.2 \pm 3.0$ MeV, respectively. However, the analysis of reaction data was obscured by rather strong kinematic constraints, consequently, the obtained result is generally considered as a hint rather than strong experimental evidence.

Until now, the ηN interaction was studied in multiple works using coupled-channel K-matrix methods [18–20] or chirally motivated coupled-channel models

[21–25]. The results confirm attraction around the ηN threshold and agree on strong energy dependence of the ηN scattering amplitude which steeply decreases farther below the threshold. The predicted ηN interaction strengths significantly differ - this is apparent from the size of a real part of the ηN scattering length which varies from the lowest values $|\mathrm{Re}(a_{\eta N})| \approx 0.2$ fm up to $|\mathrm{Re}(a_{\eta N})| \approx 1$ fm according to the model applied.

The state-of-the-art self-consistent calculations of medium and heavy η-nuclei using several ηN interaction models were presented in Refs. [26, 27]. It was found that bound η^{12}C is unlikely in models with $|\mathrm{Re}(a_{\eta N})| \lesssim 0.5$ fm and in order to reproduce the η^{25}Mg event measured by COSY@GEM rather large, $|\mathrm{Re}(a_{\eta N})| \approx 0.9$ fm is necessary. Being aware of limitations of the many-body approach, the authors further suggested existence of bound η^4He for $|\mathrm{Re}(a_{\eta N})| \approx 0.9$ fm.

The experimental status of light η-nuclei was thoroughly summarized by Krushe and Wilkins [28] which led to the conclusion that : *"The most straightforward (but not unique) interpretation of the data on light η-nuclei is that the ηd system is unbound, the η^4*He *is bound, but that the η^3*He *case is ambiguous."* The ηd system was experimentally explored through $p+n \to d+\eta$ [29–31] and $d+p \to d+p+\eta$ [32] reactions which revealed enhancement of the ηd production cross-section in the vicinity of the ηd threshold. Although Faddeev calculations in Ref. [33] strongly supported the existence of a near-threshold ηd quasi-bound or resonant state, the following work [34,35] ruled out this scenario and, in fact, the existence of ηd virtual state is more acceptable [36–38]. The η^3He system was studied in η-production experiments via $\gamma + {}^3\mathrm{He} \to \eta + {}^3\mathrm{He}$ [39,40] and $d + p \to \eta + {}^3\mathrm{He}$ [41–43] reactions at MAMI and COSY, respectively. In both cases, there is a very sharp increase of the corresponding total cross-sections near the η^3He threshold, which indicates presence of a pole. Statistically more rich $d + p$ data were analyzed by Wilkin *et al.* [44] who concluded that there is a pole with excitation energy $Q_0 = [(-0.36 \pm 0.11 \pm 0.04) \pm \mathrm{i}(0.19 \pm 0.28 \pm 0.06)]$ MeV, however, the nature of the experimental input did not allow to determine the sign of the $\mathrm{Im}(Q_0)$ which would discriminate between the quasi-bound and virtual state. In the later analysis of the same data, Xie *et al.* [45] deduced existence of the weakly bound η^3He state with $B_\eta = 0.30 \pm 0.10 \pm 0.08$ MeV and $\Gamma = 3.0 \pm 0.5 \pm 0.7$ MeV. The Krushe and Wilkins suggestion of bound η^4He has not been experimentally supported yet. This η-nucleus was searched by the WASA@COSY collaboration using $d + d \to \eta^4\mathrm{He} \to \pi^- + p + {}^3\mathrm{He};\ \pi^0 + n + {}^3\mathrm{He}$ reactions but no signal which could be assigned to η^4He was found [46].

Theoretical studies of light η-nuclear systems can be divided into two groups.

The first one is represented by Faddeev type approaches which in addition to the aforementioned investigations of ηd include calculations of η^3He and η^4He within the Alt-Grassberger-Sandhas formalism [47, 48]. Neither η^3He nor η^4He was predicted quasi-bound, however, these calculations use simplistic separable interactions which represent a certain drawback. The second group includes self-consistent variational calculations of ηd, η^3He, and η^4He which use semi-realistic NN and chirally motivated ηN interactions [49, 50] or pionless effective field theory approach [51]. They reported no quasi-bound state in ηd, while the η^3He system was found bound for ηN interaction with $|\mathrm{Re}(a_{\eta N})|$ close to 1 fm, and η^4He was bound for $|\mathrm{Re}(a_{\eta N})| \gtrsim 0.7$ fm. In the recent work [52] which is part of this thesis, the variational calculations were extended to η^6Li and the effect of η absorption on the onset of η-nuclear binding was explored.

K^--nuclei

The study of the low energy $\bar{K}N$ interaction has attracted attention of theorists as well as experimentalists for over decades. While the K^+N interaction is generally accepted as weakly repulsive [53], more unsettled situation remains in the case of the K^-N interaction. Both K^-p scattering and reaction data [54–56] together with measurements of the K^--hydrogen [57–59] clearly indicate that the K^-p interaction is repulsive at and above the K^-p threshold. There are no experimental K^-n data, nevertheless, planned measurement of the kaonic deuterium [60, 61] is expected to provide desirable information. The subthreshold K^-N interaction is considered attractive - this is indicated by the analysis of the K^- atom data [62,63] and suggested by the presence of the $\Lambda(1405)$ hadronic resonance just ≈ 27 MeV below the K^-p threshold.

The idea that the $\Lambda(1405)$ might be a molecular state of an antikaon and a nucleon was first spelled by Dalitz *et al.* [64, 65]. Since then the nature of the $\Lambda(1405)$ resonance has been a subject of considerable interest (see Ref [66] for detailed review). In the most $\bar{K}N$ interaction models, the $\Lambda(1405)$ is considered as a meson-baryon molecule, more specifically, as a $I = 0$ $\bar{K}N$ quasi-bound state affecting the $\pi\Sigma$ resonant continuum [67, 68]. This scenario suggests strong coupling between the $\bar{K}N$ and $\pi\Sigma$ channels leading to significant K^- absorption in nuclear matter. Other models consider $\Lambda(1405)$ as elementary three-quark baryon [69] or pentaquark [70].

The properties of $\bar{K}N$ interaction models are closely connected with the struc-

ture of the $\Lambda(1405)$ resonance. While phenomenological $\bar{K}N$ interaction coupled-channel models are often fixed to reproduce $\Lambda(1405)$ corresponding to just one pole of S-matrix [71–73], chirally motivated coupled-channel models [74–78], which generate $\Lambda(1405)$ dynamically, predict two poles in the complex energy plane which are assigned to this resonance [66, 79]. It is to be noted that the possible two pole structure of $\Lambda(1405)$ was reported already in 1990 within cloudy bag model [80] even before chiral approaches. Studying both energy-independent phenomenological $\bar{K}N$ potentials with one- or two-pole structure of the $\Lambda(1405)$ and a chirally motivated $\bar{K}N$ potential in Ref. [73] (see also references therein) led to the conclusion that all options reproduce experimental data equally well and provide similar results for the low-energy K^-d scattering amplitudes and characteristics of kaonic deuterium. Until now, there is neither theoretical nor experimental argument which would firmly discriminate between the one- and two-pole scenarios. Nevertheless, recent measurements of the $\pi\Sigma$ mass spectra in various reactions by collaborations at JLab [81], COSY [82], GSI [83], and J-PARC [84] exhibit the shapes and positions of the $\Lambda(1405)$ that seem to prefer the two-pole structure. Clearly, more precise measurements are badly needed.

The first study of light K^--nuclei was performed by Akaishi and Yamazaki (AY) using a phenomenological $\bar{K}N$ potential [71, 85, 86]. The authors found that few-body kaonic systems with three and more nucleons are bound by ≥ 100 MeV when the main decay mode $K^-N \to \pi\Sigma$ is energetically forbidden and thus they predicted existence of deeply bound narrow K^--nuclear states. This result triggered further theoretical studies in the few-body sector using either Faddeev [72, 87–90] or variational [91–93] approaches, nevertheless, the corresponding results considerably differ based on applied $\bar{K}N$ interaction models. While phenomenological $\bar{K}N$ potentials usually assume the PDG value of the resonance mass 1405 MeV [94], current chirally motivated models predict the position of the pole associated with the $\bar{K}N$ channel much closer (by ≈ 15 MeV) to the threshold [79]. Consequently, the chirally motivated models give considerably shallower K^-p potential and thus smaller binding energies of K^--nuclear systems.

Experimental searches for K^--nuclei have been predominantly motivated by the AY conjecture about narrow deeply bound K^--nuclear states, nevertheless, their results are quite contradictory. The FINUDA collaboration reported structure in the back-to-back Λp invariant mass spectrum of K^- stopped reaction on the ^{6}Li, ^{7}Li, and ^{12}C targets, which was interpreted as a K^-pp cluster with the binding energy $B = 115^{+6}_{-5}$ MeV and the width $\Gamma = 67^{+14}_{-11}$ MeV [95]. However, the ob-

served structure could be explained by K^- absorption on two nucleons and final state interactions [96]. The OBELIX collaboration found a structure in the Λp invariant mass spectrum from $\bar{p}$ ^{4}He annihilation, which was assigned to the K^-pp state with $B = 160 \pm 4.9$ MeV and $\Gamma \leq 24 \pm 8$ MeV [97]. Further, the K^-pp state with $B = 103 \pm 3(\text{stat}) \pm 5(\text{syst})$ MeV and $\Gamma = 118 \pm 8(\text{stat}) \pm 10(\text{syst})$ MeV was claimed to be observed in the Λp invariant mass spectrum from $p + p$ collisions by the DISTO collaboration [98], however, no sign was reported in the following $p + p$ reaction experiment performed by the HADES collaboration [99–101]. Also, no evidence of the K^-pp state was found in $\gamma + d \to K^+\pi^- X$ reaction in the energy region $E_\gamma = 1.5 - 2.4$ GeV at LEPS [102]. Exploring $d(\pi^+, K^+)$ reaction, the E27 experiment reported a possible K^-pp candidate in the $\Sigma^0 p$ channel with $B = 95^{+18}_{-17}(\text{stat})^{+30}_{-21}(\text{syst})$ MeV and $\Gamma = 162^{+87}_{-45}(\text{stat})^{+66}_{-78}(\text{syst})$ MeV [103]. Finally, the latest result was obtained in the E15 experiment using $^3\text{He}(K^-, \Lambda p)$ reaction - the observed structure was attributed to the K^-pp system with $B = 47 \pm 3(\text{stat})^{+3}_{-6}(\text{syst})$ MeV and $\Gamma = 115 \pm 7(\text{stat})^{+10}_{-20}(\text{syst})$ MeV [104].

As concerns heavier K^--nuclear systems, Hrtánková and Mareš performed recently self-consistent calculations of kaonic nuclei across the periodic table using several chirally motivated K^-N interaction models supplemented with a phenomenological K^--multi-nucleon optical potential fitted to kaonic atom data [105, 106]. They found that due to K^--multi-nucleon absorption there is substantial increase of K^--nuclear widths which are considerably larger than calculated K^- binding energies. Experimental observation of K^- states in many-body nuclear systems would thus be highly difficult or even unlikely. The K^- multi-nucleon absorption was studied by the AMADEUS collaboration [107] and rather recently the first microscopic model of K^- absorption on two nucleons has been developed [108]. New few-body and many-body calculations of K^- nuclear states taking into account multi-nucleon absorption are eagerly awaited since they could shed more light on unclear, yet thrilling situation of K^- interactions in nuclear matter.

As stated above the K^-p interaction near threshold is sufficiently strong to form a quasi-bound state. Using a phenomenological $\bar{K}N$ potential this quasi-bound state was identified by AY with the $\Lambda(1405)$ resonance [109]. Calculations of few-body $\Lambda^* \equiv \Lambda(1405)$ systems based on the above assumption led AY to a hyphotesis that Λ^* aggregates become increasingly bound with the number of constituents, eventually reaching absolute stability. We demonstrated in our paper [110], which is a part of this thesis, that such scenario is unlikely.

Λ- and ΛΛ-hypernuclear systems

Systematic studies of hyperon-nucleon YN and hyperon-hyperon YY interactions, where $Y = (\Lambda, \Sigma, \Xi, \Omega^-)$, have been performed for almost 70 years. The first hypernucleus, a bound system of nucleons and hyperons, was observed in 1952 by Danysz and Pnievski [111] who registered in emulsion experiment a slowly decaying nuclear fragment which emerged from the collision of the high energy cosmic ray proton (30 GeV) with the Ag or Br nucleus. Since then, more than 30 different Λ-hypernuclei have been observed, ranging from the lightest hypernucleus ${}^{3}_{\Lambda}$H up to ${}^{208}_{\Lambda}$Pb. Thanks to rather long lifetime ($\sim 10^{-10}$s) their Λ separation energies or excitation spectra have been measured [112, 113]. On the other hand, it has been demonstrated that Σ-hypernuclei do not form bound states, except ${}^{4}_{\Sigma}$He (see [114] and references therein). Just one Ξ-hypernucleus, ${}^{15}_{\Xi}$C (${}^{14}\mathrm{N} + \Xi$) at J-PARC [115], and no Ω-hypernucleus have been observed so far. As for systems with more than one hyperon, only three ΛΛ-hypernuclei have been reported – ${}^{6}_{\Lambda\Lambda}$He, ${}^{10}_{\Lambda\Lambda}$Be, and ${}^{13}_{\Lambda\Lambda}$B (see [114] for review).

Concerning the strangeness $\mathcal{S} = -1$ YN interaction, scarce scattering data do not provide stringent constraints. They include only 12 $\Lambda + p \to \Lambda + p$ [116, 117] and 22 $\Sigma^- + p \to \Lambda + n$, $\Sigma^+ + p \to \Sigma^+ + p$, $\Sigma^- + p \to \Sigma^- + p$, and $\Sigma^- + p \to \Sigma^0 + n$ [118, 119] cross-sections which all correspond to laboratory momenta above 100 MeV. The very existence of Λ-hypernuclei clearly proves that the ΛN interaction is attractive. However, the analysis of the scattering data gives only rough estimates of its strength, predicting the ΛN spin-singlet $a_0^{\Lambda N}$ and spin-triplet $a_1^{\Lambda N}$ scattering lengths in rather broad interval $0 < |a_0^{\Lambda N}| < 9$ fm and $0.8 < |a_1^{\Lambda N}| < 3.2$ fm, respectively [116].

The $\mathcal{S} = -1$ YN interactions are described by models taking into account the approximate SU(3) flavor symmetry of baryon-baryon interactions, which allows to take advantage of rich NN scattering data and thus supplement the poor YN database. This approach was followed by multiple boson-exchange [120–125], multi-meson-exchange [126–128], and more recent chiral LO [129] and NLO [130] models which naturally implement a couple-channel form of the $\mathcal{S} = -1$ interaction with ΛN and ΣN components.

The observed lightest s-shell Λ hypernuclear systems ${}^{3}_{\Lambda}$H, ${}^{4}_{\Lambda}$H, ${}^{4}_{\Lambda}$He, and ${}^{5}_{\Lambda}$He have irreplaceable role in the study of the ΛN interaction. Of particular interest is the in-medium ΛN interaction where the conversion between Λ and Σ known as the $\Lambda N - \Sigma N$ mixing occurs. In Refs. [131, 132], different models of the ΛN interaction were tested in Faddeev type calculations of 3- and 4-body hypernuclei with

explicitly included Λ and Σ degrees of freedom. It was found that a rather small Λ separation energy in ${}^{3}_{\Lambda}$H ($B^{\rm exp}_{\Lambda}({}^{3}_{\Lambda}{\rm H}) = 0.13(5)$ MeV [133][1]) together with experimentally measured properties of ${}^{4}_{\Lambda}$H and ${}^{4}_{\Lambda}$He provide rather important constraints which have immediately discarded some models. However, even the ΛN interaction models which give a good description of 3- and 4-body hypernuclear systems, fail to reproduce the binding energy of ${}^{5}_{\Lambda}$He, yielding 1-2 MeV overbinding [114]. Rather topical issue is the charge symmetry breaking (CSB) of the ΛN interaction. Since there are no Λn scattering data, the CSB is often studied through the energy difference between the 0^+ ground state and the 1^+ excited state of the mirror hypernuclei ${}^{4}_{\Lambda}$H and ${}^{4}_{\Lambda}$He [135, 136].

So far unobserved hypernuclear systems - Λnn ($J^\pi = 1/2^+, I = 1$) and the exited state of hypetriton ${}^{3}_{\Lambda}{\rm H}^*$ ($J^\pi = 3/2^+, I = 0$) are currently a subject of theoretical and experimental interest. Their properties would provide further constraints on the ΛN interaction and, in particular, the measured Λnn system would be extremely valuable source of information about the Λn interaction. Moreover, the above systems represent a convenient testing ground for the ΛNN force. There is rather firm theoretical consensus that both systems are unbound and their binding would be inconsistent with the properties of already observed s-shell Λ hypernuclei [137–144]. In view of these theoretical works, the claimed evidence of the bound Λnn system reported by the HypHI Collaboration [145] was quite surprising. As concerns theoretical studies of ${}^{3}_{\Lambda}{\rm H}^*$ and Λnn, Garcilazo *et al.* showed that the Λd scattering length in $J^\pi = 3/2^+$ channel indicates existence of a pole in the vicinity of the $\Lambda + d$ threshold [140]. It was demonstrated by Belyaev *et al.* [141] and more recently by Afnan and Gibson [144] that the neutral Λnn system might exists in a form of near-threshold resonance.

The ΛN interaction at very low momenta has been recently described by a $\not\pi$EFT [146]. The primary goal of this theory is not to compete with more sophisticated approaches such as chiral EFT YN interaction models [129, 130], but rather to provide more simple theoretical framework with well defined uncertainties and a minimal number of free parameters which could be constrained by experimental data. Within this approach three-body forces appear naturally at LO and predictions of the theory are independent of regulator scheme. The LO hypernuclear $\not\pi$EFT successfully resolved the ${}^{5}_{\Lambda}$He overbinding problem [146]. More recently, we applied the $\not\pi$EFT at LO in the study of the nature of Λnn and ${}^{3}_{\Lambda}{\rm H}^*$ [147].

[1]It is to be noted that the most recent STAR experiment reported higher $B^{\rm exp}_{\Lambda}({}^{3}_{\Lambda}{\rm H}) \sim 0.4$ MeV [134] which is however under current debate.

In the case of strangeness $\mathcal{S} = -2$ YN and YY interactions, the situation is even more unsettled. There are just few $\mathcal{S} = -2$ cross-section data points – $\Xi^- + p \to \Xi^- + p$, $\Xi^- + p \to \Lambda + \Lambda$, and $\Xi^- + p \to \Xi^0 + n$, all for laboratory momenta above 200 MeV (see [148] and references therein) and no $\Lambda\Lambda$ scattering data. The analysis of $\Lambda\Lambda$ invariant mass ${}^{12}\mathrm{C}(K^-, K^+\Lambda\Lambda X)$ reaction data yielded $\Lambda\Lambda$ spin-singlet scattering length $a_0^{\Lambda\Lambda} = -1.2 \pm 0.6$ fm [149] which together with $a_0^{\Lambda\Lambda} = -0.79^{-1.13}_{+0.29}$ fm [150] (analysis of the STAR collaboration data [151]) suggest that the $\Lambda\Lambda$ interaction is moderately attractive. This is further supported by $\Lambda\Lambda$-hypernuclear data [114].

The strangeness $\mathcal{S} = -2$ interaction is described by several meson-exchange [152–156] and chiral LO and NLO [148, 157] interaction models. Again, the implemented broken flavor SU(3) symmetry allows to connect $\mathcal{S} = -2$, -1, and 0 baryon-baryon interactions and thus to employ $\mathcal{S} = -1$ and $\mathcal{S} = 0$ scattering data which compensate considerable lack of the $\mathcal{S} = -2$ experimental input. However, after using these techniques there still remain uncertainties in the underlying free parameters. It was even stated in Ref. [148] that the chiral NLO interaction should be considered to be of preliminary and exploratory nature until new $\mathcal{S} = -2$ experimental data are available .

Much theoretical effort has been made to search for possible binding in s-shell $\Lambda\Lambda$ hypernuclei, which would complement just one experimentally observed s-shell system ${}^{\;\;6}_{\Lambda\Lambda}\mathrm{He}$. Newly observed double-$\Lambda$ hypernuclei would certainly put highly needed constraints on the strangeness $\mathcal{S} = -2$ interaction models in the same way as they do in the $\mathcal{S} = -1$ sector. The ${}^{\;\;4}_{\Lambda\Lambda}\mathrm{H}$ ($J^\pi = 1^+;\ I = 0$) system was studied in Refs. [158–160], however, the results are not conclusive, suggesting either no bound state or very weak binding. Several theoretical works agree that ${}^{\;\;5}_{\Lambda\Lambda}\mathrm{H} - {}^{\;\;5}_{\Lambda\Lambda}\mathrm{He}$ ($J^\pi = 1/2^+;\ I = 1/2$) isodublet is particle stable with $\Delta B_{\Lambda\Lambda} \sim 0.5$ to 1 MeV [160–163]. Currently, the study of the neutral $\Lambda\Lambda nn$ ($J^\pi = 0^+;\ I = 1$) system is rather topical. Indeed, an example of its importance is the persistent ambiguity in interpretation of the AGS-E906 experiment [164] referred to as the E906 puzzle. First, the signal was assigned to the bound ${}^{\;\;4}_{\Lambda\Lambda}\mathrm{H}$ system [164] but more recent analyses suggested that the decay of the ${}^{\;\;7}_{\Lambda\Lambda}\mathrm{He}$ [165] or $\Lambda\Lambda nn$ [166] hypernucleus might provide more plausible interpretation. It was claimed that a particle stability of the $\Lambda\Lambda nn$ system is within uncertainties of the baryon-baryon interactions [167], however, later study concluded that the system is unbound and located just above the $\Lambda + \Lambda + n + n$ threshold [168]. In this thesis, the onset of $\Lambda\Lambda$ hypernuclear binding was addressed within $\not\pi$EFT at LO [169]. The virtue of this work with respect to the aforementioned predominantly phenomenological studies is that we describe consistently the whole

set of s-shell $\Lambda\Lambda$ hypernuclei. This allowed us to make rather detailed predictions of the particle stability of s-shell $\Lambda\Lambda$ hypernuclear systems. It is to be noted that experimental search for ${}^{5}_{\Lambda\Lambda}$H is included in the recent J-PARC proposal [170].

The hypernuclear physics is vivid scientific discipline with many open questions which are predominantly related to the underlying $\mathcal{S} = -1$ and $\mathcal{S} = -2$ baryon-baryon interactions. Although considerable theoretical as well as experimental effort has been made in past decades, the interactions are not well understood yet, certainly not on the level of the NN interaction. It is to be noted, that rather recently new information has been provided by lattice HAL QCD calculations of the $\Lambda\Lambda$ and ΞN interactions near the physical point [171] and also by $p\Lambda$ and $\Lambda\Lambda$ correlations studied via femtoscopy of $p-p$ and $p-\mathrm{Pb}$ collisions [172]. Finally, the hypernuclear physics has interdisciplinary nature since it lies at the intersection of nuclear and elementary particle physics. Moreover, it has been shown in numerous works that hypernuclear interactions, and three-body forces in particular, play a significant role in the astrophysics of neutron stars (see [173] and references therein).

Chapter 2

Interactions of hadrons

This chapter deals with hadronic interactions considered in this thesis. The first part is devoted to models of meson-baryon interactions. We introduce ηN interaction models employed in our study of η nuclei. Further, we discuss current status of $\bar{K}N$ interaction models together with the Akaishi-Yamazaki phenomenological potential used by these authors to provide an estimate of the two-body Λ^* system binding energy which led to their suggestion of stable Λ^*-matter. The second part provides the description of the LO (hyper)nuclear $\not\pi$EFT interaction. In our work, we used meson-baryon interactions only as input, consequently, they are discussed here just briefly - more detailed description is beyond the scope of this thesis and can be found in enclosed references. On the other hand, the LO (hyper)nuclear $\not\pi$EFT is introduced in more detail, since we fitted parameters of the theory directly to experimental data and we deem that our results require deeper understanding of the applied approach.

2.1 Meson-baryon interactions

The state-of-the-art description of meson-baryon interactions at low energies is based on chiral approaches which reflect underlying symmetries of QCD. The corresponding effective SU(3) Lagrangians at LO or NLO of chiral perturbation theory (ChPT) are used to describe interactions between the pseudoscalar meson octet (π, K, η) and the ground state baryon octet (N, Λ, Σ, Ξ), which naturally results in a multi-channel formalism. In particular, for the ηN interaction the relevant meson-baryon channels are : πN, ηN, $K\Lambda$, and $K\Sigma$; for the $\bar{K}N$ interaction : $\bar{K}N$, $\pi\Lambda$, $\pi\Sigma$, $\eta\Lambda$, $\eta\Sigma$, and $K\Xi$. Due to the presence of the near-threshold hadronic resonances $N^*(1535)$ (ηN interaction) and $\Lambda(1405)$ ($\bar{K}N$ interaction), ChPT is not

directly applicable and nonperturbative couple-channel techniques have to be employed. The current description of meson-baryon interaction is provided by so-called *chirally motivated coupled-channel models* which use technique of T-matrix resummation in combination with the chiral theory [21–25, 74–78]. Within this approach hadronic resonances are generated dynamically and their masses and widths come out as predictions.

The central piece of these models is a coupled-channel potential V_{ij} which reflects SU(3) symmetry and structure of the underlying chiral Langrangian where indices i and j run over considered meson-baryon channels. The scattering amplitudes of meson-baryon interactions are determined by solution of the coupled-channel Lippmann-Schwinger equation for the T-matrix

$$T_{ij} = V_{ij} + V_{ik} G_k T_{kj}, \tag{2.1}$$

where G_k is the meson-baryon Green's function.

A rather large amount of meson-baryon channels (note that one should also consider different charge states) are for the purpose of few- or many-body calculations often reduced to a single channel. Hyodo and Weise [174] proposed a procedure which aims to construct an effective potential V^{eff} in a single channel under requirement that the resulting amplitude is identical to the solution of a full coupled-channel problem for a selected channel 1 ($\bar{K}N$,ηN)

$$T^{\text{eff}} = V^{\text{eff}} + V^{\text{eff}} G_1 T^{\text{eff}} = T_{11}. \tag{2.2}$$

The effective potential is then sum of the bare interaction in channel 1 and all contributions from the $N-1$ channels

$$V^{\text{eff}} = V_{11} + \sum_{2 \le i \le N} V_{1i} G_i V_{i1} + \sum_{2 \le i,j \le N} V_{1i} G_i T_{ij}^{(N-1)} G_j V_{j1}, \tag{2.3}$$

where $T_{ij}^{(N-1)}$ is a resummation of interactions in remaining channels other then 1

$$T_{ij}^{(N-1)} = V_{ij}^{(N-1)} + \sum_{1 \le k \le N} V_{ik}^{(N-1)} G_k^{(N-1)} T_{kj}^{(N-1)}. \tag{2.4}$$

The corresponding single-channel scattering amplitude, emerging as a result of the above procedure, is complex and its imaginary part represents absorption into all channels which have been reduced.

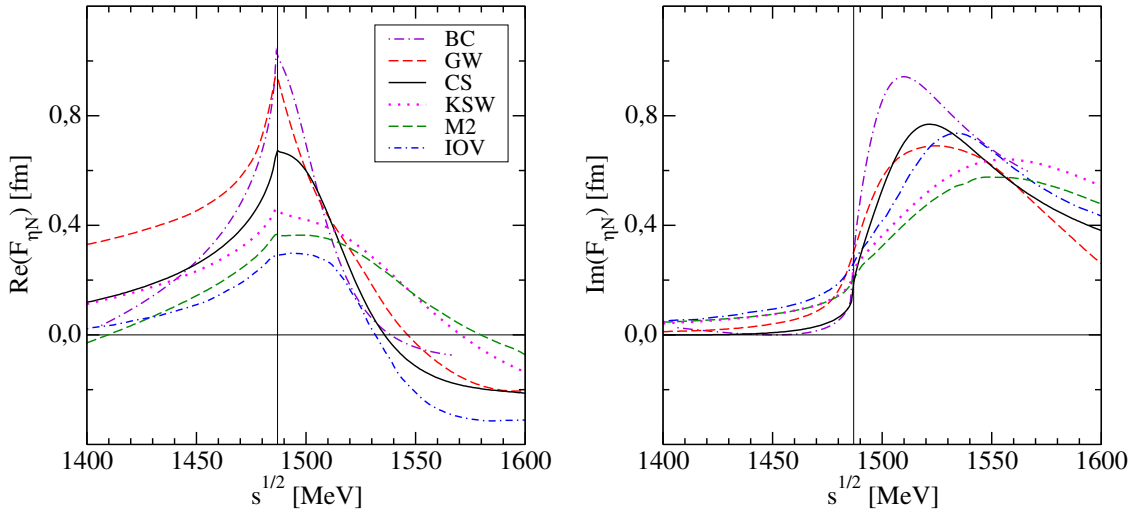

Figure 2.1: Real (left panel) and imaginary (right panel) parts of the s-wave ηN scattering amplitude $F_{\eta N}$ as a function of $\sqrt{s}$ predicted by different ηN interaction models - BC [21] (dot-dashed violet line), GW [20] (dashed red line), CS [22] (solid black line), KSW [23] (dotted purple line), M2 [24] (dashed green line), and IOV [25] (dot-dashed blue line). The ηN threshold is marked by the thin vertical line. The figure is partially adopted from Ref. [27], complemented with the BC ηN scattering amplitude.

The s-wave ηN interaction is considered attractive both above and below threshold [28, 53] but the question about its strength is still unresolved. Zero charge of the η-meson and its very short lifetime ($\tau_\eta \approx 5 \times 10^{-19}$s [94]) obstruct its use in a particle beam, consequently, elastic $\eta N \to \eta N$ scattering can hardly be applied as a source of experimental information. Instead, the ηN interaction is usually studied through $\pi + N \to \pi + N$, $\pi^- + p \to \eta + n$, $\gamma + N \to \eta + N$, $\gamma + N \to \pi + N$, $\pi^- + p \to K^0 + \Lambda$, and $\pi^- + p \to \eta + \eta'$ scattering or reaction data [175–180] which are analyzed within various coupled-channel models. The ηN scattering length $a^{\eta N}$ is complex; its imaginary part represents absorption into always opened πN, $\pi\pi N$, and γN channels. Its size, predicted by various studies, spans rather broad range $0.18 \lesssim \mathrm{Re}(a^{\eta N}) \lesssim 1.05$ fm and $0.16 \lesssim \mathrm{Im}(a^{\eta N}) \lesssim 0.49$ fm [53][1]. Such large uncertainties are induced by differences in applied coupled-channel models which in addition do not use the same sets of experimental data to constrain their low energy parameters.

In Fig. 2.1, we compare s-wave ηN scattering amplitudes $F_{\eta N}$ predicted by

[1] In this section we use opposite sign convention for the scattering length and scattering amplitudes with respect to the remaining part of the thesis. Positive means attraction here while negative denotes repulsion. This convention is often applied in a construction of meson-baryon interactions.

selected chirally motivated ηN interaction models - BC [21], CS [22], KSW [23], M2 [24], IOV [25] and by the K-matrix analysis of the $\pi N \to \pi N$, $\gamma N \to \pi N$, and $\gamma N \to \eta N$ reaction data (GW) [20].

All real and imaginary parts of the ηN scattering amplitude displayed in the figure are strongly energy dependent due to the presence of the $N^*(1535)$. The positive real parts around the ηN threshold indicate attraction, however, their magnitude significantly differs. Relatively strong attraction in the subthreshold region together with small η absorption, given by size of $\mathrm{Im}(F_{\eta N})$ below threshold (particularly in the BS, GW, CS models), are favorable for the existence of narrow η-nuclear quasi bound states studied in this work.

The energy dependence of $F_{\eta N}$ is expressed using the Mandelstam variable

$$s = (E_\eta + E_N)^2 - (\mathbf{p}_\eta + \mathbf{p}_N)^2, \tag{2.5}$$

where for the quasi-bound η-nuclear system $E_\eta = m_\eta - B_\eta$, $E_N = m_N - B_N$ and B_η (B_N) is the η (nucleon) binding energy. In the 2-body cm frame the $(\mathbf{p}_\eta + \mathbf{p}_N)^2$ term is equal to zero and

$$\sqrt{s} = m_\eta + m_N - B_\eta - B_N = \sqrt{s_{\mathrm{th}}} - B_\eta - B_N, \tag{2.6}$$

where $\sqrt{s_{\mathrm{th}}}$ is a position of the ηN threshold (denoted in the figure by the thin vertical line). Consequently, for a quasi-bound ηN system $\sqrt{s} < \sqrt{s_{\mathrm{th}}}$ and the ηN interaction is determined by the subthreshold part of the scattering amplitude. Moreover, in few- and many-body systems the $(\mathbf{p}_\eta + \mathbf{p}_N)^2$ term is no longer equal to zero and causes an additional downward energy shift [181].

Complex energy-dependent ηN scattering amplitudes enter our few-body calculations of η-nuclei; they are used to derive an effective ηN potential (for more details see Eq. (4.1) in Chapter 4). In our work, we are interested in the question what is the lightest nuclear system in which the onset of η binding can appear. Therefore, we consider ηN interaction models which yield one of the largest attraction playing strongly in favor of the formation of η-nuclear quasi-bound states - CS [22] and GW [20]. It is to be stated that the BS model was not available at the time of our study. Nevertheless, one can expect that the results for the BS model should not significantly affect conclusions of our study due to its similarity to the GW model at threshold and rapidly decreasing $\mathrm{Re}(F_{\eta N})$ below the threshold. This implies even smaller attraction with respect to GW almost in the entire subthreshold region shown in Fig 2.1.

The negative charge and much longer lifetime of the K^--meson than the one of η ($\tau_{K^-} \approx 1.23 \times 10^{-8}$s [94]) makes possible to use kaonic beams in order to explore free space $\bar{K}N$ interaction. In particular, measurements of the K^-p elastic scattering and reactions [54–56], K^-p threshold branching ratios [182, 183], and the strong interaction shift and width of the 1s energy level in kaonic hydrogen [57–59] led to rather strict constraints on the K^-p interaction at and above threshold. These experimental data are frequently used as input in order to fix free parameters of various models of the $\bar{K}N$ interaction.

Figure 2.2 presents comparison of the real (left) and imaginary (right) parts of K^-p (upper panels) and K^-n (lower panels) s-wave scattering amplitudes, predicted by different chirally motivated models - Prague (P) [74], Kyoto-Munich (KM) [75], Murcia (M1 and M2) [76], Bonn (B2 and B4) [77], Barcelona (BCN) [78] and phenomenological Akaishi-Yamazaki potential (AY) [71], which were obtained by reducing all considered meson-baryon channels just into the single one - K^-N (see Eqs. (2.2), (2.3), and (2.4)). It is apparent that rather rich K^-p experimental data provide stringent constraints on predicted K^-p scattering amplitudes at and above threshold, which mostly agree remarkably well. Deviation of the Bonn models is due to no s-wave projection of the interaction kernel with respect to other chiral models [79]. On the other hand, there is significant model dependence of the subthreshold K^-p scattering amplitudes which are strongly energy dependent due to the presence of dynamically generated isospin $I = 0$ hadronic resonance $\Lambda(1405)$ located just ≈ 27 MeV below the K^-p threshold.

There are no experimental K^-n data so far. Predictions of theoretical models mostly agree on its moderate attraction both above and below threshold (see the lower panel of Fig. 2.2 for K^-n scattering amplitudes). Since K^-n interaction includes contribution only from isospin $I = 1$ channel, the corresponding scattering amplitudes are not affected by $\Lambda(1405)$, which leads to their weak energy dependence. For comparative analysis of different chirally motivated models see Ref. [79].

We are predominantly interested in the AY $\bar{K}N$ interaction model which was used in Ref. [109] to quantify the binding energy of the two-body $\Lambda^* \equiv \Lambda(1405)$ system. As already mentioned, $\Lambda(1405)$ affects the $I = 0$ channel which contributes only to F_{K^-p} where it is responsible for strong energy dependence. Once we compare F_{K^-p} in Fig. 2.2 predicted by AY to the results of other models it is obvious that its scattering amplitude differs not only quantitatively (imaginary part) but also qual-

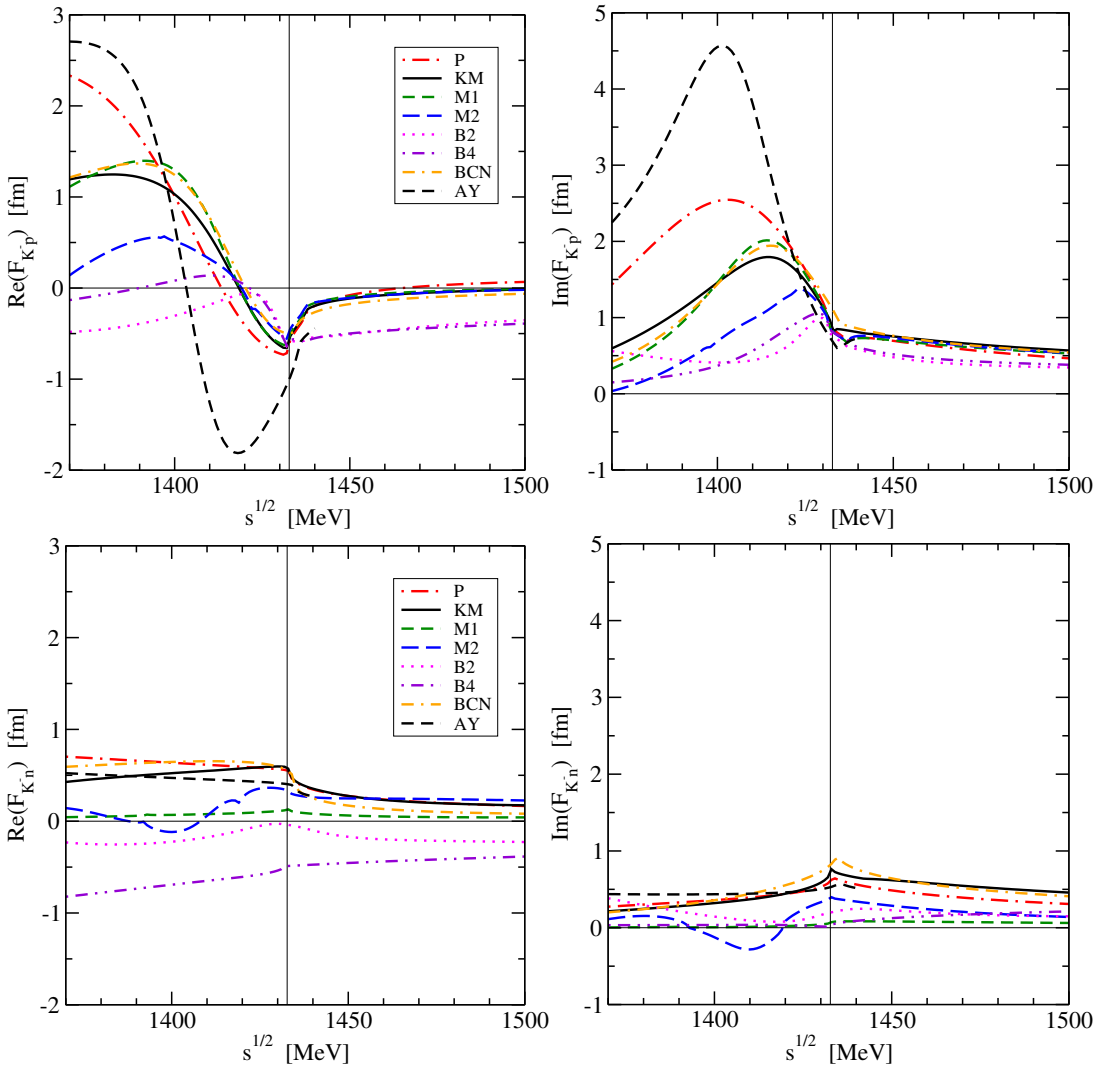

Figure 2.2: Real (left panel) and imaginary (right panel) parts of the s-wave K^-p (upper panel) and K^-n (lower panel) scattering amplitudes as a function of $\sqrt{s}$ predicted by different $\bar{K}N$ interaction models - P [74] (dot-dashed red line), KM [75] (solid black line), M1 (dashed green line) and M2 (dashed blue line) [76], B2 (dotted red line), B4 (double-dot-dashed purple line) [77], BCN (dot-dashed yellow line) [78], and AY (dashed black line) [71]. The thin vertical lines mark threshold energies. The figure is partially adopted from Ref. [106], complemented with the AY and BCN scattering amplitudes.

itatively (real part). Unlike chirally motivated approaches the AY $\bar{K}N$ interaction model is based on a simple energy independent Gaussian potential

$$V_m^I(r) = C_m^I \exp\left(-\frac{1}{b^2}r^2\right), \tag{2.7}$$

where $b = 0.66$ fm, I stands for isospin, and $m \in \left\{\bar{K}N - \bar{K}N, \bar{K}N - \pi\Sigma, \bar{K}N - \pi\Lambda\right\}$

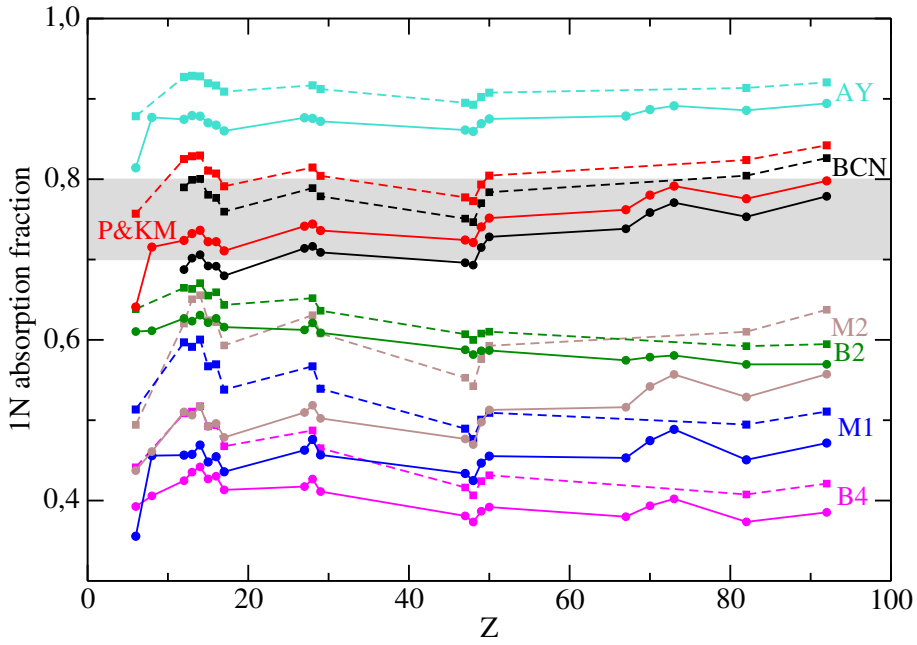

Figure 2.3: The fraction of K^- absorption on a single nucleon (1N) in various kaonic atoms with proton number Z calculated for various $\bar{K}N$ interaction models. The circles connected by solid lines assume K^- absorption in lower atomic states, while squares connected by dashed lines represent K^- absorption in higher atomic states (for more details see Ref. [184]). The gray shaded area indicates the range of 1N absorption fractions suggested by the bubble chamber experiments [185–187]. Results based on the P and KM interaction models are very close and they are represented by the same line. The figure is adopted from the author's publication [188] complemented with the AY 1N absorption fraction.

denotes projection of the potential into different two-body meson-baryon channels. The only parameters of the potential are the C_m^I amplitudes which are constrained in order to roughly reproduce free K^-p scattering [55] and kaonic hydrogen data [57,58] together with the energy and width of the $\Lambda(1405)$ resonance. It is a relevant question to what extent is the six parameter AY potential reliable in the subthreshold region since even more sophisticated chirally motivated approaches start to differ (scattering amplitudes) once extrapolated below the threshold.

Recently, several models of the $\bar{K}N$ interaction yielding considerably different s-wave K^-n and subthreshold K^-p scattering amplitudes were tested by Friedman and Gal against kaonic atoms data, referred in short as *kaonic atoms test* [184]. For each interaction model the authors used corresponding free space K^-N scattering amplitudes as input in order to derive an in-medium single nucleon optical potential within the '$t\rho$' approximation. In addition, the authors included a phenomenological term representing K^- multi-nucleon processes - its parameters were then fitted

for each single-nucleon potential using 65 kaonic atoms data points (see [62] and references therein). Next, fractions of the K^- single-nucleon absorption at rest were calculated for various kaonic atom species and they were compared with the data from bubble chamber experiments (for more details see Ref. [184]).

In Fig. 2.3, we show the single-nucleon (1N) absorption fraction in different kaonic atoms denoted by the corresponding proton number Z calculated for various $\bar{K}N$ interaction models - AY, BCN, P, KM, M1, M2, B2, and B4. It is obvious that only the P, KM, and BCN models pass the *kaonic atoms test*, yielding results which are in agreement with experiment. On the other hand, the AY phenomenological model clearly gives too large (1N) absorption fraction and its validity is thus questionable.

2.2 (Hyper)nuclear ⧸EFT

An effective field theory (EFT) of short-range forces for particles with low momenta Q which are much smaller then their mass m, energy difference between their ground state and first excited state, or the mass of the lightest particle exchanged among them was introduced by van Kolck [189]. This theory can be successfully applied in nuclear physics to the description of the NN interaction at small Q, where pions do not enter as explicit degrees of freedom and the ones which remain are nucleons [190]. This so called pionless EFT (⧸EFT) has been thoroughly reviewed in multiple works [191–194]. The ⧸EFT Lagrangian density is expressed as a sum of one-body $\mathcal{L}^1$, two-body $\mathcal{L}^2$, three-body $\mathcal{L}^3$, ... contributions each composed of nucleon fields and their derivatives. It was illustrated that the corresponding two-body NN scattering amplitude can be matched to all orders of effective range expansion [189]. The power counting of the theory is given by two scales [189] - the first one is the breakdown scale M of the theory associated with the pion mass m_π and the second one is the so called unnaturally small scale connected to the inverse of the NN scattering length in spin-singlet and spin-triplet channels.

The LO ⧸EFT Lagrangian contains two-body momentum independent contact terms, one per each s-wave spin-singlet and spin-triplet NN channel, associated with scattering lengths. It was demonstrated in Ref. [195] that strong cutoff dependence in the three-body s-wave $I = 1/2$, $S = 1/2$ channel (which corresponds to the ^{3}H ground state) calls for introduction of a nonderivative three-body contact interaction to the LO, which enters nonperturbatively alongside with the two-body terms. In calculations of 4-nucleon ^{4}He system [196] and 4- and more-body bosonic systems (^{4}He atoms) [197,198], where the same EFT approach can be applied as well, it was

found that no 4- or more-body contact interactions are necessary at LO.

The LO ≠EFT was applied in a study of s-shell single-Λ and double-Λ hypernuclear systems as well [146, 147, 169]. Here, the breakup scale of the theory is higher than in the nuclear case – it is $2m_\pi$ since one-pion-exchange between ΛN and $\Lambda\Lambda$ is forbidden by isospin invariance.

The NLO includes a momentum dependent contact term with four fields and two derivatives which can be associated with an effective range correction [189, 190]. The inclusion of the NLO term within Gaussian regularization scheme (described later in this section) is restricted by the Wigner bound [199, 200] which enforces its perturbative treatment [189]. However, starting 4-body system this leads to strong regulator dependencies which have to be accounted for by a perturbative inclusion of a 4-body force promoted to the NLO [201].

Even higher order corrections then include p-wave, tensor, spin-orbit, d-wave and further contributions to the s-wave interaction, however, they have been mostly applied on the two-body level (see [194] and references therein). Their study in few-body nuclear systems is still an open task. The LO theory works very well for s-shell nuclear and hypernuclear systems [146, 147, 169, 195, 196] and, in addition, is successfully used in a study of s-shell nuclei based on lattice predictions for higher pion masses [202–205]. However, it seems that one can encounter difficulties with its application to p-shell nuclear systems. This is suggested by the calculation of ^{16}O [204] which is predicted unbound.

In this thesis we apply the LO nuclear, single- and double-Λ hypernuclear ≠EFT interactions [169]. The corresponding Lagrangian density is expressed as

$$\mathcal{L}^{(\mathrm{LO})} = \sum_B B^\dagger (\mathrm{i}\partial_0 + \frac{\nabla^2}{2m_B}) B - \mathcal{V}_2 - \mathcal{V}_3, \tag{2.8}$$

where $B = (N, \Lambda)$ are nucleon and Λ baryonic fields. The $\mathcal{V}_2$ and $\mathcal{V}_3$ terms stand for all possible 2- and 3-body s-wave contact terms with no derivatives, respectively, which can be constructed out of B. Each of these terms corresponds to a particular s-wave 2- or 3-body channel and it is connected to one low-energy-constant (LEC).

The contact interactions introduced by $\mathcal{V}_2$ and $\mathcal{V}_3$ in Eq. (2.8) include divergencies and therefore, they have to be regularized and renormalized [189]. Here, we use a local Gaussian regulator with momentum cutoff λ which has been successfully employed in previous works [146, 198, 202–205]

$$\delta_\lambda(\mathbf{r}) = \left(\frac{\lambda}{2\sqrt{\pi}}\right)^3 \exp\left(-\frac{\lambda^2}{4}\mathbf{r}^2\right), \tag{2.9}$$

where λ is inversely proportional to the range of an interaction $\sim 1/\lambda$. Consequently, the Gaussian regulator (2.9) smears the contact interaction over a certain cutoff dependent distance and in the contact limit $\lambda \to \infty$ it becomes the Dirac $\delta(\mathbf{r})$ function. This procedure yields two-body V_2 and three-body V_3 potentials which together with the kinetic energy T_k enter the total LO $\not\pi$EFT Hamiltonian $H_\lambda^{(\mathrm{LO})}$ [169]:

$$\begin{aligned} H_\lambda^{(\mathrm{LO})} &= T_\mathrm{k} + V_2 + V_3, \\ \text{where } V_2 &= \textstyle\sum_{I,S} C_\lambda^{I,S} \sum_{i<j} \mathcal{P}_{ij}^{I,S} \delta_\lambda(\mathbf{r}_{ij}) \\ \text{and } V_3 &= \textstyle\sum_{I,S,\alpha} D_{\lambda,\alpha}^{I,S} \sum_{i<j<k} \mathcal{Q}_{ijk}^{I,S,\alpha} \sum_{\mathrm{cyc}} \delta_\lambda(\mathbf{r}_{ij}) \delta_\lambda(\mathbf{r}_{jk}). \end{aligned} \tag{2.10}$$

Here, $\mathcal{P}_{ij}^{I,S} = \mathcal{P}_{ij}^I \mathcal{P}_{ij}^S$ and $\mathcal{Q}_{ijk}^{I,S,\alpha} = \mathcal{Q}_{ijk}^I \mathcal{Q}_{ijk}^S \mathcal{Q}_{ijk}^\alpha$ are the projection operators to 2- and 3-body s-wave isospin-spin (I,S) channels, respectively (for more details see Appendix A). The index $\alpha = \{NNN, \Lambda NN, \Lambda\Lambda N\}$ denotes different particle content of 3-body channels in order to distinguish between s-wave NNN and $\Lambda\Lambda N$ channels with the same $I = 1/2$, $S = 1/2$ quantum numbers. The corresponding projector $\mathcal{Q}_{ijk}^\alpha$ is defined in Eq. (A.15). Throughout this work we use notation with α only when we work simultaneously with the nuclear and double-Λ hypernuclear LO $\not\pi$EFT otherwise it is neglected. The 2- and 3-body low-energy-constants (LECs) $C_\lambda^{I,S}$ and $D_{\lambda,\alpha}^{I,S}$ are fixed for each λ by the same set of experimental data.

In the case of finite λ, the Hamiltonian $H_\lambda^{(\mathrm{LO})}$ is regulator dependent. This can be clarified using representation of the Dirac function $\delta(\mathbf{r})$ through derivatives of the Gaussian regulator $\delta_\lambda(\mathbf{r})$ in Eq. (2.9) [206]

$$\delta(\mathbf{r}) = \sum_{klm=0}^{\infty} \frac{1}{k!l!m!} \left(-\frac{1}{\lambda^2}\right)^{k+l+m} \partial_x^{2k}\, \partial_y^{2l}\, \partial_z^{2m}\, \delta_\lambda(\mathbf{r}). \tag{2.11}$$

After some algebraic manipulation one can in return express $\delta_\lambda(\mathbf{r})$ as a series of derivatives of $\delta(\mathbf{r})$ with increasing order

$$\delta_\lambda(\mathbf{r}) = \delta(\mathbf{r}) + \frac{\nabla_r^2}{\lambda^2}\delta(\mathbf{r}) - 2\left(\frac{\nabla_r^2}{\lambda^2}\right)^2 \delta(\mathbf{r}) + \dots \quad . \tag{2.12}$$

The Gaussian regulator thus induces not only the cutoff independent leading order interaction but also cutoff and momentum dependent sub-leading contributions starting with $\nabla_r^2\delta(\mathbf{r})$ (Q^2; NLO). Moreover, $\delta_\lambda(\mathbf{r})$ does not commute with the permutation operator further introducing p-wave interaction, which however exhibits the same behavior as higher orders in Eq. (2.12) and starts to vanish with increas-

ing λ [207]. It is to be noted that p-wave contribution can be projected out by the projection operators in $H_\lambda^{(\mathrm{LO})}$ (2.10).

Equation (2.12) implies that higher order contributions enter as powers of (Q/λ). Consequently, the momentum cutoff λ can be understood as a certain scale parameter with respect to a typical momentum Q [146]. Once $C_\lambda^{I,S}$ and $D_{\lambda,\alpha}^{I,S}$ in the $H_\lambda^{(\mathrm{LO})}$ (2.10) are fixed for certain λ, all calculated observables which were not employed to fit LECs, exhibit cutoff dependence. For $\lambda \gg Q$ this dependence becomes residual with dominant contribution $\mathcal{O}(Q/\lambda)$. It is further suppressed with λ approaching the regulator group invariant limit $\lambda \to \infty$ [146]

$$O(\lambda) = O(\lambda \to \infty) + \alpha \frac{Q}{\lambda} + \beta \left(\frac{Q}{\lambda}\right)^2 + \dots \quad . \tag{2.13}$$

In order to suppress regularization error, the calculated observable $O(\lambda)$ for finite but different values of λ is extrapolated as $O(\lambda) = b_0 + b_1/\lambda + b_2/\lambda^2 + \dots$ where b_0 is associated with the LO prediction $O(\lambda \to \infty)$.

As demonstrated earlier, the cutoff dependence is caused by sub-leading contributions which further iterate in the corresponding few-body Schrödinger equation and thus can lead to a highly non-trivial system-specific $O(\lambda)$ behavior. The dependence in Eq. (2.13) is guaranteed only for $\lambda \gg Q$ which can be fulfilled for a high enough cutoff value.

It is to be stated that in view of the $\not\pi$EFT formalism the finite value of λ does not have any physical interpretation and it is basically used as a tool to provide a scale to renormalized LECs and to perform extrapolation to $\lambda \to \infty$ [189], i.e. to obtain regulator independent results. Therefore, it should not be misunderstood that some new high momentum physics enters with increasing λ. Instead, in the $\lambda \to \infty$ limit there is just the LO contribution. This certainly introduces a systematic error since the LO describes physics only for very small, strictly speaking zero momenta. Calculated $O(\lambda \to \infty)$ observables (2.13) thus should not be considered as an accurate predictions - the missing sub-leading terms would improve physical description at higher Q. Using a LO theory thus introduces *truncation error* which can be quantified as $(Q/M)^2$ [204], i.e. by the order of a missing NLO term which introduces the largest uncertainty, where Q is the typical momentum scale in the studied system and M is the breakup scale of the theory. For nuclear LO $\not\pi$EFT the truncation error is rather high $\approx 30\%$ [204]. For single-Λ and double-Λ hypernuclear LO $\not\pi$EFT it is $\approx 9\%$ [146, 169].

There are in total 5 two-body (NN, ΛN, $\Lambda\Lambda$) and 5 three-body (NNN, ΛNN,

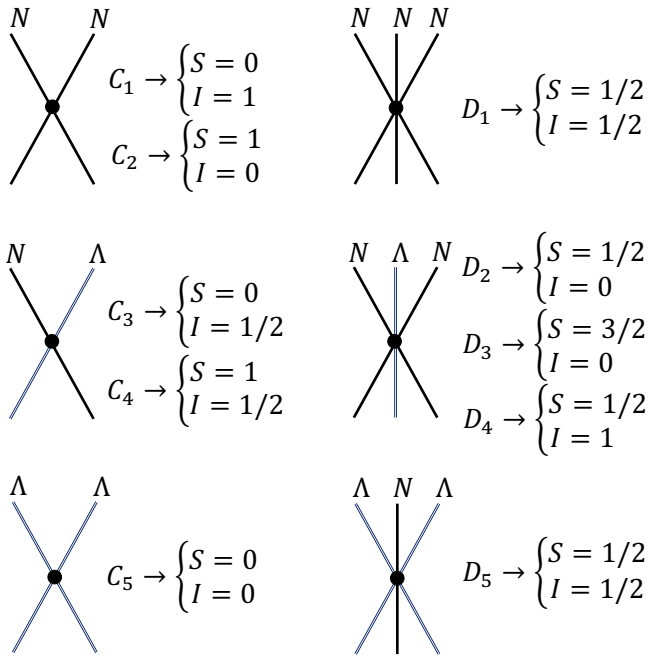

Two-body LECs :

C_1 $(C_\lambda^{I=1,S=0})$: a_0^{NN} = -18.63 fm [208]

C_2 $(C_\lambda^{I=0,S=1})$: $B(^2\mathrm{H})$ = 2.22452 MeV [209]

C_3 $(C_\lambda^{I=1/2,S=0})$: $a_0^{\Lambda N}$

C_4 $(C_\lambda^{I=1/2,S=1})$: $a_1^{\Lambda N}$

C_5 $(C_\lambda^{I=0,S=0})$: $a_0^{\Lambda\Lambda}$

Three-body LECs :

D_1 $(D_{\lambda,NNN}^{I=1/2,S=1/2})$: $B(^3\mathrm{H})$ = 8.482 MeV [210]

D_2 $(D_{\lambda,\Lambda NN}^{I=0,S=1/2})$: $B_\Lambda(^3_\Lambda\mathrm{H})$ = 0.13(5) MeV [133]

D_3 $(D_{\lambda,\Lambda NN}^{I=0,S=3/2})$: $E_{exc}(^4_\Lambda\mathrm{H}, 1^+)$ = 1.09(2) MeV [211]

D_4 $(D_{\lambda,\Lambda NN}^{I=1,S=1/2})$: $B_\Lambda(^4_\Lambda\mathrm{H}, 0^+)$ = 2.16(8) MeV [212]

D_5 $(D_{\lambda,\Lambda\Lambda N}^{I=1/2,S=1/2})$: $\Delta B_{\Lambda\Lambda}(^6_{\Lambda\Lambda}\mathrm{He})$ = 0.67(17) MeV [213]

Figure 2.4: The s-wave contact terms in different isospin-spin (I, S) channels with respective bare LECs considered in the LO (hyper)nuclear $\not\pi$EFT Lagrangian density in Eq. (2.8) (upper part) associated with their regularized form fixed by listed low-energy data (lower part). For more details see the text. The upper part of the figure was adopted from the author's publication [169].

Table 2.1: Values of spin-singlet $a_0^{\Lambda N}$ and spin-triplet $a_1^{\Lambda N}$ scattering lengths[3] used to fit hypernuclear 2-body LECs together with effective ranges $r_0^{\Lambda N}$ and $r_1^{\Lambda N}$ (in fm). Corresponding Λ separation energies $B_\Lambda({}^5_\Lambda\mathrm{He})$ (in MeV), predicted within $\not\pi$EFT for $\lambda \to \infty$ are to be compared with the experimental value $B_\Lambda({}^5_\Lambda\mathrm{He}) = 3.12(2)$ MeV [133].

	$a_0^{\Lambda N}$	$r_0^{\Lambda N}$	$a_1^{\Lambda N}$	$r_1^{\Lambda N}$	$B_\Lambda({}^5_\Lambda\mathrm{He}; \lambda \to \infty)$ [146]
Alexander B [117]	-1.80	2.80	-1.60	3.30	3.01(10)
NSC97f [123]	-2.60	3.05	-1.71	3.33	2.74(11)
χEFT(LO) [129]	-1.91	1.40	-1.23	2.20	3.96(08)
χEFT(NLO) [130]	-2.91	2.78	-1.54	2.27	3.01(06)

[3] We use the effective range expansion sign convention defined as $k\mathrm{cotg}(\delta) = -\frac{1}{a_s} + \frac{1}{2} r_s k^2 + \cdots$.

$\Lambda\Lambda N$) LECs which are summarized together with the corresponding low energy observables applied to fix their values in Fig. 2.4. The nuclear LECs $C_\lambda^{I=0,S=1}$, $C_\lambda^{I=1,S=0}$, and $D_{\lambda,NNN}^{I=1/2,S=1/2}$ are fitted to the deuteron binding energy, NN spin-singlet scattering length a_0^{NN}, and to the triton binding energy, respectively. Hypernuclear two-body LECs $C_\lambda^{I=1/2,S=0}$, $C_\lambda^{I=1/2,S=1}$ are fixed by the ΛN scattering length in a spin-singlet $a_0^{\Lambda N}$ and spin-triplet $a_1^{\Lambda N}$ channel. Three-body hypernuclear LECs $D_\lambda^{I=0,S=1/2}$, $D_\lambda^{I=1,S=1/2}$, and $D_\lambda^{I=0,S=3/2}$ are fitted to the experimental values of Λ separation energies $B_\Lambda({}^3_\Lambda\mathrm{H})$, $B_\Lambda({}^4_\Lambda\mathrm{H}, 0^+)$ [$B_\Lambda({}^\mathrm{A}_\Lambda\mathrm{X}) = B({}^\mathrm{A}_\Lambda\mathrm{X}) - B({}^{\mathrm{A}-1}\mathrm{X})$, where $B(\dots)$ is the binding energy] and the excitation energy $E_\mathrm{exc}({}^4_\Lambda\mathrm{H}, 1^+)$. The LECs of the double-Λ hypernuclear part $C_\lambda^{I=0,S=0}$ and $D_{\lambda,\Lambda\Lambda N}^{I=1/2,S=1/2}$ are fixed by the spin-singlet $\Lambda\Lambda$ scattering length $a_0^{\Lambda\Lambda}$ and experimental $\Delta B_{\Lambda\Lambda}({}^6_{\Lambda\Lambda}\mathrm{He}) = B_{\Lambda\Lambda}({}^6_{\Lambda\Lambda}\mathrm{He}) - 2B_\Lambda({}^5_\Lambda\mathrm{He})$ $\left[B_{\Lambda\Lambda}({}^\mathrm{A}_{\Lambda\Lambda}\mathrm{X}) = B({}^\mathrm{A}_{\Lambda\Lambda}\mathrm{X}) - B({}^{\mathrm{A}-2}\mathrm{X})\right]$.

Since $a_0^{\Lambda N}$ and $a_1^{\Lambda N}$ are not constrained sufficiently well by experiment, we use their values given by direct analysis of scattering data [117] or predicted by several models of the ΛN interaction [123, 129, 130]. Considered $a_0^{\Lambda N}$ and $a_1^{\Lambda N}$ are given in Table. 2.1. The $\not\pi$EFT approach was applied to s-shell Λ hypernuclei and, among others, the experimental value of the Λ separation energy B_Λ in ${}^5_\Lambda$He was successfully reproduced [146] as demonstrated in the last column of Table 2.1. There is no strict experimental constraint on the $a_0^{\Lambda\Lambda}$ scattering length, consequently, we consider $a_0^{\Lambda\Lambda} \in \langle -1.9; -0.5 \rangle$ fm range proposed by the analysis of $\Lambda\Lambda$ correlations in heavy-ion collisions [150].

We stress that the (hyper)nuclear LO $\not\pi$EFT provides us with a unified description of s-shell nuclei, Λ- and $\Lambda\Lambda$ hypernuclei. In Table 2.2, we summarize few-body systems together with scattering lengths which are employed as input to constrain

Table 2.2: Few-body systems and scattering lengths which are employed to constrain the LO $\not$EFT (red) together with nuclear and hypernuclear systems which are prediction of the theory (black).

Strangeness	A=2	A=3	A=4	A=5	A=6
$\mathcal{S}=0$	a_0^{NN} $^2\mathrm{H}(1^+)$	$^3\mathrm{H}(\frac{1}{2}^+)$	$^4\mathrm{He}(0^+)$		
$\mathcal{S}=-1$	$a_0^{\Lambda N}$ $a_1^{\Lambda N}$	$^3_\Lambda\mathrm{H}(\frac{1}{2}^+)$ $^3_\Lambda\mathrm{H}(\frac{3}{2}^+)$ $\Lambda nn(\frac{1}{2}^+)$	$^4_\Lambda\mathrm{H}(0^+)$ $^4_\Lambda\mathrm{H}(1^+)$	$^5_\Lambda\mathrm{He}(\frac{1}{2}^+)$	
$\mathcal{S}=-2$	$a_0^{\Lambda\Lambda}$	$\Lambda\Lambda n(\frac{1}{2}^+)$	$^4_{\Lambda\Lambda}\mathrm{H}(1^+)$ $\Lambda\Lambda nn(0^+)$	$^5_{\Lambda\Lambda}\mathrm{H}(\frac{1}{2}^+)$	$^6_{\Lambda\Lambda}\mathrm{He}(0^+)$

the theory (red color). The black color then marks systems which come out as a prediction of the LO (hyper)nuclear $\not$EFT . Since we consider here full isospin symmetry, i.e. the same mass of the proton and neutron, no charge symmetry breaking effects (CSB), and no Coulomb interaction, the theory can in addition to the systems presented in the table predict their degenerate equivalents: $^3\mathrm{H}-{}^3\mathrm{He}$, $^4_\Lambda\mathrm{H}-{}^4_\Lambda\mathrm{He}$, $^5_{\Lambda\Lambda}\mathrm{H}-{}^5_{\Lambda\Lambda}\mathrm{He}$, $\Lambda\Lambda n-\Lambda\Lambda p$ isodublets and $\Lambda nn-{}^3_\Lambda\mathrm{H}-{}^3_\Lambda\mathrm{He}$, $\Lambda\Lambda nn-{}^4_{\Lambda\Lambda}\mathrm{H}-{}^4_{\Lambda\Lambda}\mathrm{He}$ isotriplets. It is to be noted that CSB enters $\not$EFT at higher orders [214]. This can be seen for nuclear part from the fact that the NN scattering length in a spin-singlet channel, which is applied to fit 2-body $C_\lambda^{I=1,S=0}$ LEC, is associated with the experimental nn scattering length. For example, using experimental np scattering length in the spin-singlet channel instead, which is a bit larger, has only small impact on LO $\not$EFT predictions - the change in the ^{4}He bound state energy is less than 2% and in the Λ separation energy $B_\Lambda(^5_\Lambda\mathrm{He})$ it is about 1% [146].

Figure 2.5 presents an example of a Stochastic Variational Method (SVM) calculation of $B_\Lambda(^5_\Lambda\mathrm{He})$ within the LO $\not$EFT . For each cutoff λ, LECs in $H_\lambda^{(\mathrm{LO})}$ (2.10) are fitted to the same set of low energy observables given in Fig. 2.4 plus values of spin-singlet and spin-triplet ΛN scattering lengths predicted by the χEFT(NLO) model (see Table 2.1). The Λ separation energies of $^5_\Lambda$He for different λ, obtained as $B_\Lambda(^5_\Lambda\mathrm{He};\ \lambda)=B(^5_\Lambda\mathrm{He};\ \lambda)-B(^4\mathrm{He};\ \lambda)$, are shown in the figure as black dots with the corresponding error induced by the SVM. We see that for small values of cutoff λ, $B_\Lambda(^5_\Lambda\mathrm{He};\ \lambda)$ exhibits non-trivial behavior due to regulator dependent higher order terms induced by the finite cutoff. Once λ reaches high enough value $\lambda\approx 3$ fm^{-1}, calculated $B_\Lambda(^5_\Lambda\mathrm{He};\ \lambda)$ start to show $\sim 1/\lambda$ behavior (2.13) gradually suppressing cutoff dependent contributions. The black solid line then indicates two-parameter

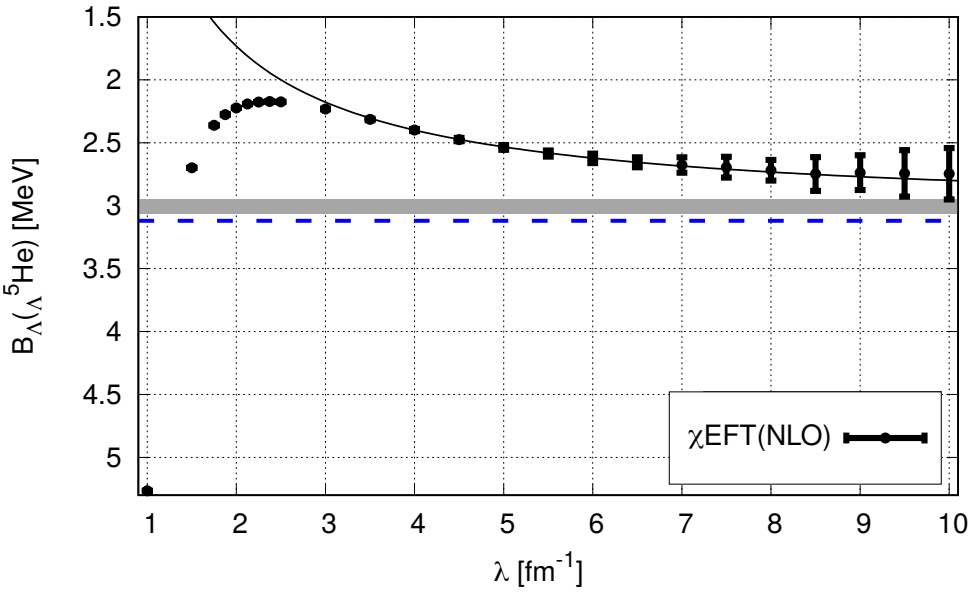

Figure 2.5: The Λ separation energy $B_\Lambda(^5_\Lambda\mathrm{He})$ as a function of the cutoff λ in LO $\not\pi$EFT using the χEFT(NLO) set of ΛN scattering lengths given in Table 2.1. Black dots denote results of Stochastic Variational Method calculations (for more details see Chapter 3) for different finite λ, the corresponding error bars mark numerical uncertainties induced by the few-body method. Solid black line illustrates a two-parameter fit b_0+b_1/λ, starting from $\lambda = 4\,\mathrm{fm}^{-1}$. Gray horizontal band gives $\lambda \to \infty$ extrapolation uncertainties. Dashed horizontal line denotes the experimental value $B_\Lambda(^5_\Lambda\mathrm{He})$=3.12(2) MeV [133]. The figure was adopted from Ref. [146].

fit $b_0 + b_1/\lambda$ of calculated $B_\Lambda(^5_\Lambda\mathrm{He};\ \lambda)$ values yielding $B_\Lambda(^5_\Lambda\mathrm{He};\ \infty) = 3.01(06)$ MeV, denoted by the gray horizontal band, which agrees well with the experimental Λ separation energy $B_\Lambda^{\mathrm{exp}}(^5_\Lambda\mathrm{He})$ denoted by the blue dashed line.

The current version of the hypernuclear $\not\pi$EFT [146, 169] considers only N and Λ degrees of freedom. Consequently, effects related to $\Lambda N - \Sigma N$ mixing are not accounted for by explicit incorporation of Σ, which would lead to coupled channel formalism, but they are partially included through ΛN and ΛNN low energy constants [146]. In the case of the $\Lambda\Lambda$ interaction there exist couplings to higher lying ΞN and $\Sigma\Sigma$ channels which are included implicitly in the two-body $\Lambda\Lambda$ scattering length. However, fixing $\Lambda\Lambda N$ LEC to $\Delta B_{\Lambda\Lambda}(^6_{\Lambda\Lambda}\mathrm{He})$ introduces certain error since in this system ΞN channel is partially Pauli blocked, unlike lighter $\Lambda\Lambda$-hypernuclei. According to G-matrix calculations [215] disregarding Pauli blocking effectively increases $\Delta B_{\Lambda\Lambda}(^6_{\Lambda\Lambda}\mathrm{He})$ by ≈ 0.25 MeV which indicates that the $\Lambda\Lambda N$ force in 5-, 4-, and 3-body s-shell $\Lambda\Lambda$-hypernuclear systems has to be appropriately modified.

Chapter 3

Methodology

This thesis addresses a topical issue of interactions of hadrons in few-body systems, namely η-nuclei, Λ^* systems, Λ-, and $\Lambda\Lambda$ hypernuclei. Rapid improvement of both numerical methods and computational facilities allowed to develop highly accurate tools for the description of these systems.

Few-body bound states studied in this work are calculated within the SVM with a correlated Gaussian basis which proved to yield quite accurate solutions competible with other few-body techniques. For the purpose of our study we developed a new efficient SVM code which has been employed to get a precise solution of the N-body Shrödinger equation

$$H\Psi = E\Psi \tag{3.1}$$

for $N \leq 8$. This allowed us to relate underlying interaction models with N-body observables and thus put our present understanding of interactions of hadrons at low-energies to the test with properties of experimentally observed hadronic systems.

In order to describe both few-body bound and continuum regions, we extended the SVM using two methods - the Inverse Analytic Continuation in the Coupling Constant (IACCC) and the Complex Scaling Method (CSM). This allowed us to study resonances, virtual states or to calculate phase shifts using a complex scaled Continuum Level Density (CLD).

The aim of this chapter is to provide the reader with main features of the above methods which served in this work as a tool to study interactions of hadrons in few-body systems. All the considered techniques are firmly established and frequently used in nuclear physics, hadronic physics or in quantum chemistry. Therefore, we skip tedious mathematical derivations which would mostly duplicate previous works, listed in enclosed references.

We start with an introduction of correlated Gaussian basis states used in our calculations. Then we present the Stochastic Variational Method which is applied in the selection of an appropriate basis set. Finally, we introduce IACCC and CSM which are employed in our study of few-body continuum. For completeness the description of various continuum phenomena which can occur on a two-body level are given in Appendix B.

3.1 Correlated Gaussian basis

Properties of a few-body system are affected by various phenomena which arise as a result of highly non-trivial interparticle dynamics encoded in the Hamiltonian H. Special care has to be payed to ensure that the total wave function Ψ given by H is described properly while computational complexity is maintained at a reasonable level.

The wave function Ψ is usually approximated using a carefully selected trial function $F(\alpha)$ where its variational parameters $\alpha = (\alpha_1, \alpha_2, ...)$ can be determined minimizing corresponding expectation value of the total energy

$$E(\alpha) = \frac{\langle F(\alpha)|H|F(\alpha)\rangle}{\langle F(\alpha)|F(\alpha)\rangle}. \tag{3.2}$$

In order to address effects related to correlations between particles the trial function is often factorized in a form proposed by Jastrow [216]

$$F = \prod_{l>k=1}^{N} f_{kl}(\mathbf{r}_k - \mathbf{r}_l), \tag{3.3}$$

where F is written as a product of functions f_{kl} explicitly dependent on a relative distance between particles $\mathbf{r}_k - \mathbf{r}_l$. Here, we follow the work of Suzuki and Varga [217] who expressed each f_{kl} using Gaussian

$$F(\alpha) = \prod_{l>k=1}^{N} \exp\left[-\frac{(\mathbf{r}_k - \mathbf{r}_l)^2}{\alpha_{kl}^2}\right] = \exp\left[-\sum_{l>k=1}^{N} \frac{(\mathbf{r}_k - \mathbf{r}_l)^2}{\alpha_{kl}^2}\right], \tag{3.4}$$

where α_{kl} stands for $N(N-1)/2$ non-linear parameters. In principle, other forms of f_{kl} are possible as well, such as correlated exponential functions applied in Ref. [218], however, they mostly lead to rather complicated expressions which make their application to systems of more than three particles rather difficult.

In order to separate intrinsic and center of mass part of $F(\alpha)$ (3.4), single particle coordinates $\mathbf{r}_i$ are transformed into the Jacobi coordinate set $\mathbf{x}_k$,

$$\mathbf{x}_k = \sum_{i=1}^{N} U_{ki}\mathbf{r}_i, \quad \mathbf{r}_i - \mathbf{r}_j = \sum_{k=1}^{N} \left(U_{ik}^{-1} - U_{jk}^{-1}\right)\mathbf{x}_k, \tag{3.5}$$

where U is a transformation matrix defined as

$$U = \begin{pmatrix} -1 & 1 & 0 & \cdots & 0 \\ -\frac{m_1}{m_{1-2}} & -\frac{m_2}{m_{1-2}} & 1 & \cdots & 0 \\ \vdots & & & & \vdots \\ -\frac{m_1}{m_{1-(N-1)}} & -\frac{m_2}{m_{1-(N-1)}} & \cdots & \cdots & 1 \\ -\frac{m_1}{m_{1-N}} & -\frac{m_2}{m_{1-N}} & \cdots & \cdots & \frac{m_N}{m_{1-N}} \end{pmatrix} \tag{3.6}$$

and $m_{1-i} = m_1 + m_2 + \cdots + m_i$ is the sum of the first i particle masses. The Jacobi vectors $\mathbf{x}_1, \ldots, \mathbf{x}_{N-1}$ now describe intrinsic degrees of freedom whereas $\mathbf{x}_N$ is the center of mass coordinate. Performing the transformation (3.5) and neglecting the center of mass part of $F(\alpha)$ (3.4) defines the correlated Gaussian

$$F(A) = \mathrm{e}^{-\frac{1}{2}\mathbf{x}^T A \mathbf{x}}, \tag{3.7}$$

where $\mathbf{x}^T = (\mathbf{x}_1, ..., \mathbf{x}_{N-1})$ and A is the $(N-1)$ dimensional matrix

$$A_{ij} = \sum_{kl}^{N-1} \left(U_{ki}^{-1} - U_{li}^{-1}\right)^T \frac{1}{\alpha_{kl}^2} \left(U_{kj}^{-1} - U_{lj}^{-1}\right). \tag{3.8}$$

The matrix A is symmetric and depends on $N(N-1)/2$ parameters. Further, from the condition of square integrability of the correlated Gaussian (3.7) A has to be positive definite.

Functions $\psi^i(A^i) \equiv F(A^i)$ (3.7) with different matrices A^i represent a dense basis (for discussion on its completeness see [219] and references therein). In most cases, approximating the total wave function Ψ with just one $F(A)$ (3.7) does not yield accurate results, therefore, we express Ψ as linear combination of K correlated Gaussian basis states $\psi^i(A^i)$

$$\Psi = \sum_{i=1}^{K} c_i \ \psi^i(A^i) \tag{3.9}$$

selecting appropriate values of non-linear parameters in each A^i matrix. This basis set was first used in a study of molecular and atomic systems [220, 221]. The application to few-body nuclei was proposed by Suzuki and Varga [217] and it was demonstrated in later works that an extended version of correlated Gaussian basis states is highly efficient in the description of few-body systems with both central and non-central interactions (see [219, 222–225] and references therein).

3.1.1 Angular momentum part

The correlated Gaussian in Eq. (3.7) is spherically symmetric and applicable only to few-body systems with the total orbital momentum $L = 0$ and positive parity. In order to describe higher orbital momenta $L > 0$, basis states $\psi^i(A^i)$ have to be supplemented with the angular momentum part $\theta_{LM_L}(\mathbf{x})$ [219]

$$\psi^i_{LM_L}(A^i;\ \mathbf{x}) = \mathrm{e}^{-\frac{1}{2}\mathbf{x}^T A^i \mathbf{x}}\ \theta_{LM_L}(\mathbf{x}), \tag{3.10}$$

where M_L is projection of L along the third axis. The angular part $\theta_{LM_L}(\mathbf{x})$ can be expressed using solid spherical harmonics $\mathcal{Y}_{lm}(r)$ in the form [219]

$$\theta_{LM_L}(\mathbf{x}) = \left[\left[\left[\ [\mathcal{Y}_{l_1}(\mathbf{x}_1) \otimes \mathcal{Y}_{l_2}(\mathbf{x}_2)]_{L_{12}} \otimes \mathcal{Y}_{l_3}(\mathbf{x}_3)\right]_{L_{123}} \cdots\right]_{L_{1\ldots(N-2)}} \otimes \mathcal{Y}_{l_{N-1}}(\mathbf{x}_{N-1})\right]_{LM_L}, \tag{3.11}$$

where

$$\mathcal{Y}_{lm}(r) = r^l \mathrm{Y}_{lm}(r) \tag{3.12}$$

and $[\ \otimes\ ]$ is a coupling through Clebsch-Gordan coefficients. In general, there are various configurations $L_{\mathrm{conf}} = (...((l_1, l_2)L_{12}, l_3)L_{123}...)L$ which yield the same L. Since angular momenta of relative motion l_i are not conserved quantities, a sufficient amount of L_{conf} should be considered to obtain good description of the studied system [219]. This means that basis states (3.10) would be dependent on the corresponding configuration of the $\theta_{LM_L}(\mathbf{x})$ part. Those L_{conf} with high l_i are often neglected to prevent an excessively large amount of configurations [226]. However, as pointed out in Ref. [219] this approach starts to be highly inefficient with an increasing amount of particles where the number of L_{conf} increases dramatically.

In our calculations we describe the angular momentum part $\theta_{LM_L}(\mathbf{x})$ using the Global Vector Representation (GVR) [217, 219, 223, 225]. This approach is considerably more effective since it implicitly includes large variety of possible configurations which would have to be otherwise considered through vectorial coupled product

(3.11). Following Ref. [225] the $\theta_{LM_L}(\mathbf{x})$ part of a correlated Gaussian is for the system with given parity π expressed as

$$\begin{aligned} &\theta_{LM_L}(\mathbf{u}_1, \mathbf{u}_2;\ \mathbf{x}) = \left[\mathcal{Y}_{L_1}(\mathbf{v}_1) \otimes \mathcal{Y}_{L_2}(\mathbf{v}_2)\right]_{LM_L}, \\ &\mathbf{v}_1 = \mathbf{u}_1^T\mathbf{x}, \qquad \mathbf{v}_2 = \mathbf{u}_2^T\mathbf{x}, \end{aligned} \tag{3.13}$$

where $L_1 = L$, $L_2 = 0$ for natural parity states $(-1)^L = \pi$ and $L_1 = L$, $L_2 = 1$ for unnatural parity states $(-1)^{L+1} = \pi$. Global vectors $\mathbf{v}_1$ and $\mathbf{v}_2$ depend on $(N-1)$ parameters contained in vectors $\mathbf{u}_1$ and $\mathbf{u}_2$, respectively.

As demonstrated in Ref. [219] the angular part in the GVR form (3.13) can be expressed as a linear combination of all possible vector coupled products (3.11) with different configurations. Consequently, defining the spatial part of the correlated Gaussian basis state using GVR

$$\psi^{(\mathrm{spatial})}_{LM_L}(A, \mathbf{u}_1, \mathbf{u}_2; \mathbf{x}) = e^{-\mathbf{x}^T A \mathbf{x}} \left[\mathcal{Y}_{L_1}(\mathbf{u}_1^T\mathbf{x}) \otimes \mathcal{Y}_{L_2}(\mathbf{u}_2^T\mathbf{x})\right]_{LM_L} \tag{3.14}$$

ensures that all possible configurations L_{conf} are included. Elements of the matrix A and vectors $\mathbf{u}_1$, and $\mathbf{u}_2$ are then regarded as continuous parameters defining a given basis state. Another advantage of GVR is that the corresponding matrix elements can be expressed in a compact form and, moreover, antisymmetrization (symmetrization) and dependence on a size of the system are accounted for without considerable effort.

For a system with the total angular momentum J, and parity π we construct a correlated Gaussian basis state within the (L, S) coupling scheme

$$\psi^i_{(L^iS^i)J^\pi M_J\ TM_T}(A^i, \mathbf{u}^i_1, \mathbf{u}^i_2; \mathbf{x}) = \left[\psi^{(\mathrm{spatial})}_{L^i}(A^i, \mathbf{u}^i_1, \mathbf{u}^i_2) \otimes \psi^{(\mathrm{spin})}_{S^i}\right]_{JM_J} \psi^{(\mathrm{isospin})}_{IM_I} \tag{3.15}$$

where S^i stands for the total spin coupled to L^i in order to obtain the total angular momentum J. Both the spin $\psi^{(\mathrm{spin})}_{S^iM_{S^i}}$ and isospin $\psi^{(\mathrm{isospin})}_{IM_I}$ parts, where I stands for the total isospin with projection to the third axis M_I, are addressed in more detail in the following subsection. For given J there can be several different (L^i, S^i) components (sometimes referred to as channels) contributing to the total wave function $\Psi_{J^\pi M_J I M_I}$. This is in particular important for systems with realistic interactions with a non-central part such as the tensor or $\mathbf{L}.\mathbf{S}$ force which introduce coupling between different channels. Consequently, in this specific case, we consider basis states (3.15) with all possible (L^i, S^i) components. Calculation of matrix elements of different operators is briefly commented in Appendix A.

3.1.2 Spin and isospin part

For nucleons the spin $\psi^{(\mathrm{spin})}_{SM_S}$ and isospin $\psi^{(\mathrm{isospin})}_{IM_I}$ parts of the N-body correlated Gaussian basis state are constructed by applying subsequent coupling of single particle spin and isospin. This procedure can be for $\psi^{(\mathrm{spin})}_{SM_S}$ (or equivalently $\psi^{(\mathrm{isospin})}_{IM_I}$) written as

$$\psi^{(\mathrm{spin})}_{SM_S} = \left[\left[\cdots\left[\left[\left|\frac{1}{2}\right\rangle \otimes \left|\frac{1}{2}\right\rangle\right]_{S_{12}} \otimes \left|\frac{1}{2}\right\rangle\right]_{S_{123}} \cdots \otimes \left|\frac{1}{2}\right\rangle\right]_{S_{12\ldots(N-1)}} \otimes \left|\frac{1}{2}\right\rangle\right]_{SM_S}, \tag{3.16}$$

where S_{12} is the total spin of the first two coupled particles, S_{123} first three etc. Consequently, the coupling of single particle spin states $\left|\frac{1}{2}\right\rangle$ does not have to be unique and for a given spin S various spin configurations $S_{\mathrm{conf}} = (S_{12}, S_{123}, \ldots, S_{12\ldots(N-1)})$ (or equivalently I_{conf}) can exist.

Possible spin and isospin configurations create a discrete basis set. In order to obtain correct description of a few-body system with spin and isospin dependent interactions all S_{conf} and I_{conf} have to be considered. For example, the binding energy of ^{6}Li with the Minnesota NN interaction [227] and just one spin and isospin configuration is ≈ 2 MeV lower with respect to the full calculation [228].

We use the isospin part $\psi^{(\mathrm{isospin})}_{IM_I}$ to distinguish between different particles, namely nucleons, η meson, Λ^*, and Λ hyperons considered in this work. Both η and Λ have isospin $I = 0$, consequently, their coupling to the nuclear part $\psi^{(\mathrm{nuclear})}_{IM_I}$ can be expressed as

$$\psi^{(\mathrm{isospin})}_{IM_I} = \psi^{(\mathrm{nuclear})}_{IM_I} \otimes |0_\eta\rangle \tag{3.17}$$

for η-nuclei and

$$\begin{aligned} \psi^{(\mathrm{isospin})}_{IM_I} &= \psi^{(\mathrm{nuclear})}_{IM_I} \otimes |0_\Lambda\rangle\,, \\ \psi^{(\mathrm{isospin})}_{IM_I} &= \psi^{(\mathrm{nuclear})}_{IM_I} \otimes |0_\Lambda\rangle \otimes |0_\Lambda\rangle\,, \end{aligned} \tag{3.18}$$

for Λ- and $\Lambda\Lambda$-hypernuclei, respectively. While η meson is spinless particle and its coupling to the nuclear spin part is equivalent to Eq. (3.17), Λ hyperons as spin $\frac{1}{2}$ fermions contribute to the overall coupling of Eq. (3.16) where N now stands for number of nucleons plus Λs. Hypothetical systems consisting solely of spin $\frac{1}{2}$ Λ^*s are studied using a spin-dependent $\Lambda^*\Lambda^*$ interaction, consequently, the isospin part is dropped out and the spin part is described in the same way as for nucleons.

3.1.3 Symmetrization and antisymmetrization

For fermions antisymmetrization of the correlated Gaussian basis state (3.15) is performed using the operator

$$\mathcal{A} = \sum_{i=1}^{N!} \mathrm{sgn}(\mathcal{P}_i)\ \mathcal{P}_i, \tag{3.19}$$

where the sum runs over all possible particle permutations. Each permutation is then understood as an exchange of single particle indices given by the permutation operator $\mathcal{P}_i$

$$\mathcal{P}_i(1,..,N) = (p_i(1),...,p_i(N)) \tag{3.20}$$

and $\mathrm{sgn}(\mathcal{P}_i)$ stands for corresponding permutation parity.

An effect of $\mathcal{P}_i$ on a set of single particle coordinates $\mathbf{r} = (\mathbf{r}_1,...,\mathbf{r}_N)$ can be expressed using the permutation matrix C_i

$$\mathcal{P}_i\mathbf{r} = C_i\mathbf{r}, \tag{3.21}$$

where

$$(C_i)_{kl} = \begin{cases} 1 & l = p_i(k) \\ 0 & \text{otherwise} \end{cases}. \tag{3.22}$$

The set of Jacobi coordinates $\mathbf{x} = (\mathbf{x}_1,...,\mathbf{x}_N)$, connected with the single particle coordinates through the transformation matrix U (3.6), is then permuted as

$$\mathcal{P}_i\mathbf{x} = UC_iU^{-1}\mathbf{x} = T_i\mathbf{x}, \tag{3.23}$$

where T_i now represents the permutation matrix related to the Jacobi coordinates. It readily follows that the form of correlated Gaussians with the GVR representation of the orbital momentum part (3.15) allows to express the action of the operator $\mathcal{P}_i$ as a transformation of the correlation matrix A and global vectors $\mathbf{u}_1$, $\mathbf{u}_2$

$$\mathcal{P}_i\psi^{(\mathrm{space})}_{LM_L}(A,\mathbf{u}_1,\mathbf{u}_2) = \psi^{(\mathrm{space})}_{LM_L}(T_i^TAT_i, T_i^T\mathbf{u}_1, T_i^T\mathbf{u}_2). \tag{3.24}$$

This property is highly convenient. The permutation does not change the form of basis states, consequently, all relevant matrix elements are written in a compact way and the action of the permutation operator $\mathcal{P}_i$ is simply expressed through their dependence on A, $\mathbf{u}_1$, and $\mathbf{u}_2$. On the other hand the construction of the orbital

momentum part based on subsequent coupling of partial waves (3.11) does not have this advantage and an extra effort is necessary.

The spin $\psi^{(\mathrm{spin})}_{SM_S}$ and isospin part $\psi^{(\mathrm{isospin})}_{IM_I}$ of the basis state (3.15) are permuted explicitly by changing corresponding particle indices.

For bosons, the parity of permutation $\mathrm{sgn}(\mathcal{P}_i)$ in Eq. (3.19) is neglected, which converts $\mathcal{A}$ into the symmetrization operator $\mathcal{S}$. Systems with more then one type of fermions (bosons) are antisymmetrized (symmetrized) at once and redundant permutations given by mixing between different particle species are neglected owing to the fact that the corresponding isospin matrix elements are effectively zero.

3.2 Stochastic Variational Method

The few-body Schrödinger equation (3.1) is solved using the expansion of $\Psi_{J^\pi M_J I M_I}$ in a finite basis of K correlated Gaussians (3.15)

$$\begin{aligned}\Psi_{J^\pi M_J\ I M_I}(\mathbf{x}) &= \sum_{i=1}^{K} c_i\ \psi^i_{(L^i S^i) J^\pi M_J\ I M_I}(A^i, \mathbf{u}^i_1, \mathbf{u}^i_2;\ \mathbf{x}) \\ &= \sum_{i=1}^{K} c_i\ \left[\psi^{(\mathrm{spatial})}_{L^i}(A^i, \mathbf{u}^i_1, \mathbf{u}^i_2;\ \mathbf{x}) \otimes \psi^{(\mathrm{spin})}_{S^i}\right]_{J^\pi M_J} \psi^{(\mathrm{isospin})}_{IM_I},\end{aligned} \tag{3.25}$$

where c_i are linear variational parameters. Using the Ritz variational method we reformulate Eq. (3.1) as a generalized eigenvalue problem

$$\begin{gathered}\mathcal{H}\mathbf{c} = E\mathcal{N}\mathbf{c}, \\ \mathcal{H}_{ij} = \left\langle \psi^i | H | \psi^j \right\rangle, \quad \mathcal{N}_{ij} = \left\langle \psi^i | \psi^j \right\rangle,\end{gathered} \tag{3.26}$$

where its solution yields eigenvalues E^β and corresponding sets of variational parameters $\mathbf{c}^\beta$. The $\mathcal{H}$ and $\mathcal{N}$ are the real symmetric Hamiltonian and overlap matrices, respectively. We have omitted lower indices with quantum numbers of each basis state ψ^i for the sake of simplicity. It is mathematically guaranteed that with an increasing number of basis states each eigenvalue E^β in Eq. (3.26) decreases. Moreover, if the Hamiltonian H has M discrete eigenvalues ϵ^β (bound states) then each of M lowest E^β in Eq. (3.26) converges from above to the corresponding ϵ^β. For more details and proof see Theorem 3.3 and and 3.5 in [219]. This allows us to formulate variational procedure where we search for a converged solution with an increasing number of basis states.

An important task is to find such states $\psi^i_{(L^iS^i)J^\pi M_J\ IM_I}(A^i, \mathbf{u}^i_1, \mathbf{u}^i_2;\ \mathbf{x})$ with appropriate values of parameters in matrix A^i and global vectors $\mathbf{u}^i_1, \mathbf{u}^i_2$, which yield converged result for a reasonable number of basis states. It should be stressed that our basis is dense and any state can be expressed as a linear combination of other correlated Gaussians with different $(A, \mathbf{u}_1, \mathbf{u}_2)$. Consequently, using basis states with carefully selected parameters can significantly reduce their amount necessary to describe the studied system with sufficient accuracy. On the other hand, straightforward methods such as a carefully selected grid of continuous parameters $(A, \mathbf{u}_1, \mathbf{u}_2)$ for each $(L^i, S^i, S^i_{\rm conf}, I^i_{\rm conf})$ quickly leads to an excessively large basis dimension, as pointed out in Ref. [226].

3.2.1 Stochastic Variational Method algorithm

In our work we use the SVM presented by Suzuki and Varga [217] which proved to be highly efficient in the selection of relevant basis states. The SVM was successfully used together with the correlated Gaussian basis in calculations of few-body systems [217,219,222,223,225]; it yields very accurate results competible with other few-body techniques [224].

The SVM algorithm is described in Table 3.1. The procedure is based on a step-by-step systematic construction of a finite basis set where each correlated Gaussian is being stochastically optimized with respect to the total bound state energy $E_{\rm B}$ of the system. We start with the first basis state randomly selecting its discrete parameters $(L^1,\ S^1,\ S^1_{\rm conf},\ I^1_{\rm conf})$ and vectors $\mathbf{u}^1_1,\ \mathbf{u}^1_2$. The correlation matrix A^1 is optimized through parameters α^1_{kl} (3.4) and then calculated using transformation (3.8). First, all α^1_{kl} are initialized randomly selecting their values from a predefined interval $\langle \alpha_{\rm min};\ \alpha_{\rm max}\rangle$. Then each α_{kl} is stochastically tested kk-times by a random selection of its new value and calculating corresponding energy $E_{\rm B} = \frac{\langle\psi^1|H|\psi^1\rangle}{\langle\psi^1|\psi^1\rangle}$ using $\psi^1_{(L^1S^1)J^\pi M_J\ IM_I}(A^1, \mathbf{u}^1_1, \mathbf{u}^1_2;\ \mathbf{x})$. The whole procedure is repeated mm-times on top of individual testing of each α_{kl}. In the end, we choose such parameter set which yields the lowest bound state energy $E_{\rm B}$. Fixing the first basis state we proceed to the stochastic optimization of the second one. Repeating the above procedure we randomly choose $(L^2,\ S^2,\ S^2_{\rm conf},\ I^2_{\rm conf},\ \mathbf{u}^2_1,\ \mathbf{u}^2_2)$. The stochastic optimization of the correlation matrix A^2 is then performed similarly but $E_{\rm B}$ is now calculated by solving the generalized eigenvalue problem $\mathcal{H}\mathbf{c} = E\mathcal{N}\mathbf{c}$ for two basis states where the first one is fixed. From the parameters of the second basis state we again choose those which yield the lowest $E_{\rm B}$. Any further i-th state is then selected in the same way keeping the previous $i-1$ states intact.

Table 3.1: Stochastic Variational Method algorithm.

K	
1	**Selection of the first basis state** (total number of basis states $K = 1$) Select randomly $(L^1,\ S^1,\ S^1_{\rm conf},\ I^1_{\rm conf})$ Select randomly vectors $\mathbf{u}^1_1,\ \mathbf{u}^1_2$ **Optimization of A^1 matrix** Select randomly the parameter set α^1_{kl} Calculate the total energy $E_{\rm B} = \frac{\langle\psi^1\|H\|\psi^1\rangle}{\langle\psi^1\|\psi^1\rangle}$ Fix the basis state with corresponding $(L^1,\ S^1,\ S^1_{\rm conf},\ I^1_{\rm conf},\ A^1,\ \mathbf{u}^1_1,\ \mathbf{u}^1_2)$ which yields the lowest $E_{\rm B}$ among the tested sets of α^1_{kl} Store $\langle\psi^1\|H\|\psi^1\rangle$, $\langle\psi^1\|\psi^1\rangle$, and $E_{\rm B}$ of the fixed basis state
⋮	⋮
i	**First $(i-1)$ basis states fixed, addition of the i-th basis state** (total number of basis states $K = i$) Select randomly $(L^i,\ S^i,\ S^i_{\rm conf},\ I^i_{\rm conf})$ Select randomly vectors $\mathbf{u}^i_1, \mathbf{u}^i_2$ **Optimization of A^i matrix** Select randomly the parameter set α^i_{kl} Calculate matrix elements of $\mathcal{H}_{ij}, \mathcal{N}_{ij}$ for $j = 1, ..., i$ Check positive definitness of $\mathcal{N}$ (if not, select a new set of α^i_{kl}) Check linear dependence (Eq. (3.27)) of tested ψ^i with respect to $\psi^j\ j = 1, ..., i-1$ (if not, select new set of α^i_{kl}) Calculate the lowest eigenvalue $E_{\rm B}$ of $\mathcal{H}\mathbf{c} = E\mathcal{N}\mathbf{c}$ (Eq. (3.31)) Fix the basis state with corresponding $(L^i,\ S^i,\ S^i_{\rm conf},\ I^i_{\rm conf},\ A^i,\ \mathbf{u}^i_1,\ \mathbf{u}^i_2)$ which yields the lowest $E_{\rm B}$ among the tested sets of α^i_{kl} Solve the generalize eigenvalue problem $\mathcal{H}\mathbf{c} = E\mathcal{N}\mathbf{c}$ using fixed ψ^i Store $\mathcal{H}_{ij},\ \mathcal{N}_{ij},\ E^\beta$, and $\mathbf{c}^\beta$ for $\beta = 1, ..., i$
⋮	⋮

Performing the stochastic optimization of the matrix A^i we check for each tested parameter set α_{kl}^i positive definitness of the corresponding overlap matrix $\mathcal{N}$ and linear dependence with respect to the previously selected basis states. In our calculations we require

$$\frac{< \psi^i|\psi^j >}{\sqrt{< \psi^i|\psi^i >< \psi^j|\psi^j >}} < 0.99 \quad \text{for} \quad j = 1, ..., i-1. \tag{3.27}$$

Possible values of ($L,\ S,\ S_{\rm conf},\ I_{\rm conf}$) are given by properties of the system and can be easily determined. Vectors $\mathbf{u}_1,\ \mathbf{u}_2$ enter GVR (3.13) just through their direction, consequently, they are for convenience normalized to one. The parameters α_{kl} are being randomly chosen from the interval $\langle \alpha_{\rm min};\ \alpha_{\rm max} \rangle$ carefully predefined to cover all parts of the total wave function $\Psi_{J^\pi M_J\ IM_I}$. Large values of α contribute to large interparticle distances often important in the description of shallow bound states whereas small α are related to small distances which have significant role in compact systems or bare interactions with a short-range repulsive core.

For the i-th basis state ψ^i the SVM relies on a quite large number (≈ 1000) of randomly selected sets of α_{kl}^i. Each ψ^i with newly chosen set is then tested by calculating the lowest $E_{\rm B}$ of $\mathcal{H}\mathbf{c} = E\mathcal{N}\mathbf{c}$, which provides us with the key information about its most optimal choice. Certainly, a full solution of the generalized eigenvalue problem for each tested α_{kl}^i set is highly inefficient due to their amount. Here, we follow the same procedure as given in Ref. [217] using the full generalized eigenvalue solution of previously fixed $i-1$ basis states. Then the $\mathcal{H}\mathbf{c} = E\mathcal{N}\mathbf{c}$ problem for i basis states can be formulated as

$$\begin{pmatrix} E^1 & 0 & \dots & 0 & \langle \Psi^1|H|\psi^i\rangle \\ 0 & & \dots & & \\ \vdots & & & \vdots & \vdots \\ 0 & & \dots & E^{i-1} & \langle \Psi^{i-1}|H|\psi^i\rangle \\ \langle \psi^i|H|\Psi^1\rangle & & \dots & \langle \psi^i|H|\Psi^{i-1}\rangle & \langle \psi^i|H|\psi^i\rangle \end{pmatrix} \begin{pmatrix} c_1 \\ \vdots \\ \vdots \\ c_{i-1} \\ c_i \end{pmatrix}$$
$$= E \begin{pmatrix} 1 & 0 & \dots & 0 & \langle \Psi^1|\psi^i\rangle \\ 0 & & \dots & & \\ \vdots & & & \vdots & \vdots \\ 0 & & \dots & 1 & \langle \Psi^{i-1}|\psi^i\rangle \\ \langle \psi^i|\Psi^1\rangle & & \dots & \langle \psi^i|\Psi^{i-1}\rangle & \langle \psi^i|\psi^i\rangle \end{pmatrix} \begin{pmatrix} c_1 \\ \vdots \\ \vdots \\ c_{i-1} \\ c_i \end{pmatrix}, \tag{3.28}$$

where E^β and Ψ^β (3.25) for $\beta = 1, ..., i-1$ are eigenvalues and corresponding eigenfunctions obtained for fixed $i-1$ basis states. The matrix on the r.h.s. of Eq. (3.28) can be conveniently transformed to identity matrix applying the Gram-Schmidt orthogonalization procedure

$$|\tilde{\psi}^i> = \frac{|\psi^i> + \sum_{\beta=1}^{i-1} |\Psi^\beta >< \Psi^\beta|\psi^i>}{\sqrt{< \psi^i|\psi^i> + \sum_{\beta=1}^{i-1} < \psi^i|\Psi^\beta >< \Psi^\beta|\psi^i>}}. \tag{3.29}$$

Consequently, one can express Eq. (3.28) in a more convenient form

$$\begin{pmatrix} E^1 & 0 & \dots & 0 & q_1 \\ 0 & & \dots & & \\ \vdots & & & \vdots & \vdots \\ 0 & & \dots & E^{i-1} & q_{i-1} \\ q_1 & & \dots & q_{i-1} & a \end{pmatrix} \begin{pmatrix} c_1 \\ \vdots \\ \vdots \\ c_{i-1} \\ c_i \end{pmatrix} = E \begin{pmatrix} c_1 \\ \vdots \\ \vdots \\ c_{i-1} \\ c_i \end{pmatrix}, \tag{3.30}$$

where $q_j =< \Psi^j|H|\tilde{\psi}^i >$ and $a =< \tilde{\psi}^i|H|\tilde{\psi}^i >$. The eigenvalues for i basis states are then obtained as roots of a secular equation

$$\prod_{\beta=1}^{i-1}(E^\beta - E)\left[(a-E) - \sum_{m=1}^{i-1} \frac{q_m^2}{E^m - E}\right] = 0. \tag{3.31}$$

In Fig. 3.1, we present as an example the SVM calculation of the $J^\pi = \frac{1}{2}^+$ ground state of ^{3}H ($I = \frac{1}{2},\ M_I = -\frac{1}{2}$) using the realistic NN interaction G3RS [229] with central, tensor, and spin-orbit part (we omit $\mathbf{L}^2$ and $(\mathbf{L}.\mathbf{S})^2$ terms). We consider all possible (L, S) channels - with natural parity $(0, \frac{1}{2})$, $(2, \frac{3}{2})$ and unnatural parity $(1, \frac{1}{2})$, $(1, \frac{3}{2})$ together with all corresponding spin and isospin configurations. In the left panel we illustrate that with an increasing basis dimension the ground state energy E_B decreases and for a certain number of basis states it starts to converge. The probabilities of different (L, S) channels in the corresponding total wave function $\Psi_{J^\pi\ IM_I}$ are shown in the right panel, where we demonstrate that their contribution stabilizes with the converged SVM solution.

3.2.2 Excited states

The SVM can be readily extended to a calculation of bound excited states. For a certain system we can directly calculate $(J^\pi;\ IM_I)$ bound state with the lowest

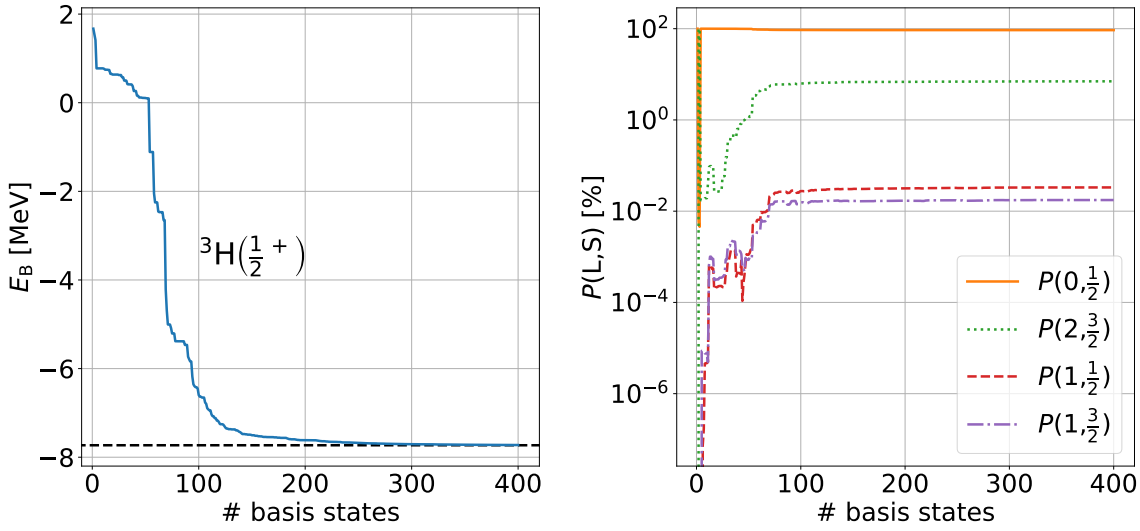

Figure 3.1: SVM calculation of the $J^\pi = \frac{1}{2}^+$ ground state of ^{3}H using the realistic NN interaction G3RS [229] with $\mathbf{L}^2$ and $(\mathbf{L}.\mathbf{S})^2$ terms omitted. Convergence of the corresponding ground state energy E_B (blue solid line) with an increasing number of basis states is shown in the left panel. The black dashed line denotes the calculated ground state energy of the same system presented in Ref. [225]. In the right panel we show evolution of the $P(L,S)$ probabilities to find considered (L,S) channels in the total wave function with increasing number of basis states.

energy. Consequently, we access the ground and several other excited states each with different quantum numbers. If we are interested in the n-th lowest $(J^\pi;\ IM_I)$ bound state, the SVM method has to be modified. The stochastic optimization of basis states is then performed with respect to the n-th lowest eigenenergy E^n. This change does not induce any additional computational cost since E^n can be directly calculated as the n-th lowest root of the secular equation (3.31).

We stress that the SVM is applicable only to the bound states (ground as well as exited states). In the case of unbound states the method tries to converge to the lowest dissociation threshold. In particular, unstable states with a certain width (resonances) which exist in a few-body continuum can not be directly studied using the SVM and further techniques have to be applied.

3.3 Continuum

The theoretical study of a few-body continuum is rather non-trivial task. Unlike bound states, continuum phenomena such as resonances or virtual states do not directly exist as eigenstates of the Hamiltonian H but they are embedded in its continuum spectrum where they manifest through various properties of scat-

tering states. According to the generally accepted picture, resonances and virtual states predominantly correspond to poles of S-matrix [230, 231]. We will follow this assumption in this work. A direct calculation of these poles, in particular for few-body systems, remains complicated. We apply two different methods implemented as an extension of the previously discussed SVM with the correlated Gaussian basis. The first approach, the IACCC, relies on analytic continuation of the S-matrix pole from a bound region, where we can apply appropriate bound state techniques, to a continuum region. The second approach, the CSM, introduces a complex-dilation transformation to the few-body Schrödinger equation (3.1). Resonances are then related to quadratically-integrable functions in the same way as bound states and are described using L^2 basis of correlated Gaussians. Discussion of main properties of S-matrix poles on the two-body level, which provides useful grounds for better understanding of IACCC and CSM is given in Appendix B. More details can be found in relevant textbooks [230, 231].

3.3.1 (Inverse) Analytic Continuation in the Coupling Constant

The Analytic Continuation in the Coupling Constant (ACCC) method [232] has been successfully applied in various calculations of few-body resonances and virtual states [233, 234]. It provides rather convenient way how to extend applicability of the SVM into the continuum region [233, 235]. The starting point of the ACCC method is a few-body Hamiltonian H consisting of a physical part H^{phys} and an auxiliary attractive part H^{aux} which introduces a bound state for a certain value of α

$$H = H^{\text{phys}} + \alpha\ H^{\text{aux}}. \tag{3.32}$$

By decreasing the strength α the bound state moves closer to the threshold and for a certain α_0 it turns into a resonance or virtual state. It was demonstrated for a two-body system that in a vicinity of the branching point α_0 the square root of energy $k = \sqrt{E}$ behaves as $k \approx (\alpha - \alpha_0)$ for $l = 0$ (s-wave) and $k \approx \sqrt{\alpha - \alpha_0}$ for $l > 0$ [232]. Defining new variable $x = \sqrt{\alpha - \alpha_0}$ one obtains two branches $k(x)$ and $k(-x)$ where the former one describes the motion of the S-matrix pole assigned to a bound state on a positive imaginary k-axis to the third quadrant of a k-plane. Using analyticity of the function $k(x)$ one can continue from a bound region $\alpha > \alpha_0$ to a resonance

region $\alpha < \alpha_0$. In practice this is done by constructing a Padé approximant

$$k(x) \approx \mathrm{i}\frac{\sum_{j=0}^{M} c_j x^j}{1 + \sum_{j=1}^{N} d_j x^j} \tag{3.33}$$

of the function $k(x)$ using $M+N+1$ bound state solutions $\{(x_i, k_i); i = 1, \ldots, M+N+1\}$ for different values of $\alpha > \alpha_0$. The evaluation of the Padé approximant (3.33) at $x = \sqrt{-\alpha_0}$ yields complex k which is assigned to the physical resonance solution $k^2 = E_r - \mathrm{i}\Gamma/2$ corresponding to the Hamiltonian H^{phys}. For more details regarding the ACCC method see [231].

The ACCC method suffers from two drawbacks which are predominantly of numerical nature. The first issue is high sensitivity of a numerical solution to precise determination of the branching point value α_0 [232]. The second obstacle appears with increasing orders M and N of the Padé approximant (3.33) when the numerical solution starts to deteriorate.

Rather recently Horáček *et al.* [236] have introduced a modified version of the ACCC method called the Inverse Analytic Continuation in the Coupling Constant (IACCC) method which provides more robust numerical stability. Starting in the same manner as in the ACCC case, we consider the Hamiltonian (3.32) and calculate series of bound states for different values of $\alpha > \alpha_0$. Next, we construct a Padé approximant of a function $\alpha(\kappa)$, where $\kappa = -\mathrm{i}k$, using a relevant set of bound state solutions

$$\alpha(\kappa) \approx \frac{P_M(\kappa)}{Q_N(\kappa)} = \frac{\sum_{j=0}^{M} c_j \kappa^j}{1 + \sum_{j=1}^{N} d_j \kappa^j}. \tag{3.34}$$

Resonance or virtual state parameters of the physical Hamiltonian H^{phys} are then readily obtained by setting $\alpha = 0$ as a root of a simple polynomial equation

$$P_M(\kappa) = 0. \tag{3.35}$$

We note that the determination of complex polynomial roots might be a very sensitive problem, nevertheless, most modern numerical libraries are able to handle this issue with satisfactory accuracy.

A precise calculation of bound state energies used to determine the coefficients of the Padé approximant (3.34) requires a special care. We define a grid $\{\alpha_i; \alpha_i > \alpha_0\}$ covering a rather large part of the bound state region. For each α_i we use the SVM to determine independently a set of basis states which provide solution for the binding energy E_i with accuracy $\approx 10^{-4}$ MeV. Next, we merge all determined sets

into a larger basis checking linear dependency and numerical stability of the overlap matrix. This procedure allows us to calculate any $E_i(\alpha_i)$ inside the considered bound state region in a highly efficient way just by diagonalizing the Hamiltonian matrix in the larger basis set. For each IACCC calculation we perform thorough checks of the independence of our prediction on a specific choice of the bound state energies $E_i(\alpha_i)$ and degrees of the Padé approximant (3.34).

3.3.2 Complex Scaling Method

The Complex Scaling Method [237] has proved to be a reliable tool for the description of few-body resonances [238]. The main ingredient is a transformation $U(\theta)$ of relative coordinates $\mathbf{r}$ and their conjugate momenta $\mathbf{k}$

$$U(\theta)\mathbf{r} = \mathbf{r}e^{\mathrm{i}\theta}, \qquad U(\theta)\mathbf{k} = \mathbf{k}e^{-\mathrm{i}\theta}, \tag{3.36}$$

where θ is a real positive scaling angle. Applying this transformation to the Schrödinger equation (3.1) one obtains its complex scaled version

$$H(\theta)\Psi(\theta) = E(\theta)\Psi(\theta), \tag{3.37}$$

where $H(\theta) = U(\theta)HU^{-1}(\theta)$ is the complex scaled Hamiltonian and $\Psi(\theta) = U(\theta)\Psi$ is the corresponding wave function. For large enough θ, the divergent asymptotic part of the resonance wave function is suppressed and $\Psi(\theta)$ is normalizable - possible resonant states can then be obtained as discrete solutions of Eq. (3.37) in the same way as bound states.

The role of the transformation (3.36) can be easily demonstrated on the 2-body level. The complex scaled Schrödinger equation (3.37) with a short-range central potential acquires the form

$$\left\{\frac{\hbar^2}{2\mu}\left[-\frac{d^2}{dr^2} + \frac{l(l+1)}{r^2}\right]e^{-2\mathrm{i}\theta} + V(re^{\mathrm{i}\theta})\right\}\Psi_l(k,r;\ \theta) = E(\theta)\Psi_l(k,r;\ \theta), \tag{3.38}$$

where μ is the reduced mass and l is the orbital momentum. Following the analysis of asymptotic behavior of its solutions given in Ref. [238] we obtain at large relative distances

$$\Psi_l(k,r;\ \theta) \xrightarrow[r\to\infty]{} \left[f_l^+(k;\ \theta)e^{-\mathrm{i}kre^{\mathrm{i}\theta}} - (-)^l f_l^-(k;\ \theta)e^{\mathrm{i}kre^{\mathrm{i}\theta}}\right], \tag{3.39}$$

where $f_l^+(k;\ \theta)$ and $f_l^-(k;\ \theta)$ are the complex scaled Jost functions representing

asymptotic amplitudes of incoming and outgoing waves, respectively. For resonances $k = \kappa - \mathrm{i}\gamma$ and bound states $k = \mathrm{i}\gamma$ the $f_l^+(k;\ \theta)$ is zero (see Appendix B) and the asymptotic behavior is given by the complex scaled outgoing part

$$\begin{array}{lll} e^{\mathrm{i}kr}|_{k=\kappa-\mathrm{i}\gamma} = e^{\mathrm{i}\kappa r}e^{\gamma r} & & e^{(-\kappa\sin\theta+\gamma\cos\theta)r}e^{\mathrm{i}(\kappa\cos\theta+\gamma\sin\theta)r} \\ & \xrightarrow{U(\theta)} & \\ e^{\mathrm{i}kr}|_{k=\mathrm{i}\gamma} = e^{-\gamma r} & & e^{-\gamma r\cos\theta}e^{-\mathrm{i}\gamma r\sin\theta} \end{array} . \tag{3.40}$$

Clearly, the bound state asymptotic form remains unchanged under the CSM transformation (3.36) whereas for resonant states at $\theta > \theta_r = \arctan(\gamma/\kappa)$ the divergent asymptotic part is regularized.

The maximal value of θ is given by analytic properties of the complex scaled Hamiltonian $H(\theta)$, in particular, by potential $V(\theta)$. In our work we are dealing with Gaussian potentials, which limits $\theta < \frac{\pi}{4}$ to prevent divergence of their complex scaled version. Consequently, resonant poles which would require $\theta_r \geq \frac{\pi}{4}$ are beyond the reach of CSM.

A mathematically rigorous formulation of the complex scaling method for a two-body system results in the ABC theorem [237] which provides description of the behavior of a complex scaled energy $E(\theta)$ with respect to θ :

1. Bound state energies remain unaffected.

2. Continuum spectrum rotates clockwise in a complex energy plane by angle 2θ from the real axis with its center of rotation at a relevant threshold.

3. For $\theta > \theta_r = \arctan(\gamma/\kappa) = \frac{1}{2}\arctan(\Gamma/2E_r)$ corresponding to the resonance energy E_r and width Γ, the resonance is described by a quadratically-integrable function and its energy and width are given by a complex energy $E(\theta) = E_r - \mathrm{i}\Gamma/2$ which does not change with the increasing scaling angle θ.

The outcome of the ABC theorem can be applied with minor modifications also to few-body resonances [238].

In this work, we expand the complex scaled total few-body wave function $\Psi(\theta)$ in a finite basis of correlated Gaussians (3.15)

$$\Psi(\theta) = \sum_{i=1}^{K} c_i(\theta)\ \psi^i. \tag{3.41}$$

Both energies $E(\theta)$ and corresponding coefficients $c_i(\theta)$ are then obtained using the

c-variational principle [239] as a solution of the generalized eigenvalue problem

$$\sum_{j=1}^{K} \left(\psi^i|H(\theta)|\psi^j\right) c_j^\alpha(\theta) = E^\alpha(\theta) \sum_{j=1}^{K} \left(\psi^i|\psi^j\right) c_j^\alpha(\theta), \tag{3.42}$$

where $(|)$ stands for the c-product (bi-orthogonal product) [238,240]. Moiseyev *et al.* proved that the solutions of Eq. (3.42) are stationary solutions in the complex variational space, and as $K \to \infty$ the exact solutions of the complex scaled Schrödinger equation (3.37) are obtained [239]. We stress that the c-variational principle is a stationary principle, consequently, with increasing number of basis states K there is no upper or lower bound to an exact solution [241].

In Fig. 3.2, we show as an example complex scaled eigenenergies $E^\alpha(\theta)$ obtained by solving Eq. (3.42) for a toy 3-body system with interaction tuned to reproduce one 3-body bound state and one 1+1+1 resonance (for details on this notation see Appendix B). In agreement with the ABC theorem the CSM transformation (3.36) yields in Eq. (3.42) three types of solutions $E^\alpha(\theta) = \left\{E^b(\theta), E^r(\theta), E^c(\theta)\right\}$. While the bound state energy $E^b(\theta)$ remains intact with increasing θ, discretized complex scaled continuum eigenenergies $E^c(\theta)$ rotate by angle 2θ. For $\theta > \theta_r \approx 5.7°$, the

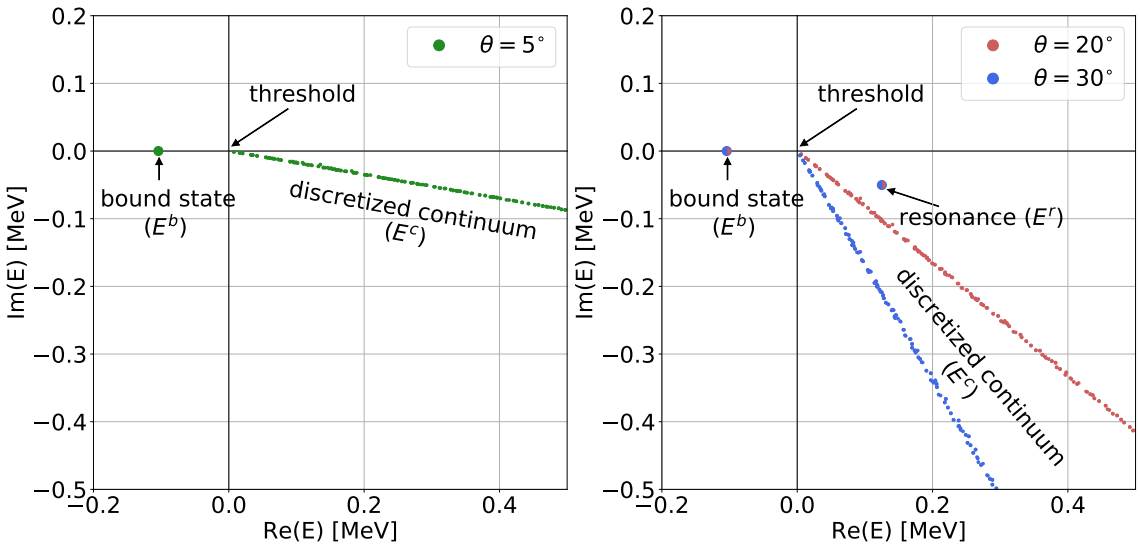

Figure 3.2: Complex scaled eigenenergies $E^\alpha(\theta)$, obtained by solving Eq. (3.42), for a toy 3-body system with an interaction tuned to reproduce one 3-body bound state and one 1+1+1 resonance with $\theta_r \approx 5.7°$. We show calculated $E^\alpha(\theta)$ and corresponding three types of solutions $E^b(\theta)$, $E^r(\theta)$, and $E^c(\theta)$ for three different scaling angles θ. For the $\theta < \theta_r$ case, calculated complex eigenenergies $E^\alpha(\theta = 5°)$ are presented in the left panel, while for the $\theta > \theta_r$ case eigenenergies $E^\alpha(\theta = 20°)$ and $E^\alpha(\theta = 30°)$ are plotted in the right panel.

resonance energy $E^r(\theta)$ is isolated from the $E^c(\theta)$ set and does not exhibit rotation. In the left panel, we present CSM for $\theta = 5°$ scaling angle which is not large enough to reveal the resonance position. In the right panel, we show CSM for $\theta = 20°$ and $30°$ which yield the resonance energy $E(\theta = 20°) = 0.1251 - \mathrm{i}0.0502$ MeV and $E(\theta = 30°) = 0.1248 - \mathrm{i}0.0502$ MeV.

In fact, due to a finite dimension of the basis set the resonance energy $E(\theta) \equiv E^r(\theta)$ (3.42) moves with increasing scaling angle along the θ-trajectory even for $\theta > \theta_r$, featuring residual θ dependence [238, 242]. It was demonstrated that following the generalized virial theorem [239, 243] the best estimate of a resonance energy is given by the most stationary point of the θ-trajectory, i.e. such $E(\theta_{\mathrm{opt}})$ for which the residual θ dependence is minimal but not necessarily equal to zero

$$\left|\frac{\mathrm{d}E(\theta)}{\mathrm{d}\theta}\right|_{\theta_{\mathrm{opt}}} \approx 0. \tag{3.43}$$

A real scaling angle θ is frequently used in finite basis CSM calculations with satisfactory results [242, 244, 245]. However, identifying the resonance energy with $E(\theta_{\mathrm{opt}})$ using the θ-trajectory ($\mathrm{Im}(\theta) = 0$, $\mathrm{Re}(\theta)$ changing) is still approximate. As pointed out by Moiseyev [241] the resonance stationary condition requires exact equality in Eq. (3.43), which can be achieved in a finite basis set by considering complex θ_{opt}. Consequently, taking θ real introduces certain theoretical error and it is problematic to quantify how much the result obtained using the θ-trajectory technique deviates from the true CSM resonance solution (zero derivative in Eq. (3.43)).

Following Aoyama *et al.* [238] we use both θ-trajectory and β-trajectories ($\mathrm{Re}(\theta)$ fixed, $\mathrm{Im}(\theta)$ changing) to locate the position of the true CSM solution. In the above work it was numerically demonstrated that for certain $\mathrm{Re}(\theta_{\mathrm{opt}})$ the θ-trajectory approaches the stationary point and then starts to move away. On the other hand, the β-trajectories are roughly circles with decreasing radius as the corresponding $\mathrm{Re}(\theta)$ approaches $\mathrm{Re}(\theta_{\mathrm{opt}})$. In view of orthogonality of the θ- and β-trajectories at given scaling angle θ, the true CSM solution is then located inside the area given by circular β-trajectories. More specifically, it is identified as the center of the circular β-trajectory with the smallest radius where the CSM error is given by the size of this radius [238]. In our work we found that for a certain $\mathrm{Re}(\theta)$ close to $\mathrm{Re}(\theta_{\mathrm{opt}})$ the β-trajectory starts to oscillate within a small region around the true CSM solution (for illustration see Fig. C.2 in Appendix C). It is caused mainly by a finite basis which allows to get resonance solution within certain accuracy. By increasing the basis set the circular trajectory could be recovered for this particular $\mathrm{Re}(\theta)$.

The determination of appropriate correlated Gaussian basis states ψ^i which yield a stable CSM resonance solution is a non-trivial task. To our knowledge, there have been in principle two approaches applied to the selection of a relevant basis in previous works. The first one incorporates at certain point geometrical expansion of non-linear variational parameters of the matrix A^i (3.15) [238, 246]. The second one uses the SVM to optimize the basis of ψ^i with respect to the energy of discretized continuum states around the expected resonance position $E_r = \mathrm{Re}(E)$ [242, 247]. We found that both options could be satisfactorily applied only to relatively narrow resonances. We admit that one can in principle use geometrical expansion also for broader resonances, however, the amount of basis states dramatically increases with the size of the system which makes this approach highly tedious.

Here, we present a more efficient procedure to determine an appropriate basis set for an accurate description of both narrow and broad resonances. Before applying the CSM we supplement the Hamiltonian H with an additional harmonic oscillator (HO) trap

$$H^{\mathrm{trap}}(b) = H + V^{\mathrm{HO}}(b), \quad V^{\mathrm{HO}}(b) = \frac{\hbar^2}{2mb^4} \sum_{j<k} r_{jk}^2, \tag{3.44}$$

where m is an appropriate mass scale and b is the HO trap length. The potential $V^{\mathrm{HO}}(b)$ gives rise to a HO spectrum of the ground and excited states which is affected by the presence of a resonance in the Hamiltonian H [248]. For a given trap length b we select basis states ψ^i (3.15) using the SVM, optimizing the variational parameters for the ground state energy and then subsequently for energies of excited states of $H^{\mathrm{trap}}(b)$ up to a certain maximal energy E_{max}. We select E_{max} in a way that a possible resonance position and width satisfy $E_{\mathrm{max}} > E_r + \Gamma/2$. The SVM procedure prefers basis states which promote interparticle distances r_{jk} in a specific region given by the trap length b. By increasing b we enlarge the r_{jk} region covered by correlated Gaussians ψ^i. For certain b, once r_{jk} region is large enough, the CSM resonance solution for the Hamiltonian H starts to stabilize and both short range and suppressed long range asymptotic parts of a resonance wave function are described sufficiently well. Choosing b beyond this certain point slightly improves the description of suppressed long range part and adds only minor corrections to the CSM resonance energy solution $E^\alpha(\theta)$ in Eq. (3.42). In order to further enhance accuracy of our CSM solutions we employ a HO trap length grid $\{b_k\}$ and for each grid point we independently select correlated Gaussians in a way mentioned above. Then we merge basis states determined for each b_k into a larger basis while checking linear dependency and numerical stability of an overlap matrix.

Continuum level density, phase shifts, virtual states

The CSM is highly useful in determination of a position of few-body resonances, moreover, the range of its applicability can be easily extended to calculations of phase shifts. This idea was firstly presented by Suzuki *et al.* [249] who demonstrated that the Continuum Level Density (CLD), obtained approximately from CSM eigenvalue solutions of Eq. (3.42), leads to reliable phase shifts predictions. The same conclusion was made by Odsuren *et al.* [250, 251] who pointed out that calculated phase shifts can be used to reveal possible near-threshold virtual states which can not be obtained as an isolated solution within the CSM [251].

We start with the level density $\rho(E)$ given by the Hamiltonian H, which is defined as the summation over discrete eigenvalues E_i and integration over continuous ones. It can be equivalently expressed using the Green's function $G^+ = (E - H)^{-1}$

$$\rho(E) = \sum_{\text{disc.}} \delta(E - E_i) + \int_{\text{cont.}} \delta(E - E_i) = -\frac{1}{\pi} \text{Im} \left\{ \text{Tr} \left[\frac{1}{E - H} \right] \right\}. \tag{3.45}$$

The CLD $\Delta(E)$ is then defined as a difference between $\rho(E)$ obtained from the full Hamiltonian H and $\rho_0(E)$ related to its asymptotic part H_0 [250]

$$\Delta(E) = \rho(E) - \rho_0(E) = -\frac{1}{\pi} \text{Im} \left\{ \text{Tr} \left[\frac{1}{E - H} - \frac{1}{E - H_0} \right] \right\}. \tag{3.46}$$

Due to the subtraction of ρ_0, $\Delta(E)$ reflects the effect of finite range interactions. The CLD (3.46) can be directly related to the scattering phase shifts $\delta(E)$ [252, 253]

$$\Delta(E) = \frac{1}{\pi} \frac{d\delta(E)}{dE}. \tag{3.47}$$

In order to determine $\Delta(E)$ from the CSM eigenvalue solutions $E^\alpha(\theta)$ (3.42), we introduce its complex scaled version

$$\Delta_\theta(E) = U(\theta)\Delta(E)U^{-1}(\theta) = -\frac{1}{\pi} \text{Im} \left\{ \text{Tr} \left[\frac{1}{E - H(\theta)} - \frac{1}{E - H_0(\theta)} \right] \right\}, \tag{3.48}$$

where $U(\theta)$ is the complex scaling transformation with scaling angle θ (3.36) and $H(\theta)$ ($H_0(\theta)$) is the full (asymptotic) complex scaled Hamiltonian. It was proved that three types of solutions of the complex scaled Schrödinger equation - bound states $|\Psi^b)$, resonant states $|\Psi^r)$, and continuum states $|\Psi^c)$ - fulfill extended com-

pleteness relation [254]

$$\sum_{b=1}^{K_b} |\Psi^b)(\Psi^b| + \sum_{r=1}^{K_r^\theta} |\Psi^r)(\Psi^r| + \int_{L_\theta^E} dE^c |\Psi^c)(\Psi^c| = 1, \tag{3.49}$$

where $|)$ stands for bi-orthogonal states. Here, K_b is the number of bound state solutions. The number of resonance states solutions K_r^θ depends on the scaling angle θ, i.e. the angle θ has to be large enough to reveal a resonance as an isolated square integrable solution. The L_θ^E is a branch cut in a complex energy plane given by a rotated continuum. For a finite number K of square integrable basis states, such as correlated Gaussians applied in this work, the extended completeness relation holds only approximately [254]

$$\sum_{b=1}^{K_b} |\Psi^b)(\Psi^b| + \sum_{r=1}^{K_r^\theta} |\Psi^r)(\Psi^r| + \sum_{c=1}^{K-K_b-K_r^\theta} |\Psi^c)(\Psi^c| \approx 1, \tag{3.50}$$

where $|\Psi^b)$, $|\Psi^r)$, and $|\Psi^c)$ now represent eigenstates obtained as a solution of the generalized eigenvalue problem (3.42) for a given scaling angle θ. Using Eqs. (3.48) and (3.50) one can approximate, after some minor algebraic adjustments (for details see [249]), complex scaled CLD $\Delta_\theta(E)$ as

$$\begin{aligned} \Delta_\theta(E) \;&\approx\; \Delta_\theta^K(E) = \\ &-\; \frac{1}{\pi}\left[\sum_{b=1}^{K_b} \frac{1}{E-E^b} + \sum_{r=1}^{K_r^\theta} \frac{1}{E-E^r} + \sum_{c=1}^{K-K_b-K_r^\theta} \frac{1}{E-E^c} - \sum_{c=1}^{K} \frac{1}{E-E_0^c}\right] \end{aligned} \tag{3.51}$$

where E^b, E^r and E^c are the bound state, resonance and discretized continuum energies, respectively, obtained as the CSM eigenvalue solutions $E^\alpha(\theta)$ (3.42) for the full Hamiltonian H. Complex energies E_0^c then correspond to the eigenvalue solutions for H_0.

Scattering phase shifts are obtained from $\Delta_\theta^K(E)$ using Eq. (3.47) which leads to rather simple relation between their values and CSM eigenvalue solutions

$$\delta_\theta^N(E) = K_b\pi + \sum_{r=1}^{K_r^\theta} \delta^r(E) + \sum_{c=1}^{K-K_b-K_r^\theta} \delta^c(E) - \sum_{r=1}^{K} \delta_0^c(E), \tag{3.52}$$

where

$$\begin{aligned}\delta^r(E) &= \text{arccotg}\left(\frac{\text{Re}(E^r)-E}{\text{Im}(E^r)}\right),\\ \delta^c(E) &= \text{arccotg}\left(\frac{\text{Re}(E^c)-E}{\text{Im}(E^c)}\right),\\ \delta_0^c(E) &= \text{arccotg}\left(\frac{\text{Re}(E_0^c)-E}{\text{Im}(E_0^c)}\right).\end{aligned} \tag{3.53}$$

Since the CSM allows to clearly distinguish resonance solutions from a discretized continuum, it is apparent that using Eq. (3.52) one can directly separate resonance $\delta^K_{\theta,R}(E)$ and continuum $\delta^K_{\theta,C}(E)$ contributions to the $\delta^K_\theta(E)$

$$\delta^K_{\theta,R}(E) = \sum_{r=1}^{K_r^\theta}\delta^r(E), \quad \delta^K_{\theta,C}(E) = \sum_{c=1}^{K-K_b-K_r^\theta}\delta^c(E) - \sum_{r=1}^{K}\delta_0^c(E). \tag{3.54}$$

Further, it has been demonstrated that the discretized continuum CSM eigenvalue solutions, and thus $\delta^K_{\theta,C}(E)$, are strongly affected by the presence of a near-threshold pole, such as a virtual state, which can not be revealed as an isolated CSM solution [251]. If there is just one near-threshold pole its position can be extracted from $\delta^K_{\theta,C}(E)$ using scattering length a and effective range r evaluated within the effective range expansion (ERE) (B.11). The position of the pole is then determined from (a, r) by applying Eq. (B.12), more precisely, we connect the pole position with the primary pole k_0^- which has the main effect on $\delta^K_{\theta,C}(E)$.

We stress that due to a finite basis set the extended completeness relation (3.50) is approximate and both $\Delta^K_\theta(E)$ and $\delta^K_{\theta,R}(E)$ depend in principle on the complex scaling angle θ. It was demonstrated that a sufficiently large number of basis states provides reliable approximation [249, 250]. Nevertheless, to address this effect we determine the above quantities for different scaling angles θ and consider the uncertainty introduced by the θ-dependence as the error of our calculations.

Chapter 4

Results

In this section, we highlight selected results of our few-body calculations of hadronic systems, namely, of η-nuclei, hypothetical $\Lambda(1405)$-systems, and single-$\Lambda(1116)$ and double-$\Lambda(1116)$ hypernuclei. Corresponding key publications with more results and their detailed discussion are enclosed in Appendix D. Our work was presented at international conferences, published, submitted, or is being prepared for submission in relevant scientific journals.

The enclosed works are result of joint effort of several co-authors. Nevertheless, it is to be stressed that all underlying few-body calculations presented either in this thesis or given in the enclosed works were made entirely by the author himself and thus represent his original work.

Our calculations were performed using the SVM code with a correlated Gaussian basis extended using the CSM and IACCC methods into continuum region. This code was developed by the author during his Ph.D. study. In fact, we started with a publicly accessible SVM program [255] which is, however, considerably restricted to simple bound $L = 0$ systems with central forces. Moreover, it is written in *Fortran* in a way which makes calculations computationally demanding already at 4-body level. This motivated us to develop from the beginning a new C++ code where we included correlated Gaussian basis states with GVR (3.13) in order to describe systems with $L > 0$. Further, we included complete sets of different spin and isospin configurations (for more details see Subsection 3.1.2) which are essential for the correct description of systems with spin and isospin dependent interactions. We implemented non-central tensor and spin-orbit forces as well. Finally, we supplemented our code with the CSM and IACCC techniques in order to describe not only the bound but also unbound region (resonances, virtual states). We checked correctness of our code in rather thorough benchmark calculations - the results are presented in Appendix C.

We stress that considerable amount of effort was focused on computational efficiency and parallelization of the code. As will the reader notice from presented results we deal with few-body systems up to $A = 8$, which is not trivial[1].

4.1 η - nuclei

First, we studied few-body η-nuclei which, if observed, might provide important constraints on the underlying ηN interaction. Although there is a general consensus that the s-wave near-threshold ηN interaction is mildly attractive due to the presence of the $N^*(1535)$ resonance [28], most ηN interaction models [20–25] significantly differ both in the predicted ηN interaction strength and its energy dependence. Consequently, the theoretical study of light η-nuclei, and of the onset of η-nuclear binding in particular, is highly important. Strong attraction in the ηd, η^3He, and η^4He systems, has been confirmed in the corresponding near-threshold production cross-sections [28, 256], however, there is no conclusive experimental evidence of any η-nuclear quasi-bound state so far.

We explored light η-nuclei for two different ηN interaction models - GW [20] and CS [22], which yield the strongest ηN attraction and are thus most favorable for forming η-nuclear bound states. We performed self-consistent SVM calculations of η-nuclear states in the s-shell ^{3}He, and ^{4}He and p-shell ^{6}Li nuclei. We discussed the effect of non-perturbative inclusion of ηN absorption on the corresponding η separation energy B_η in these systems in order to reveal further implications for the onset of η-nuclear binding.

Here, we show selected results from our publications *EPJ Web Conf.* ***181****, 01011 (2018)* and *EPJ Web Conf.* ***199****, 02022 (2019)* enclosed in Appendix D.1 and D.2, respectively. Some of these results were also published in Refs. [228, 257].

In our study of η-nuclear quasi-bound states we used the Minnesota NN central potential (with $u = 1$ parameter) [227] which reproduces well properties of ground states of s-shell and light p-shell nuclei. The Coulomb potential was included as well. The interaction of the η meson with nucleons was described by a complex two-body energy dependent effective potential derived from the coupled-channel meson-baryon interaction models GW [20] and CS [22]. The form of the ηN potential was taken

[1] In this chapter A stands for number of particles in a few-body system (or number of nucleons in η-nuclear systems studied here), while in the previous Chapter 3 we used N instead to avoid confusion with the correlated Gaussian matrix (3.8).

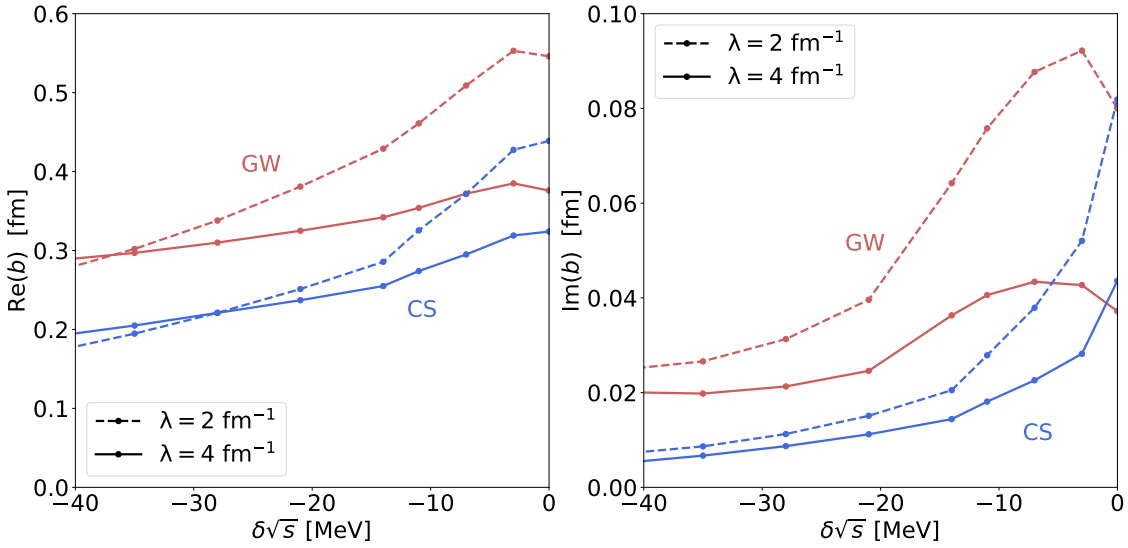

Figure 4.1: Subthreshold behavior of the complex amplitude b (4.1) as a function of $\delta\sqrt{s} < 0$ for the GW and CS interaction models and two values of the cutoff $\lambda = 2$ and 4 fm^{-1}. The real part of b is shown in the left panel, while the imaginary part is given in the right panel.

according to [49] as

$$V_{\eta N}(\delta\sqrt{s}, r) = \frac{4\pi}{2\mu_{\eta N}} b(\delta\sqrt{s})\rho_\lambda(r), \qquad \rho_\lambda(r) = \left(\frac{\lambda}{2\sqrt{\pi}}\right)^3 \exp\left(-\frac{\lambda^2}{4}r^2\right), \tag{4.1}$$

where $\mu_{\eta N}$ stands for the reduced ηN mass, $\delta\sqrt{s} = \sqrt{s} - \sqrt{s_{\rm th}}$ is energy shift with respect to the ηN threshold, λ is a scale parameter which is inversely proportional to the range of $V_{\eta N}$, and $b(\delta\sqrt{s})$ is the energy dependent complex amplitude. The value of λ is connected to the EFT momentum cutoff; its upper bound corresponds to a vector-meson exchange $\lambda \leq 3.9$ fm^{-1} or more restrictively to $\lambda \leq 3.0$ fm^{-1} excluding ρN channel from dynamical generation of the $N^\star(1535)$ resonance [50].

For given λ the amplitude $b(\delta\sqrt{s})$ was fitted to complex energy dependent phase shifts derived from the subthreshold ($\delta\sqrt{s} < 0$) scattering amplitude $F_{\eta N}(E)$ of the corresponding ηN interaction model [49]. Figure. 4.1 presents the real (left panel) and imaginary (right panel) parts of b as a function of $\delta\sqrt{s} < 0$ for the GW and CS interaction models and two values of $\lambda = 2$ and 4 fm^{-1}.

The energy dependence of the $V_{\eta N}$ is treated self-consistently. We search for such SVM solution that fulfills $\delta\sqrt{s_{\rm sc}} = \langle\delta\sqrt{s_{\rm sc}}\rangle$ where $\delta\sqrt{s}$ enters $V_{\eta N}$ and $\langle\delta\sqrt{s}\rangle$ is obtained from the SVM solution for a given value of $\delta\sqrt{s}$ [50]

$$\left\langle \delta\sqrt{s} \right\rangle = -\frac{B}{A} - \xi_N \frac{1}{A} \left\langle T_N \right\rangle + \frac{A-1}{A} E_\eta - \xi_A \xi_\eta \left(\frac{A-1}{A} \right)^2 \left\langle T_\eta \right\rangle , \tag{4.2}$$

where B is the total binding energy, $\langle T_N \rangle$ and $\langle T_\eta \rangle$ denotes kinetic energy of nucleons and η, and A is a number of nucleons. The energy $E_\eta = \langle \psi | H - H_N | \psi \rangle$ where the H_N is the Hamiltonian of the nuclear core, $\xi_{N(\eta)} = m_{N(\eta)}/(m_N + m_\eta)$, and $\xi_A = A m_N/(A m_N + m_\eta)$.

Fig. 4.2 illustrates the self-consistent procedure for the η^4He system, calculated using the GW ηN interaction and $\lambda = 4$ fm^{-1}. Considering just the real part of $V_{\eta N}(\delta\sqrt{s})$ (4.1) in the respective few-body Hamiltonian we performed SVM calculations for different $\delta\sqrt{s}$ grid points. Next, for each ground state solution we calculated $\langle \delta\sqrt{s} \rangle$ using Eq. (4.2). The figure shows evolution of the bound state energy E_B, $\langle \delta\sqrt{s} \rangle$, and $\langle H_\mathrm{N} \rangle$ with a value of $\delta\sqrt{s}$ entering $V_{\eta N}(\delta\sqrt{s})$. The green dashed line marks the condition $\delta\sqrt{s} = \langle \delta\sqrt{s} \rangle$. The self-consistent solution is then located at the intersection of the green solid and dashed lines - in this particular point $\left\langle \delta\sqrt{s_\mathrm{sc}} \right\rangle = \delta\sqrt{s_\mathrm{sc}}$. The intersection of the black vertical line with the red line then gives the self-consistent value of E_B.

The imaginary part of $V_{\eta N}$ is significantly smaller than its real part (notice different y-axis scales in Fig. 4.1). This allows to calculate the width Γ_η of the η-nuclear state perturbatively [49]. The SVM calculations are thus performed only for the real part of the ηN potential and Γ_η is evaluated using the expression

$$\Gamma_\eta = -2 \frac{\langle \Psi_{g.s.} | \mathrm{Im}(V_{\eta N}) | \Psi_{g.s.} \rangle}{\langle \Psi_{g.s.} | \Psi_{g.s.} \rangle}, \tag{4.3}$$

where $|\Psi_{g.s.}\rangle$ is the SVM solution for the η-nuclear ground state corresponding to the real part of $V_{\eta N}$.

In Fig. 4.3 we show results of our self-consistent calculations of η^3He, η^4He, and η^6Li - the η separation energy B_η and width Γ_η. Here, we used η^3He and η^4He systems in order to benchmark the self-consistent procedure against the results of Refs. [49, 50]. Calculations were performed using the GW and CS ηN interaction models and two values of the parameter $\lambda = 2$ and 4 fm^{-1}. For the GW model the η^6Li quasi-bound state was found rather deep below the threshold for both values of λ: with $B_\eta(\lambda = 2) = 2.17$ MeV, $\delta\sqrt{s_\mathrm{sc}}\,|_{\lambda=2} = -21.47$ MeV and $B_\eta(\lambda = 4) = 6.40$ MeV, $\delta\sqrt{s_\mathrm{sc}}\,|_{\lambda=4} = -33.11$ MeV. On the other hand the CS model yielded the η^6Li quasi-bound state only for $\lambda = 4$ fm^{-1} with $B_\eta(\lambda = 4) = 0.68$ MeV,

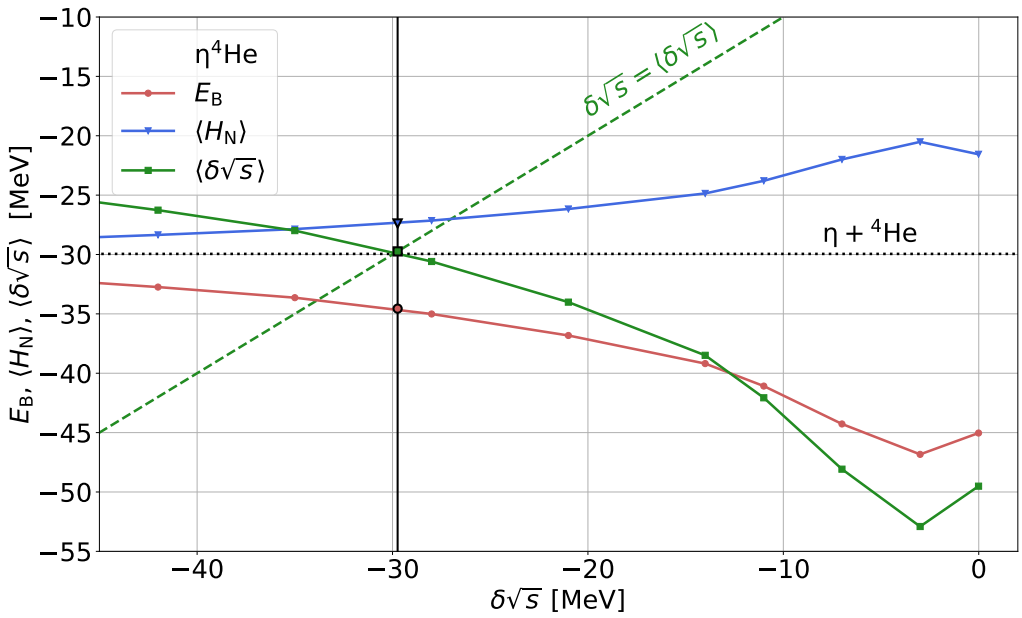

Figure 4.2: Self-consistent calculation of the η^4He ground state using the Minnesota NN potential with the Coulomb interaction and the GW ηN effective potential $V_{\eta N}(\delta\sqrt{s})$ (4.1) with the cutoff $\lambda = 4$ fm^{-1}. The red, blue and green symbols denote calculated total bound state energies E_B, $\langle \delta\sqrt{s} \rangle$ (4.2), and bound state energies related to the nuclear part of the total Hamiltonian $\langle H_N \rangle$ for different $\delta\sqrt{s}$ entering the $V_{\eta N}(\delta\sqrt{s})$, respectively. The green dashed line indicates $\delta\sqrt{s} = \langle \delta\sqrt{s} \rangle$ condition. The intersection of the black vertical line with the red line then gives the self-consistent value of E_B. The black dotted line stands for the $\eta + ^4$ He dissociation threshold. All calculations were performed using the SVM, and taking into account just the real part of $V_{\eta N}(\delta\sqrt{s})$.

$\delta\sqrt{s_{sc}}\,|_{\lambda=4} = -21.68$ MeV.

Another possible way how to calculate Γ_η is to solve the generalized eigenvalue problem for a complex Hamiltonian (with the imaginary part of $V_{\eta N}$ included) using variationally selected SVM basis states for the real part of $V_{\eta N}$. This approach, already used in SVM calculations of kaonic nuclei [93], yields complex eigenenergy of the quasi-bound state $E = \mathrm{Re}(E) + \mathrm{iIm}(E)$ and consequently the width $\Gamma_\eta = -2\mathrm{Im}(E)$. The method takes into account the effect of the non-zero imaginary part of $V_{\eta N}$ on the binding energy. Namely, $\mathrm{Im}(V_{\eta N})$ acts as repulsion lowering the binding energy of an η-nuclear system and thus making the η meson less bound.

Figure 4.4 demonstrates the convergence of the SVM calculation with increasing number of basis states for the η^4He system using the same interaction as in Fig. 4.2 and $\delta\sqrt{s} = -28$ MeV. The SVM selects basis states using just the real part of $V_{\eta N}$. In each step, i.e. for a certain number of basis states, we study two following

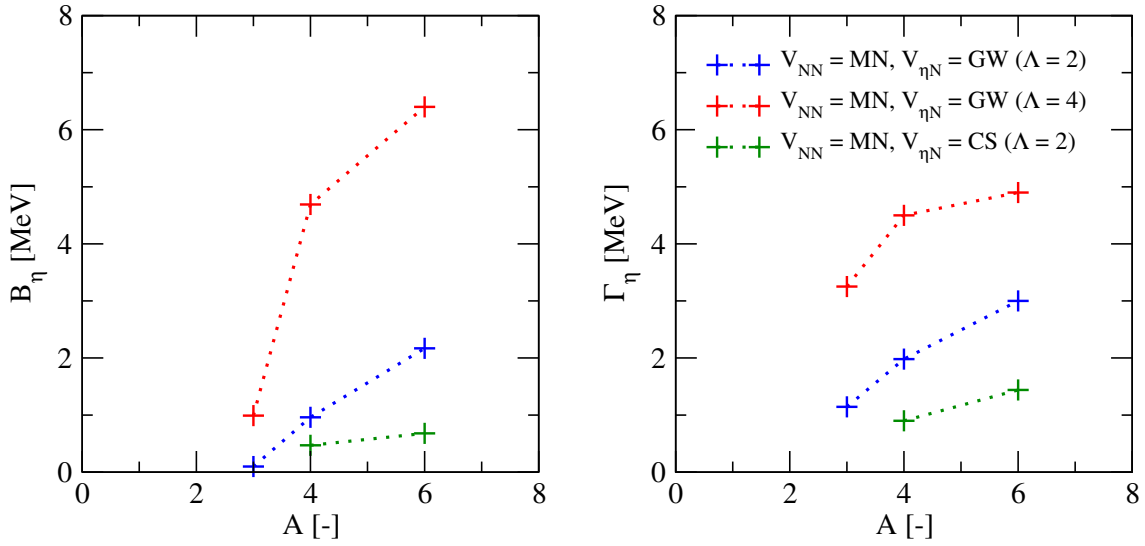

Figure 4.3: SVM calculations of the η separation energy B_η and width Γ_η of the η^3He, η^4He, and η^6Li quasi-bound states using the Minnesota NN potential with the Coulomb force and two ηN interaction models - GW and CS. The figure is adopted from the author's publication [52].

options: In the first (real) case, we calculate the ground state energy E_B using only $\mathrm{Re}(V_{\eta N})$ and the width Γ_η is evaluated by applying Eq. (4.3) (red solid lines). In the second (cmplx) case, we include both the real and imaginary parts of $V_{\eta N}$ into the Hamiltonian and solve a complex generalized eigenvalue problem which yields the complex energy E. Corresponding $E_\mathrm{B} = \mathrm{Re}(E)$ and $\Gamma_\eta = -2\mathrm{Im}(E)$ are depicted by blue dashed lines. While there is almost negligible difference between the obtained values of Γ_η, the non-perturbative inclusion of $\mathrm{Im}(V_{\eta N})$ makes η^4He less bound. This scenario is rather general and it is observed in all our calculations. The most sizable effect on E_B is for $\delta\sqrt{s}$ close to the ηN threshold where the (relative) contribution of the imaginary amplitude $\mathrm{Im}(b)$ in $V_{\eta N}$ (4.1) is largest (see Fig. 4.1 right panel).

In Table 4.1, we compare two approaches of treating $\mathrm{Im}(V_{\eta N})$ introduced above: the (real) case and the complex eigenvalue problem (cmplx) case. Calculations of the η^3He and η^4He systems were performed within the GW model. It is apparent that including $\mathrm{Im}(V_{\eta N})$ in the (cmplx) case has rather significant effect in η^3He ($\delta\sqrt{s_\mathrm{sc}}$ close to the threshold), which decreases with a larger energy shift $\delta\sqrt{s_\mathrm{sc}}$ with respect to the threshold (η^4He). For the ηN model CS (not shown in the table), the η^3He is not bound while in η^4He the effect of $\mathrm{Im}(V_{\eta N})$ is smaller (few tens of eV) due to the lower value of $\mathrm{Im}(V_{\eta N})$ than in the GW model. Table 4.1 illustrates that the size of the change in B_η caused by $\mathrm{Im}(V_{\eta N})$ is related to the magnitude of the subthreshold energy shift $\delta\sqrt{s}$. More precisely, the strength of $\mathrm{Im}(V_{\eta N})$ as a

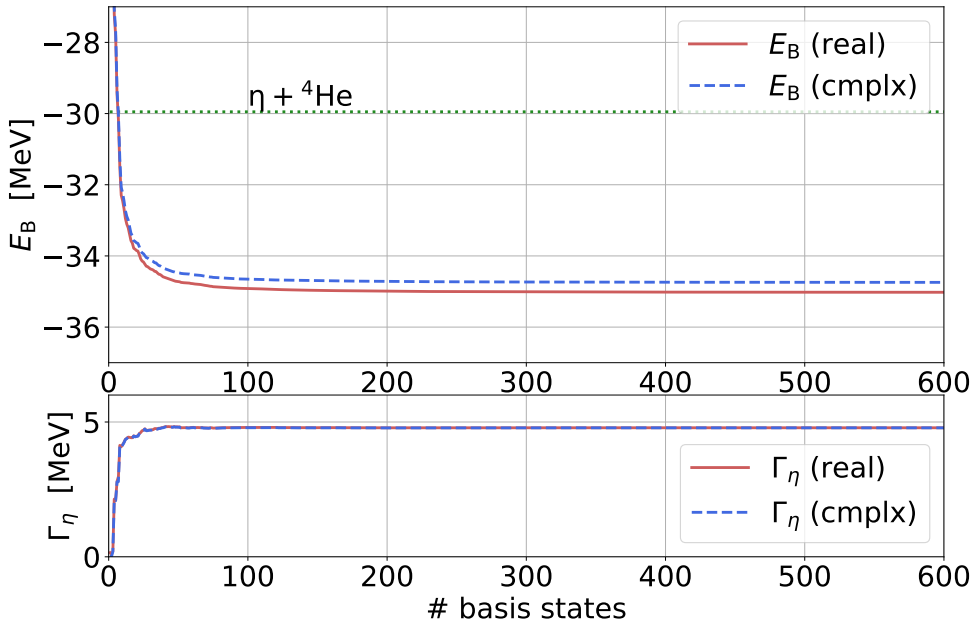

Figure 4.4: SVM calculation of the η^4He quasi-bound state using the same interactions as in Fig. 4.2 and $\delta\sqrt{s} = -28$ MeV. We show convergence of the corresponding quasi-bound state energy E_B (upper panel) and width Γ_η (lower panel) for both (real) and (cmplx) case denoted by solid red and blue dashed lines, respectively. For more detail regarding the (real) and (cmplx) case see the text.

Table 4.1: Comparison of self-consistent SVM calculations using two different evaluations of width Γ_η - the (real) case and the (cmplx) case. Calculations were performed for the Minnesota NN potential with the Coulomb force and the GW ηN model. The η binding energy B_η and self-consistent energy shift $\delta\sqrt{s_\mathrm{sc}}$ are shown as well. The table is adopted from the author's publication [52].

η^3He		B_η [MeV]	Γ_η [MeV]	$\delta\sqrt{s_\mathrm{sc}}$ [MeV]
$\lambda = 2$	(real)	0.11	1.37	-9.23
	(cmplx)	-0.25	1.32	-8.87
$\lambda = 4$	(real)	1.01	3.32	-13.18
	(cmplx)	0.36	3.44	-12.72

η^4He		B_η [MeV]	Γ_η [MeV]	$\delta\sqrt{s_\mathrm{sc}}$ [MeV]
$\lambda = 2$	(real)	0.97	2.17	-19.64
	(cmplx)	0.77	2.22	-19.50
$\lambda = 4$	(real)	4.62	4.38	-29.73
	(cmplx)	4.40	4.41	-29.60

function of $\delta\sqrt{s}$ has for both CS and GW interaction models maximum just below the threshold, as shown in Fig. 4.1. Furthermore, it is also apparent that the (cmplx) case confirms the width estimation using Eq. (4.3) yielding very close widths in all presented cases.

4.2 Λ^* - matter

We performed both SVM (few-body) and Relativistic Mean-Field (RMF; many-body) calculations of Λ^*-nuclei in response to Akaishi and Yamazaki (AY) suggestion that systems composed of purely $\Lambda^* \equiv \Lambda(1405)$ $[(\bar{K}N + \pi\Sigma)_{I=0}]$ constituents reach absolute stability for mass number $A \gtrapprox 8$ [109] . Using a $\sigma - \omega$ meson exchange model constrained by the binding energy of the two-body $\Lambda^*\Lambda^*$ system we evaluated B/A (binding energy per Λ^*) as a function of A and thus explored stability of the Λ^*-matter.

In this section we present selected results from our publication *Phys. Lett. B* ***785****, 90 (2018)* and manuscript submitted to *Int. Jour. of Mod. Phys. A* enclosed in Appendix D.3 and D.4, respectively. This work was also published in Ref. [258].

We considered Λ^* as a stable point-like particle with no further internal structure. Next, motivated by a successful RMF description of medium and heavy nuclei [259] we approached purely Λ^* systems in the same way. The corresponding Λ^* interaction was then described by an exchange of the scalar σ and vector ω meson fields entering the RMF Lagrangian density

$$\mathcal{L} = \bar{\Lambda}^* \left[\mathrm{i}\gamma^\mu D_\mu - (M_{\Lambda^*} - g_{\sigma\Lambda^*}\sigma) \right] \Lambda^* + (\sigma, \omega_\mu \,\text{free-field terms}) \,, \tag{4.4}$$

where $D_\mu = \partial_\mu + \mathrm{i}\, g_{\omega\Lambda^*}\, \omega_\mu$, Λ^* is a baryonic field, and $M_{\Lambda^*} = 1405$ MeV is the mass of Λ^*. Other parameters such as meson masses m_i $(i = \sigma, \omega)$ or corresponding coupling constants to the nucleon field g_{iN}, which enter yet to be determined $g_{i\Lambda^*} = \alpha_i g_{iN}$ coupling constants of Λ^* to the σ or ω meson fields, were taken from the linear HS model for atomic nuclei [260]. In this study, we excluded the Coulomb field and the ρ meson exchange from the RMF Lagrangian density (4.4) simply guided by the fact that Λ^* has no charge and it is $I = 0$ baryon.

In order to fix the scaling parameters α_σ and α_ω which determine the couplings in Eq. (4.4), we used the corresponding σ-ω meson exchange $\Lambda^*\Lambda^*$ potentials derived

either by Machleidt [261]

$$V_{\Lambda^*\Lambda^*}(r) = g^2_{\omega\Lambda^*}(1+\tfrac{1}{2}\tfrac{m^2_\omega}{M^2_{\Lambda^*}})\,Y_\omega(r) - g^2_{\sigma\Lambda^*}\,(1-\tfrac{1}{4}\tfrac{m^2_\sigma}{M^2_{\Lambda^*}})\,Y_\sigma(r) + g^2_{\omega\Lambda^*}\tfrac{1}{6}\left(\tfrac{m_\omega}{M_{\Lambda^*}}\right)^2 Y_\omega(r)(\vec{\sigma}_1\cdot\vec{\sigma}_2) \tag{4.5}$$

or by Dover-Gal [262]

$$V_{\Lambda^*\Lambda^*}(r) = g^2_{\omega\Lambda^*}\,(1+\tfrac{1}{8}\tfrac{m^2_\omega}{M^2_{\Lambda^*}})\,Y_\omega(r) - g^2_{\sigma\Lambda^*}\,(1-\tfrac{1}{8}\tfrac{m^2_\sigma}{M^2_{\Lambda^*}})\,Y_\sigma(r) + g^2_{\omega\Lambda^*}\tfrac{1}{6}\left(\tfrac{m_\omega}{M_{\Lambda^*}}\right)^2 Y_\omega(r)(\vec{\sigma}_1\cdot\vec{\sigma}_2)\ , \tag{4.6}$$

where $Y_{i=\sigma,\omega}(r) = \exp(-m_i r)/(4\pi r)$.

We used SVM together with the $V_{\Lambda^*\Lambda^*}$ potentials in Eqs. (4.5) and (4.6) to fit the scaling parameters α_σ and α_ω to the binding energy of the two-body $\Lambda^*\Lambda^*$ system $B(\Lambda^*\Lambda^*) = B((\bar{K}\bar{K}NN)_{I=0}) - 2B((\bar{K}N)_{I=0}) = 40$ MeV (we either kept $\alpha_\omega = 1$ fixed and changed α_σ or vice versa). The binding energies of the $(\bar{K}N)_{I=0}$ and $(\bar{K}\bar{K}NN)_{I=0}$ systems were adopted from the $\bar{K}N$ interaction model of Akaishi and Yamazaki [88] (for more details see Table 1 in Appendix D.3 and corresponding discussion).

In Fig. 4.5, we show calculated B/A (left panel) and rms radii $r_{\rm rms}$ (right panel) of several Λ^* systems as a function of the mass number A. Results, presented in the figure, are obtained using SVM and the Machleidt form of the $V_{\Lambda^*\Lambda^*}$ potential (4.5). We found that there is no significant difference between calculated properties of few-body Λ^* systems fitting either α_σ or α_ω (in fact, obtained results deviate from each other within less than 8%), consequently, we show as an example only the case with $\alpha_\omega = 1$ and α_σ fitted. While black color denotes our SVM results obtained by completely neglecting relativistic mass correction terms $\sim (m_{i=\sigma,\omega}/M_{\Lambda^*})^2$ in $V_{\Lambda^*\Lambda^*}$ (4.5), red color represents results taking into account mass corrections without the last term in Eq. (4.5) $\sim (\vec{\sigma}_1\cdot\vec{\sigma}_2)$. It is apparent that these two sets of calculations yield very similar results and both suggest rather steep increase of B/A. Further inclusion of the term $\sim (\vec{\sigma}_1\cdot\vec{\sigma}_2)$ (blue) has significant effect and B/A decreases by roughly 30% for all considered Λ^* systems with $A > 2$. In the right panel we show corresponding rms radii $r_{\rm rms}$ as a function of A. We observe that $r_{\rm rms}$ first increases, however, already at $A = 5$ starts to drop down and in all considered cases does not exceed 0.85 fm. This questions the treatment of Λ^* as a point-like particle without inner structure.

Next, in the left panel of Fig. 4.6, we present RMF calculations of the binding

energy per Λ^* (B/A) as a function of A. Red and blue colors indicate results obtained using the RMF Lagrangian density (4.4) where the scaling parameter α_σ ($\alpha_\omega = 1$) was fitted to $B(\Lambda^*\Lambda^*) = 40$ MeV using the Machleidt (red) and Dover-Gal (blue) $V_{\Lambda^*\Lambda^*}$ potentials in Eqs. (4.5) and (4.6), respectively, with all terms included. We also show B/A obtained with the non-linear RMF model NL-SH [263] (black) where α_σ parameter was fitted to $B(8\Lambda^*)$ predicted by the corresponding Dover-Gal RMF calculations (blue). B/A for atomic nuclei obtained with the NL-SH RMF model are plotted for comparison as well (green). We see that in all presented cases the binding energy per Λ^* saturates for $A \geq 120$ and does not exceed 100 MeV. Consequently, the calculated binding energy per Λ^* is not large enough to reduce the effective in-medium mass of Λ^* below that of the lightest $\Lambda(1116)$ hyperon, thus leaving Λ^* systems unstable with respect to strong decay.

In the right panel of Fig. 4.6, we compare the binding energy per Λ^* calculated within the SVM (blue) and RMF approach (red) using the Machleidt type of $V_{\Lambda^*\Lambda^*}$ (4.5) with all terms included. It is clear that while RMF results saturate, naive analysis of SVM calculations limited only to few-body systems might indeed suggest that B/A can for certain A become large enough to ensure stability of Λ^* systems.

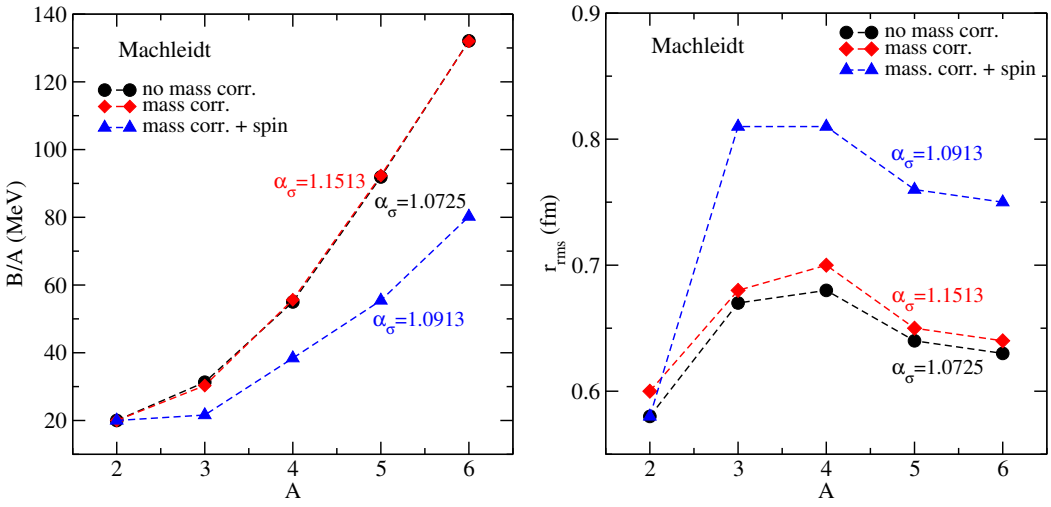

Figure 4.5: Binding energy per Λ^*, B/A (left panel) and rms radius r_{rms} (right panel) of Λ^* systems as a function of mass number A, calculated using SVM and Machleidt type of the $V_{\Lambda^*\Lambda^*}$ potential (4.5). Black, red, and blue colors denote results obtained with no mass correction $\sim (m_{i=\sigma,\omega}/M_{\Lambda^*})^2$ in the $V_{\Lambda^*\Lambda^*}$, with mass corrections but neglected spin-dependent part, and full $V_{\Lambda^*\Lambda^*}$, respectively. Values of α_σ ($\alpha_\omega = 1$) fitted to $B(\Lambda^*\Lambda^*)$=40 MeV are given as well. The figure is adopted from the author's publication [188].

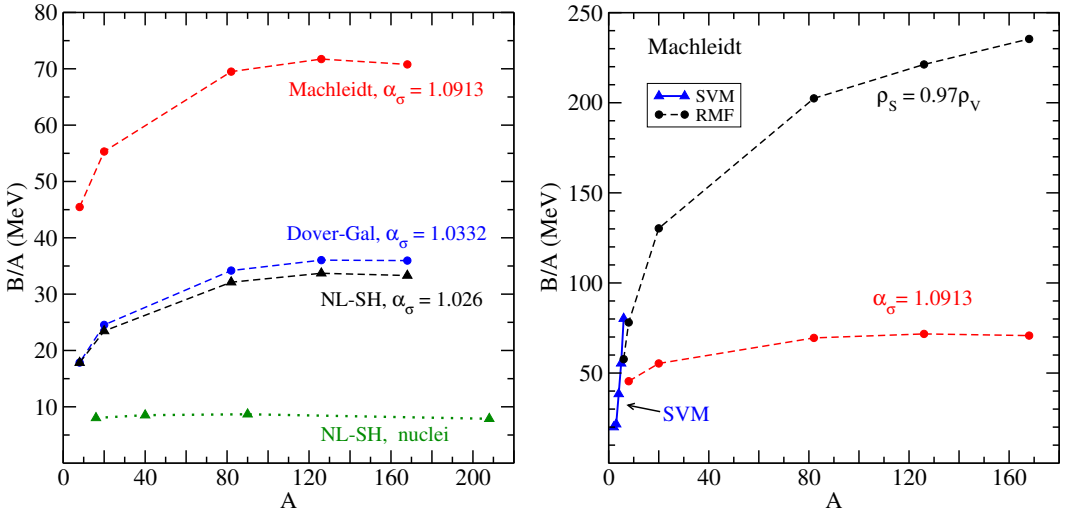

Figure 4.6: Binding energy per Λ^*, B/A as a function of increasing mass number A calculated using the HS and NL-SH RMF model. In the left panel we show results obtained with the HS model where the scaling parameter α_σ ($\alpha_\omega = 1$) is fitted to the $B(\Lambda^*\Lambda^*)$=40 MeV using either the full Machleidt (red) or Dover-Gal (blue) form of $V_{\Lambda^*\Lambda^*}$ given in Eqs. (4.5) and (4.6). The results obtained with the NL-SH RMF model are depicted in black color. Results for atomic nuclei predicted by the NL-SH RMF model are given in green. In the right panel we show the comparison between SVM (blue) and HS RMF (red) results for the full Machleidt type of $V_{\Lambda^*\Lambda^*}$. Equivalent RMF results but with fixed scalar baryonic density $\rho_s = 0.97\rho_v$ (black) are presented in the same panel as well. The figure is adopted from the author's publication [188].

In fact, this particular observation of B/A behavior in non-relativistic calculation of few-body Λ^* systems was used as the cornerstone for the AY suggestion of the Λ^*-matter stability. However, one must be aware that rather large binding energies in these systems certainly require relativistic approach which was omitted in Ref. [109]. In our SVM calculations, relativistic treatment would mean at least incorporation of the relativistic kinetic energy term and higher order relativistic mass corrections in $V_{\Lambda^*\Lambda^*}$. On the other hand, the RMF model implicitly takes into accounts relativistic effects which are entirely connected with the saturation mechanism in Λ^* systems. Due to the Lorenz covariance there are two densities - scalar ρ_s related to the σ attractive field and baryonic density ρ_v related to the ω repulsive field. As described in more detail in our publications enclosed in Appendices D.3 and D.4, with increasing baryon density ρ_v the scalar density ρ_s rapidly shrinks with respect to ρ_v which suppresses the attraction from the σ meson field. In order to demonstrate significance of this mechanism in Λ^* systems we fix $\rho_s = 0.97\rho_v$,

which corresponds to the fraction in the nuclear system ^{16}O (black color in the right panel of Fig. 4.6). The corresponding RMF calculations then predict steep increase of B/A rather similar to the one suggested by the SVM calculations.

4.3 s-shell hypernuclear systems

The major part of our results concerns the theoretical study of s-shell hypernuclei. We applied the $\not\pi$EFT representation of nucleon [189,195,196] and Λ [146,169] interactions at leading order (LO). The nucleon LO $\not\pi$EFT as well as three-body ΛNN and $\Lambda\Lambda N$ contact terms were constrained by experimental data. Being restricted by the lack of experimental information on the two-body level, the ΛN and $\Lambda\Lambda$ contact terms were fixed by selected sets of ΛN scattering lengths given in Table 2.1 - Alexander B, NSC97f, χEFT(LO), and χEFT(NLO) and a certain range of $\Lambda\Lambda$ scattering lengths. For more details about the hypernuclear $\not\pi$EFT at LO see Section 2.2.

First, we explored the nature of the $\Lambda(1116)$-hypernuclear Λnn ($J^\pi = 1/2^+$, $I = 1$) and ${}^3_\Lambda\mathrm{H}^*$ ($J^\pi = 3/2^+$, $I = 0$) systems using the LO $\not\pi$EFT nuclear and Λ-hypernuclear interactions. Applying both the CSM and IACCC techniques we performed the first EFT continuum calculation of these systems. We obtained position of the Λnn as well as the ${}^3_\Lambda\mathrm{H}^*$ states in a continuum for several ΛN interaction strengths. Further, we performed equivalent calculations using phenomenological NN and ΛN potentials in order to address differences between the $\not\pi$EFT and phenomenological approach.

In addition to the nuclear and Λ-hypernuclear LO $\not\pi$EFT interactions employed in the study of hypernuclear continuum [147], we constructed $\not\pi$EFT representation of the $\Lambda\Lambda$-hypernuclear interaction at the same order. Applying these interactions we performed SVM calculations of $A \leq 6$ s-shell $\Lambda\Lambda$ hypernuclei for different $\Lambda\Lambda$ interaction strengths and we explored the onset of $\Lambda\Lambda$ hypernuclear binding [169].

Below, we present selected results from our publications *Phys. Lett. B* ***808****, 135614 (2020)*, *Phys. Lett. B* ***797****, 134893 (2019)* and manuscript *arXiv:2003.09862 [nucl-th]* enclosed in Appendices D.5, D.7, and D.6, respectively.

4.3.1 Nature of the Λnn and ${}^3_\Lambda\mathrm{H}^*(J^\pi = 3/2^+, I = 0)$ states

We studied the movement of the Λnn and ${}^3_\Lambda\mathrm{H}^*$ S-matrix poles from a bound region to a continuum and further to their physical positions given by the Hamilto-

nian (2.10), which was induced by an auxiliary attractive potential $V^{\mathrm{IACCC}} = \alpha H^{\mathrm{aux}}$ (3.32).

We used the 3-body potential V_3^{IACCC} which ensured that properties of the 2-body part of the ⧸EFT Hamiltonian (2.10) such as scattering lengths or deuteron binding energy remained unaffected. Its form was selected to be the same as of the ⧸EFT 3-body potential (2.10)

$$V_3^{\mathrm{IACCC}} = d_\lambda^{I,S} \sum_{i<j<k} \mathcal{Q}_{ijk}^{I,S} \sum_{cyc} \mathrm{e}^{-\frac{\lambda^2}{4}\left(r_{ij}^2 + r_{jk}^2\right)}, \tag{4.7}$$

where the amplitude $d_\lambda^{I,S}$ defines its strength, corresponding to the parameter α in Eq. (3.32), and is negative for an attractive auxiliary potential. The projection operator $\mathcal{Q}_{ijk}^{I,S}$ ensures that the potential affects only a particular (I,S) three-body channel - $(1,\frac{1}{2})$ for Λnn or $(0,\frac{3}{2})$ for ${}^{3}_{\Lambda}\mathrm{H}^{*}$. If not explicitly mentioned λ in V_3^{IACCC} is equal to the ⧸EFT cutoff λ.

We started our study of three-body hypernuclear continuum states with the Λnn system. To demonstrate the cutoff dependence of the theory, we present in Fig. 4.7 the trajectories $E_{\Lambda nn}(d_\lambda^{I=1,S=1/2},\lambda)$ of the Λnn resonance pole, calculated using the IACCC method for different values of cutoff λ, and for a representative set of $a_s^{\Lambda N}$ - NSC97f. With decreasing attraction of V_3^{IACCC}, the resonance poles move along circular trajectories in the complex energy plane starting from the $\Lambda{+}n{+}n$ threshold to the physical end points where $d_\lambda^{I=1,S=1/2} = 0$. It can be deduced from the figure that the trajectories $E_{\Lambda nn}(d_\lambda^{I=1,S=1/2},\lambda)$ and the physical end points converge with increasing cutoff. We reach stabilized results already for $\lambda = 2.5$ fm^{-1}.

The excited state of the hypertriton ${}^{3}_{\Lambda}\mathrm{H}^{*}(J^\pi = 3/2^+, I = 0)$ might be considered as a good candidate for a near-threshold resonance. Indeed, several works demonstrated the emergence of a bound state by increasing rather moderately the ΛN interaction strength. Applying the IACCC method we follow the pole trajectory given by the amplitude of the auxiliary 3-body force $d_\lambda^{I=0,S=3/2}$ from a bound region to its physical position in a Λ+deuteron $(\Lambda + d)$ continuum. In Fig. 4.8 we show the ${}^{3}_{\Lambda}\mathrm{H}^{*}$ pole momentum $k = \sqrt{2\mu_{\Lambda d}[E({}^{3}_{\Lambda}\mathrm{H}^{*}) - E_B({}^{2}\mathrm{H})]}$, $\mu_{\Lambda d} = m_d m_\Lambda/(m_d + m_\Lambda)$, as a function of $d_\lambda^{I=0,S=3/2}$ for the Alexander B ΛN scattering lengths and $\lambda = 6$ fm^{-1}. We observe that with decreasing auxiliary attraction the imaginary part of the momentum $\mathrm{Im}(k)$ decreases from a positive value (bound state) to a negative value (unbound state) whereas the real part $\mathrm{Re}(k)$ remains equal to zero. This behavior is regarded as the definition of a virtual state [230].

In Fig. 4.9 we show the physical solutions (with no auxiliary force) corresponding

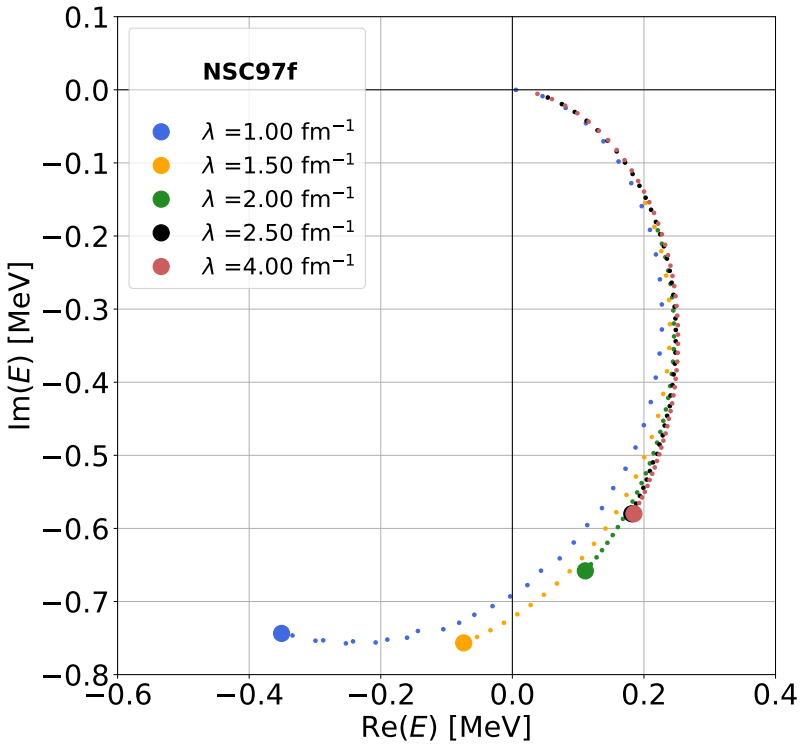

Figure 4.7: Trajectories of the Λnn resonance pole in a complex energy plane determined by a decreasing attractive strength of the auxiliary three-body force $d_\lambda^{I=1,S=1/2}$ for several cutoffs λ and the NSC97f set of ΛN scattering lengths. Small dots mark IACCC solutions for different $d_\lambda^{I=1,S=1/2}$, larger symbols stand for the physical position of the Λnn pole ($d_\lambda^{I=1,S=1/2} = 0$). Notice the almost overlapping trajectories for $\lambda = 2.50$ fm^{-1} and $\lambda = 4.00$ fm^{-1}. The figure is adopted from the author's publication [147].

to the $\not\pi$EFT Hamiltonian H (2.10). Here, the real Re(E) and imaginary Im(E) parts of the Λnn resonance energy (left panel) and the energy E_v of the virtual state ${}^{3}_{\Lambda}\mathrm{H}^*$ (right panel) are plotted as a function of the cutoff λ for the ΛN scattering length versions listed in Table 2.1. The calculated energies in the both hypernuclear systems depend strongly on the input ΛN interaction strength. In the case of ${}^{3}_{\Lambda}\mathrm{H}^*$, we obtain for all considered ΛN scattering lengths a virtual state solution. On the other hand, in the case of the Λnn system the $\not\pi$EFT predicts a resonant state. Moreover, only NSC97f and χEFT(NLO) yield the ΛN interaction strong enough to ensure for $\lambda \geq 2$ fm^{-1} the Λnn pole position in the fourth quadrant of a complex energy plane (Re(E) > 0, Im(E) < 0), i.e. they predict a physical Λnn resonance.

In Fig. 4.9 we also demonstrate stability of our solutions with respect to the cutoff λ. The calculated energies vary smoothly beyond the value $\lambda = 2$ fm^{-1} and already at $\lambda = 4$ fm^{-1} they stabilize within extrapolation uncertainties at an asymptotic

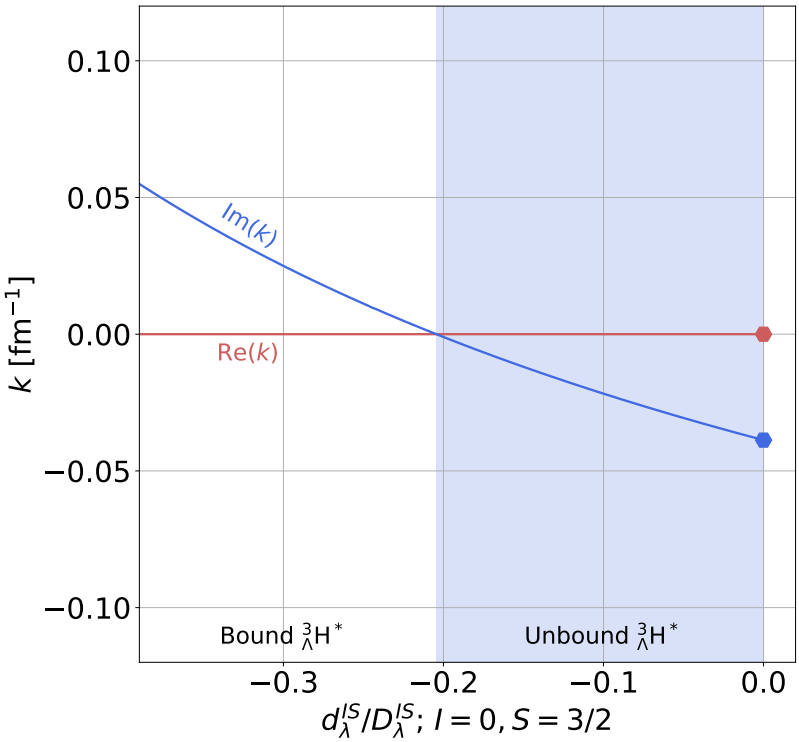

Figure 4.8: Imaginary (blue) and real (red) parts of the ${}^{3}_{\Lambda}\mathrm{H}^{*}$ pole momentum k as a function of $d_\lambda^{I=0,S=3/2}$ calculated for the Alexander B set and $\lambda = 6$ fm^{-1}, normalized to the physical three-body LEC $D_\lambda^{I=0,S=3/2}$. Unbound region is determined through the IACCC method. Dots mark the physical solution for $d_\lambda^{I=0,S=3/2} = 0$. The figure is adopted from the author's publication [147].

value corresponding to the renormalization scale invariance limit $\lambda \to \infty$. This is illustrated in the right panel, where we present for the Alexander B case the extrapolation function and the asymptotic value including the extrapolation error for the energy E_v of the ${}^{3}_{\Lambda}\mathrm{H}^{*}$ virtual state. It is to be noted that one might naively expect clear dependence on the strength of the ΛN spin-triplet interaction which solely enters the ${}^{3}_{\Lambda}\mathrm{H}^{*}$ hypernuclear part on a two-body level. However, the dominance of the spin-triplet interaction is undermined by 3-body force in the $\left(0, \frac{3}{2}\right)$ channel compensating the size of the spin-singlet scattering length $a_0^{\Lambda N}$, being fixed by the $B_\Lambda({}^{4}_{\Lambda}\mathrm{H}^{*})$ experimental value.

The existence of the ${}^{3}_{\Lambda}\mathrm{H}^{*}$ virtual state is further confirmed by the CSM. We do not see any sign of a resonance for all sets of ΛN scattering lengths, cutoffs, or auxiliary 3-body force values $d_\lambda^{I=0,S=3/2}$. From the rotated discretized CSM continuum spectra we calculated the s-wave Λd phase shifts $\delta_{3/2}^{\Lambda d}$ for the $J^\pi = 3/2^+$ channel using Eq. (3.52). The calculated phase shifts for different ΛN interaction strengths and $\lambda = 6$ fm^{-1} presented in Fig. 4.10 exhibit clear enhancement close to threshold,

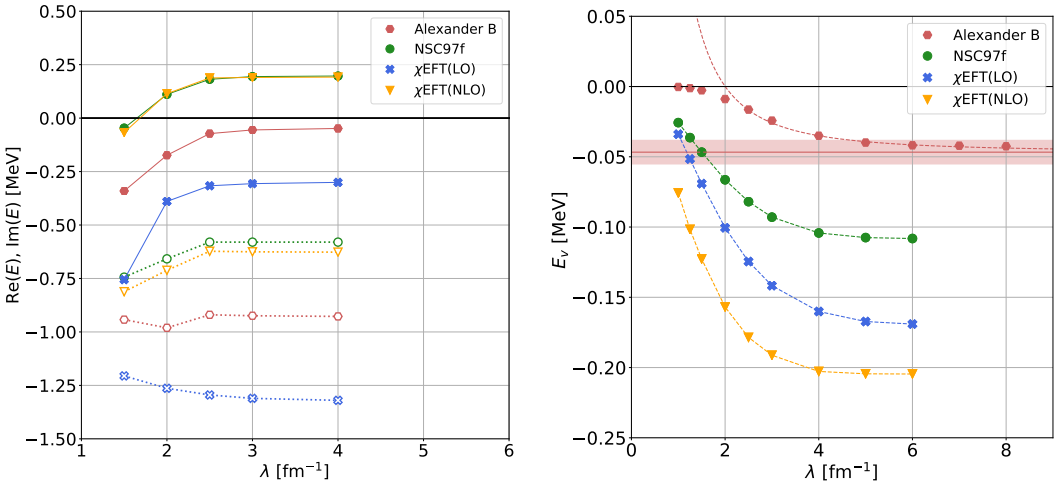

Figure 4.9: Real Re(E) (full symbols) and imaginary Im(E) (empty symbols) parts of the Λnn resonance energy (left panel) and energy E_v of the ${}^{3}_{\Lambda}\mathrm{H}^{*}$ virtual state (right panel) as a function of cutoff λ, calculated using the IACCC method for several ΛN interaction strengths. For the ${}^{3}_{\Lambda}\mathrm{H}^{*}$ virtual state (right panel) and Alexander B we perform extrapolation for $\lambda \to \infty$. The red dashed line is the extrapolation function, the solid red line and shaded area mark the contact limit and the extrapolation error. The figure is adopted from the author's manuscript [264].

implying proximity of a pole. The shaded areas in the figure reflect the phase shift dependence on the rotation angle θ, which we checked for a rather broad interval $15° < \theta < 20°$.

Our work represents the first EFT study of the Λnn and ${}^{3}_{\Lambda}\mathrm{H}^{*}$ hypernuclear systems in a continuum. Therefore, we found it appropriate to discuss difference of our approach with respect to the previous calculations of the Λnn resonance performed by Afnan and Gibson using a phenomenological approach [144]. Following their work we neglected three-body force but instead of separable non-local two-body potentials we employed one range Gaussians

$$V(r) = \sum_{I,S} \hat{\mathcal{P}}_{I,S}\; C_{I,S}\; \exp\left(-\frac{\lambda_{I,S}^2}{4} r^2\right) \tag{4.8}$$

to describe s-wave interaction in nuclear $I, S = (0,1),\ (1,0)$ and hypernuclear $I, S = (1/2,1),\ (1/2,0)$ two-body channels. Here, $\hat{\mathcal{P}}_{I,S}$ is the projection operator. The parameters $C_{I,S}$ and $\lambda_{I,S}$ were fitted to the values of a_s and r_s listed in [144]. Moreover, we took into account $a_s^{\Lambda N}$ and $r_s^{\Lambda N}$ related to Alexander B and χEFT(LO) given in Table 2.1.

The calculated Λnn pole trajectories for the Phen-2B potential (4.8) are presented in Fig. 4.11, left panel. The auxiliary interaction is in the form of a three-

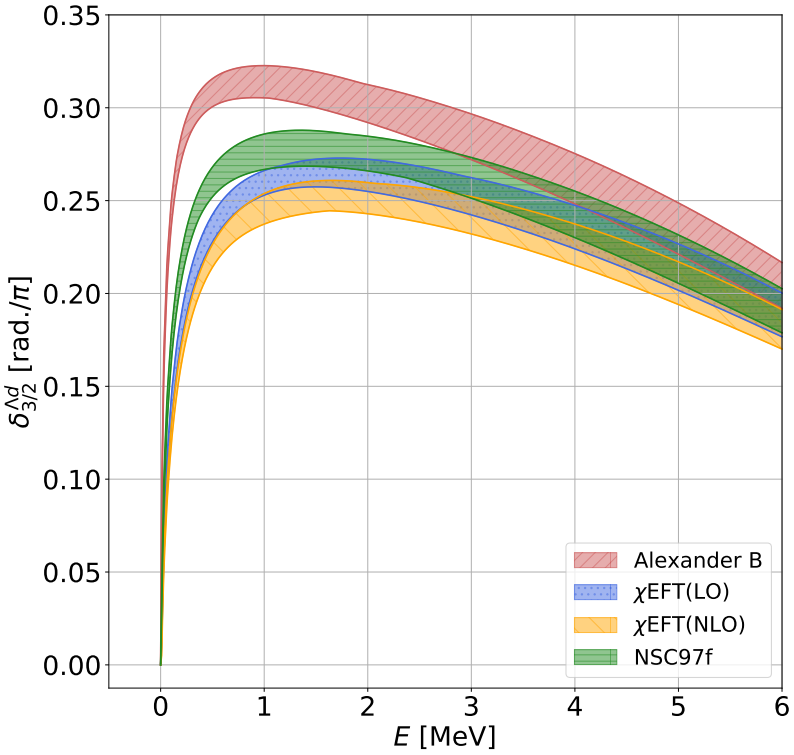

Figure 4.10: S-wave Λd phase shifts in the $J^\pi = 3/2^+$ channel $\delta^{\Lambda d}_{3/2}$ as a function of energy E above the Λ+d threshold, extracted from the continuum level density of the rotated CSM spectra (3.52). The phase-shifts are calculated for cutoff $\lambda = 6$ fm^{-1} and several ΛN interaction strengths. Shaded areas mark uncertainty introduced by the rotation angle θ within interval $15° < \theta < 20°$. The figure is adopted from the author's publication [147].

body force (4.7) with cutoff $\lambda = 1$ fm^{-1}. We observe that calculated physical pole positions (filled larger symbols) are in good agreement with those presented in Ref. [144] (empty symbols). Indeed, as might be expected the position of the near-threshold Λnn resonance is predominantly given by low-momentum characteristics of the interaction - a_s and r_s which are the same in both cases.

In order to reveal the relation between the LO $\not\pi$EFT and phenomenological approaches discussed above, one can consider the finite cutoff λ_s which gives roughly the same values of r_s as used in the above phenomenological calculations. Such a value, $\lambda_s \approx 1.25$ fm^{-1} for NSC97f andχEFT(NLO), yields in addition $B_\Lambda(^5_\Lambda\mathrm{He})$ remarkably close to experiment [265]. As explained by the authors one might understand that λ_s absorbs into LECs NLO contributions of the theory which are likely to increase its precision, however, success of this procedure is not in general guaranteed for all systems. Indeed, higher orders above NLO which behave as powers of (Q/λ) are induced as well and are not suppressed by $\lambda \to \infty$. In Fig. 4.11, right panel, we

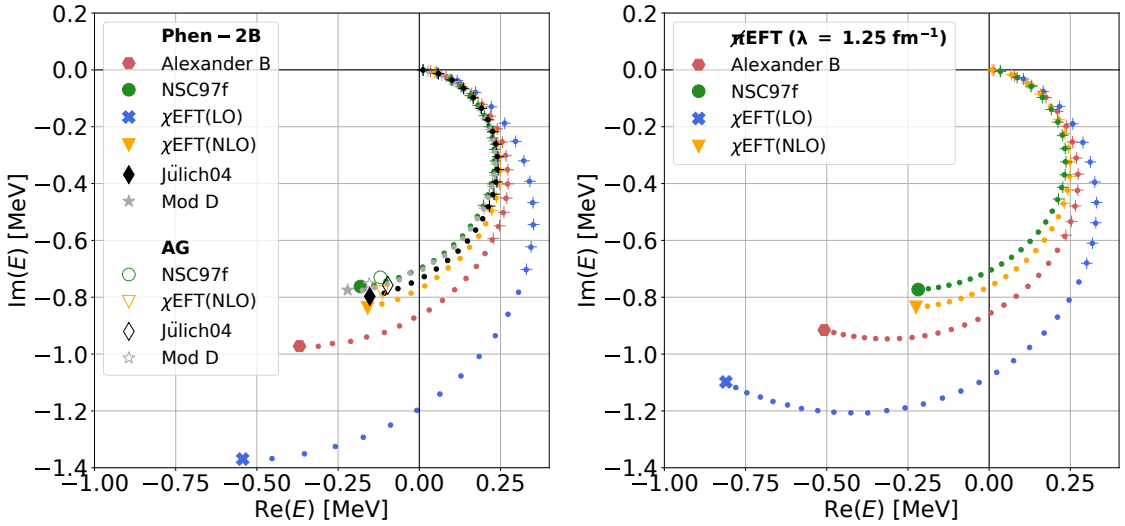

Figure 4.11: Trajectories of the Λnn resonance pole in a complex energy plane given by decreasing $d_\lambda^{I=1,S=1/2}$ for several ΛN interaction strengths. Left panel: Calculations using the ΛN and NN phenomenological potential Phen-2B (4.8). Larger full symbols stand for the physical position of the Λnn pole ($d_\lambda^{I=1,S=1/2} = 0$), empty symbols mark corresponding solutions obtained by Afnan and Gibson (AG) [144] for the same scattering lengths and effective ranges used to fix potential Phen-2B (4.8). Right panel: $\not\pi$EFT calculations for cutoff $\lambda = 1.25$ fm^{-1}. In a region accessible by CSM we also show for each IACCC solution (dots) the one obtained by CSM (crosses) for the same amplitude of the auxiliary three-body force. The figure is adopted from the author's manuscript [264].

present Λnn pole trajectories calculated using the $\not\pi$EFT for this specific λ_s value and several ΛN interaction strengths. One notices very close positions of the Λnn resonance calculated for χEFT(NLO) and NSC97f using the Phen-2B potential (left panel) and the $\not\pi$EFT (right panel). The LO $\not\pi$EFT for $\lambda = 1.25$ fm^{-1} could thus be considered as a suitable phenomenological model which yields good predictions for 4- and 5- body hypernuclei and hypertriton [146, 265].

In addition, in both panels of Fig. 4.11 we compare the Λnn pole positions calculated within the CSM and IACCC method for the same values of $d_\lambda^{I=1,S=1/2}$ located in the area reachable by the CSM. We see remarkable agreement between IACCC (dots) and CSM (crosses) solutions, which provides benchmark of the calculations and demonstrates high precision of our results.

In Fig. 4.12 we show B_Λ of remaining s-shell hypernuclear systems, calculated using the Phen-2B potential (4.8). The hypertriton ground state ${}^3_\Lambda\mathrm{H}(\mathrm{J}^\pi = 1/2^+, \mathrm{I} = 0)$ is in most cases overbound, calculated $B_\Lambda({}^3_\Lambda\mathrm{H})$ are consistent with those obtained by Afnan and Gibson using separable non-local potentials fitted to the same ΛN

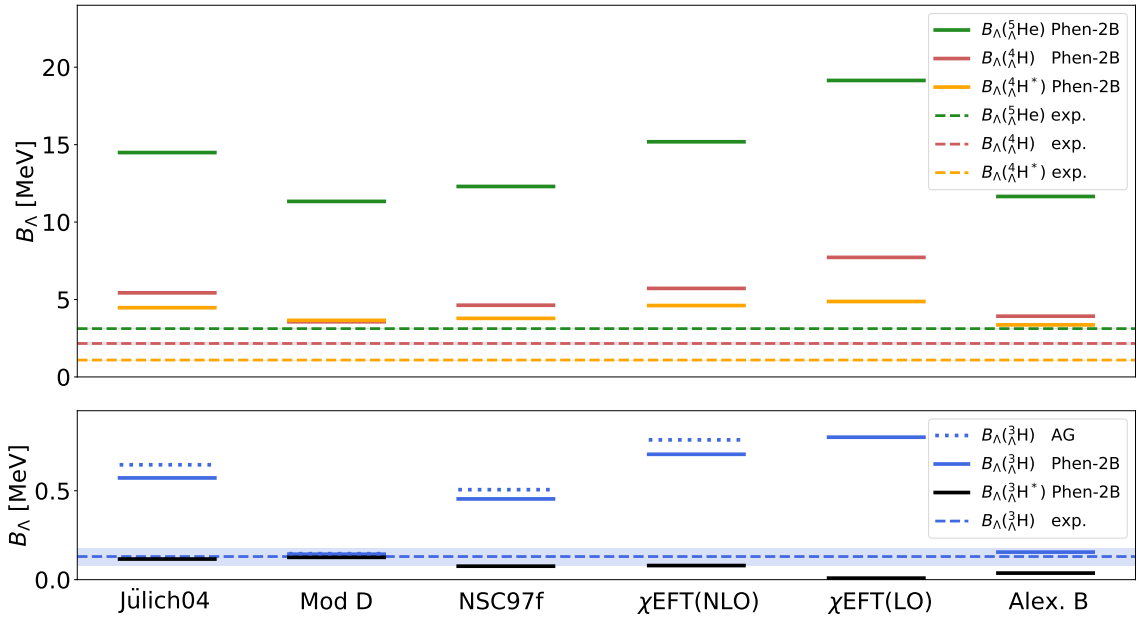

Figure 4.12: Λ separation energies B_Λ from SVM calculations using various ΛN interaction strengths of the Phen-2B interaction (4.8). The nuclear part is given by the same form of a phenomenological potential. Experimental values of B_Λ are marked by dashed horizontal lines. The figure is adopted from the author's manuscript [264].

interaction strengths [144]. The excited state of hypertriton ${}^3_\Lambda\text{H}^*$ turns to be bound, which is in disagreement with previous theoretical calculations [139, 143]. Heavier s-shell systems are considerably overbound as well, regardless of which specific set of $a_s^{\Lambda N}$ and $r_s^{\Lambda N}$ is fitted. Overbinding of s-shell hypernuclear systems brought about by the Phen-2B interaction (4.8) clearly indicates a missing piece which would introduce necessary repulsion. This could be provided by introducing a ΛNN three-body force. In fact, Afnan and Gibson stated that more detailed study of the Λnn resonance including three-body forces should be considered [144]. In $\not\pi$EFT , additional repulsion is included right through the ΛNN force fitted for each cutoff λ to experimental values of B_Λ in 3- and 4-body hypernuclei. As a result, though both the Phen-2B (as well as AG) interaction and the $\not\pi$EFT for $\lambda = 1.25$ fm^{-1} yield close positions of the Λnn resonance (see Fig. 4.11), the interplay between three-body forces in the $\not\pi$EFT exhibits large effect which completely removes overbinding presented for the Phen-2B interaction in Fig. 4.12, yielding correct $B_\Lambda({}^5_\Lambda\text{He})$, exact $B_\Lambda({}^3_\Lambda\text{H})$, $B_\Lambda({}^4_\Lambda\text{H})$, and $E_{\text{exc}}({}^4_\Lambda\text{H}^*)$ plus unbound ${}^3_\Lambda\text{H}^*$ as presented in Fig. 4.9. This suggests that the sensitivity of the Λnn system to the three-body ΛNN force is relatively small.

4.3.2 Lightest ΛΛ hypernuclei

In Table 4.2 we assess the onset of ΛΛ hypernuclear binding using a representative value $a_{\Lambda\Lambda} = -0.8$ fm, the Alexander B set of ΛN scattering lengths, and cutoff λ=4 fm^{-1}. The first row of the table shows calculated Λ separation energies of s-shell double-Λ hypernuclei for the three-body $\Lambda\Lambda N$ term fitted to the experimental $\Delta B_{\Lambda\Lambda}({}^{6}_{\Lambda\Lambda}\mathrm{He})$ (the so called Nagara event [213]). In this case we obtain ${}^{5}_{\Lambda\Lambda}\mathrm{H}$ system convincingly bound, while ${}^{4}_{\Lambda\Lambda}\mathrm{H}$, $\Lambda\Lambda nn$, and $\Lambda\Lambda n$ hypernuclei are predicted unbound. Reduction of the repulsive $\Lambda\Lambda N$ LEC in order to make ${}^{4}_{\Lambda\Lambda}\mathrm{H}$ just particle stable overbinds ${}^{6}_{\Lambda\Lambda}\mathrm{He}$ by ≈1.5 MeV (second row in Table 4.13). Reducing further the $\Lambda\Lambda N$ LEC one binds the neutral systems, first $\Lambda\Lambda nn$ (third row) and then $\Lambda\Lambda n$ (fourth row), at a price of overbinding further ${}^{6}_{\Lambda\Lambda}\mathrm{He}$. In fact, the particle stability of these $A = 3, 4$ neutral ΛΛ systems is incompatible with the ${}^{6}_{\Lambda\Lambda}\mathrm{He}$ binding energy datum for all values of cutoff λ and scattering length $a_{\Lambda\Lambda}$ considered in our work. These results suggest that the $A = 3, 4$ light neutral ΛΛ hypernuclei are unbound within a large margin.

Calculated values of the Λ separation energy $B_{\Lambda}({}^{5}_{\Lambda\Lambda}\mathrm{H})$ are shown in Fig. 4.13. Several representative values of the ΛΛ scattering length were used: $a_{\Lambda\Lambda}$=-0.5, -0.8, and -1.9 fm. Again, the choice of $a_{\Lambda\Lambda}$ determines the one ΛΛ LEC required at LO, while the $\Lambda\Lambda N$ LEC was fitted to $\Delta B_{\Lambda\Lambda}({}^{6}_{\Lambda\Lambda}\mathrm{He})$=0.67±0.17 MeV. Results presented in the figure are predominantly calculated for the ΛN interaction terms constrained by the Alexander B set of ΛN scattering lengths $a_s^{\Lambda N}$. For cutoff λ=4 fm^{-1} we also show $B_{\Lambda}({}^{5}_{\Lambda\Lambda}\mathrm{H})$ calculated using three other $a_s^{\Lambda N}$ sets - χEFT(LO), χEFT(NLO), and NSC97f, demonstrating that the dependence on ΛN interaction strength is rather weak when it comes to Λ separation energies in double-Λ hypernuclei. Calculated

Table 4.2: Λ separation energies $B_{\Lambda}({}^{A}_{\Lambda\Lambda}\mathrm{Z})$ for A=3–6, calculated using $a_{\Lambda\Lambda}$=−0.8 fm, cutoff λ=4 fm^{-1}, and the Alexander B set of ΛN scattering lengths. In each row a $\Lambda\Lambda N$ LEC was fitted to the underlined binding energy constraint - experimental $\Delta B_{\Lambda\Lambda}({}^{6}_{\Lambda\Lambda}\mathrm{He})$ or just bound ${}^{4}_{\Lambda\Lambda}\mathrm{H}$, $\Lambda\Lambda nn$, or $\Lambda\Lambda n$ systems in the given order. The table is adopted from the author's publication [169].

Constraint (MeV)	$\Lambda\Lambda n$	$\Lambda\Lambda nn$	${}^{4}_{\Lambda\Lambda}\mathrm{H}$	${}^{5}_{\Lambda\Lambda}\mathrm{H}$	${}^{6}_{\Lambda\Lambda}\mathrm{He}$
$\Delta B_{\Lambda\Lambda}({}^{6}_{\Lambda\Lambda}\mathrm{He})$=<u>0.67</u>	–	–	–	1.21	3.28
$B_{\Lambda}({}^{4}_{\Lambda\Lambda}\mathrm{H})$=<u>0.05</u>	–	–	0.05	2.28	4.76
$B(\Lambda\Lambda nn)$=<u>0.10</u>	–	0.10	0.86	4.89	7.89
$B(\Lambda\Lambda n)$=<u>0.10</u>	0.10	15.15	18.40	22.13	25.66

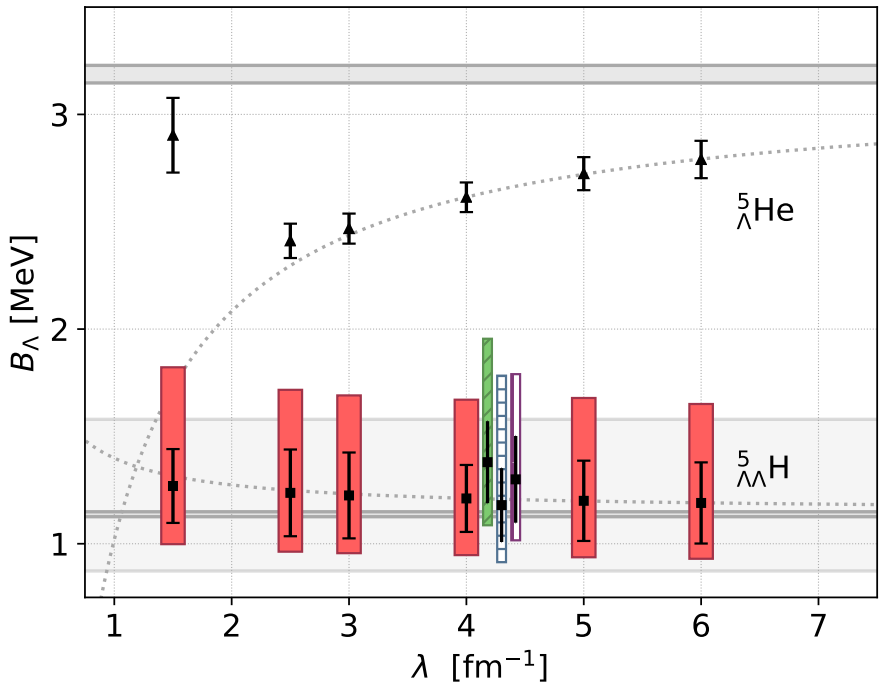

Figure 4.13: Λ separation energies $B_\Lambda({}^{5}_{\Lambda\Lambda}\mathrm{H})$ and $B_\Lambda({}^{5}_{\Lambda}\mathrm{He})$ from SVM calculations as a function of the cutoff λ. Error bars (in black) reflect the experimental uncertainty inherent in the ${}^{3}_{\Lambda}$H, ${}^{4}_{\Lambda}$H, ${}^{4}_{\Lambda}$H* and ${}^{6}_{\Lambda\Lambda}$He binding-energy input data, and (red) rectangles include also varying $a_{\Lambda\Lambda}$ between -0.5 to -1.9 fm. The ΛN set of scattering lengths is Alexander B, with results for χEFT(LO), χEFT(NLO), and NSC97f sets shown from left to right in this order for λ=4 fm^{-1}. Dotted lines show extrapolations, as $\lambda \to \infty$, to the respective scale renormalization invariance limits marked by gray horizontal bands. The wider ${}^{5}_{\Lambda\Lambda}$H band accounts for uncertainties in the experimental values of binding energies used in extrapolation to $\lambda \to \infty$. The figure is adopted from the author's publication [169].

values of $B_\Lambda({}^{5}_{\Lambda}\mathrm{He})$ using Alexander B $a_s^{\Lambda N}$, compatible with those from Ref. [146], are also shown in the figure. One observes that ${}^{5}_{\Lambda\Lambda}$H comes out particle stable over a broad range of finite cutoff values used in the calculations.

The calculated B_Λ values shown in Fig. 4.13 exhibit renormalization scale invariance in the limit $\lambda \to \infty$. To figure out the associated $B_\Lambda(\lambda \to \infty)$ values, we extrapolated $B_\Lambda(\lambda)$ for $\lambda \geq 4$ fm^{-1} using a power series in the small parameter Q/λ (2.13). The corresponding extrapolation curves (dotted lines in Fig. 4.13) converge to asymptotic values $B_\Lambda(\infty)$ within extrapolation uncertainties (gray horizontal bands). ${}^{5}_{\Lambda\Lambda}$H remains particle stable in this limit with Λ separation energy $B_\Lambda(\infty) = 1.14 \pm 0.01^{+0.44}_{-0.26}$ MeV, where the first uncertainty is due to the extrapolation (2.13) and the second one is due to the $a_{\Lambda\Lambda}$ and B_Λ uncertainties.

4.4 p-shell systems within LO $\not\pi$EFT

Motivated by the successful LO $\not\pi$EFT description of s-shell systems, we investigated whether this approach is applicable to p-shell nuclei. We constructed the SU(4)-symmetric version of a nuclear $\not\pi$EFT interaction at leading order [266] which allowed us to perform SVM calculations up to ^{8}Be. In comparison with the standard nuclear LO $\not\pi$EFT [189, 195, 196] applied in our work so far, this interaction omits spin dependence on a two-body level. We note that the SU(4) form is certainly a simplification, nevertheless, as pointed out in Ref. [266] it has some success in heavier nuclei [267, 268] which gives credibility to this approach.

For each value of cutoff we constrained the two-body NN contact term by the deuteron binding energy $B(^2\mathrm{H}) = 2.22$ MeV, and the three-body NNN contact term by the triton binding energy $B(^3\mathrm{H}) = 8.48$ MeV. Further, we considered the nucleon mass $m_\mathrm{N} = 938$ MeV. Using this interaction we performed SVM calculations for different nuclear systems with $A \leq 8$ and we studied cutoff dependence of obtained ground state energies. For more details about the LO $\not\pi$EFT see Section 2.2.

Here, we present selected results from the manuscript *arXiv:2003.09862* which is enclosed in Appendix D.8.

In Fig. 4.14 we show results of our calculations of s-shell ^{2}H, ^{3}H, ^{4}He and p-shell $^3\mathrm{H}(S = 3/2)$, ^{4}H, ^{5}He, ^{6}Li, ^{7}Li, and ^{8}Be ground states for different values of cutoff λ. Since the ground state energies of ^{2}H and ^{3}H were employed as a constraint of the theory, they exhibit no sign of λ dependence. The calculated ground state energy of ^{4}He converges with increasing cutoff λ, which was checked by calculations for $\lambda \in \langle 4; 10\rangle$ fm^{-1}, not displayed in the figure. Studying the p-shell nuclear region we found that for each considered p-shell system there exists a specific cutoff λ_c for which the corresponding ground state is no longer bound. In fact, we obtained bound p-shell systems only for rather small values of cutoffs $\lambda < \lambda_c$, while for $\lambda > \lambda_c$ we observed that following dissociation thresholds : $^2\mathrm{H} + \mathrm{n}$ ($^3\mathrm{H}(S = 3/2)$), $^3\mathrm{H} + \mathrm{n}$ (^{4}H), $^4\mathrm{He} + \mathrm{n}$ (^{5}He), $^2\mathrm{H} + ^4\mathrm{He}$ (^{6}Li), $^3\mathrm{H} + ^4\mathrm{He}$ (^{7}Li), and $^4\mathrm{He} + ^4\mathrm{He}$ (^{8}Be) assigned to the corresponding s-shell subcomponents are energetically more favorable. Our results suggest that the nuclear LO $\not\pi$EFT is not able to sustain bound states in p-shell nuclei in the renormalization group invariant limit $\lambda \to \infty$. This result is in disagreement with the experimental observation that both ^{6}Li, and ^{7}Li ground states are bound. Moreover, in the absence of Coulomb repulsion the ^{8}Be ground state is expected

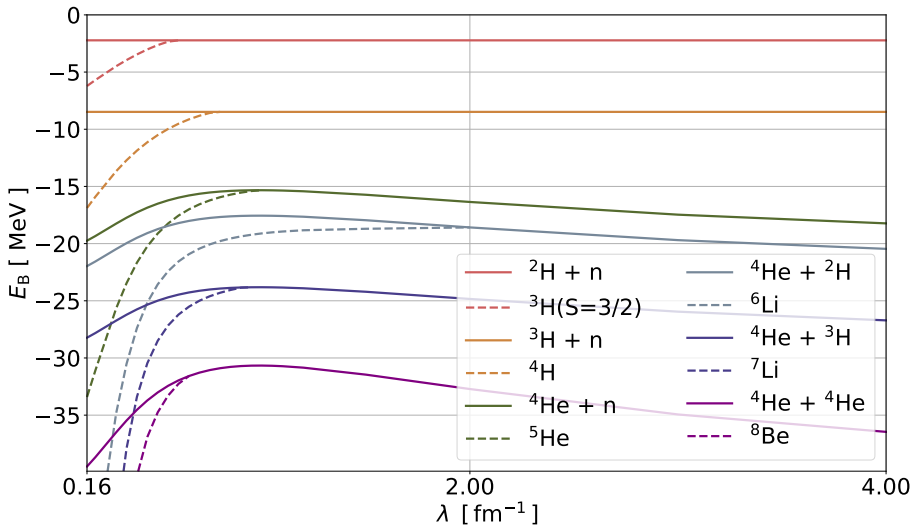

Figure 4.14: Ground state energies E_B of different p-shell nuclear systems calculated using the SU(4)-symmetric version of the nuclear LO $\not\pi$EFT interaction as a function of increasing cutoff λ (dashed lines). For each p-shell system we show calculated energy of the lowest dissociation threshold (solid line). Ground state energy of each p-shell system and their lowest dissociation threshold are drawn using the same color. The energy of ^{2}H + n, ^{3}H + n, and ^{4}He + n thresholds corresponds directly to the ground state energy of ^{2}H, ^{3}H, and ^{4}He, respectively. All calculations are performed using SVM. The table is adopted from the author's manuscript [269].

to become bound as well [270, 271]. Our work in Appendix D.8 further illustrates that observed insufficiency of the theory is not caused by its specific application to nuclear systems, but it emerges as a consequence of a more general concept of contact theories where the nuclear $\not\pi$EFT is only one of their possible applications.

Chapter 5

Summary & Outlook

In this thesis we studied interactions of hadrons, namely η, Λ, and Λ^* in few-body systems. We used either effective ηN and phenomenological NN potentials (η-nuclei), meson-exchange $\Lambda^*\Lambda^*$ potentials (Λ^*-systems), or the $\not\pi$EFT representation of nuclear, single-Λ, and double-Λ interactions (Λ-, $\Lambda\Lambda$-hypernuclei) at LO. We developed a new few-body code based on the Stochastic Variational Method with the correlated Gaussian basis (bound states) and two different continuum techniques - the Complex Scaling Method and Inverse Analytic Continuation in the Coupling Constant (resonances, virtual states). Both correctness of the code and precision of the selected few-body methods were tested in a series of benchmark calculations. The accuracy was found comparable with other few-body techniques such as the Faddeev (3-body) or Faddeev-Yakubovski (4-body) equations. We stress that the only approximation made in our few-body approach came from finite dimension of the basis set which could be, however, systematically increased in order to reach converged results.

First, we performed few-body calculations of η-nuclear quasi-bound states in s-shell ^{3}He, ^{4}He nuclei and, for the first time, also in the p-shell ^{6}Li nucleus. While the nuclear part was described using phenomenological Minnesota potential with Coulomb force, the ηN interaction was given by a complex, energy dependent, effective $V_{\eta N}$ potential which was fitted for two values of momentum cutoff $\lambda = 2,\ 4$ fm^{-1} to complex energy dependent phase shifts predicted either by the GW [20] or CS [22] ηN interaction model. The energy dependence of $V_{\eta N}$ was treated self-consistently. The imaginary part $\mathrm{Im}(V_{\eta N})$ describing η absorption in the nuclear medium was considered in two ways: either perturbatively or by its direct inclusion into the few-body Hamiltonian. In the latter case we evaluated the effect of η absorption on the

η separation energy in the studied systems.

Second, we explored stability of the Λ^*-matter suggested by Akaishi and Yamazaki [109] by performing a series of few-body (SVM) and many-body (RMF) calculations. The $\Lambda^*\Lambda^*$ interaction was described within the $\sigma - \omega$ meson-exchange model fitted to the binding energy of the two-body Λ^*-system, derived from calculated properties of K^--nuclei.

Third, we carried out thorough calculations of few-body hypernuclear systems Λnn ($J^\pi = 1/2^+,\ I = 1$) and ${}^{3}_{\Lambda}\mathrm{H}^*$ ($J^\pi = 3/2^+,\ I = 0$) within a LO $\not\pi$EFT with 2- and 3-body regulated contact terms. The ΛN LECs were associated with ΛN scattering lengths given by various interaction models and the ΛNN LECs were fitted to known Λ separation energies B_Λ in $A \leq 4$ hypernuclei and the excitation energy $E_{\mathrm{exc}}({}^{4}_{\Lambda}\mathrm{H}^*)$. Our LO $\not\pi$EFT approach, which accounts for all known s-shell hypernuclear data, represents a unique tool to describe within a unified interaction model all s-shell Λ-hypernuclei and thus addresses both Λnn and ${}^{3}_{\Lambda}\mathrm{H}^*$ in connection to the remaining s-shell hypernuclear systems. To the best of our knowledge, we performed the first continuum calculation of ${}^{3}_{\Lambda}\mathrm{H}^*$ and the first EFT continuum study of both Λnn and ${}^{3}_{\Lambda}\mathrm{H}^*$. We introduced a 3-body auxiliary attractive potential into the $\not\pi$EFT Hamiltonian and studied the movement of the Λnn or ${}^{3}_{\Lambda}\mathrm{H}^*$ poles with its decreasing attractive strength from a bound region into a continuum up to their physical position (with no auxiliary potential). This procedure allowed us to identify the nature of both states as well as their position in the hypernuclear continuum.

Further, we extended the LO $\not\pi$EFT representation of the hypernuclear single-Λ interaction to strangeness $\mathcal{S} = -2$ sector by constructing its double-Λ version. One additional $\Lambda\Lambda$ contact term was fitted to broad range of $a_{\Lambda\Lambda}$ scattering lengths suggested by the analysis of $\Lambda\Lambda$ correlation data [150], while the three-body $\Lambda\Lambda N$ contact term was fixed by the experimental value $B_{\Lambda\Lambda}({}^{6}_{\Lambda\Lambda}\mathrm{He})$ (Nagara event [213]). Performing SVM calculations of few-body $A \leq 6$ s-shell $\Lambda\Lambda$-hypernuclei we investigated the onset of the $\Lambda\Lambda$-hypernuclear binding.

Finally, we explored a possible application of the nuclear LO $\not\pi$EFT interaction to p-shell nuclei. We constructed its SU(4)-symmetric version and performed few-body calculations of selected light p-shell systems up to ^{8}Be. In particular, we studied evolution of the calculated ground state energies as a function of increasing value of the $\not\pi$EFT momentum cutoff λ.

Our self-consistent η-nuclear calculations revealed that only the GW ηN interaction model convincingly predicted the $\eta{}^{6}$Li quasi-bound state, while the CS

model yielded just bound η^6Li only for one particular value of the momentum cutoff $\lambda = 4$ fm^{-1}. Taking into account the effect of η absorption described by Im($V_{\eta N}$) we noticed a decrease of η-nuclear binding in all considered systems. We observed substantial reduction of the calculated η separation energy B_η in η^3He but rather negligible change of B_η in η^4He and η^6Li. For η^3He, the η meson was barely bound even in the GW case which predicts the largest ηN attraction in the subthreshold region among considered ηN interaction models [20–25]. In fact, the recent experiment performed by the WASA@COSY collaboration found no evidence for the η^4He quasi-bound state [46]. This suggests that the GW model, which firmly gives quasi-bound η^4He, likely overestimates the ηN attraction. On the other hand, the CS model which predicts η^4He on the verge of binding seems to be more plausible. It further indicates that neither η^6Li is likely to form a quasi-bound state and the onset of η-nuclear binding is shifted to heavier $A > 6$ nuclei.

In our study of Λ^*-systems, we demonstrated that the binding energy per Λ^*, B/A, saturates for $A \geq 120$ and does not exceed 100 MeV. Consequently, the amount of binding is not large enough to shift the in-medium Λ^* mass below the mass of the $\Lambda(1116)$ hyperon and thus to ensure stability of Λ^*-matter with respect to strong decay. We illustrated that the saturation mechanism is a purely relativistic effect which once neglected leads to a steep increase of B/A as a function of A in both few- and many-body systems.

Using the LO $\not\pi$EFT nuclear and hypernuclear interactions we found that the binding of the Λnn and ${}^3_\Lambda$H* systems is in serious disagreement with experimentally observed properties of 4- and 5-body Λ-hypernuclei. Further, we predicted that Λnn exists in a form of a resonance which is located close to the $\Lambda + n + n$ threshold. The corresponding pole position depends strongly on the strength of the ΛN interaction. For some ΛN scattering length sets [e.g., NSC97f and χEFT(NLO)], it might be located in the fourth quadrant of a complex energy plane, i.e., it exists as a true resonance with Re(E) > 0. In this case, the resonance energy most likely does not exceed $E_r \approx 0.3$ MeV and its width Γ is rather large – $1.16 \leq \Gamma \leq 2.00$ MeV. For weaker ΛN interaction strengths the Λnn pole position moves into the third quadrant Re(E) < 0 and it corresponds to a subthreshold resonance (a virtual state with width). Our prediction is directly connected to the ongoing Λnn resonance search at the JLab E12-17-003 experiment [272]. The ${}^3_\Lambda$H* system is firmly predicted to exist in a form of a virtual state in the vicinity of the $\Lambda + {}^2$H threshold. We demonstrated that its near-threshold position enhances calculated s-wave $\Lambda + {}^2$H phase shifts in the $J^\pi = 3/2^+$ channel. The predicted nature of the ${}^3_\Lambda$H* system will be likely put to

the test in the near-future JLab C12-19-002 experiment [273] which is currently in its final stage of approval. The results of our ${}^{3}_{\Lambda}\mathrm{H}^{*}$ phase shift study played a key role in the recent work [274] where it was pointed out that measuring the $\Lambda + {}^{2}\mathrm{H}$ two-particle momentum correlation functions in high-energy heavy-ion collisions might be a valuable source of information about the underlying ΛN interaction.

In our study of the onset of $\Lambda\Lambda$-hypernuclear binding within the LO $\not\pi$EFT , we found that the size of the $a_{\Lambda\Lambda}$ scattering length needs to be rather large, $|a_{\Lambda\Lambda}| > 1.5$ fm, to bind the ${}^{4}_{\Lambda\Lambda}\mathrm{H}$ hypernucleus. This seriously questions particle stability of this system. The neutral $\Lambda\Lambda n$ and $\Lambda\Lambda nn$ hypernuclei were found unbound by a wide margin. If any of these systems was observed it would call the sound Nagara event ${}^{6}_{\Lambda\Lambda}\mathrm{He}$ into question. On the other hand, we found that particle stability of the ${}^{5}_{\Lambda\Lambda}\mathrm{H}$ hypernucleus is robust, which plays in favor of the upcoming ${}^{5}_{\Lambda\Lambda}\mathrm{H}$ experiment in the J-PARC facility (the P75 proposal [170]).

Starting with a LO $\not\pi$EFT interaction we found that binding of light p-shell nuclei could persist only for finite, rather small values of the regulator cutoff. Once the cutoff increases and the interaction approaches the contact limit, systems become unbound at a certain system-specific value of the cutoff. Indeed, our calculations indicate that at LO it is not possible to sustain p-shell bound states when the theory approaches the regularization group invariant limit. We found that the main source of binding comes from the residual p-wave interaction at small cutoff values, which once removed (projected out) yields unbound p-shell systems even for smaller cutoff values.

Hadronic interactions at low and intermediate energies are not fully understood yet. A theoretical study of mesic nuclei certainly deserves further attention. First, the self-consistent treatment of these systems is still approximate and it would be desirable to derive more accurate representation of the strong energy dependence of meson-nucleon interactions in few-body systems. Second, it would be interesting to perform calculations directly using coupled-channel potentials. Third, since the existence of η-nuclear quasi-bound states in few-body systems seems to be rather unlikely, it is topical to perform a detailed study of the continuum region. Hand in hand with the issue of η-nuclei goes the theoretical study of $\bar{K}$ few-body systems which could be performed using the same techniques.

Our investigation of s-shell $\Lambda\Lambda$-hypernuclei could be further extended by performing comprehensive continuum calculations of unbound $\Lambda\Lambda n$, $\Lambda\Lambda nn$, and ${}^{4}_{\Lambda\Lambda}\mathrm{H}$

systems within the LO $\not\pi$EFT . Recent experimental progress in $\Lambda\Lambda$ femtoscopy (the STAR and ALICE collaboration) [150, 151, 172, 275] makes this work highly desirable. Indeed, such a study for an acceptable region of $a_{\Lambda\Lambda}$ scattering lengths could provide a clarifying answer whether these systems could be observed in experiment.

In the current version of the LO hypernuclear $\not\pi$EFT Σ and Ξ degrees of freedom entering through $\Lambda N - \Sigma N$ and $\Lambda\Lambda - \Xi N - \Sigma\Sigma$ couplings, respectively, are not explicitly included but they are accounted for implicitly in two- and three-body contact terms. They should be considered in future more detailed calculations.

We believe that a low-energy theory such as the $\not\pi$EFT is extremely useful in the study of hypernuclear systems. In fact, rather small number of low energy constants which can be directly constrained by experimental data make this theory highly useful with respect to χEFT approaches where the large number of parameters starts to be problematic. Consequently, it is highly desirable to contribute to the further development of the $\not\pi$EFT formalism, more precisely, to study its extension to higher orders - NLO and N^{2}LO in few-body systems. An interesting task would be to incorporate a non-zero effective range. Another important topic is the extension of a $\not\pi$EFT to p-shell nuclear systems. In particular, one should be able to describe possible binding of the lightest stable p-shell nuclei ^{6}He and ^{6}Li. Since the Λ hyperon binds to the nuclear core predominantly in s-wave, a correct description of the nuclear core would allow to directly proceed to p-shell hypernuclear systems. Rather strong confirmation of future studies would be to reproduce stabilization of the nuclear core ^{5}He by the presence of Λ (with $B_\Lambda^{\rm exp}({}^6_\Lambda{\rm He}) \approx 4.18(10)$ MeV [112]).

To summarize, we demonstrated in this thesis that current theoretical progress allows to apply highly reliable few-body techniques to the study of various bound and unbound hadronic systems. However, the few-body code developed here is versatile enough and can be directly employed in various few-body systems exceeding the scope of this work, e.g. in atomic physics or quantum chemistry.

List of abbreviations

ACCC	Analytic Continuation in the Coupling Constant
AG	Afnan-Gibson
AY	Akaishi-Yamazaki
CLD	Continuum Level Density
ChPT	Chiral Perturbation Theory
CSB	Charge Symmetry Breaking
CSM	Complex Scaling Method
DMC	Diffusion Monte Carlo
DVR-FV	Discrete Variable Representation in Finite Volume
EFT	Effective Field Theory
ERE	Effective Range Expansion
FE-CS	Faddeev equations with Complex Scaling
GVR	Global Vector Representation
IACCC	Inverse Analytic Continuation in the Coupling Constant
HO	Harmonic Oscillator
LEC	Low Energy Constant
LO, NLO, N^2LO, ...	Leading Order, Next-to-Leading Order, Next-to-next-to-Leading Order, ...
$\not\pi$EFT	pionless Effective Field Theory
QCD	Quantum Chromodynamics
RMF	Relativistic Mean-Field

SVD-CAP	Slow-Variable Discretization coupled with Complex Absorbing Potential
SVM	Stochastic Variational Method

References

[1] S. Muroya, A. Nakamura, C. Nonaka, and T. Takaishi, Prog. Theor. Phys. **110**, 615 (2003).

[2] V. Bernard and U.-G. Meißner, Nucl. Phys. A **489**, 647 (1988).

[3] V. Bernard, R. L. Jaffe, and U.-G. Meißner, Nucl. Phys. B **308**, 753 (1988).

[4] G. E. Brown and M. Rho, Phys. Rev. Lett. **66**, 2720 (1991).

[5] T. Hatsuda and S. Lee, Phys. Rev. C **46**, 34(R) (1992).

[6] B. D. Kaplan and A. E. Nelson, Phys. Lett. **175**, 57 (1986).

[7] A. E. Nelson and B. D. Kaplan, Phys. Lett. B **192**, 193 (1987).

[8] P. J. Ellis, R. Knorren, and M. Prakash, Phys. Lett. B **349**, 11 (1995).

[9] R. S. Bhalerao and L. C. Liu, Phys. Rev. Lett. **54**, 865 (1985).

[10] R. A. Arndt, J. M. Ford, and L. D. Roper, Phys. Rev. D **32**, 1085 (1985).

[11] R. M. Brown *et al.*,Nucl. Phys. B **153**, 89 (1979).

[12] Q. Haider, L.C. Liu, Phys. Lett. B **172**, 257 (1986); Phys. Rev. C **34**, 1845 (1986).

[13] R. E. Chrien *et al.*, Phys. Rev. Lett. **60**, 2595 (1988).

[14] J. D. Johnson *et al.*, Phys. Rev. C **47**, 2571 (1993).

[15] G. A. Sokol and L. N. Pavlyuchenko, Phys. Atom. Nuclei **71**, 509 (2008).

[16] A. Budzanovski *et al.* (COSY@GEM collaboration), Phys. Rev. C **79**, 012201(R) (2009).

[17] S. V. Afanasiev *et al.*, Nucl. Phys. B **219**, 255 (2011).

[18] A. M. Green and S. Wycech, Phys. Rev. C **55**, 2167(R) (1997).

[19] A. M. Green and S. Wycech, Phys. Rev. C **60**, 035208 (1999).

[20] A. M. Green and S. Wycech, Phys. Rev. C **71**, 014001 (2005).

[21] P. C. Bruns and A. Cieplý, Nucl. Phys. A **992**, 121630 (2019).

[22] A.Cieplý and J. Smejkal, Nucl. Phys. A **919**, 46 (2013).

[23] N.Kaiser, P. B. Siegel, and W. Weise, Phys. Lett. B **362**, 23 (1995).

[24] M. Mai, P.C. Bruns, and U.-G. Meißner, Phys. Rev. D **86**, 094033 (2012).

[25] T. Inoue, E. Oset, and M. J. Vicente Vacas, Phys. Rev. C **65**, 035204 (2002).

[26] E. Friedman, A. Gal, and J. Mareš, Phys. Lett. B **725**, 334 (2013).

[27] A. Cieplý, E. Friedman, A. Gal, and J. Mareš, Nucl. Phys. A **925**, 126 (2014).

[28] B. Krusche and C. Wilkin, Prog. Part. Nucl. Phys. **80**, 43 (2015).

[29] Plouin, P. Fleury, and C. Wilkin, Phys. Rev. Lett. **65**, 690 (1990).

[30] H. Calén *et al.*, Phys. Rev. Lett. **79**, 2642 (1997).

[31] H. Calén *et al.*, Phys. Rev. Lett. **80**, 2069 (1998).

[32] R. Bilger *et al.*, Phys. Rev. C **69**, 014003 (2004).

[33] N. V. Shevchenko *et al.*, Phys. Rev. C **58**, 3055(R) (1998).

[34] A. Deloff, Phys. Rev. C **61**, 024004 (2000).

[35] H. Garcilazo, M.T. Peña, Phys. Rev. C **61**, 064010 (2000); Phys. Rev. C **63**, 021001(R) (2001).

[36] A. Fix, H. Arenhövel, Eur. Phys. J. A **9**, 119 (2000); Nucl. Phys. A **697**, 277 (2002).

[37] S. Wycech, A. M. Green, Phys. Rev. C **64**, 045206 (2001).

[38] H. Garcilazo, Phys. Rev. C **67**, 067001 (2003).

[39] M. Pfeiffer *et al.*, Phys. Rev. Lett. **92**, 252001 (2004).

[40] F. Pheron *et al.*, Phys. Lett. B **709**, 21 (2012).

[41] J. Smyrski *et al.*, Phys. Lett. B **649**, 258 (2007).

[42] T. Mersmann *et al.*, Phys. Rev. Lett. **98**, 242301 (2007).

[43] H. H. Adam *et al.*, Phys. Rev. C **75**, 014004 (2007).

[44] C. Wilkin *et al.*, Phys Lett. B **654**, 92 (2007).

[45] J.-J. Xie *et al.*, Phys. Rev. C **95**, 015202 (2017).

[46] P. Adlarson *et al.* (WASA@COSY collaboration), Nucl. Phys. A **959**, 102 (2017).

[47] A. Fix and H. Arenhövel, Phys. Rev. C **68**, 044002 (2003).

[48] A. Fix and O. Kolesnikov, Phys. Lett. B **772**, 663 (2017); Phys. Rev. C **97**, 044001 (2018).

[49] N. Barnea, E. Friedman, and A. Gal, Phys. Lett. B **747**, 345 (2015).

[50] N. Barnea, E. Friedman, and A. Gal, Nucl. Phys. A **968**, 35 (2017).

[51] N. Barnea, B. Bazak, E. Friedman, and A. Gal, Phys. Lett. B **771**, 297 (2017).

[52] M. Schäfer, N. Barnea, E. Friedman, A. Gal, and J. Mareš, EPJ Web Conf. **199**, 02022 (2019).

[53] V. Metag, M. Nanova, and E. Ya. Paryev, Prog. Part. Nucl. Phys. **97**, 199 (2017).

[54] D. Evans *et al.*, J. Phys. G **9**, 885 (1983).

[55] A. D. Martin, Nucl. Phys. B **179**, 33 (1981).

[56] J. Ciborowski *et al.*, J. Phys. G **8**, 13 (1982).

[57] M. Iwasaki *et al.*, Phys. Rev. Lett. **78**, 3067 (1997).

[58] T. M. Ito *et al.*, Phys. Rev. C **58**, 2366 (1998).

[59] M.Bazzi *et al.* (SIDDHARTA collaboration), Phys. Lett. B **704**, 113 (2011); Nucl. Phys. A **881**, 88 (2012).

[60] C. Curceanu *et al.*, Nucl. Phys. A **914**, 251 (2013).

[61] C. Curceanu *et al.*, Acta Phys. Pol. B **51**, 251 (2020).

[62] C. J. Batty, E. Friedman, and A. Gal, Phys. Rep. **287**, 385 (1997).

[63] E. Friedman, A. Gal, Phys. Rep. **452**, 89 (2007).

[64] R. H. Dalitz and S. F. Tuan, Phys. Rev. Lett. **2**, 425 (1959).

[65] R. H. Dalitz, T. C. Wong, and G. Rajasekaran, Phys. Rev. **153**, 1617 (1967).

[66] T. Hyodo and D. Jido, Prog. Part. Nucl. Phys **67**, 55 (2012).

[67] M. Jones, R. H. Dalitz, and R. R. Horgan, Nucl. Phys. B **129**, 45 (1977).

[68] W. Weise, Nucl. Phys. A **835**, 51 (2010).

[69] N. Isgur and G. Karl, Phys. Rev. D **18**, 4187 (1978).

[70] T. Inoue, Nucl. Phys. A **790**, 530 (2007).

[71] Y. Akaishi and T. Yamazaki, Phys. Rev. C **65**, 044005 (2002).

[72] N. V. Shevchenko, A. Gal, J. Mareš, Phys. Rev. Lett. 98, 082301 (2007).

[73] N. V. Shevchenko, Few Body Syst. **58**, 6 (2017).

[74] A. Cieplý and J. Smejkal, Nucl. Phys. **A** 881, 115 (2012).

[75] Y. Ikeda, T. Hyodo, and W. Weise,Nucl. Phys. A **881**, 98 (2012).

[76] Z. H. Guo and J. A. Oller, Phys. Rev. C **87**, 035202 (2013).

[77] M. Mai and U.-G. Meißner, Nucl. Phys. A **900**, 51 (2013).

[78] A. Feijoo, V. Magas, and À. Ramos, Phys. Rev. C **99**, 035211 (2019).

[79] A Cieplý, M. Mai, U.-G. Meißner, and J. Smejkal, Nucl. Phys. A **954**, 17 (2016).

[80] P. J. Fink Jr., G. He, R. H. Landau, and J. W. Schnick, Phys. Rev. C **41**, 2720 (1990).

[81] K. Moriya *et al.* (CLAS collaboration), Phys. Rev. Lett. **112**, 082004 (2014).

[82] I. Zychor *et al.*, Phys. Lett. B **660**, 167 (2008).

[83] G. Agakishiev *et al.* (HADES collaboration), Phys. Rev. C **87**, 025201 (2013).

[84] H. Asano *et al.* (J-PARC E31 collaboration), AIP Conf. Proc. **2130**, 040018 (2019).

[85] T. Yamazaki and Y. Akaishi, Phys. Lett. B **535**, 70 (2002).

[86] T. Yamazaki and Y. Akaishi, Phys. Rev. C **76**, 045201 (2007).

[87] Y. Ikeda, T. Sato, Prog. Theor. Phys. **124**, 533 (2010).

[88] S. Maeda, Y. Akaishi, and T. Yamazaki, Proc. Jpn. Acad. Ser. B **89**, 418 (2013).

[89] J. Révai, N. V. Shevchenko, Phys. Rev. C **90**, 034004 (2014).

[90] S. Marri, S. Z. Kalantari, Eur. Phys. J. A **52**, 282 (2016).

[91] A. Doté, T.Hyodo, and W. Weise, Phys. Rev. C **79**, 014003 (2009).

[92] N. Barnea, A. Gal, and E. Z. Liverts, Phys. Lett. B **712**, 132 (2012).

[93] S. Ohnishi *et al.*, Phys. Rev. C **95**, 065202 (2017).

[94] P. A. Zyla *et al.* (Particle Data Group), Prog. Theor. Exp. Phys. **2020**, 083C01 (2020).

[95] M. Agnello *et al.* (FINUDA collaboration), Phys. Rev. Lett. **94**, 212303 (2005).

[96] V. K. Magas, E. Oset, A. Ramos, and H. Toki, Phys. Rev. C **74**, 025206 (2006).

[97] G. Bendiscioli *et al.*, Nucl. Phys. A **789**, 222 (2007).

[98] T. Yamazaki *et al.*, Phys. Rev. Lett. **104**, 132502 (2010).

[99] L. Fabbietti *et al.* (HADES collaboration), Nucl. Phys. A **914**, 60 (2013).

[100] G. Agakishiev *et al.* (HADES collaboration), Phys. Lett. B **742**, 242 (2015).

[101] E. Epple and L. Fabbietti, Phys. Rev. C **92**, 044002 (2015).

[102] A. O. Tokiyasu *et al.* (LEPS collaboration), Phys. Lett. B **728**, 616 (2014).

[103] Y. Ichikawa *et al.*, Prog. Theor. Exp. Phys. **2015**, 021D01 (2015).

[104] S. Ajimura *et al.* (J-PARC E15 collaboration), Phys. Lett. B **789**, 620 (2019).

[105] J. Hrtánková and J. Mareš, Phys. Lett. B **770**, 342 (2017).

[106] J. Hrtánková and J. Mareš, Phys. Rev. C **96**, 015205 (2017).

[107] R. D. Grande *et al.* (AMADEUS collaboration), Eur. Phys. J. C **79**, 190 (2019).

[108] J. Hrtánková and À. Ramos, Phys. Rev. C **101**, 035204 (2020).

[109] Y. Akaishi and T. Yamazaki, Phys. Lett. B **774**, 522 (2017).

[110] J. Hrtánková et al, Phys. Lett. B **785**, 90 (2018).

[111] M. Danysz and J. Pniewski, Phil. Mag. **44**, 348 (1953).

[112] D. H. Davis, Nucl. Phys. A **754**, 3c (2005).

[113] R. H. Dalitz, Nucl. Phys. A **754**, 14 (2005).

[114] A. Gal, E. V. Hungerford, and D. J. Millener, Rev. Mod. Phys. **88**, 035004 (2016).

[115] K. Nakazawa *et al.* Prog. Theor. Exp. Phys. **3**, 033D02 (2015).

[116] B. Sechi-Zorn, B. Kehoe, J. Twitty, R. A. Burnstein Phys. Rev. **175**, 1735 (1968).

[117] G. Alexander *et al.*, Phys. Rev. **173**, 1452 (1968).

[118] R. Engelmann, H. Filthuth, V. Hepp, and E. Kluge, Phys. Lett. **21**, 587 (1966).

[119] F. Eisele, H. Filthuth, W. Fölisch, V. Hepp, G. Zech, Phys. Lett. B **37**, 204 (1971).

[120] M. M. Nagels, T. A. Rijken, and J. J. de Swart, Phys. Rev. D **15**, 2547 (1977).

[121] M. M. Nagels, T. A. Rijken, and J. J. de Swart, Phys. Rev. D **20**, 1633 (1979).

[122] P. M. M. Maessen, T. A. Rijken, and J. J. de Swart, Phys. Rev. C **40**, 2226 (1989).

[123] T. A. Rijken, V. G. J. Stoks, and Y. Yamamoto, Phys. Rev. C **59**, 21 (1999).

[124] T. A. Rijken and Y. Yamamoto, Phys. Rev. C **73**, 044008 (2006).

[125] M. M. Nagels, T. A. Rijken, and Y. Yamamoto, Phys. Rev. C 99, 044003 (2019).

[126] B. Holzenkamp, K. Holinde, and J. Speth, Nucl. Phys. A **500**, 485 (1989).

[127] A. Reuber, K. Holinde, and J. Speth, Nucl. Phys. A **570**, 543 (1994).

[128] J. Haidenbauer and U.-G. Meißner, Phys. Rev. C **72**, 044005 (2005).

[129] H. Polinder, J. Haidenbauer, and U.-G. Meißner, Nucl. Phys. A **779**, 244 (2006).

[130] J. Haidenbauer *et al.*, Nucl. Phys. A **915**, 24 (2013).

[131] A. Nogga, H. Kamada, W. Glöcke, Phys. Rev. Lett. **88**, 172501 (2002).

[132] A. Nogga, Nucl. Phys. A **914**, 140 (2013).

[133] M. Jurič *et al.*, Nucl. Phys. B **52**, 1 (1973).

[134] J. Adam *et al.* (STAR collaboration), Nat. Phys. **16**, 409 (2020).

[135] A. Gal, Phys. Lett. B **744**, 352 (2015).

[136] D.Gazda and A. Gal, Phys. Rev. Lett. **116**, 122501 (2016); Nucl. Phys. A **954**, 161 (2016).

[137] B. W. Downs and R. H. Dalitz, Phys. Rev. **114**, 593 (1959).

[138] H. Garcilazo, J. Phys. G **13**, 63 (1987).

[139] K. Miyagawa, H. Kamada, W. Glöckle, and V. Stoks, Phys. Rev. C **51**, 2905 (1995).

[140] H. Garcilazo, T. Fernández-Caramés, and A. Valcarce, Phys. Rev. C **75**, 034002 (2007); **76**, 034001 (2007).

[141] V. B. Belyaev, S. A. Rakityansky, W. Sandhas, Nucl. Phys. A **803**, 210 (2008).

[142] A. Gal, H. Garcilazo, Phys. Lett. B **736**, 93 (2014).

[143] E. Hiyama, S. Ohnishi, B. F. Gibson, and T. A. Rijken, Phys. Rev. C **89**, 061302(R) (2014).

[144] I. R. Afnan and B. F. Gibson, Phys. Rev. C **92**, 054608 (2015).

[145] C. Rappold *et al.* (HypHI Collaboration), Phys. Rev. C **88**, 041001(R) (2013).

[146] L. Contessi, N. Barnea, and A. Gal, Phys. Rev. Lett. **121**, 102502 (2018).

[147] M. Schäfer, B. Bazak, N. Barnea, and J. Mareš, Phys. Lett. B, 135614 (2020).

[148] J. Haidenbauer, U.-G. Meißner, and S. Petschauer, Nucl. Phys. A **954**, 273 (2016).

[149] A. M. Gasparyan, J. Haidenbauer, and C. Hanhart, Phys. Rev. C **85**, 015204 (2012).

[150] K. Morita, T. Furumoto, and A. Ohnishi, Phys. Rev. C **91**, 024916 (2015).

[151] L. Adamczyk *et al.* (STAR collaboration), Phys. Rev. Lett. **114**, 022301 (2015).

[152] V. G. J. Stoks and T. A. Rijken, Phys. Rev. C **59**, 3009 (1999).

[153] K. Tominaga *et al.*, Nucl. Phys. A **642**, 483 (1998).

[154] M. Yamaguchi *et al.*, Prog. Theor. Phys. **105**, 627 (2001).

[155] T. A. Rijken and Y. Yamamoto, arXiv:nucl-th/0608074 (2006).

[156] M. M. Nagels, T. A. Rijken, and Y. Yamamoto, arXiv:1504.02634 [nucl-th] (2015).

[157] H. Polinder, J. Haidenbauer, and U.-G. Meißner, Phys. Lett. B **653**, 29 (2007).

[158] I. N. Filikhin and A. Gal, Phys. Rev. Lett **89**, 172502 (2002).

[159] Nemura at al., Phys. Rev. C **67**, 051001(R) (2003).

[160] H. Nemura, S. Shinmura, Y. Akaishi, and K. S. Myint, Phys. Rev. Lett. **94**, 202502 (2005).

[161] I. N. Filikhin and A. Gal, Nucl. Phys. A **707**, 491 (2002).

[162] I. N. Filikhin, A. Gal, and V. M. Suslov, Phys. Rev. C **68**, 024002 (2003).

[163] D. E. Lanskoy and Y. Yamamoto, Phys. Rev. C **69**, 014303 (2004).

[164] J. K. Ahn *et al.*, Phys. Rev. Lett. **87**, 132504 (2001).

[165] S. D. Randeniya and E. V. Hungerford, Phys. Rev. C **76**, 064308 (2007).

[166] S. Blesser, M. Bölting, T. Gaitanos, J. Pochodzalla, F. Schupp, and M. Steinen, Phys. Lett. B **790**, 502 (2019).

[167] J.-M. Richard, Q. Wang, and Q. Zhao, Phys. Rev. C **91**, 014003 (2015).

[168] H. Garcilazo *et al.*, Chin. Phys. C **41**, 0741102 (2017).

[169] L. Contessi, M. Schäfer, N. Barnea, A. Gal, J. Mareš, Phys. Lett. B **797**, 134893 (2019).

[170] J-PARC, P75, http://j-parc.jp/researcher/Hadron/en/pac_1901/pdf/P75_2019-09.pdf, 18.7.2020.

[171] K. Sasaki *et al.* (HAL QCD collaboration), Nucl. Phys. A **998**, 121737 (2020).

[172] S. Acharya *et al.* (ALICE collaboration), Phys. Lett. B **797**, 134822 (2019); Phys. Rev. C **99**, 024001 (2019).

[173] L. Tolos and L. Fabbietti, Prog. Part. Nucl. Phys. **112**, 103770 (2020).

[174] T. Hyodo and W. Weise, Phys. Rev. C **77**, 035204 (2008).

[175] George Washington University, INS Data Analysis Center, The SAID partial-wave analysis facility, *http://gwdac.phys.gwu.edu/analysis/pin_analysis.html*, 23.7.2020.

[176] S. Prakhov *et al.* (Crystal Ball collaboration), Phys. Rev. C **72**, 015203 (2005).

[177] F. Bulos *et al.*, Phys. Rev. **187**, 1827 (1969).

[178] W. B. Richards *et al.*, Phys. Rev. D **1**, 10 (1970).

[179] J. Feltesse *et al.*, Nucl. Phys. B **93**, 242 (1975).

[180] A. Baldini, V. Flaminio, W. G. Moorhead, and D. R. O. Morrison, *Total Cross-Sections for Reactions of High Energy Particles (Including Elastic, Topological, Inclusive and Exclusive Reactions)*, vol. 12a of Landolt-Boernstein - Group I Elementary Particles, Nuclei and Atoms, Springer, 1988.

[181] A. Cieplý, E. Friedman, A. Gal, D. Gazda, and J. Mareš, Phys. Lett. B **702**, 402 (2011).

[182] D. N. Tovee *et al.*, Nucl. Phys. B **33**, 493 (1971).

[183] R. J. Nowak *et al.*, Nucl. Phys. B **139**, 61 (1978).

[184] E. Friedman and A. Gal, Nucl. Phys. A **959**, 66 (2017).

[185] H. Davis *et al.*, Nuovo Cimento **53A**, 313 (1968).

[186] J.W. Moulder *et al.*, Nucl. Phys. B **35**, 332 (1971).

[187] C. Vander Velde-Wilquet, J. Sacton, J. H. Wickens, D. N. Tovee, D. H. Davis, Nuovo Cimento **39A**, 538 (1977).

[188] J. Hrtánková *et al.*, arXiv:2007.05829 [nucl-th] (2020), submitted to Int. Jour. of Mod. Phys. A.

[189] U. van Kolck, Nucl. Phys. A **645**, 273 (1999).

[190] J.-W. Chen, G. Rupak, and M. J. Savage, Nucl. Phys. A **653**, 386 (1999).

[191] F. Bedaque and U. van Kolck, Annu. Rev. Nucl. Part. Sci. **52**, 339 (2002).

[192] D. R. Phillips, Czech. J. Phys. **52**, B49 (2002).

[193] L. Platter, Few Body Syst. **46**, 139 (2009).

[194] H.-W. Hammer, S. Känig, and U. van Kolck, Rev. Mod. Phys. **92**, 025004 (2020).

[195] P. F. Bedaque, H. W. Hammer, and U. van Kolck, Phys. Rev. Lett. **82**, 463 (1999); Nucl. Phys. A **646**, 444 (1999).

[196] L. Platter, H.-W. Hammer, and U. G. Meißner, Phys. Lett. B **607**, 254 (2005).

[197] L. Platter, H.-W. Hammer, and U.-G. Meißner, Phys. Rev. A **70**, 052101 (2004).

[198] B. Bazak, M. Eliyahu, and U. van Kolck, Phys. Rev. A **94**, 052502 (2016).

[199] E.P. Wigner, Phys. Rev. **98**, 145 (1955).

[200] D.R. Phillips and T.D. Cohen, Phys. Lett. B **390**, 7 (1997).

[201] B. Bazak *et al.* Phys. Rev. Lett. **122**, 143001 (2019).

[202] N. Barnea *et al.*, Phys. Rev. Lett. **114**, 052501 (2015).

[203] J. Kirscher *et al.*, Phys. Rev. C **92**, 054002 (2015).

[204] L. Contessi *et al.*, Phys. Lett. B **772**, 839 (2017).

[205] J. Kirscher, E. Pazy, J. Drachman, N. Barnea, Phys. Rev. C **96**, 024001 (2017).

[206] A. Kempf *et al.*, J. Phys. A: Math. Theor. **47**, 415204 (2014).

[207] L. Contessi, *private communication* 2019.

[208] G. A. Miller, M. K. Nefkens, and I. Slaus, Phys. Rep. **1**, 194 (1990).

[209] C. Van Der Leun and C. Alderliesten, Nucl. Phys. A **380**, 261 (1982).

[210] J. E. Purcell *et al.*, Nucl. Phys. A **848**, 1 (2010).

[211] T. O. Yamamoto *et al.* (J-PARC E13 collaboration), Phys. Rev. Lett. **115**, 222501 (2015).

[212] A. Esser *et al.* (MAMI A1 collaboration), Phys. Rev. Lett. **114**, 232501 (2015); F. Schulz *et al.* (MAMI A1 collaboration), Nucl. Phys. A **954**, 149 (2016).

[213] K. Nakazawa and KEK-E176, KEK-E373, and J-PARC E07 collaborators, Nucl. Phys. A **835**, 207 (2010).

[214] S. König, H. W. Grießhammer, H.-W. Hammer, and U. van Kolck, J. Phys. G **43**, 055106 (2016).

[215] I. Vidaña, À. Ramos, A. Polls, Phys. Rev. C **70**, 024306 (2004).

[216] R. Jastrow, Phys. Rev. **98**, 1479 (1955).

[217] K. Varga and Y. Suzuki, Phys. Rev. C **52**, 2885 (1995).

[218] Y. K. Ho, Phys. Rev. A **48**, 4780 (1993).

[219] Y. Suzuki, K. Varga, *Stochastic Variational Approach to Quantum-Mechanical Few-Body Problems*, Springer (1998).

[220] S. F. Boys, Proc. R. Soc. London, Ser. A **258**, 402 (1960).

[221] S. A. Alexander, H. J. Monkhorst, and K. Szalewicz, J. Chem. Phys. **85**, 5821 (1986).

[222] Y. Suzuki, J. Usukura, and K. Varga, J. Phys. G: Atom., Mol., and Opt. Phys. **31**, 31 (1998).

[223] K. Varga, Y. Suzuki, and J. Usukura, Few-Body Syst. **24**, 81 (1998).

[224] H. Kamada *et al.*, Phys. Rev. C **64**, 044001 (2001).

[225] Y. Suzuki, W. Horiuchi, M. Orabi, K. Arai, Few-Body Syst. **42**, 33 (2008).

[226] K. Varga, Y. Ohbayasi, Y. Suzuki, Phys. Lett. B **396**, 1 (1997).

[227] D.R. Thompson, M. Le Mere, and Y. C. Tang, Nucl. Phys. A **286**, 53 (1977).

[228] A. Cieplý *et al.*, PoS Hadron2017, 203 (2017).

[229] R. Tamagaki, Prog. Theor. Phys. **39**, 91 (1968).

[230] J. R. Taylor, *Scattering Theory: Quantum Theory on Nonrelativistic Collisions*, Willey, 99 edition (1972).

[231] V. I. Kukulin, V. M. Krasnopol'sky, and J. Horáček, *Theory of resonances, Principles and Applications*, Kluwer Academic Publishers (1989).

[232] V. M. Kukulin and V. M. Krasnopol'sky, J. Phys. A **10**, 33 (1977); V. M. Krasnopol'sky, and V. I. Kukulin, Phys. Lett. A **69**, 251 (1978); V. I. Kukulin, V. M. Krasnopol'sky, and M. Miselkhi, Sov. J. Nucl. Phys. **29**, 421 (1979).

[233] N. Tanaka, Y. Suzuki, K. Varga, and R. G. Lovas, Phys. Rev. C **59**, 1391 (1999).

[234] R. Lazauskas, E. Hiyama, J. Carbonell, Phys. Lett. B **791**, 335 (2019) and references therein.

[235] N. Tanaka, Y. Suzuki, and K. Varga, Phys. Rev. C **56**, 562 (1997).

[236] J. Horáček and L. Pichl, Commun. Comput. Phys. **21**, 1154 (2017).

[237] J. Augilar and J. M. Combes, Commun. Math. Phys. **22**, 269 (1971); E. Balslev and J.M. Combes, Commun. Math. Phys. **22**, 280 (1971).

[238] S. Aoyama, T. Myo, K. Katō, K. Ikeda, Prog. Theor. Phys **116**, 1 (2006).

[239] N. Moiseyev, P.R. Certain, F. Weinhold, Mol. Phys. **36**, 1613 (1978).

[240] N. Moiseyev, *Non-Hermitian Quantum Mechanics*, Cambridge University Press, (2011).

[241] N. Moiseyev, Phys. Rep. **302**, 212 (1998).

[242] J. Zs. Mezei, A. T. Kruppa, K. Varga, Few Body Syst. **41**, 233 (2007).

[243] R. Yaris, P. Winkler, J. Phys. B **11**, 1475 (1978).

[244] D. V. Fedorov, E. Garrido, and A. S. Jensen, Few-Body Syst. **33**, 153 (2003).

[245] E. Hiyama, M. Isaka, M. Kamimura, T. Myo, and T. Motoba, Phys. Rev. C **91**, 054316 (2015).

[246] W. Horiuchi and Y. Suzuki, Few Body Syst. **54**, 2407 (2013).

[247] J. Usukura and Y. Suzuki, Phys. Rev A **66**, 010502(R) (2002).

[248] T. D. Fedorov *et al.*, Few Body Syst. **45**, 191 (2009).

[249] R. Suzuki, T. Myo, and K. Kato, Prog. Theor. Phys. **113**, 1273 (2005).

[250] M. Odsuren, K. Kato, M. Aikawa, and T. Myo, Phys. Rev. C **89**, 034322 (2014).

[251] M. Odsuren *et al.*, Phys. Rev. C **95**, 064305 (2017).

[252] R. D. Levine, *Quantum Mechanics of Molecular Rate Processes*, Clarendon Press, Oxford, (1969).

[253] S. Shlomo, Nucl. Phys. **A** 539, 17 (1992).

[254] T. Myo, A. Ohnishi, and K. Kato, Prog. Theor. Phys. **99**, 801 (1998) and references therein.

[255] K. Varga and Y. Suzuki, Comput. Phys. Commun. **106**, 157 (1997).

[256] H. Machner, J. Phys. G **42**, 043001 (2015).

[257] J. Mareš *et al.*, Acta Phys. Polonica B **51**, 129 (2020).

[258] J. Hrtánková *et al.*, AIP Conf. Proc. **2130**, 040016 (2019).

[259] B. D. Serot and J. D. Walecka, Adv. Nucl. Phys. **16**, 1 (1986).

[260] C. J. Horowitz and B. D. Serot, Nucl. Phys. A **368**, 503 (1981).

[261] R. Machleidt, Adv. Nucl. Phys. **19**, 189 (1989).

[262] C. B. Dover and A. Gal, Prog. Part. Nucl. Phys. **12**, 171 (1984).

[263] M. M. Sharma, M. A. Nagarajan, and P.Ring, Phys. Lett. B **312**, 377 (1993).

[264] M. Schäfer, B. Bazak, N. Barnea, and J. Mareš, arXiv:2007.10264 [nucl-th], Phys. Rev. C, submitted (2020).

[265] L. Contessi, N. Barnea, and A. Gal, AIP Conf. Proc. **2130**, 040012 (2019).

[266] S. König, H. W. Grießhammer, H. W. Hammer, and U. van Kolck, Phys. Rev. Lett. **118**, 202501 (2017).

[267] T. De Forest, Jr., Phys. Rev. **139**, B1217 (1965).

[268] Y. S. Lutostansky and V. N. Tikhonov, JETP Lett. **102**, 7 (2015).

[269] M. Schäfer, L. Contessi, and J. Kirscher, arXiv:2003.09862 [nucl-th]„ Phys. Lett. B submitted (2020).

[270] S. A. Afzal, A. A. Z. Ahmad, and S. Ali, Rev. Mod. Phys. **41**, 247 (1969).

[271] R. Higa, H. W. Hammer, and U. van Kolck, Nucl. Phys. A **809**, 171 (2008).

[272] JLab, E12-17-003, https://www.jlab.org/exp_prog/proposals/17/PR12-17-003.pdf, 18.7.2020.

[273] JLab, C12-19-002, https://www.jlab.org/exp_prog/proposals/19/PR12-19-002.pdf, 18.7.2020.

[274] J. Haidenbauer, arXiv:2005.05012 [nucl-th] (2020).

[275] A. Ohnishi, K. Morita, K. Miyahara, and T. Hyodo, Nucl. Phys. A **954**, 294 (2016).

[276] I. A. Baz, Y. B. Zeld'ovich, A. M. Perelomov, *Scattering, Reactions and Decay in Nonrelativistic Quantum Mechanics*, Nauka (1971).

[277] L. P. Kok, Phys. Rev. Lett. **45**, 427 (1980).

[278] Y. Ikeda, T. Hyodo, D. Jido, H. Kamano, T. Sato, and K. Yazaki, Prog. Theor. Phys. **125**, 1205 (2011).

[279] T. Hyodo, Phys. Rev. Lett. **111**, 132002 (2013).

[280] N. P. Heydenburg and G. M. Temmer, Phys Rev. **104**, 123 (1956).

[281] M. Odsuren, Y. Kikuchi, T. Myo, M. Aikawa, and K. Kato, Phys. Rev. C **92**, 014322 (2015).

[282] R. B. Wiringa and S. C. Pieper, Phys. Rev. Lett. **89**, 182501 (2002).

[283] B. S. Pudliner, V. R. Pandharipande, J. Carlson, S. C. Pieper, R. B. Wiringa, Phys. Rev. C **56**, 1720 (1997).

[284] F.F. Ruffino *et al.*, Few Body Syst. **58**, 113 (2017).

[285] M. Baldo *et al.*, Phys. Rev. C **86**, 064001 (2012).

[286] E. A. Kolganova, A. K. Motovilov, and Y. K. Ho, Nucl. Phys. A **684**, 623c (2001).

[287] J. Blandon, V. Kokoouline, and F. Masnou-Seeuws, Phys. Rev A **75**, 042508 (2007).

[288] P. Klos, S. König, H.-W. Hammer, J. E. Lynn, and A. Schwenk, Phys. Rev. C **98**, 034004 (2018).

[289] V. N. Ostrovsky and E. A. Solovev, Sov. Phys. JETP **35**, 89 (1972).

List of author's publications

Publications in scientific journals

1. M. Schäfer, B. Bazak, N. Barnea, and J. Mareš,
   The continuum spectrum of hypernuclear trios
   arXiv:2003.08636 [nucl-th], Phys. Lett. B **808**, 135614 (2020).
   Impact Factor: 4.384 (2019)

2. M. Schäfer, B. Bazak, N. Barnea, and J. Mareš,
   Nature of the Λnn $(J^\pi = 1/2^+, I = 1)$ *and* ${}^{3}_{\Lambda}\mathrm{H}^*$ $(J^\pi = 3/2^+, I = 0)$ *states*
   arXiv:2007.10264 [nucl-th], Phys. Rev. C, submitted.
   Impact Factor: 2.988 (2019)

3. M. Schäfer, L. Contessi, and J. Kirscher,
   Stability of fermionic states with contact theories
   arXiv:2003.09862 [nucl-th], Phys. Lett. B, to be submitted (2020).
   Impact Factor: 4.384 (2019)

4. L. Contessi, M. Schäfer, N. Barnea, A. Gal, and J. Mareš,
   The onset of $\Lambda\Lambda$ *hypernuclear binding*
   arXiv:1905.06775 [nucl-th], Phys. Lett. B **797**, 134893 (2019).
   Impact Factor: 4.384 (2019)

5. J. Hrtánková, N. Barnea, E. Friedman, A. Gal, J. Mareš, and M. Schäfer,

$\Lambda^\star$(1405)-matter: stable or unstable?
arXiv:1805.11368 [nucl-th], Phys. Lett. B **785**, 90 (2018).
Impact Factor: 4.384 (2019)

6. J. Hrtánková, M. Schäfer, J. Mareš, A. Gal, E. Friedman, and N. Barnea,
   Λ^* matter and its stability
   arXiv:2007.05829 [nucl-th], Int. J. Mod. Phys. A, submitted.
   Impact Factor: 1.486 (2019)

7. J. Mareš, A. Cieplý, J. Hrtánková, M. Schäfer, B. Bazak, N. Barnea, E. Friedman, and A. Gal,
   Calculations of η nuclei, K^- atoms and K^- nuclei,
   Acta Phys. Polonica B **51**, 129 (2020).
   Impact Factor: 0.651 (2019)

Conference proceedings

1. J. Hrtánková, N. Barnea, E. Friedman, A. Gal, J. Mareš, M. Schäfer,
   On the stability of Λ(1405) matter,
   Proc. HYP2018, Portsmouth, USA, 24. - 29. 6. 2018,
   arXiv:1904.01928 [nucl-th], AIP Conf. Proc. **2130**, 040016 (2019).

2. M. Schäfer, N. Barnea, E. Friedman, A. Gal, J. Mareš,
   Calculations of η-nuclear quasi-bound states in few-body systems,
   Proc. MESON2016, Krakow, Poland, 7. - 12. 6. 2018,
   EPJ Web Conf. **199**, 03008 (2019).

3. N. Barnea, B. Bazak, E. Friedman, A. Gal, A. Cieplý, J. Mareš, M. Schäfer,
   Onset of η nuclear binding,
   Proc. EXA 2017, Wien, Austria 11. - 15. 9. 2017,
   arXiv: 1712.05643 [nucl-th], EPJ Web Conf. **181**, 01011 (2018).

4. A. Cieplý, J. Mareš, M. Schäfer, N. Barnea, B. Bazak, E. Friedman, A. Gal, *Eta-mesic nuclei*,
   Proc. HADRON 2017, Salamanca, Spain, 25. - 29. 9. 2017,
   arXiv: 1712.07982 [nucl-th], PoS Hadron2017, 203 (2017).

5. M. Schäfer, H. Feldmeier, J. Mareš, T. Neff,
   Structure of light hypernuclei in the framework of Fermionic Molecular Dynamics,
   Proc. HYP 2015, Sendai, Japan, 7. - 12. 9. 2015,
   JPS Conf. Proc. **17**, 012002 (2017).

6. M. Schäfer, H. Feldmeier, J. Mareš, T. Neff,
   Structure of light hypernuclei in the framework of Fermionic Molecular Dynamics,
   Proc. 53rd Int. Winter Meeting on Nuclear Physics, Bormio, Italy, 26. - 30. 1. 2015,
   PoS Bormio2015, 036 (2015).

Conference presentations

1. Theia-Strong2020 Workshop,
   Speyer, Germany, 25. - 29. 11. 2019.
   (oral presentation)

2. ECT* Workshop on Recent progress and perspective in STRANge EXotic atoms studies and related topics (STRANEX2019),
   Trento, Italy, 21. - 25. 10. 2019.
   (oral presentation)

3. The 64th IPS Conference 2018,
   Jerusalem, Israel, 9. 12. 2018.
   (oral presentation)

4. 13th International Conference on Hypernuclear and Strange Particle Physics (HYP2018),

Portsmouth, USA, 24. - 29. 6. 2018.
(poster)

5. 16th International Workshop on Meson Physics (MESON2016),
   Krakow, Poland, 7. - 12.6. 2018.
   (oral presentation)

6. ECT* Workshop on Advances and Open Problems in Low-Energy Nuclear and Hadronic Strangeness Physics (ASTRA2017),
   Trento, Italy, 23. - 27. 10. 2017.
   (oral presentation)

7. International Nuclear Physics Conference (INPC2016),
   Adelaide, Australia, 11. - 16. 9. 2016.
   (poster)

8. 28th Indian-Summer School - Ab Initio Methods in Nuclear Physics,
   Praha, Czech Republic, 29. 8. - 2. 9. 2016,
   (oral presentation)

9. 12th International Conference on Hypernuclear and Strange Particle Physics (HYP2015),
   Sendai, Japan, 7. - 12. 9. 2015.
   (oral presentation)

10. 4th Int. School for Strangeness Nuclear Physics,
    Sendai, Japan, 3. - 5. 9. 2015.
    (oral presentation + poster)

11. 6th Czech - slovak student scientific conference,
    Košice, Slovakia, 14. - 15. 5. 2015.
    (oral presentation)

12. 53rd Winter Meeting on Nuclear Physics,
    Bormio, Italy, 26. - 30.1. 2015.
    (oral presentation)

13. 26th Indian-Summer School: Low Energy Hadron Physics,
    Prague, Czech Republic, 2. - 7. 9. 2014.
    (oral presentation)

Appendix A

Matrix elements

In this appendix, we comment on calculations of matrix elements in a correlated Gaussian basis (3.15). It is to be stressed that we do not present here full derivation leading to specific analytical expressions, which have been already thoroughly given in Refs. [219, 225]. As illustrated in Subsection 3.2.1, the cornerstone of the SVM is a step-by-step stochastic selection of appropriate basis states which are being tested on a calculated bound state energy. Consequently, corresponding matrix elements which enter either the overlap $\mathcal{N}$ or Hamiltonian $\mathcal{H}$ matrices (3.26) have to be calculated many times in each step and their efficient evaluation is thus crucial.

Although we study few-body systems composed of different particles interacting via various potentials, we will give here as an example of two-body interaction terms the NN force which has the most complicated structure among those applied in our calculations (NN, ηN, $\Lambda^*\Lambda^*$, ΛN, $\Lambda\Lambda$). We consider the NN two-body interaction between particles k and l in the form

$$\begin{aligned} V_{kl} =& V_{\rm c}(r_{kl}) + V_{\rm c}^{\sigma}(r_{kl})(\boldsymbol{\sigma}_k \cdot \boldsymbol{\sigma}_l) + V_{\rm c}^{\tau}(r_{kl})(\boldsymbol{\tau}_k \cdot \boldsymbol{\tau}_l) + V_{\rm c}^{\sigma\tau}(r_{kl})(\boldsymbol{\sigma}_k \cdot \boldsymbol{\sigma}_l)(\boldsymbol{\tau}_k \cdot \boldsymbol{\tau}_l) \\ &+ \left\{V_{\rm T}(r_{kl}) + V_{\rm T}^{\tau}(r_{kl})(\boldsymbol{\tau}_k \cdot \boldsymbol{\tau}_l)\right\} S_{kl} + \left\{V_{\rm LS}(r_{kl}) + V_{\rm LS}^{\tau}(r_{kl})(\boldsymbol{\tau}_k \cdot \boldsymbol{\tau}_l)\right\} (\mathbf{L}\cdot\mathbf{S})_{kl}, \end{aligned} \tag{A.1}$$

where $V_m^n(r_{kl}),\ n = \{\cdot, \sigma, \tau, \sigma\tau\},\ m = \{\mathrm{c}, \mathrm{T}, \mathrm{LS}\}$ are radial functions which depend on the relative distance $r_{kl} = |\mathbf{r}_k - \mathbf{r}_l|$ between particles k and l . The $\boldsymbol{\sigma}_{k(l)}$ and $\boldsymbol{\tau}_{k(l)}$ denote Pauli matrices in spin and isospin space, respectively. We consider only the central (c), tensor (T), and spin-orbit (LS) interaction while the quadratic orbital momentum $\sim \mathbf{L}_{kl}^2$, quadratic spin-orbit $\sim (\mathbf{L}\cdot\mathbf{S})_{kl}^2$, and charge dependent terms were not taken into account.

The expression (A.1) is rather general. We stress that different representations

of the NN interaction using either

$$P_{kl}^{\sigma} = \frac{1}{2}\left[1 + (\boldsymbol{\sigma}_k \cdot \boldsymbol{\sigma}_l)\right], \qquad P_{kl}^{\tau} = \frac{1}{2}\left[1 + (\boldsymbol{\tau}_k \cdot \boldsymbol{\tau}_l)\right], \tag{A.2}$$

where P_{kl}^{σ} (P_{kl}^{τ}) is the spin(isospin)-exchange operator or

$$\begin{aligned} \mathcal{P}_{kl}^{S=0} &= \frac{1}{4}\left[1 - (\boldsymbol{\sigma}_k \cdot \boldsymbol{\sigma}_l)\right], & \mathcal{P}_{kl}^{I=0} &= \frac{1}{4}\left[1 - (\boldsymbol{\tau}_k \cdot \boldsymbol{\tau}_l)\right], \\ \mathcal{P}_{kl}^{S=1} &= \frac{1}{4}\left[3 + (\boldsymbol{\sigma}_k \cdot \boldsymbol{\sigma}_l)\right], & \mathcal{P}_{kl}^{I=1} &= \frac{1}{4}\left[3 + (\boldsymbol{\tau}_k \cdot \boldsymbol{\tau}_l)\right], \end{aligned} \tag{A.3}$$

where $\mathcal{P}^{S=0}$, $\mathcal{P}^{I=0}$, $\mathcal{P}^{S=1}$, and $\mathcal{P}^{I=1}$ are projectors into spin-singlet, isospin-singlet, spin-triplet, and isospin-triplet channels, respectively, can be easily transformed into the form (A.1).

In order to facilitate the calculation of matrix elements we express the spatial and spin part of each operator term considered here using an appropriate spherical tensor of rank κ. The identity $\mathbb{1}$ and kinetic energy T_k are spherical tensors of rank $\kappa = 0$. The same holds for the central interaction - the radial part $V(r_{kl})$ and the spin-dependent term $(\boldsymbol{\sigma}_k \cdot \boldsymbol{\sigma}_l)$. The tensor force S_{kl} can be expressed in the form

$$S_{kl} = 3(\boldsymbol{\sigma}_l \cdot \hat{\mathbf{r}}_{kl})(\boldsymbol{\sigma}_k \cdot \hat{\mathbf{r}}_{kl}) - \boldsymbol{\sigma}_k \cdot \boldsymbol{\sigma}_l = \sqrt{24\pi}\left[Y_2(\hat{\mathbf{r}}_{kl}) \otimes [\boldsymbol{\sigma}_k \otimes \boldsymbol{\sigma}_l]_2\right]_{00}, \tag{A.4}$$

i.e. as a coupled product of the spherical harmonics $Y_{2\mu}(\hat{\mathbf{r}}_{kl})$ of rank $\kappa = 2$ (spatial part) and the spherical tensor $[\boldsymbol{\sigma}_k \otimes \boldsymbol{\sigma}_l]_{2\mu}$ of rank $\kappa = 2$ (spin part). Here, $\mu = -\kappa, \ldots, \kappa$ denotes different spherical tensor components, $\hat{\mathbf{r}}_{kl} = (\mathbf{r}_k - \mathbf{r}_l)/r_{kl}$, and $[\otimes]$ is a coupling through Clebsch-Gordan coefficients. The spin-orbit interaction can be transformed from its cartesian form into a spherical basis as

$$(\mathbf{L} \cdot \mathbf{S})_{kl} = -\sqrt{3}\left[\mathbf{L}_{kl} \otimes \mathbf{S}_{kl}\right]_{00}, \tag{A.5}$$

where both $\mathbf{L}_{kl}$ and $\mathbf{S}_{kl}$ are now spherical tensors of rank $\kappa = 1$. Consequently, each operator term O discussed here so far[1] can be uniformly expressed as

$$O = \left[O_{\kappa}^{(\text{spatial})} \otimes O_{\kappa}^{(\text{spin})}\right]_{00} O^{(\text{isospin})}. \tag{A.6}$$

[1]All operator terms mentioned in this appendix have spatial, spin, and isospin components. If any of these components is not explicitly given, we assume that there is an identity operator $\mathbb{1}$ acting in the corresponding spatial, spin, or isospin space (e.g. $\mathbb{1} \equiv \mathbb{1}^{(\text{spatial})}\ \mathbb{1}^{(\text{spin})}\ \mathbb{1}^{(\text{isospin})}$, $T_{\text{k}} \equiv T_{\text{k}}\ \mathbb{1}^{(\text{spin})}\ \mathbb{1}^{(\text{isospin})}$, $V_{\text{c}}(r_{kl}) \equiv V_{\text{c}}(r_{kl})\ \mathbb{1}^{(\text{spin})}\ \mathbb{1}^{(\text{isospin})}$, etc.).

Matrix elements in the correlated Gaussian basis (3.15) can then be factorized as

$$\langle \psi^i_{(L^iS^i)J^\pi M_J\ IM_I} | O | \psi^j_{(L^jS^j)J^\pi M_J\ IM_I} \rangle =$$

$$= \left[\langle \psi^{(\mathrm{spatial})}_{L^i} | \otimes \langle \psi^{(\mathrm{spin})}_{S^i} | \right]_{JM_J} \left[O^{(\mathrm{spatial})}_\kappa \otimes O^{(\mathrm{spin})}_\kappa \right]_{00} \left[|\psi^{(\mathrm{spatial})}_{L^j}\rangle \otimes |\psi^{(\mathrm{spin})}_{S^j}\rangle \right]_{JM_J}$$

$$\langle \psi^{(\mathrm{isospin})}_{IM_I} | O^{(\mathrm{isospin})} | \psi^{(\mathrm{isospin})}_{IM_I} \rangle =$$

$$= (\psi^{(\mathrm{spatial})}_{L^i} || O^{(\mathrm{spatial})}_\kappa || \psi^{(\mathrm{spatial})}_{L^j})\ (\psi^{(\mathrm{spin})}_{S^i} || O^{(\mathrm{spin})}_\kappa || \psi^{(\mathrm{spin})}_{S^j})\ \langle \psi^{(\mathrm{isospin})}_{IM_I} | O^{(\mathrm{isospin})} | \psi^{(\mathrm{isospin})}_{IM_I} \rangle$$

$$\sum_{M_{L^i} M_{S^i}} \sum_{M_{L^j} M_{S^j}} \begin{bmatrix} L^i & S^i & J \\ M_{L^i} & M_{S^i} & M_J \end{bmatrix} \begin{bmatrix} L^j & S^j & J \\ M_{L^j} & M_{S^j} & M_J \end{bmatrix}$$

$$\sum_{\mu=-\kappa}^{\kappa} \frac{(-1)^{\kappa-\mu}}{\sqrt{2\kappa+1}} \begin{bmatrix} L^j & \kappa & L^i \\ M_{L^j} & \mu & M_{L^i} \end{bmatrix} \begin{bmatrix} S^j & \kappa & S^i \\ M_{S^j} & \mu & M_{S^i} \end{bmatrix} =$$

$$= (\psi^{(\mathrm{spatial})}_{L^i} || O^{(\mathrm{spatial})}_\kappa || \psi^{(\mathrm{spatial})}_{L^j})\ (\psi^{(\mathrm{spin})}_{S^i} || O^{(\mathrm{spin})}_\kappa || \psi^{(\mathrm{spin})}_{S^j})\ \langle \psi^{(\mathrm{isospin})}_{IM_I} | O^{(\mathrm{isospin})} | \psi^{(\mathrm{isospin})}_{IM_I} \rangle$$

$$\mathcal{D}(L^i, S^i, L^j, S^j, J, M_J; \kappa), \tag{A.7}$$

where we have for simplicity omitted $(A^i, \mathbf{u}^i_1, \mathbf{u}^i_2;\ \mathbf{x})$ with respect to our notation for a basis state used in Eq. (3.15). The $\mathcal{D}(L^i, S^i, L^j, S^j, J, M_J; \kappa)$ term represents summation over different Clebsch-Gordan coefficients [ ] and it is independent of reduced matrix elements (|| ||) which were obtained by applying the Wigner-Eckart theorem

$$\langle J^i M_{J^i} | O_{\kappa\mu} | J^j M_{J^j} \rangle = \begin{bmatrix} J^j & \kappa & J^i \\ M_{J^j} & \mu & M_{J^i} \end{bmatrix} (J^i || O_\kappa || J^j). \tag{A.8}$$

It is apparent from Eq. (A.7) that matrix elements are non-zero only if $|L^j - \kappa| \leq L^i \leq |L^j + \kappa|$ and $|S^j - \kappa| \leq S^i \leq |S^j + \kappa|$. Since randomly selected or stochastically optimized continuous parameters in A^i, $\mathbf{u}^i_1$, $\mathbf{u}^i_2$ enter only the spatial part, the spin and isospin parts together with $\mathcal{D}$ are calculated just once before the whole SVM procedure - this considerably reduces the computational effort.

The factorization presented in Eq. (A.7) is general and it is applied to all two-body $XY \in \{NN, \eta N, \Lambda^*\Lambda^*, \Lambda N, \Lambda\Lambda\}$ interactions considered here. As discussed in Subsection 3.1.2 we distinguish between particle species using the isospin part of the

basis state $\psi^{isospin}_{IM_I}$. Consequently, for systems composed of different particle species we supplement two-body XY interaction terms with a projection operator in the isospin space

$$\mathcal{P}^{XY}_{kl} = \begin{cases} 1 & \text{if } kl \sim XY \\ 0 & \text{otherwise} \end{cases} \tag{A.9}$$

which yields a non-zero isospin matrix element in Eq. (A.7) only if kl particle pair in $\psi^{isospin}_{IM_I}$ is associated with one particle of type X and one particle of type Y (which is denoted by '$\sim$').

In our work, we consider only a central three-body potential among particles k, l, and m with a spatial part in a Gaussian form

$$V_{klm} = d \sum_{\text{cyc}} \mathrm{e}^{-\frac{\lambda^2}{4}(r^2_{kl}+r^2_{lm})}, \tag{A.10}$$

where d and λ are real parameters representing the amplitude and width of the Gaussian potential, respectively. The cyclic sum $\sum_{\text{cyc}}$ stands for summation over different orders of particle indices $V_{klm} \longrightarrow V_{klm} + V_{mkl} + V_{lmk}$. As the spin part we use either identity or one of the projectors

$$\begin{aligned} \mathcal{Q}^{S=1/2}_{klm} &= \frac{1}{6}\left[3 - (\boldsymbol{\sigma}_k \cdot \boldsymbol{\sigma}_l) - (\boldsymbol{\sigma}_l \cdot \boldsymbol{\sigma}_m) - (\boldsymbol{\sigma}_m \cdot \boldsymbol{\sigma}_k)\right], \\ \mathcal{Q}^{S=3/2}_{klm} &= \frac{1}{6}\left[3 + (\boldsymbol{\sigma}_k \cdot \boldsymbol{\sigma}_l) + (\boldsymbol{\sigma}_l \cdot \boldsymbol{\sigma}_m) + (\boldsymbol{\sigma}_m \cdot \boldsymbol{\sigma}_k)\right], \end{aligned} \tag{A.11}$$

into the spin $S = 1/2$ or $S = 3/2$ three-body channels. The isospin dependent three-body operators are applied only to the NNN force

$$\begin{aligned} \mathcal{Q}^{I=1/2}_{klm} &= \frac{1}{6}\left[3 - (\boldsymbol{\tau}_k \cdot \boldsymbol{\tau}_l) - (\boldsymbol{\tau}_l \cdot \boldsymbol{\tau}_m) - (\boldsymbol{\tau}_m \cdot \boldsymbol{\tau}_k)\right], \\ \mathcal{Q}^{I=3/2}_{klm} &= \frac{1}{6}\left[3 + (\boldsymbol{\tau}_k \cdot \boldsymbol{\tau}_l) + (\boldsymbol{\tau}_l \cdot \boldsymbol{\tau}_m) + (\boldsymbol{\tau}_m \cdot \boldsymbol{\tau}_k)\right], \end{aligned} \tag{A.12}$$

where $\mathcal{Q}^{I=1/2}_{klm}$ and $\mathcal{Q}^{I=1/2}_{klm}$ are projectors into the isospin $I = 1/2$ and $I = 3/2$ three-body channels, respectively.

Both the spatial (A.10) and different spin (A.11) parts of the central three-body potential are spherical tensor operators of rank $\kappa = 0$. Matrix elements of $\mathcal{Q}^{S=1/2}_{klm}$, $\mathcal{Q}^{S=3/2}_{klm}$, $\mathcal{Q}^{I=1/2}_{klm}$, and $\mathcal{Q}^{I=3/2}_{klm}$ can be easily evaluated through $(\sigma_i \cdot \sigma_j)$ and $(\tau_i \cdot \tau_j)$ matrix elements. Since we are aware only of published matrix elements for a Gaussian three-body potential (A.10) with the total orbital momentum $L = 0$ [198] and thus without GVR (3.13) we present here a full analytical expression for $L \geq 0$ matrix

elements for natural parity ($\pi = (-1)^L$) basis states applied and benchmarked (see Appendix C) in our study

$$\langle \psi_{L^i}(A^i, \mathbf{u}_1^i, \mathbf{u}_2^i) | \mathrm{e}^{-\frac{\lambda^2}{4}\left(r_{kl}^2 + r_{lm}^2\right)} | \psi_{L^j}(A^j, \mathbf{u}_1^j, \mathbf{u}_2^j) \rangle =$$

$$= \frac{1}{(4\pi)^2} \left(\frac{(2\pi)^{N-1}}{\det(B)} \right)^{3/2} \left(\frac{\det(C)}{\det(C + \lambda^2/2 \; \mathbb{1})} \right)^{3/2} (2L+1)!! \tag{A.13}$$

$$\left(\rho_{ij} - (\Gamma^i)^T C \Gamma^j + \frac{\det C \; (\Gamma^i)^T C \Gamma^j + \lambda^2/2 \; (\Gamma^i)^T C C \Gamma^j}{\det(C + \lambda^2/2 \; \mathbb{1})} \right)^L ,$$

where $L^i = L^j = L$ and

$$\begin{aligned} B &= A^i + A^j & \rho_{ij} &= (\mathbf{u}_1^i)^T B \mathbf{u}_1^j \\ w_i^\alpha &= U_{ki}^{-1} - U_{li}^{-1} & \Gamma_\beta^j &= (\mathbf{w}^\beta)^T B^{-1} \mathbf{u}_1^j \\ w_i^\beta &= U_{li}^{-1} - U_{mi}^{-1} & \Gamma_\alpha^i &= (\mathbf{w}^\alpha)^T B^{-1} \mathbf{u}_1^i \\ C_{\alpha\beta}^{-1} &= (\mathbf{w}^\alpha)^T B^{-1} \mathbf{w}^\beta \end{aligned} \tag{A.14}$$

with the matrix U defined in Eq. (3.6).

For systems with more particle species we distinguish between different $XYZ \in \{NNN, \Lambda NN, \Lambda\Lambda N\}$ three-body interactions by applying a projector in the isospin space

$$\mathcal{Q}_{klm}^{XYZ} = \begin{cases} 1 & \text{if } klm \sim XYZ \\ 0 & \text{otherwise} \end{cases} \tag{A.15}$$

which is just a direct extension of its two-body $\mathcal{P}_{kl}^{XY}$ equivalent (A.9). It yields non-zero isospin matrix element in Eq. (A.7) only if klm particle triplet in $\psi_{IM_I}^{isospin}$ is associated with one particle of type X, one particle of type Y, and one particle of type Z.

Appendix B

Two-body system and poles of S-matrix

A two-body system of point-like particles with masses m_1 and m_2 interacting via spherically symmetric potential is described by the Schrödinger equation

$$\left\{\frac{\hbar^2}{2\mu}\left[-\frac{d^2}{dr^2}+\frac{l(l+1)}{r^2}\right]+V(r)\right\}\Psi_l(k,r)=E\Psi_l(k,r), \tag{B.1}$$

where $\mu=\frac{m_1m_2}{m_1+m_2}$ is the reduced mass, l denotes the orbital momentum of relative motion, and $E=\frac{k^2}{2\mu}$ is the total energy corresponding to the relative momentum k. The wave function $\Psi_l(k,r)$ of Eq. (B.1) regular at $r=0$ then has the asymptotic form [230]

$$\Psi_l(k,r)\to\frac{\mathrm{i}}{2}\left[f_l(k)h_l^-(kr)-f_l(k)^\star h_l^+(kr)\right],\quad h_l^\pm(kr)\to e^{\pm\mathrm{i}(kr-l\pi/2)}, \tag{B.2}$$

where $f_l(k)$ is the Jost function and $h_l^\pm(kr)$ stand for spherical Ricatti-Hankel functions. The first term of the asymptotic form represents an incoming wave and the second one an outgoing wave. Consequently, $f_l(k)$ and $f_l(k)^\star$ can be understood as corresponding asymptotic amplitudes of the incoming and outgoing part, respectively. The S-matrix is then expressed as

$$S_l(k)=\frac{f_l(k)^\star}{f_l(k)} \tag{B.3}$$

and its poles are related to zeros of the Jost function $f_l(k_0)=0$. Here, we assume that the Jost function has good analytic properties and can be evaluated for given k. Once the relative momentum approaches the position of a pole k_0, $f_l(k)$ goes to zero and the asymptotic behavior of the wave function (B.2) is given by the outgoing

term

$$\lim_{k\to k_0} \Psi_l(k,r) = \Psi_l(k_0,r) \to f_l(k_0)^\star e^{\mathrm{i}k_0 r}. \tag{B.4}$$

For $\mathrm{Im}(k_0) > 0$, the wave function (B.4) decreases exponentially and $\Psi_l(k_0, r)$ is a normalizable solution of Eq. (B.1). It corresponds to an eigenstate of the Hamiltonian H with energy $E = \frac{k_0^2}{2\mu}$. Since H is hermitian, the energy E is real, which implies that k_0 has to be purely imaginary. Poles with $\mathrm{Im}(k) > 0$ are then located only on the positive part of the imaginary momentum axis and correspond to bound states.

The situation is rather different for poles with $\mathrm{Im}(k_0) < 0$ which do not correspond to normalizable solutions. For $\mathrm{Re}(k_0) = 0$, the wave function increases exponentially - this type of solution is in general referred to as a *virtual* or *anti-bound* state due to its opposite asymptotic behavior with respect to a bound solution. Once the pole moves from the negative part of the imaginary momentum axis to the third quadrant of the complex momentum plane ($\mathrm{Re}(k) > 0$; $\mathrm{Im}(k) < 0$), the asymptotic part (B.4) starts to oscillate. Its form $\sim \exp\{\mathrm{iRe}(k_0)r\}\exp\{-\mathrm{Im}(k_0)r\}$ corresponds to an outgoing wave with an exponentially increasing amplitude which can be interpreted as a decaying state [231]. This type of an S-matrix pole is called a *resonance*. Due to the Schwarz reflection principle, the Jost function satisfies relation $f_l(k) = f_l(-k^\star)^\star$ [230]. Consequently, each resonance pole $k_0 = \mathrm{Re}(k_0) + \mathrm{iIm}(k_0)$ is accompanied by another pole called an *anti-resonance* at the position $-k_0^\star = -\mathrm{Re}(k_0) + \mathrm{iIm}(k_0)$.

The positions of bound state, virtual state, resonance, and anti-resonance poles in the complex momentum plane (k-plane) are illustrated in Fig. B.1 (left panel). The corresponding complex energy plane (E-plane) related to the k-plane as $E = \frac{k^2}{2\mu}$ is shown on the right panel. The transformation from k to E is in fact two-to-one and the E-plane has two Riemann sheets. The first sheet called *physical* represents the upper half of the k-plane ($\mathrm{Im}(k) > 0$) with bound state poles whereas the second *nonphysical* sheet corresponds to the lower half ($\mathrm{Im}(k) < 0$) with virtual states, resonances, and anti-resonances.

Resonances are often interpreted using a time-dependent wave function (B.4)

$$\lim_{k\to k_0} \Psi_l(k,r;\ t) \sim \Psi_l(k_0,r)\ \exp\left\{-\frac{\mathrm{iRe}(E_0)}{\hbar}t\right\}\exp\left\{\frac{\mathrm{Im}(E_0)}{\hbar}t\right\}, \tag{B.5}$$

where E_0 is the complex resonance energy corresponding to the complex momentum k_0. For resonant poles $\mathrm{Im}(E_0)$ is negative and the corresponding amplitude decreases exponentially with time. This can be associated with the finite lifetime τ of such a

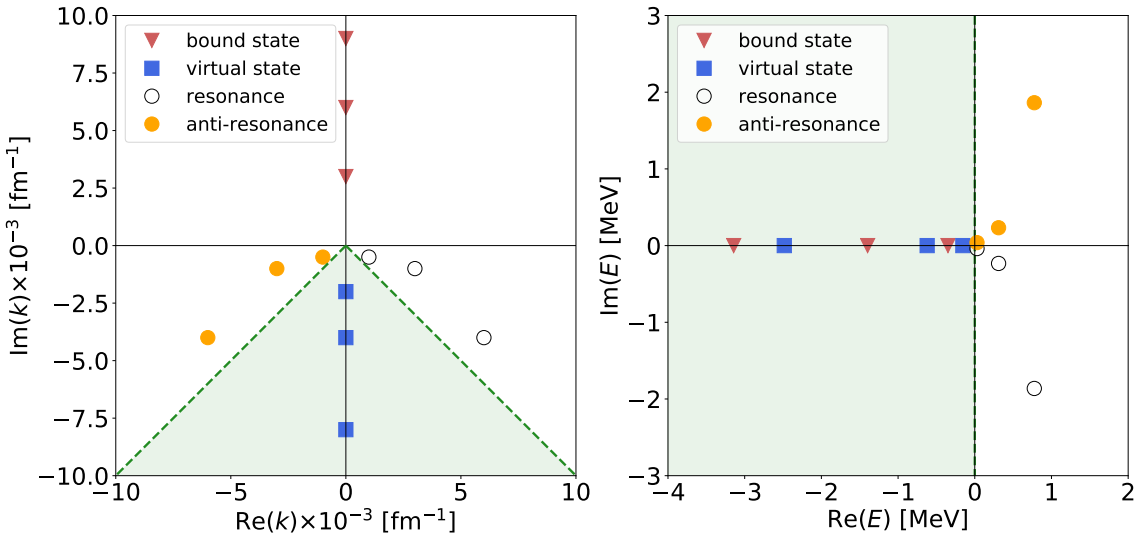

Figure B.1: Position of bound state, virtual state, resonance, and anti-resonance poles in the complex momentum plane (left panel) and their corresponding positions in the complex energy plane (right panel). The transformation between k-plane and E-plane is performed using $E = \frac{k^2}{2\mu}$ where μ=1 MeV. The green dashed line indicates border of the *subthreshold resonance* region $0 < |\mathrm{Re}(k)| < -\mathrm{Im}(k)$ denoted by green shaded area.

state [276]

$$\tau = -\frac{\hbar}{\mathrm{Im}(E_0)} = \frac{2\hbar}{\Gamma}, \tag{B.6}$$

where Γ is a width of the resonance. The complex resonance energy is then usually written in a form

$$E_0 = E_r - \mathrm{i}\frac{\Gamma}{2}, \tag{B.7}$$

where E_r stands for the resonance energy referring to its real part $\mathrm{Re}(E_0)$.

A rather interesting phenomenon are S-matrix poles with $\mathrm{Im}(k_0) < 0$ (resonant or anti-resonant) which satisfy condition $0 < |\mathrm{Re}(k_0)| < -\mathrm{Im}(k_0)$ presented in Fig. B.1 by green shaded area. Corresponding complex energies E_0 have then a negative real part, consequently, this type of poles is sometimes referred to as a *subthreshold resonance* or a *virtual state with width*. To the best of our knowledge, there is no solid physical interpretation of such resonances, nevertheless, they are in general regarded as *nonphysical*, i.e. they are not considered as physically observable resonances with certain lifetime. However, their existence can still influence experimentally observable quantities such as scattering phase shifts. As an example we give a diproton spin-singlet case with an estimated s-wave pole at $E_0^{\mathrm{pp}} \approx -0.14 - \mathrm{i}0.47$ MeV enhancing near-threshold $p-p$ phase shifts [231, 277]. Throughout this work we

implicitly consider resonances with $\mathrm{Re}(E) > 0$, if not mentioned otherwise.

The effect of a resonance can be experimentally observed in two-body scattering, more precisely, in scattering phase shifts and cross sections. For a small interval around the resonance position E_r corresponding phase shifts $\delta(E)$ can be decomposed into a slowly varying background $\delta_{\mathrm{bg}}(E)$ and a resonant contribution $\delta_r(E)$ [230]

$$\delta_r(E) = -\arctan\frac{\Gamma/2}{E - E_r}. \tag{B.8}$$

Consequently, a resonance pole close to the real energy axis manifests as a sudden increase in $\delta(E)$ by π with its center at $\delta_r(E_r) = \pi/2$. The increase is sharper with smaller Γ while for a large width (resonance pole farther from the real energy axis) $\delta_r(E)$ contributes over wider range of energies and $\delta_r(E_r)$ can be outweighed by $\delta_{\mathrm{bg}}(E)$. It is to be noted that there is no unique correspondence between experimentally observable phenomena in scattering phase shifts and a resonance as zero of the Jost function [230]. Poles far from the real axis can hardly have noticable effect on $\delta(E)$ and on the other hand, there might exist resonant-like phase shift phenomena without any zero in $f_l(k)$. Moreover, a near-threshold virtual state can exhibit similar effect on two-body scattering as a resonance. To conclude, careful interpretation of experimental phase shifts, preferably connected with underlying theoretical models, is desirable.

It is highly useful to connect the position k_0 of near-threshold poles with properties of the scattering amplitude $\mathcal{F}_l(k)$ at low momenta. From the relation between $\mathcal{F}_l(k)$ and $S_l(k)$

$$\mathcal{F}_l(k) = \frac{S_l(k) - 1}{2\mathrm{i}k} = \frac{e^{\mathrm{i}\delta_l(k)}\sin\delta_l(k)}{k} \tag{B.9}$$

we obtain that S-matrix poles manifest themselves as poles of the corresponding scattering amplitude. Using the s-wave ($l = 0$) effective range expansion (ERE) up to k^2

$$k\mathrm{cotg}\delta_0 = -\frac{1}{a} + \frac{r}{2}k^2 + \ldots, \tag{B.10}$$

where a is the scattering length and r is the effective range, we can approximate the amplitude $\mathcal{F}_0(k)$ in the near-threshold momentum region as

$$\mathcal{F}_0(k) = \frac{1}{k\mathrm{cotg}\delta_0 - \mathrm{i}k} \approx \left[-\frac{1}{a} - \mathrm{i}k + \frac{r}{2}k^2\right]^{-1}. \tag{B.11}$$

The amplitude has then two poles and their position k_0 is given by the first two

Table B.1: Classification of s-wave primary pole k_0^- (B.12) as a function of the scattering length a and effective range r.

Bound state	$a > 0$,	$r < a/2$	
Virtual state	$a < 0$,	$r > 0$	
	$a < 0$,	$r < 0$,	$a < 2r$
Virtual state with width (subthreshold resonance)	$a < 0$,	$r < 0$,	$2r < a < r$
Resonance	$a < 0$,	$r < 0$,	$r < a$

parameters of ERE - the scattering length and the effective range

$$k_0^{\pm} = \frac{\mathrm{i}}{r}\left[1 \pm \sqrt{1 - \frac{2r}{a}}\right]. \tag{B.12}$$

A detailed study of both primary k_0^- and conjugate k_0^+ poles as a function of a and r was performed in Refs. [278, 279]. The primary pole is located closer to the physical scattering axis ($\mathrm{Im}(k) = 0$, $\mathrm{Re}(k) \geq 0$) and it has the main affect on the corresponding scattering amplitude $\mathcal{F}_0(k)$ [278].

In Table B.1, we present classification of the primary pole k_0^- as a function of the s-wave scattering length a and effective range r based on Eq. (B.12). While the bound state option is clearly related to $a > 0$, the $a < 0$ case allows three different scenarios - a virtual state, a virtual state with width, and a resonance. Moreover, it is apparent that just from the knowledge of a scattering length itself one can deduce only the bound or unbound characteristics of a pole. In fact, taking into account only the first term of ERE (B.11) one obtains the pole position $k_0 = \mathrm{i}/a$, consequently, finer classification of an unbound case requires knowledge of an effective range. Both resonances and virtual states with width appear only for $r < 0$.

The most striking difference between a two-body system and a few-body case is the existence of various thresholds. Already at 3-body level, a system consisting of particles a, b, and c might have three different 2-body thresholds associated with corresponding 2-body continua - $(ab) + c$, $(bc) + a$, and $(ac) + b$ where () stands for a bound two-body subsystem. Moreover, there is a 3-body threshold $a + b + c$ connected with the 3-body continuum. Consequently, abc S-matrix poles can have in principle different structures predominantly affecting only a certain part of the corresponding continuum. In order to distinguish different resonant characteristics we adopt notation $N_1 + N_2 + \cdots + N_m$ where m stands for the number of bound

subsystems inside a few-body resonance and $\{N_i, i = 1, \ldots, m\}$ are the numbers of particles in each subsystem.

The presence of few-body S-matrix poles associated with two bound subsystems could be revealed in scattering experiments measuring two-body phase shifts and cross sections. In this specific case conclusions of our discussion concerning the effect of two-body S-matrix poles on scattering observables can be applied as well. As an example the resonant 0^+ ground state of ^{8}Be can be viewed as a near-threshold $\alpha + \alpha$ (4+4) resonance which dominates elastic s-wave $\alpha - \alpha$ scattering at low energies [280]. Another example is the s-wave Λ scattering off ^{2}H dominated by the weakly bound hypertriton ground state in $J^\pi = 1/2^+$ channel and a possible (2+1) near-threshold excited state in $J^\pi = 3/2^+$ channel studied in this work [147]. In the case of more than two bound subsystems different experimental techniques have to be employed. For example, the measurement of photodisintegration cross sections of the ^{9}Be(γ, n) 2 ^{4}He reaction reveals sharp peak just above the $^8\mathrm{Be} + \mathrm{n}$ threshold, which was then used in subsequent theoretical works [251,281] to address the nature of the first excited $1/2^+$ state of ^{9}Be. These studies led to the conclusion that the $1/2^+$ state exists as the $^8\mathrm{Be} + \mathrm{n}$ virtual state rather than the $\alpha + \alpha + n$ (4+4+1) resonance. Another example is the experimental search for a possible Λnn (1+1+1) hypernuclear resonance which should be produced in $^3\mathrm{H}(e, e'K^+)\Lambda$ reaction and visible in the corresponding Λ missing mass spectrum [272].

Appendix C

Benchmark calculations

We test our recently developed SVM code extended with the CSM and IACCC methods to few-body continuum using series of benchmark calculations. In the first part, we present SVM calculations of few-body bound states using several phenomenological as well as realistic potentials. In the second part, we show benchmark IACCC and CSM calculations of few-body resonances.

It is to be stressed that the factorization (A.7) appears crucial in SVM calculations with realistic potentials which would not be numerically feasible otherwise.

C.1 Bound states

We demonstrate correctness of our SVM code calculating properties of few-body nuclear ground states - ^{2}H, ^{3}H, ^{3}He, and ^{4}He for four different interaction models with the Coulomb interaction included - the Minnesota with $u = 1$ parameter (Minn) [227], Argonne V4' (AV4') [282], Argonne V8' (AV8') [283], and Gaussian soft core G3RS [229] two-body potentials. For G3RS we omit $\mathbf{L}^2$ and $(\mathbf{L}.\mathbf{S})^2$ terms. We made this specific choice since all our results up to AV4' can be directly compared with detailed calculations presented in Ref. [225] (see Tables 1 and 2 in that work) which were obtained using the same method - SVM with the correlated Gaussian basis with GVR (3.15). While the Minn and the AV4' potential consider only the central interaction the AV8' and G3RS include non-central tensor and spin-orbit terms as well. Further, both AV4' and AV8' have a strong repulsive contribution at short relative distances (hard-core), which can be challenging for their application in few-body calculations.

In this subsection we use $(\hbar c)^2/m = 41.47$ MeV $\cdot$ fm^2 and $e^2 = 1.440$ MeV $\cdot$ fm. In each calculation, we consider all possible (L, S) components (3.15) which can

Table C.1: Results of SVM calculations of the ^{2}H($J^\pi = 1^+$) ground state using different NN potentials. We show both the ground state energy E and individual contributions to E - the kinetic term $\langle T_{\rm k}\rangle$ and the central $\langle V_{\rm c}\rangle$, tensor $\langle V_{\rm T}\rangle$, and spin-orbit $\langle V_{\rm LS}\rangle$ parts of the potential. The rms radius $\sqrt{\langle r^2\rangle}$ and individual probabilities $P(L,S)$ to find considered (L,S) channels in the total wave function are presented as well. For each calculation we give the number of basis states $\#basis$ used to obtain converged SVM solution. All energies are given in MeV, rms radii are given in fm.

	Potential	Minn [227]	AV4' [282]	AV8' [283]	G3RS [229]
^{2}H(1^+)	E	-2.202	-2.245	-2.243	-2.277
	$\langle T_{\rm k}\rangle$	10.490	11.419	19.885	16.479
	$\langle V_{\rm c}\rangle$	-12.692	-13.664	-4.458	-7.295
	$\langle V_{\rm T}\rangle$			-16.645	-11.461
	$\langle V_{\rm LS}\rangle$			-1.024	0
	$\sqrt{\langle r^2\rangle}$	1.947	2.020	1.961	1.979
	$P(0,1)$	100	100	94.223	95.220
	$P(2,1)$			5.777	4.780
	$\#basis$	10	30	50	30

contribute to the total wave function of the J^π ground state. We also use a complete set of possible spin and isospin configurations. Due to rather high amount of numerical values presented here as well as very small discrepancies between our results and those obtained in Ref. [225], we do not show specific values given in that work. Instead, we make a general statement that for the ^{2}H system the ground state energy as well as other properties presented here slightly differ in the third decimal place and for ^{3}H, ^{3}He, and ^{4}He in the second decimal place with respect to Ref [225]. We remind that within SVM we select basis states stochastically. This means that although we use the same method as in Ref. [225] our basis sets are different which is the reason of these small numerical discrepancies. For example, in Ref. [225] the authors compared their ^{3}H, ^{3}He, and ^{4}He SVM results using the correlated Gaussian basis with either the GVR or orbital momentum part expanded into partial waves (3.11) and they differed at the same numerical order (second decimal place). Identical level of precision was obtained in Ref. [224] comparing SVM results for ^{4}He using the AV8' potential with other few-body techniques.

In Table C.1, we present our SVM results for the deuteron 1^+ ground state. We show the calculated bound state energy E as well as individual contributions from the kinetic and different potential terms (central, tensor, and spin-orbit) to E. The

Table C.2: Results of SVM calculations of the ^{3}H($J^\pi = 1/2^+$), ^{3}He($J^\pi = 1/2^+$), and ^{4}He($J^\pi = 0^+$) ground states using different NN potentials with the Coulomb force included. We show the same ground state properties as in Table C.1 plus the Coulomb contribution $\langle V_{\rm Coul}\rangle$ to the ground state energy E. All energies are given in MeV, the rms radii are given in fm.

	Potential	Minn [227]	AV4' [282]	AV8' [283]	G3RS [229]
^{3}H($\frac{1}{2}^+$)	E	-8.39	-8.99	-7.77	-7.74
	$\langle T_{\rm k}\rangle$	27.21	37.20	47.60	40.29
	$\langle V_{\rm c}\rangle$	-35.60	-46.19	-22.51	-26.82
	$\langle V_{\rm T}\rangle$			-30.86	-21.18
	$\langle V_{\rm LS}\rangle$			-2.00	-0.03
	$\sqrt{\langle r^2\rangle}$	1.71	1.67	1.76	1.79
	$P(0,\frac{1}{2})$	100	100	91.39	92.91
	$P(2,\frac{3}{2})$			8.55	7.04
	$P(1,\frac{1}{2})$			0.04	0.03
	$P(1,\frac{3}{2})$			0.02	0.02
	$\#basis$	400	400	400	400
^{3}He($\frac{1}{2}^+$)	E	-7.71	-8.30	-7.09	-7.08
	$\langle T_{\rm k}\rangle$	26.69	36.43	46.66	39.47
	$\langle V_{\rm c}\rangle$	-35.07	-45.42	-21.99	-26.25
	$\langle V_{\rm Coul}\rangle$	0.67	0.69	0.65	0.64
	$\langle V_{\rm T}\rangle$			-30.45	-20.91
	$\langle V_{\rm LS}\rangle$			-1.96	-0.03
	$\sqrt{\langle r^2\rangle}$	1.74	1.69	1.79	1.82
	$P(0,\frac{1}{2})$	100	100	91.44	92.95
	$P(2,\frac{3}{2})$			8.50	7.00
	$P(1,\frac{1}{2})$			0.04	0.03
	$P(1,\frac{3}{2})$			0.02	0.02
	$\#basis$	400	400	400	400
^{4}He(0^+)	E	-29.95	-32.06	-25.10	-25.29
	$\langle T_{\rm k}\rangle$	58.09	86.86	101.64	86.94
	$\langle V_{\rm c}\rangle$	-88.88	-119.76	-54.94	-66.22
	$\langle V_{\rm Coul}\rangle$	0.83	0.84	0.77	0.76
	$\langle V_{\rm T}\rangle$			-67.90	-46.64
	$\langle V_{\rm LS}\rangle$			-4.65	-0.13
	$\sqrt{\langle r^2\rangle}$	1.41	1.39	1.49	1.51
	$P(0,0)$	100	100	85.77	88.45
	$P(2,2)$			13.87	11.29
	$P(1,1)$			0.36	0.26
	$\#basis$	400	400	800	600

root-mean-square (rms) radius and probabilities of considered (L, S) components in the ground state wave function are presented as well. The calculated ^{2}H ground state energy for AV4' can be compared to the results given in Ref. [284] for several few-body models - their predictions yield $E = -2.245$ MeV, which agree with our SVM calculation. In the same work one can also find the ^{2}H ground state energy for AV8' which slightly differs from our result. On the other hand, more detailed study for the same system with AV8' in Ref. [285] shows remarkable agreement with our predictions.

Results of our SVM calculations of the ^{3}H, ^{3}He, and ^{4}He ground states are given in Table C.2. Again, we present the same quantities as in the deuteron case. For AV4', the predicted ^{3}H ground state energy agrees with results presented in Ref. [284]. We did not find any numerical result for the ^{4}He system with AV4' including the Coulomb interaction, consequently, we compare calculated ground state energy with no Coulomb force $E = -32.89$ MeV with the equivalent result given in Ref. [284].

Three-body force

Benchmark calculations of a three-body force are performed using "toy" nuclear-like few-body systems composed of fermions with nucleon mass $m = 938.858$ MeV interacting with two- and three-body potentials

$$\begin{aligned} V_2 &= C_2 \sum_{i<j} \mathrm{e}^{-\frac{\lambda^2}{4} r_{ij}^2}, \\ V_3 &= D_3 \sum_{i<j<k} \sum_{\mathrm{cyc}} \mathrm{e}^{-\frac{\lambda^2}{4}(r_{ij}^2 + r_{jk}^2)}, \end{aligned} \tag{C.1}$$

where $C_2 = -337.616$ MeV, $D_3 = 244.626$ MeV, and $\lambda = 2$ fm^{-1}. Calculated SVM binding energies for several systems are compared with results obtained using the Diffusion Monte Carlo (DMC) technique in Table C.3 - one can see good agreement with respect to the DMC results. While for the ^{3}H-like system we use correlated Gaussian three-body potential matrix element with total orbital momentum $L = 0$ where no global vectors (3.13) are required, ^{3}n- and ^{4}Li-like systems have $L = 1$ and global vectors (3.13) are included.

Table C.3: Calculated ground state energies of several few-body systems using either our SVM code E(SVM) or DMC method E(DMC). All calculations are performed using potential in Eq. (C.1) and considering just one (L, S) component in the corresponding correlated Gaussian basis (3.15). All energies are in MeV.

System	(L, S)	E(SVM)	E(DMC) [207]
^{2}H(1^+)	(0,1)	-87.90	
^{3}n($1/2^-$)	(1,1/2)	-104.30	-104.26
^{3}H($1/2^+$)	(0,1/2)	-198.37	-198.32
^{4}Li(1^-)	(1,1)	-215.56	-214.90

C.2 Resonances

We benchmark our CSM and IACCC codes by calculating resonance positions in two different three-body systems studied in previous works. The first system has one 3-body bound state and one 2+1 resonance (with 2-body bound state). The second system is borromean with no bound state and one 1+1+1 resonance in the three-body continuum. In both cases, we perform rather detailed comparison between IACCC and ACCC results. We also discuss stability of our continuum calculations, more specifically, we show residual dependence on the complex scaling angle θ (CSM) and degrees of the Padé approximant (IACCC and ACCC method).

2+1 resonance

A model system of three identical bosons with mass $m = 939$ MeV interacting with the two-body s-wave potential

$$\begin{aligned} V(r) &= V_1 \mathrm{e}^{-0.2r^2} + V_2 \mathrm{e}^{-0.01(r-5)^2}, \\ V_1 &= -55 \text{ MeV}, \\ V_2 &= 1.5 \text{ MeV} \end{aligned} \tag{C.2}$$

was used in several works in order to benchmark few-body resonance methods. Results of previous studies using different few-body techniques - the Faddeev equation with complex scaling (FE-CS) [244, 286], the slow-variable discretization coupled with a complex absorbing potential (SVD-CAP) [287], and the discrete variable representation in finite volume (DVR-FV) [288] are summarized in Table C.4. It was found that potential (C.2) supports one two-body and one three-body bound state plus one three-body 2+1 resonance existing just few hundred keV above the

Table C.4: Collected results of a 2- and 3-body system of identical bosons with the nucleon mass interacting with s-wave potential (C.2). We show the 2-body ground state, 3- body ground state, and 3-body (2+1) resonance energy $E_{2\mathrm{B}}$, $E_{3\mathrm{B}}$, and $E(resonance)$, respectively, calculated using different few-body techniques. In some cases ground state energies were not presented in corresponding papers. Only the real part of the resonance is given in Ref. [288]. All energies are in MeV.

Model	$E_{2\mathrm{B}}$	$E_{3\mathrm{B}}$	E(resonance)	
FE-CS [286]			-5.9525	- i0.4034
FE-CS [244]	-6.76	-37.22	-5.96	- i0.40
SVD-CAP [287]		-37.35	-5.31	- i0.12
DVR-FV [288]	-6.756(1)	-37.30(5)	-5.32(1)	

two-body threshold. It can be noticed that while the above mentioned works agree on bound state energies, the resonance positions differ. In fact this dichotomy with respect to FE-CS results was firstly pointed out by Blandon *et al.* [287] using SVD-CAP method where it came out as a surprise since the other benchmark calculations presented in their work agreed. Moreover, the other study using DVR-FV method [288] yielded the resonance energy in agreement with [287] and thus questioned the FE-CS results [244, 286].

Using SVM with the correlated Gaussian basis we obtain two-body bound state energy $E_{2\mathrm{B}} = -6.754$ MeV and three-body bound state energy $E_{3\mathrm{B}} = -37.245$ MeV, which is in reasonable agreement with the results of previous works given in Table C.4.

In order to calculate the position of the 2+1 resonance within the IACCC method we introduce an additional three-body attractive potential

$$V_3^{\mathrm{IACCC}} = d \sum_{i<j<k} \sum_{\mathrm{cyc}} \mathrm{e}^{-\frac{\lambda^2}{4}(r_{ij}^2 + r_{jk}^2)}, \tag{C.3}$$

where $\lambda = 1$ fm^{-1} and the strength parameter d is negative for attraction. In fact, the introduction of the three-body potential simplifies our study since the two-body bound state energy $E_{2\mathrm{B}}$ does not change with d and the corresponding two-body threshold remains at the same position. By increasing attractive strength of the auxiliary potential (C.3) the 2+1 resonant pole moves towards the two-body threshold and at $\bar{d}_0 \approx -11.545$ MeV a bound excited state emerges in addition to the ground state.

Applying the SVM we calculate $M + N + 1$ bound excited state energies E_i for

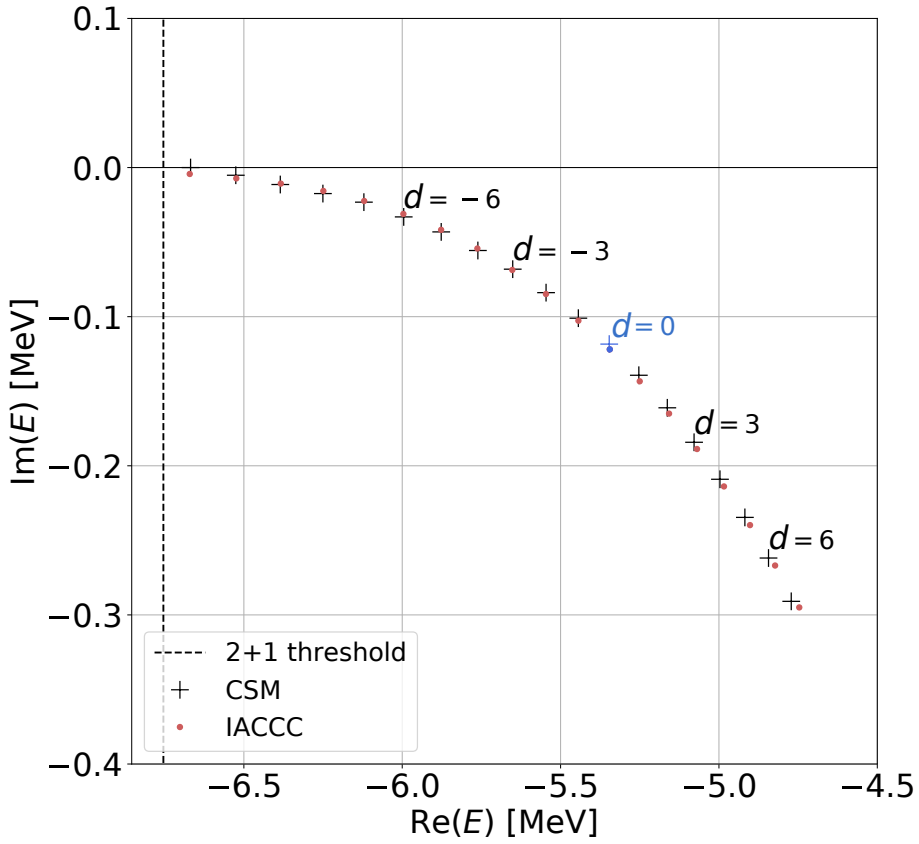

Figure C.1: Calculated 2+1 resonance positions for different strengths d of auxiliary potential (C.3) using either CSM (crosses) or IACCC method (dots). For CSM we present resonance positions which correspond to the most stationary point of respective θ-trajectory. IACCC solutions are obtained using Padé approximant (3.34) of degree (12,12). Calculated CSM and IACCC resonance positions with no auxiliary potential ($d = 0$) are in blue color.

different $d_i < \bar{d}_0$ and we construct a Padé approximant of degree (M, N) (3.34) using the SVM solutions $\{d_i(\kappa_i);\ i = 1, ..., M+N+1\}$. Here, $\kappa_i = -\mathrm{i}k_i$ and k_i is the excited state momentum with respect to the nearest 2+1 threshold $k_i = \sqrt{2\mu(E_i - E_{2\mathrm{B}})}$ where μ is the reduced mass in 2+1 decay channel. Corresponding IACCC pole positions are then obtained as roots of the polynomial equation (3.35).

CSM resonant solutions are obtained using an appropriate basis of correlated Gaussians, more specifically, we select corresponding basis states applying the HO trap technique described in Section 3.3.2. We find that already for the trap length $b = 30$ fm, CSM solutions stabilize and do not change with increasing b any further. We perform CSM calculations for several strengths d of the auxiliary potential (C.3) using different values of the complex scaling angle θ ranging from 1° up to 45° with 1° step. For each d we search for the corresponding 2+1 resonance θ-trajectory

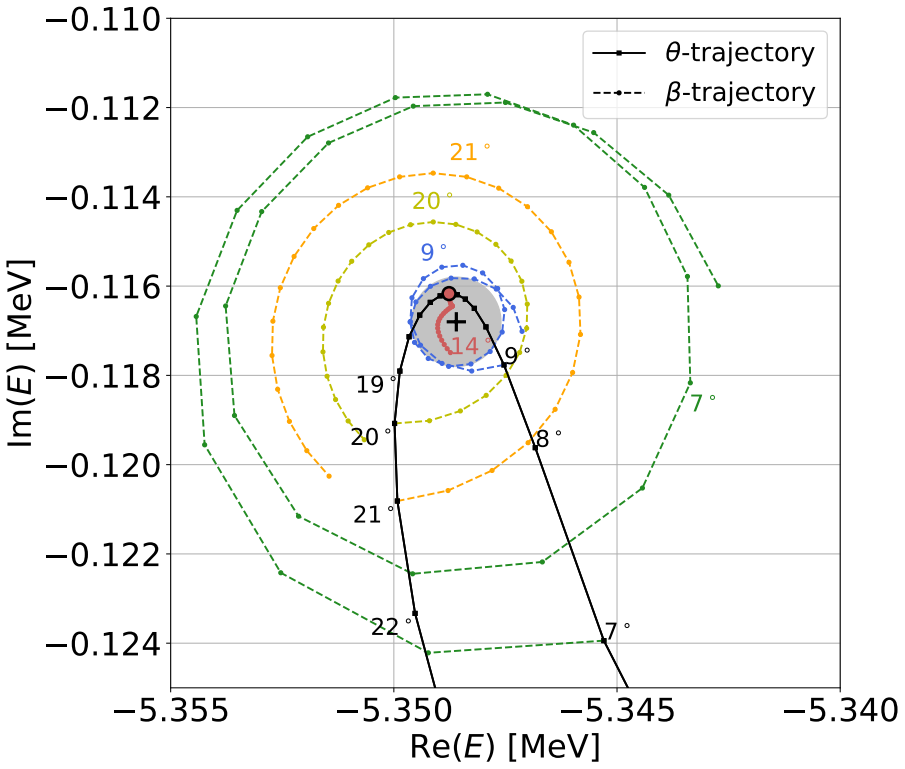

Figure C.2: 2+1 resonance θ-trajectory (Im(θ)=0; black solid line) and β-trajectories (colored dotted lines) showing movement of corresponding $E(\theta)$ as a function of θ in the complex energy plane. β-trajectories are presented for several different Re(θ) changing Im(θ) from 0 to 0.22 radians with 0.01 step. While the red dot on the θ-trajectory indicates the position of its most stationary solution $E(\theta_{\text{opt}} = 14°)$, the black cross indicates the estimated 2+1 resonance position of the true CSM solution satisfying exact equality in Eq. (3.43). The shaded gray area then shows the corresponding CSM error. The 2+1 resonance calculation is performed for $d = 0$ (i.e. with no auxiliary potential).

together with the most stationary solution $E(\theta_{\text{opt}})$.

In Fig. C.1, we compare the calculated IACCC 2+1 resonance solutions using the Padé approximant (3.34) of degree (12,12) and the corresponding CSM resonance solutions obtained as the most stationary point of the θ-trajectory for different strengths d of V_3^{IACCC} (C.3). One can see good agreement between both IACCC and CSM resonance solutions. As the strength d of the auxiliary attractive potential decreases the resonance position moves in the complex energy plane further from the 2+1 threshold. For $d = 0$ (blue marks) there is no auxiliary force and the calculated resonance position is given only by the potential in Eq. (C.2).

We now focus on the case with $d = 0$ which can be compared with the previous results summarized in Table C.4. Starting with the CSM we show in Fig. C.2 the

calculated θ-trajectory with the most stationary point at $\theta_{\text{opt}} = 14°$ and several β-trajectories for different Re(θ). The true CSM solution satisfying exact equality in Eq. (3.43) is located inside the gray area and its most probable position is marked with the black cross. Taking into account both the most probable position and error given by the shaded area we obtain the CSM resonance energy $E(\text{CSM}) = -5.3486(10) - \text{i}0.1168(10)$ MeV. Here, we constrained the true CSM solution using β-trajectory with Re(θ) = 9°. For β-trajectories with Re(θ) closer to the Re(θ_{opt}) = 14° we did not get circular shape but unstable β-trajectories inside the gray shaded area instead. We assume that this effect is related to the finite dimension of our basis set which is able to sustain stable β-trajectory only up to a certain point. Circular trajectories with Re(θ) closer to the Re(θ_{opt}) = 14° would have smaller radii and thus the error of our CSM solution further decrease.

In Table C.5, we demonstrate stability of our IACCC 2+1 resonance energy solutions with respect to different degrees (M, N) of the Padé approximant for $d = 0$ (no auxiliary force). For this particular point we present ACCC results as well. We see that both IACCC and ACCC results agree, however, we observe that numerical stability of ACCC solutions is slightly worse. In fact, it takes much more effort to obtain stable ACCC solutions due to stringent requirement on precise determination of the branching point d_0 which is used in the corresponding Padé approximant (3.33). In particular, for this case of $L = 0$ system, d_0 does not correspond to the $\bar{d}_0$ value when continuum pole turns into the bound state $E(\bar{d}_0) = 0$. Based on the interaction the branching point is shifted further from $\bar{d}_0$ ($\bar{d}_0 > d_0$) [289] and additional techniques have to be involved in order to determine its value (for

Table C.5: Stability of the 2+1 resonance energy solution obtained using either the IACCC or ACCC method with respect to increasing degree (M, N) of the Padé approximant applied in analytic continuation. Presented resonance solutions correspond to situation with no auxiliary potential (C.3). All energies are given in MeV.

(M, N)	E(IACCC)	E(ACCC)
(7,7)	-5.345 - i0.126	-5.409 - i0.157
(8,8)	-5.346 - i0.127	-5.377 - i0.115
(9,9)	-5.354 - i0.127	-5.374 - i0.117
(10,10)	-5.344 - i0.124	-5.318 - i0.123
(11,11)	-5.345 - i0.122	-5.377 - i0.134
(12,12)	-5.343 - i0.123	-5.387 - i0.122

more details see [231]). On the other hand, for IACCC calculations the issue of precise determination of d_0 is completely avoided, which leads to higher numerical stability. Summarizing our IACCC and ACCC calculations for $d = 0$ we obtain the 2+1 resonance energy $E(\text{IACCC}) = -5.34(1) - \text{i}0.12(1)$ MeV and $E(\text{ACCC}) = -5.4(1) - \text{i}0.12(2)$ MeV, where the corresponding error is estimated comparing IACCC or ACCC solutions obtained with different (M, N) ranging from (7,7) up to (12,12). We conclude that our CSM, IACCC, and ACCC resonance solutions are in agreement with the SVD-CAP [287] and SVD-FV [288] results given in Table C.4.

1+1+1 resonance

The second system tested in our benchmark calculations are three identical bosons with $(\hbar c)^2/m = 41.47$ MeV.fm^2 interacting through the two-body potential

$$\begin{aligned} V(r) &= V_1 \mathrm{e}^{-r^2} + g\ V_2\ \mathrm{e}^{-\frac{r^2}{9}}, \\ V_1 &= -120 \text{ MeV}, \\ V_2 &= 3 \text{ MeV}, \end{aligned} \tag{C.4}$$

where the parameter g defines strength of the repulsive part. The system was studied in [235] using mostly the same methods as in our work - SVM with the correlated Gaussian basis extended with the CSM and ACCC method. It was shown that for $g \gtrsim 2.5$ there is one 1+1+1 resonance while there is no two- or three-body bound state.

Here, we supplement the potential (C.4) with the additional three-body interaction (C.3) used in the previous 2+1 resonance calculations. Consequently, there are two parameters g and d defining the strength of the two-body repulsive part and three-body attraction, respectively. We perform two types of calculation: In the first case (referred as V_2^{IACCC}) we keep $d = 0$, following the work in [235], and we consider g as the IACCC coupling constant. In the second case (referred as V_3^{IACCC}) we set $g = 3$ and we use three-body parameter d as the IACCC coupling constant. For $g = 3$, $d = 0$ both cases coincide having the same interaction, consequently, corresponding V_2^{IACCC} and V_3^{IACCC} resonance solutions in this particular point have to agree. Using the SVM we obtain for $d = g = 0$ a three-body bound state with $E_{3B} = -15.733$ MeV. Further, for V_2^{IACCC} calculation the three-body system starts to be unbound at $\bar{g}_0 \approx 2.498$ whereas for V_3^{IACCC} at strength $\bar{d}_0 \approx -3.625$ MeV.

In Fig. C.3, we present 1 + 1 + 1 IACCC resonance solutions for the V_2^{IACCC}

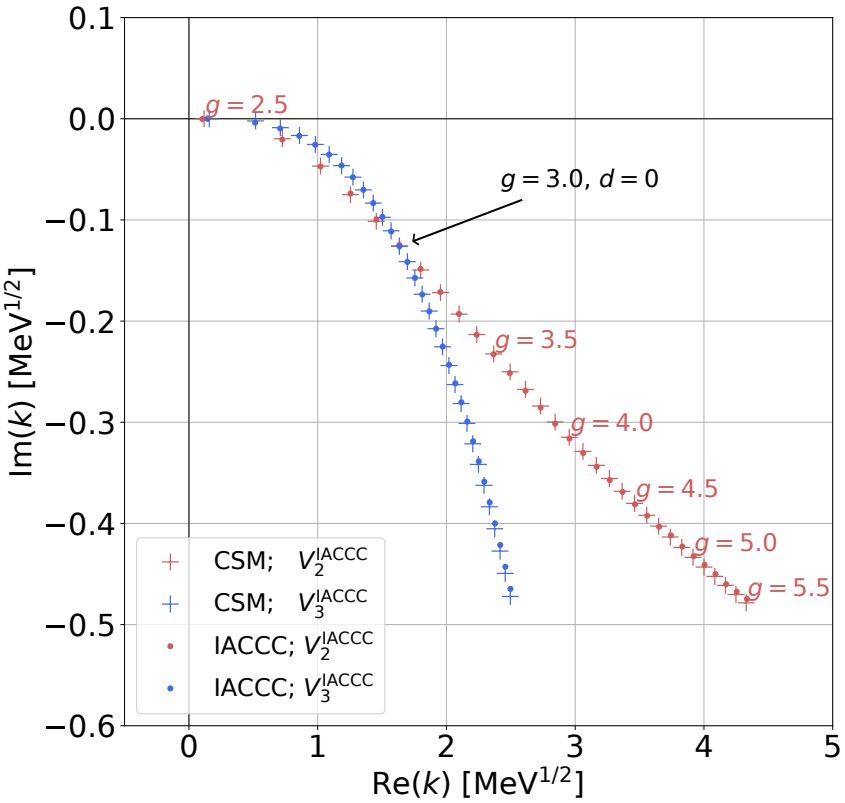

Figure C.3: Calculated 1+1+1 resonance positions for two different cases - V_2^{IACCC} (red) and V_3^{IACCC} (blue). For V_2^{IACCC} we show IACCC solutions (dots) corresponding to $d = 0$ (no auxiliary potential (C.3)) and different parameter g (C.4), while for V_3^{IACCC} we present IACCC solutions corresponding to $g = 3$ (C.4) and different strength d (C.3). IACCC results are obtained using the Padé approximant (3.34) of degree (13,13). Each IACCC solution is benchmarked against the corresponding CSM resonance position calculated using the θ-trajectory technique for the same values of d and g (crosses). Resonance solutions are presented in the complex $k = \sqrt{E}$-plane where E is the complex energy.

and V_3^{IACCC} case and different values of g and d, respectively, in the complex $k = \sqrt{E}$ - plane. Here, we use the k-plane in order to compare our results to those in Ref. [235]. The IACCC results shown in the figure are calculated using the Padé approximant (3.34) of degree (12,12). Corresponding CSM solutions $k(\theta_{\mathrm{opt}})$, obtained using the θ-trajectory technique in the same way as for the previous 2+1 resonance calculation, are shown as well. Both the IACCC and CSM results agree remarkably well. Moreover, the comparison of the V_2^{IACCC} case with the previous work [235] (see Fig. 3 in the paper) shows agreement for all V_2^{IACCC} resonant solutions with different g. We see that for $g = 3$, $d = 0$ both V_2^{IACCC} and V_3^{IACCC} IACCC calculations yield the same resonance position.

Detailed results for the 1+1+1 resonance position corresponding to $g = 3$, $d = 0$ are presented for both V_2^{IACCC} and V_3^{IACCC} cases in Table C.6. Here, we show comparison between the IACCC and ACCC methods as well as stability of their solutions with respect to increasing degrees (M, N) of the Padé approximant. We also give our result of the true CSM solution k(CSM) obtained using the β-trajectory technique in the same way as for the previous 2+1 resonance calculation. We see that all considered methods - IACCC, ACCC, and CSM yield remarkably close, mutually consistent predictions of the resonance position.

Table C.6: Stability of the 1+1+1 resonance solution obtained using either the IACCC or ACCC method with respect to increasing degree (M, N) of Padé approximant. Presented resonance solutions correspond to a situation with $d = 0$ (i.e. no auxiliary potential (C.3)) and the size of the two-body potential parameter $g = 3$ (see Eq. (C.4)). V_2^{IACCC} stands for the set of solutions obtained by performing analytical continuation in g, while V_3^{IACCC} resonance solutions are calculated using analytical continuation in d. The true CSM solution k(CSM) is shown for comparison. All resonance solutions are presented as $k = \sqrt{E}$ where E is the resonance energy. All results are given in $\mathrm{MeV}^{1/2}$.

(M, N)	k(IACCC, V_2^{IACCC})	k(ACCC, V_2^{IACCC})
(7,7)	1.6355 - i0.1241	1.6366 - i0.1249
(8,8)	1.6351 - i0.1244	1.6360 - i0.1248
(9,9)	1.6354 - i0.1241	1.6366 - i0.1246
(10,10)	1.6349 - i0.1245	1.6359 - i0.1247
(11,11)	1.6346 - i0.1248	1.6354 - i0.1249
(12,12)	1.6351 - i0.1242	1.6350 - i0.1253
(13,13)	1.6356 - i0.1242	1.6342 - i0.1259
(M, N)	k(IACCC, V_3^{IACCC})	k(ACCC, V_3^{IACCC})
(7,7)	1.6351 - i0.1262	1.6344 - i0.1256
(8,8)	1.6352 - i0.1266	1.6348 - i0.1261
(9,9)	1.6350 - i0.1262	1.6344 - i0.1258
(10,10)	1.6356 - i0.1268	1.6354 - i0.1265
(11,11)	1.6347 - i0.1253	1.6318 - i0.1244
(12,12)	1.6353 - i0.1267	1.6356 - i0.1293
(13,13)	1.6348 - i0.1258	1.6357 - i0.1235
k(CSM) = 1.6349(5) - i0.1253(5)		

Appendix D

Selected Publications

EPJ Web of Conferences **181**, 01011 (2018) https://doi.org/10.1051/epjconf/201818101011
EXA2017

Onset of η nuclear binding

Nir Barnea[1], *Betzalel* Bazak[1], *Eliahu* Friedman[1], *Avraham* Gal[1,⋆]
Aleš Cieplý[2], *Jiří* Mareš[2], and *Martin* Schäfer[2]

[1] *Racah Institute of Physics, the Hebrew University, Jerusalem 91904, Israel*
[2] *Nuclear Physics Institute, 250 69 Rez, Czech Republic*

Abstract. Recent studies of η nuclear quasibound states by the Jerusalem-Prague Collaboration are reviewed, focusing on stochastic variational method self consistent calculations of η few-nucleon systems. These calculations suggest that a minimum value $\mathrm{Re}\, a_{\eta N} \approx 1$ fm (0.7 fm) is needed to bind $\eta\,^3$He ($\eta\,^4$He).

1 Introduction

The ηN near-threshold interaction is attractive, owing to the $N^*(1535)$ resonance to which the s-wave ηN system is coupled strongly [1]. This has been confirmed in chiral meson-baryon coupled channel models that generate the $N^*(1535)$ dynamically, e.g. [2]. Hence η nuclear quasibound states may exist [3] as also suggested experimentally by the near-threshold strong energy dependence of the $\eta\,^3$He production cross sections shown in Fig. 1. However, the $\eta\,^3$He scattering length deduced in Ref. [4], $a_{\eta\,^3\mathrm{He}} = [-(2.23 \pm 1.29) + i(4.89 \pm 0.57)]$ fm, although of the right sign of its real part, does not satisfy the other necessary condition for a quasibound state pole: $-\mathrm{Re}\, a > \mathrm{Im}\, a$.

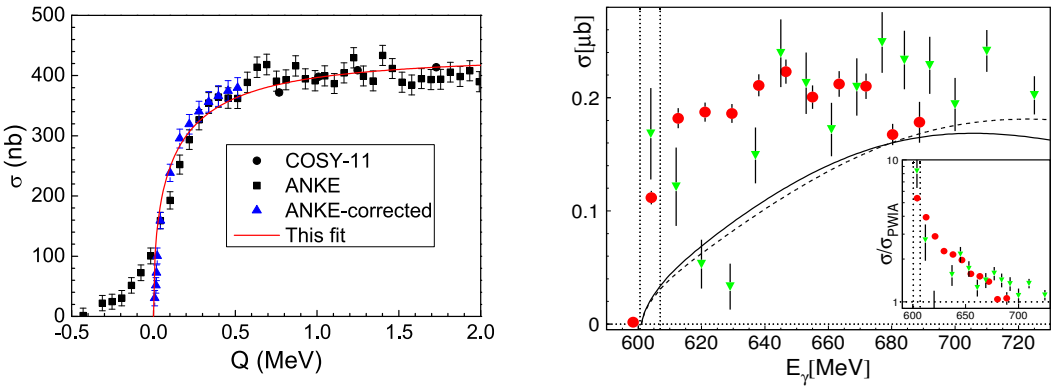

Figure 1. Near-threshold $\eta\,^3$He production cross sections. Left: $dp \to \eta\,^3$He [4]. Right: $\gamma\,^3$He $\to \eta\,^3$He [5].

⋆ Presented by A. Gal (avragal@savion.huji.ac.il) at EXA2017, Vienna, Sept. 2017

Quite generally, experimental searches for η nuclear quasibound states in proton, pion or photon induced η production reactions are inconclusive. Regarding the onset of η nuclear binding, Krusche and Wilkin [6] state: "The most straightforward (but not unique) interpretation of the data is that ηd is unbound, $\eta\,^4$He is bound, but that the $\eta\,^3$He case is ambiguous." Indeed, with $\eta\,^3$He almost bound, one might expect that the denser ^{4}He nucleus should help forming a bound $\eta\,^4$He. Nevertheless, a recent Faddeev-Yakubovsky evaluation [7] of the scattering lengths $a_{\eta\,^A\mathrm{He}}$ for both He isotopes, $A = 3, 4$, finds this not to be the case, with the denser ^{4}He apparently leading to a stronger reduction of the subthreshold ηN scattering amplitude than in ^{3}He.

The present overview reports and discusses recent few-body stochastic variational method (SVM) calculations of ηNNN and $\eta NNNN$ using several semi-realistic NN interaction models together with two ηN interaction models that, perhaps, provide sufficient attraction to bind η in the ^{3}He and ^{4}He isotopes [8–10].

2 ηN and NN interaction model input

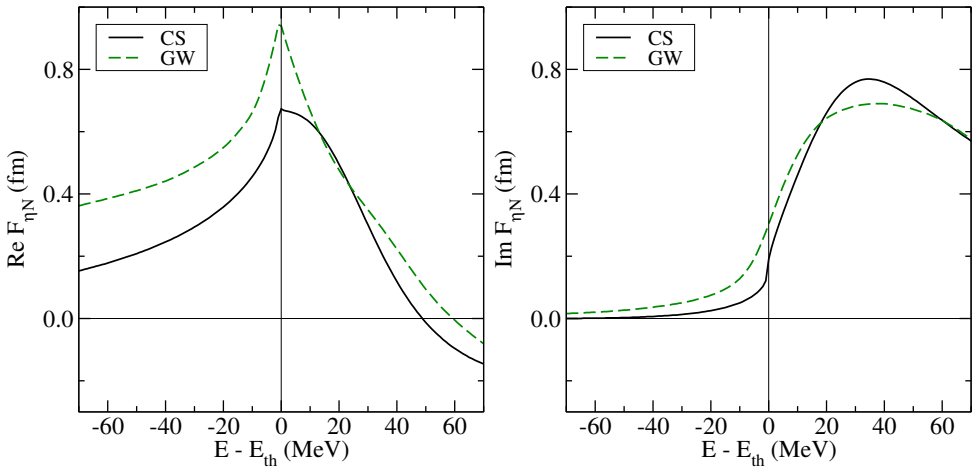

Figure 2. Real and imaginary parts of the ηN cm scattering amplitude near threshold in two meson-baryon coupled channel models: GW [11] and CS [12].

Figure 2 shows ηN s-wave scattering amplitudes $F_{\eta N}(E)$ calculated in two meson-baryon coupled-channel models across the ηN threshold where Re $F_{\eta N}$ has a cusp. These amplitudes exhibit a resonance about 50 MeV above threshold, the $N^*(1535)$. The sign of Re $F_{\eta N}$ below the resonance indicates attraction which is far too weak to bind the ηN two-body system. The threshold values $F_{\eta N}(E_{\rm th})$ are given by the scattering lengths

$$a_{\eta N}^{\rm GW} = (0.96 + i0.26)\ \text{fm}, \quad a_{\eta N}^{\rm CS} = (0.67 + i0.20)\ \text{fm}, \tag{1}$$

with lower values below threshold ($E_{\rm th} = 1487$ MeV). These free-space energy dependent subthreshold amplitudes are transformed to in-medium density dependent amplitudes, in terms of which optical potentials $V_\eta^{\rm opt}(\rho)$ are constructed and used to calculate self consistently η nuclear quasibound states. This procedure was applied in Refs. [13, 14] to several ηN amplitude models, with results for $1s_\eta$ quasibound states in models GW and CS shown in Fig. 3 from ^{12}C to ^{208}Pb.

Figure 3 demonstrates that in both of these ηN amplitude models the $1s_\eta$ binding energy increases with A, saturating in heavy nuclei. Model GW, with larger ηN real and imaginary subthreshold amplitudes than in model CS, gives correspondingly larger values of B_η and Γ_η. While model GW binds

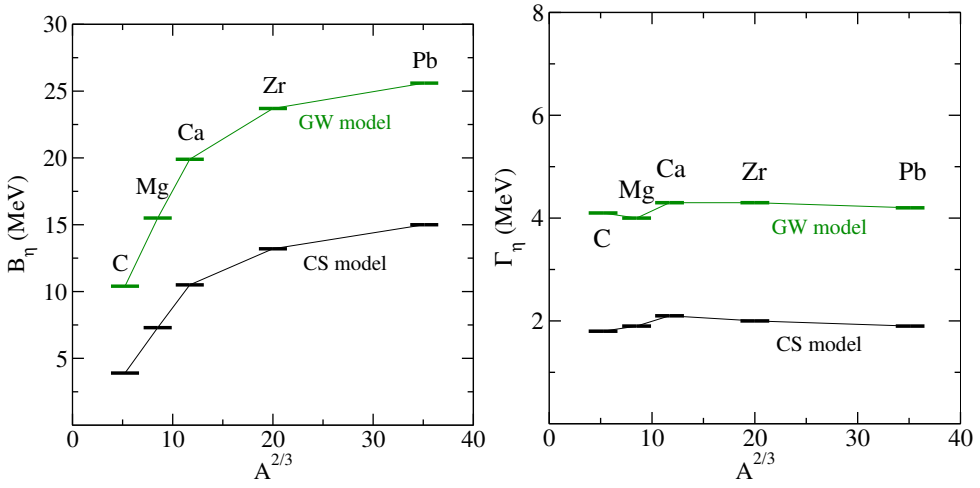

Figure 3. Binding energies B_η (left) and widths Γ_η (right) of $1s_\eta$ quasibound states across the periodic table calculated self consistently [13, 14] using the GW and CS ηN scattering amplitudes of Fig. 2.

η also in nuclei lighter than ^{12}C (not shown in the figure) this needs to be confirmed in few-body calculations.

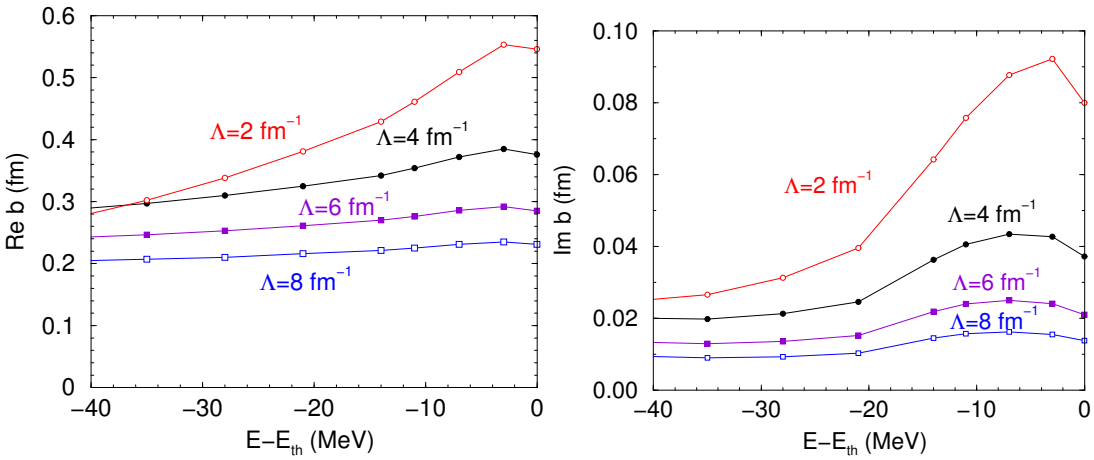

Figure 4. Real and imaginary parts of the strength function $b_\Lambda(E)$ of the effective ηN potential $v^{\rm GW}_{\eta N}(E)$, Eq. (2), obtained from the scattering amplitude $F^{\rm GW}_{\eta N}(E)$ of Fig. 2 below threshold for four values of the scale Λ [9].

Few-body calculations, in distinction from optical model calculations, require the use of effective ηN potentials $v_{\eta N}$ which reproduce the free-space ηN amplitudes below threshold. Fig. 4 shows subthreshold values of the energy dependent strength function $b_\Lambda(E)$ for $v_{\eta N}$ of the form

$$v_{\eta N}(E;r) = -\frac{4\pi}{2\mu_{\eta N}} b_\Lambda(E)\delta_\Lambda(r), \qquad \delta_\Lambda(r) = \left(\frac{\Lambda}{2\sqrt{\pi}}\right)^3 \exp\left(-\frac{\Lambda^2 r^2}{4}\right), \tag{2}$$

derived from the scattering amplitude $F^{\rm GW}_{\eta N}(E)$ of Fig. 2 for several choices of inverse range Λ. The normalized Gaussian function $\delta_\Lambda(r)$ is perceived in $\not\pi$EFT (pionless EFT) as a single ηN zero-range

Dirac $\delta^{(3)}(\mathbf{r})$ contact term (CT), regulated by using a momentum-space scale parameter Λ. Regarding the choice of Λ, substituting the underlying short range vector-meson exchange dynamics by a single regulated CT suggests that the scale Λ is limited to values $\Lambda \lesssim m_\rho$ (~4 fm^{-1}).

Similarly, a $\not\pi$EFT energy independent $v_{NN}(r)$ is derived at leading order (LO) by fitting a single regulated CT $\sim \delta_\Lambda(r)$ in each spin-isospin s-wave channel to the respective NN scattering length. A pp Coulomb interaction is included. To avoid NNN and ηNN Thomas collapse in the limit $\Lambda \to \infty$, one introduces a three-body regulated CT for each of these three-body systems [9]:

$$V_{NNN}(r_{ij}, r_{jk}) = d^\Lambda_{NNN}\, \delta_\Lambda(r_{ij}, r_{jk}), \qquad V_{\eta NN}(r_{i\eta}, r_{\eta j}) = d^\Lambda_{\eta NN}\, \delta_\Lambda(r_{i\eta}, r_{\eta j}), \tag{3}$$

where $\delta_\Lambda(r_{ij}, r_{jk}) = \delta_\Lambda(r_{ij})\delta_\Lambda(r_{jk})$. The three-nucleon CT d^Λ_{NNN} is fitted to $B_{\rm exp}(^3{\rm He})$. With no further contact terms, $B_{\rm calc}(^4{\rm He})$ is found in this $\not\pi$EFT version [15] to vary moderately with Λ and to exhibit renormalization scale invariance by approaching a finite value $B_{\Lambda\to\infty}(^4{\rm He})$=27.8±0.2 MeV that compares well with $B_{\rm exp}(^4{\rm He})$=28.3 MeV. In contrast, no η-related experimental datum is available for the ηNN CT $d^\Lambda_{\eta NN}$ to be fitted to. Two versions for choosing this CT were tested: (i) $d^\Lambda_{\eta NN} = d^\Lambda_{NNN}$, and (ii) setting $d^\Lambda_{\eta NN}$ so that ηd is just bound, i.e. $B_\eta(\eta d) = 0$. Added to $v^{\rm GW}_{\eta N}(E)$, one finds that each of these versions prevents a potential collapse of ηd, with calculated values of $B(\eta\,^A{\rm He})$ that for $\Lambda \geq 4$ fm^{-1} are nearly independent of the adopted version, as shown in Fig. 7 below.

3 Energy independent $\not\pi$EFT η nuclear few-body calculations

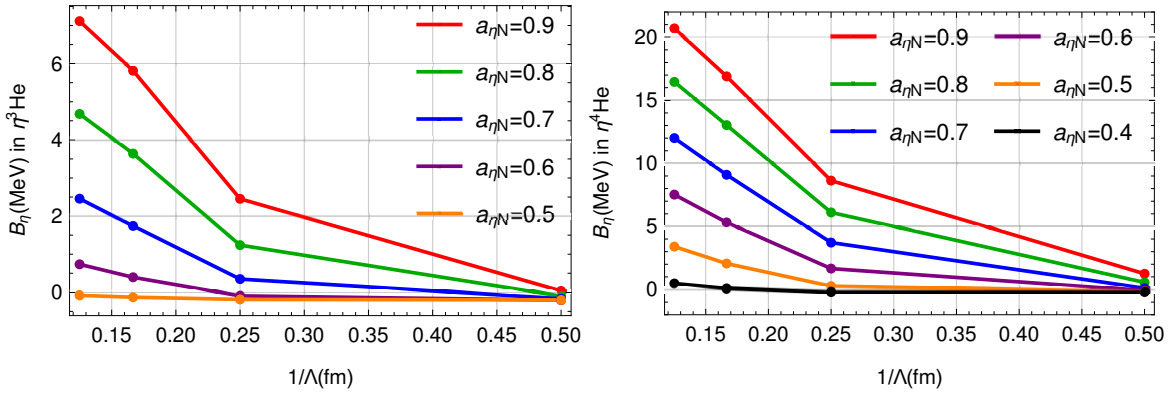

Figure 5. Separation energies B_η obtained in SVM calculations of $\eta\,^3$He (left) and $\eta\,^4$He (right) using $\not\pi$EFT NN and ηN real interactions (2) fitted to values of $a_{\eta N} < 1$ fm, plus a universal NNN and ηNN three-body CT (3), $d^\Lambda_{\eta NN} = d^\Lambda_{NNN}$, as a function of $1/\Lambda$.

Fig. 5 shows η separation energies B_η from $\not\pi$EFT SVM calculations of $\eta\,^3$He and $\eta\,^4$He using energy independent ηN potentials $v_{\eta N}(E{=}E_{\rm th}; r)$ fitted to a given real values of $a_{\eta N}$ for a few values of Λ. The figure suggests that binding $\eta\,^3$He ($\eta\,^4$He) requires that $a_{\eta N} \geq 0.55$ fm (0.45 fm), compatible with an effective value Re $a'_{\eta N}$=0.48±0.05 fm derived for a nearly bound $\eta\,^3$He [4]. For input values of $a_{\eta N}$ higher than shown in the figure, beginning at $a_{\eta N}$≈1.2 fm, the calculated binding energies $B^{A=3,4}_\eta(\Lambda > 4$ fm$^{-1})$ diverge, apparently since ηd becomes bound then at Λ=4 fm^{-1} [8]. Qualitative arguments in support of this ηd onset-of-binding value of $a_{\eta N}$ are given here in Appendix A.

4 Energy dependence in η nuclear few-body systems

Having derived energy dependent ηN potentials $v_{\eta N}(E;r)$, see Eq. (2) and Fig. 4, a two-body subthreshold input energy $\delta\sqrt{s} \equiv E - E_{\rm th}$ needs to be chosen. However, $\delta\sqrt{s}$ is not conserved in the η nuclear few-body problem, so the best one can do is to require that this choice agrees with the expectation value $\langle\,\delta\sqrt{s}\,\rangle$ generated in solving the few-body problem, as given by [10]

$$\langle\delta\sqrt{s}\rangle = -\frac{B}{A} - \xi_N\frac{1}{A}\langle T_A\rangle + \frac{A-1}{A}\mathcal{E}_\eta - \xi_A\xi_\eta\left(\frac{A-1}{A}\right)^2\langle T_\eta\rangle. \tag{4}$$

Here $\xi_{N(\eta)} = m_{N(\eta)}/(m_N + m_\eta)$, $\xi_A = Am_N/(Am_N + m_\eta)$, T_A and T_η denote the nuclear and η kinetic energy operators in appropriate Jacobi coordinates, B is the total binding energy, and $\mathcal{E}_\eta = \langle H - H_N\rangle$ with each Hamiltonian defined in its own cm frame. Self consistency (SC), $\langle\,\delta\sqrt{s}\,\rangle = \delta\sqrt{s}$, is imposed in our calculations, as demonstrated graphically in Fig. 6 (left). Applications of SC to meson-nuclear systems are reviewed in Ref. [16]. For recent K^--atom and nuclear applications see Refs. [17, 18]. More recently, Hoshino et al. [19] argued in a K^-d study that by applying this procedure one violates the requirement of total momentum conservation. In Appendix B here we show specifically for $A = 2$ that our choice of SC Eq. (4) is not in conflict with any conservation law.

Finally, we note that Eq. (4) in the limit $A >> 1$ coincides with the optical model downward energy shift (supplemented by a Coulomb term) used in recent K^- atom and nuclear studies [17, 18]:

$$\langle\delta\sqrt{s}\rangle = -B_N\frac{\rho}{\bar{\rho}} - \xi_N B_\eta\frac{\rho}{\rho_0} - \xi_N T_N\left(\frac{\rho}{\bar{\rho}}\right)^{2/3} + \xi_\eta \mathrm{Re}\,V_\eta^{\rm opt}(\delta\sqrt{s}), \tag{5}$$

where $T_N = \langle T_A\rangle/A = 23.0$ MeV at the average nuclear density $\bar{\rho}$, $B_N = B_{\rm nuc}/A \approx 8.5$ MeV is an average nucleon binding energy and B_η denotes the calculated η separation energy. All terms here are negative, thereby leading to a downward energy shift.

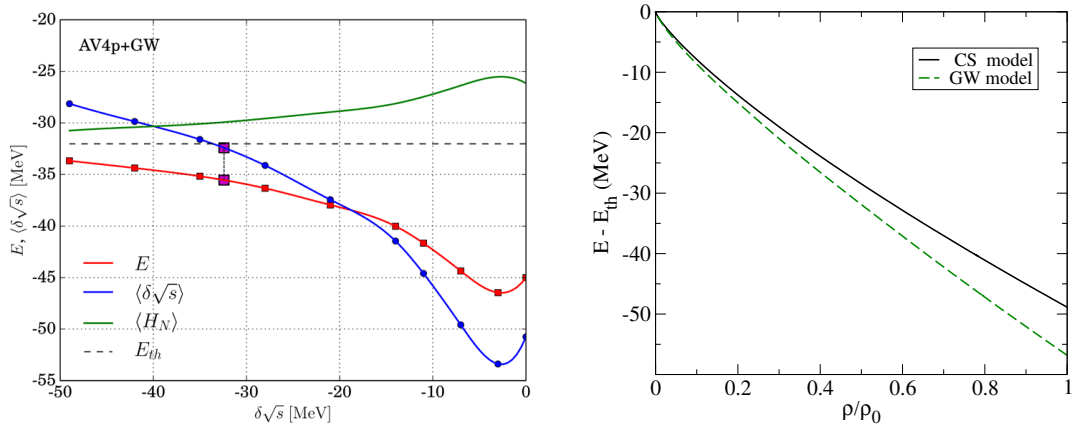

Figure 6. Left: $\eta\,^4$He bound state energy E (red, squares) and the expectation value $\langle\delta\sqrt{s}\rangle$ (blue, circles), calculated using the AV4' NN potential (denoted here AV4p), as a function of the input energy argument $\delta\sqrt{s}$ of the GW ηN potential with $\Lambda = 4$ fm^{-1}. The dotted vertical line marks the self consistent output values of $\langle\delta\sqrt{s}\rangle$ and E. The horizontal dashed line denotes the calculated ^{4}He g.s. energy, marking the threshold of η binding. The green curve shows the expectation value $< H_N >$ of the nuclear core energy. Right: subthreshold ηN energies $\delta\sqrt{s} = E - E_{\rm th}$ probed by the η nuclear optical potential as a function of the relative nuclear RMF density in Ca. Each of the two curves was calculated self consistently for a particular ηN subthreshold amplitude model.

The SC procedure is demonstrated in Fig. 6 (left) for $\eta\,^4$He binding energy calculated using the AV4' NN potential and GW ηN potential with Λ=4 fm^{-1}. The $\eta\,^4$He bound state energy E (excluding rest masses) and the output expectation value $\langle\delta\sqrt{s}\rangle$, where $\delta\sqrt{s}$ stands for the ηN cm energy with respect to its threshold value $E_{\rm th}$, are plotted as a function of the subthreshold input energy argument $\delta\sqrt{s}$ of the potential $v_{\eta N}^{\rm GW}$. The SC condition requires $\delta\sqrt{s} = \langle\delta\sqrt{s}\rangle$ which is satisfied at -32.4 MeV. The corresponding value of $E(\langle\delta\sqrt{s}\rangle)$ then represents the SC energy of $\eta\,^4$He, with $B_\eta^{\rm SC} = 3.5$ MeV, considerably less than the value $B_\eta^{\rm th} = 13$ MeV obtained by disregarding the energy dependence of $v_{\eta N}^{\rm GW}$ and using its threshold value corresponding to $\delta\sqrt{s} = 0$.

In Fig. 6 (right) we present the ηN downward energy shift $\delta\sqrt{s} = E - E_{\rm th}$ as a function of the relative nuclear density ρ/ρ_0 in Ca, evaluated self consistently via Eq. (5) in the CS and GW models. The energy shift at ρ_0 is -55 ± 10 MeV, about twice larger than the SC condition $\delta\sqrt{s} = -B_\eta$ applied in some other works, e.g. [20]. The GW shift exceeds the CS shift owing to the stronger GW amplitude of Fig. 2 and both were incorporated in the calculation of $1s_\eta$ quasibound nuclear states, Fig. 3.

5 Results of η nuclear few-body calculations

Our fully self consistent ηNN, ηNNN and $\eta NNNN$ bound-state calculations [8–10] use the following nuclear core models: (i) $\not\pi$EFT including a three-body contact term [15], (ii) AV4p, a Gaussian basis adaptation of the Argonne AV4' NN potential [21], and (iii) MNC, the Minnesota soft core NN potential [22]. Models GW [11] and CS [12] were used to generate energy dependent ηN potentials which prove too weak to bind any ηNN system when using AV4p or MNC for the nuclear core model. Calculated η separation energies B_η are shown in Figs. 7 and 8.

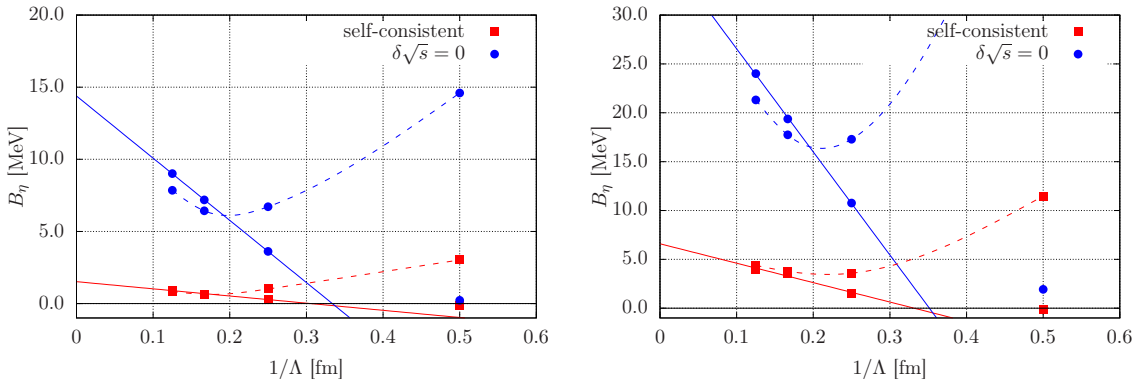

Figure 7. $B_\eta(\eta\,^3\mathrm{He})$ (left) and $B_\eta(\eta\,^4\mathrm{He})$ (right) as a function of $1/\Lambda$ from $\not\pi$EFT few-body calculations [9] using $v_{\eta N}^{\rm GW}$, with (squares) & without (circles) imposing self consistency. Solid lines: $d_{\eta NN}^\Lambda = d_{NNN}^\Lambda$, dashed lines: $d_{\eta NN}^\Lambda$ ensuring that $B_\eta(\eta d) = 0$.

Fig. 7 demonstrates in $\not\pi$EFT the moderating effect that imposing SC (red, squares) by using $v_{\eta N}^{\rm GW}(E_{\rm sc})$, rather than using threshold values $v_{\eta N}^{\rm GW}(E_{\rm th})$ (blue, circles), bears on the calculated B_η values and their Λ scale dependence [9]. Near Λ=4 fm^{-1}, imposing sc lowers $B_\eta(\eta\,^3\mathrm{He})$ by close to 5 MeV and $B_\eta(\eta\,^4\mathrm{He})$ by close to 10 MeV. The figure demonstrates that $B_\eta(\eta\,^4\mathrm{He})$ is always larger than $B_\eta(\eta\,^3\mathrm{He})$. Focusing on scale parameters near Λ=4 fm^{-1} one observes that $\eta\,^3$He is hardly bound by a fraction of MeV, whereas $\eta\,^4$He is bound by a few MeV. The choice of three-body CT $d_{\eta NN}^\Lambda$ hardly matters for $\Lambda > 4$ fm^{-1}, becoming substantial at $\Lambda < 4$ fm^{-1}.

Fig. 8 demonstrates in non-EFT calculations the dependence of B_η, calculated self consistently, on the choice of NN and ηN interaction models. Using the more realistic AV4' NN interaction results in less η binding than using the soft-core MNC NN interaction. For $v_{\eta N}^{\rm GW}$ near Λ=4 fm^{-1} the difference amounts to about 0.3 MeV for $\eta\,^3$He and about 1.5 MeV for $\eta\,^4$He; $\eta\,^3$He appears then barely bound whereas $\eta\,^4$He is bound by a few MeV. The weaker $v_{\eta N}^{\rm CS}$ does not bind $\eta\,^3$He and barely binds $\eta\,^4$He using the MNC NN interaction, implying that $\eta\,^4$He is unlikely to bind for the more realistic AV4' NN interaction. For smaller, but still physically acceptable values of Λ down to Λ = 2 fm^{-1}, $\eta\,^3$He becomes unbound and $\eta\,^4$He is barely bound using the AV4' NN and GW ηN interactions.

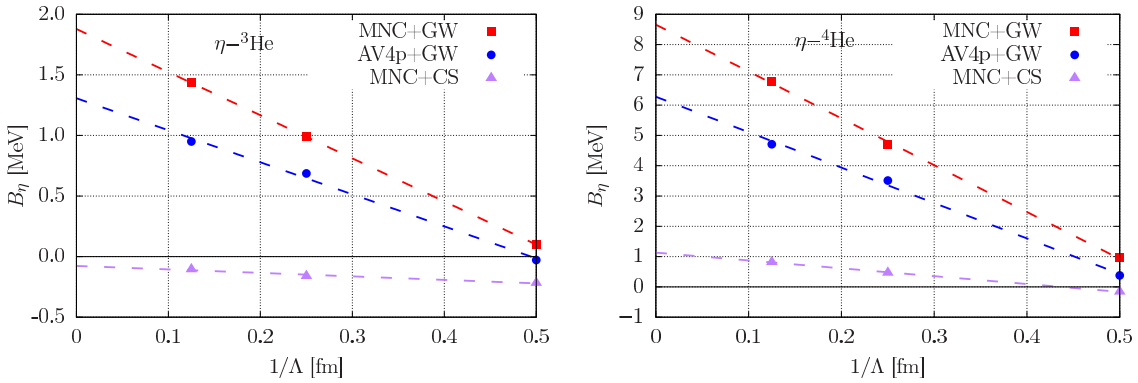

Figure 8. $B_\eta(\eta\,^3\mathrm{He})$ (left) and $B_\eta(\eta\,^4\mathrm{He})$ (right) as a function of $1/\Lambda$ from few-body calculations [10] using NN and ηN interactions, as marked, and imposing self consistency.

The B_η values calculated in Refs. [8–10] were calculated assuming real Hamiltonians, justified by Im $v_{\eta N} \ll$ Re $v_{\eta N}$ from Fig. 4. This approximation is estimated to add near threshold less than 0.3 MeV to B_η. Perturbatively-calculated widths Γ_η of weakly bound states amount to only few MeV, outdating those reported in Ref. [8].

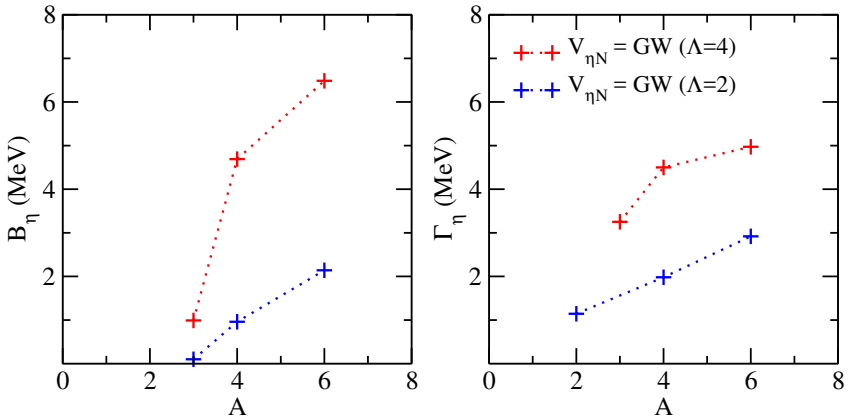

Figure 9. Preliminary SVM results for binding energies B_η (left) and widths Γ_η (right) of $1s_\eta$ quasibound states in ^{3}He, ^{4}He and ^{6}Li, calcualted using the Minnesota NN potential and the GW ηN potential for Λ = 2 and 4 fm^{-1}.

In future work it will be interesting to extend the present SVM few-body calculations to heavier nuclei, beginning with light p-shell nuclei. This represents highly non-trivial task. In Fig. 9 we

present preliminary results for $\eta\,^6$Li, using the central Minnesota NN and GW ηN potentials. In this calculation the ^{6}Li nuclear core consisted of a single $S = 1, T = 0$ spin-isospin configuration, yielding $B(^6\text{Li})$=34.66 MeV which is short by almost 2 MeV with respect to a calculation reported in Ref. [24] that used the same NN interaction while including more spin-isospin configurations. The figure suggests that $\eta\,^6$Li is comfortably bound, even for as low value of scale parameter as $\Lambda = 2$ fm^{-1}.

6 Summary

Based mostly on the AV4' results in Fig. 8, which are close to the $\not\pi$EFT results in Fig. 7, we conclude that $\eta\,^3$He becomes bound for $\mathrm{Re}\,a_{\eta N} \sim 1$ fm, as in model GW, while $\eta\,^4$He binding requires a lower value of $\mathrm{Re}\,a_{\eta N} \sim 0.7$ fm, almost reached in model CS. These $\mathrm{Re}\,a_{\eta N}$ onset values, obtained by incorporating the requirements of ηN subthreshold kinematics, are obviously *larger* than those estimated in Sect. 3 upon calculating with $v_{\eta N}(E = E_{\rm th}; r)$ threshold input. Finally, $\mathrm{Re}\,a_{\eta N} < 0.7$ fm if $\eta\,^4$He is unbound, as might be deduced from the recent WASA-at-COSY search [23].

Appendix A: Onset of ηd binding

Here we apply the Brueckner formula [25], expressing the ηd scattering length in terms of the ηN scattering length, to discuss qualitatively the onset of ηd binding. This formula was originally proposed for a system of a light meson (π meson) and two heavy static nucleons. More recently it was used to estimate the K^-d scattering length (see derivation and discussion in Ref. [26]) where the meson-nucleon mass ratio is similar to that for ηN. For ηd the Brueckner formula assumes the form

$$a_{\eta d} = \int a_{\eta d}(r)|\psi_d(\mathbf{r})|^2 \mathrm{d}\mathbf{r}\,, \tag{6}$$

$$a_{\eta d}(r) = \left(1 + \frac{m_\eta}{m_d}\right)^{-1} \frac{\tilde{a}_p + \tilde{a}_n + 2\tilde{a}_p\tilde{a}_n/r}{1 - \tilde{a}_p\tilde{a}_n/r^2}\,, \tag{7}$$

where $\tilde{a} = (1 + m_\eta/m_N)a$, with a_p and a_n standing for $a_{\eta p}$ and $a_{\eta n}$ respectively in the ηN cm system. The numerator in the Brueckner formula consists of single- and double-scattering terms, whereas the denominator provides for the renormalization of these terms by higher-order scattering terms. Since $a_p = a_n$ for the isoscalar η meson, Eq. (7) reduces to a simpler form,

$$a_{\eta d}(r) = \frac{2}{1 + \frac{m_\eta}{m_d}} \frac{\tilde{a}_{\eta N}}{1 - \tilde{a}_{\eta N}/r}\,, \tag{8}$$

which leads to the following approximate expression:

$$a_{\eta d} = \frac{2}{1 + \frac{m_\eta}{m_d}} \frac{\tilde{a}_{\eta N}}{1 - \tilde{a}_{\eta N}\langle 1/r\rangle_d}\,, \tag{9}$$

with expansion parameter $\tilde{a}\,\langle 1/r\rangle_d$, where $\langle 1/r\rangle_d \approx 0.45$ fm^{-1} for a realistic deuteron wavefunction [27]. Hence, this multiple scattering series faces divergence for sufficiently large ηN scattering length, say $a > 1.4$ fm.

Several straightforward applications of Eq. (9) are as follows:

- For $\mathrm{Re}\, a_{\eta N}^{\rm GW} = 0.96$ fm, suppressing $\mathrm{Im}\, a_{\eta N}^{\rm GW}$, one gets $a_{\eta d} = 7.46$ fm. Increasing this GW input value of $a_{\eta N}$, a critical value $a_{\eta N}^{\rm crit} = 1.40$ fm is reached at which the denominator in Eq. (9) vanishes, signaling the appearance of a zero-energy ηd bound state.
- The LO $\not\pi$EFT nuclear calculations [15] yield a more compact deuteron, $r_{\rm rms} = 1.55$ fm for $\Lambda \to \infty$ compared to the 'experimental' value $r_{\rm rms} = 1.97$ fm. Scaling the value $\langle 1/r \rangle_d = 0.45$ used in Eq. (9) by 1.97/1.55, one gets $a_{\eta d} = 18.1$ fm and $a_{\eta N}^{\rm crit} = 1.10$ fm.
- For the fully complex scattering length $a_{\eta N}^{\rm GW} = 0.96 + i0.26$ fm, one gets $a_{\eta d} = 4.66 + i4.76$ fm. Increasing $\mathrm{Re}\, a_{\eta N}$ at a frozen value of $\mathrm{Im}\, a_{\eta N}$, $\mathrm{Re}\, a_{\eta d}$ reverses its sign at $\mathrm{Re}\, a_{\eta N}^{\rm crit} = 1.35$ fm while $\mathrm{Im}\, a_{\eta d}$ keeps positive all through.
- At $\mathrm{Re}\, a_{\eta N}^{\rm crit} = 1.59$ fm, $|\mathrm{Re}\, a_{\eta d}|$ becomes larger than $\mathrm{Im}\, a_{\eta d}$, which signals a threshold ηd bound state.

Appendix B: ηN subthreshold kinematics

Here we outline the choice of the ηN subthreshold energy shift $\delta\sqrt{s} \equiv \sqrt{s_{\eta N}} - (m_N + m_\eta)$ applied in our η nuclear few-body works [8–10], see Eq. (4), with emphasis on the three-body ηd system. Since the ηN effective potential $v_{\eta N}$ discussed in Sect. 2 is energy dependent, one needs to determine as consistently as possible a fixed *input* value $\delta\sqrt{s}$ at which $v_{\eta N}$ should enter the η nuclear few-body calculation. The two-body Mandelstam variable $\sqrt{s_{\eta N}} = \sqrt{(E_\eta + E_N)^2 - (\vec{p}_\eta + \vec{p}_N)^2}$ which reduces to $(E_\eta + E_N)$ in the ηN two-body cm system is not a conserved quantity in the η nuclear few-body problem since spectator nucleons move the interacting ηN two-body subsystem outside of its cm system. We proceed to evaluate the expectation value of *output* values of $\delta\sqrt{s}$, replacing $\sqrt{s_{\eta N}}$ by $(1/A)\sum_{i=1}^{A} \sqrt{(E_\eta + E_i)^2 - (\vec{p}_\eta + \vec{p}_i)^2}$ due to the antisymmetry of the nuclear wavefunction. Expanding about the ηN threshold, one gets in leading order of p^2

$$\langle\, \delta\sqrt{s}\,\rangle \approx \frac{1}{A}\,\langle \sum_{i=1}^{A}(\mathcal{E}_\eta + \mathcal{E}_i) - \sum_{i=1}^{A}\frac{(\vec{p}_\eta + \vec{p}_i)^2}{2(m_N + m_\eta)}\,\rangle, \tag{10}$$

where $\mathcal{E}_\eta = E_\eta - m_\eta$ and $\mathcal{E}_i = E_i - m_N$. Since $\sum_{i=1}^{A}\mathcal{E}_i$ is naturally identified with the expectation value of the nuclear Hamiltonian H_N, $\sum_{i=1}^{A}\mathcal{E}_i = \langle H_N\rangle = E_{\rm nuc} = -B_{\rm nuc}$, it is natural and also consistent to identify $\mathcal{E}_\eta$ with the expectation value of $(H - H_N)$, $\mathcal{E}_\eta = \langle H - H_N\rangle$. Furthermore, recalling that $\mathcal{E}_\eta + \sum_{i=1}^{A}\mathcal{E}_i = E = -B$, where $E = \langle H\rangle$ is the total η nuclear energy and B is the total binding energy, the sum over the momentum independent part in Eq. (10) gives $[-B + (A-1)\mathcal{E}_\eta]/A$, thereby reproducing two of the four terms in Eq. (4). Note that $\mathcal{E}_\eta$ is negative and its magnitude exceeds the η separation energy B_η. The sum over the momentum dependent part of Eq. (10) yields the other two terms of Eq. (4), which we demonstrate for ηd, $A = 2$.

Since the ηd calculation employes translationally invariant coordinate sets, the total momentum vanishes sharply: $(\vec{p}_\eta + \vec{p}_1 + \vec{p}_2) = 0$. We then substitute $\vec{p}_1^{\,2}$ for $(\vec{p}_\eta + \vec{p}_2)^2$ and $\vec{p}_2^{\,2}$ for $(\vec{p}_\eta + \vec{p}_1)^2$ in the momentum dependent part in Eq. (10), resulting in momentum dependence proportional to $\vec{p}_1^{\,2} + \vec{p}_2^{\,2}$. This is rewritten as

$$\vec{p}_1^{\,2} + \vec{p}_2^{\,2} = \frac{1}{2}[(\vec{p}_1 - \vec{p}_2)^2 + (\vec{p}_1 + \vec{p}_2)^2] = 2\vec{p}_{N:N}^{\,2} + \frac{1}{2}\vec{p}_\eta^{\,2}, \tag{11}$$

where $\vec{p}_{N:N}$ is the nucleon-nucleon relative momentum operator. To obtain the η momentum operator $\vec{p}_\eta$ on the r.h.s. we used again total momentum conservation. Finally, transforming $\vec{p}_{N:N}^{\,2}$ and $\vec{p}_\eta^{\,2}$ to

intrinsic kinetic energies, $T_{N:N}$ for the internal motion of the deuteron core and T_η for that of the η meson with respect to the NN cm, one gets for this $A = 2$ special case

$$\langle \delta \sqrt{s} \rangle_{\eta d} \approx -\frac{1}{2}\left(B - \mathcal{E}_\eta + \xi_N \langle T_{N:N}\rangle + \xi_{A=2}\xi_\eta \frac{1}{2}\langle T_\eta \rangle\right), \tag{12}$$

which agrees with Eq. (4) for $A = 2$ upon realizing that $T_{N:N}$ here coincides with $T_{A=2}$ there. To get idea of the relative importance of the various terms in this expression, we assume a near-threshold ηd bound state for which both $\mathcal{E}_\eta$ and $\langle T_\eta \rangle$ are negligible (fraction of MeV each) and $B \to B_d \approx 2.2$ MeV. With $\langle T_{N:N}\rangle \to \langle T_d \rangle$, and with a deuteron kinetic energy $\langle T_d \rangle$ in the range of 10 to 20 MeV, this term provides the largest contribution to the downward energy shift which is then of order −5 MeV for the diffuse deuteron nuclear core.

Acknowledgments

The work of A.C., J.M. and M.S. was supported by the GACR Grant No. P203/15/04301S.

References

[1] R.S. Bhalerao, L.C. Liu, Phys. Rev. Lett. **54**, 865 (1985)
[2] N. Kaiser, P.B. Siegel, W. Weise, Phys. Lett. B **362**, 23 (1995)
[3] Q. Haider, L.C. Liu, Phys. Lett. B **172**, 257 (1986)
[4] J.J. Xie, W.H. Liang, E. Oset, P. Moskal, M. Skurzok, C. Wilkin, Phys. Rev. C **95**, 015202 (2017)
[5] F. Pheron et al., Phys. Lett. B **709**, 21 (2012)
[6] B. Krusche, C. Wilkin, Prog. Part. Nucl. Phys. **80**, 43 (2015)
[7] A. Fix, O. Kolesnikov, Phys. Lett. B **772**, 663 (2017)
[8] N. Barnea, E. Friedman, A. Gal, Phys. Lett. B **747**, 345 (2015)
[9] N. Barnea, B. Bazak, E. Friedman, A. Gal, Phys. Lett. B **771**, 297 (2017), **775**, 364 (2017)
[10] N. Barnea, E. Friedman, A. Gal, Nucl. Phys. A **968**, 35 (2017)
[11] A.M. Green, S. Wycech, Phys. Rev. C **71**, 014001 (2005)
[12] A. Cieplý, J. Smejkal, Nucl. Phys. A **919**, 46 (2013)
[13] E. Friedman, A. Gal, J. Mareš, Phys. Lett. B **725** 334 (2013)
[14] A. Cieplý, E. Friedman, A. Gal, J. Mareš, Nucl. Phys. A **925**, 126 (2014)
[15] J. Kirscher, E. Pazy, J. Drachman, N. Barnea, Phys. Rev. C **96**, 024001 (2017)
[16] A. Gal, E. Friedman, N. Barnea, A. Cieplý, J. Mareš, D. Gazda, Acta Phys. Polon. B **45**, 673 (2014)
[17] E. Friedman, A. Gal, Nucl. Phys. A **959**, 66 (2017)
[18] J. Hrtánková, J. Mareš, Phys. Lett. B **770**, 342 (2017), Phys. Rev. C **96**, 015205 (2017)
[19] T. Hoshino, S. Ohnishi, W. Horiuchi, T. Hyodo, W. Weise, Phys. Rev. C **96**, 045204 (2017)
[20] C. García-Recio, T. Inoue, J. Nieves, E. Oset, Phys. Lett. B **550**, 47 (2002)
[21] R.B. Wiringa, S.C. Pieper, Phys. Rev. Lett. **89**, 182501 (2002)
[22] D.R. Thompson, M. LeMere, Y.C. Tang, Nucl. Phys. A **286**, 53 (1977)
[23] P. Adlarson, et al. (WASA-at-COSY Collab.), Nucl. Phys. A **959**, 102 (2017)
[24] P. Navrátil, E. Caurier, Phys. Rev. C **69**, 014311 (2004)
[25] K.A. Brueckner, Phys. Rev. **89**, 834 (1953)
[26] A. Gal, Int. J. Mod. Phys. A **22**, 226 (2007)
[27] M. Pavón Valderrama, E. Ruiz Arriola, arXiv:nucl-th/0605078

Calculations of η-nuclear quasi-bound states in few-body systems

M. Schäfer[1,2,*], N. Barnea[3], E. Friedman[3], A. Gal[3], and J. Mareš[2]

[1]Czech Technical University in Prague, Faculty of Nuclear Sciences and Physical Engineering, Břehová 7, 11519 Prague 1, Czech Republic
[2]Nuclear Physics Institute, Academy of Sciences of Czech Republic, 250 69 Řež, Czech Republic
[3]Racah Institute of Physics, The Hebrew University, Jerusalem 91904, Israel

Abstract. We report on our Stochastic Variational Method (SVM) calculations of η-nuclear quasi-bound states in s-shell nuclei as well as the very recent calculation of the p-shell nucleus ^{6}Li. The ηN potentials used were constructed from ηN scattering amplitudes obtained within coupled-channel models that incorporate $N^\star(1535)$ resonance. We found that η^6Li is bound in the ηN interaction models that yield Re$a_{\eta N} \geq 0.67$ fm. Additional repulsion caused by the imaginary part of ηN potentials shifts the onset of η-nuclear binding to η^4He, yielding very likely no quasi-bound state in η^3He.

1 Introduction

The current status of our theoretical studies of η-nuclear quasi-bound states, including discussion of the self-consistent treatment of the strong energy dependence of ηN scattering amplitudes derived from coupled-channel meson-baryon interaction models have been discussed thoroughly in Refs. [1–3]. So far, few-body calculations of η-nuclear quasi-bound states have been restricted to s-shell nuclei up to η^4He. In this contribution, we present our first SVM calculation of the η-nuclear quasi-bound state in the p-shell nuclear system η^6Li, taking into account all possible spin-isospin configurations. Moreover, we focus on the effect of the imaginary part of the complex $V_{\eta N}$ potential on the η binding energy B_η. We show that the effect could be considerable in light η-nuclear systems and must be taken into account in the study of the onset of η-nuclear binding.

2 Theoretical approach

Properties of η-nuclear quasi-bound states are studied within the SVM with a correlated Gaussian basis [4]. This approach was successfully applied in our previous calculations of s-shell η-nuclei and proved itself as highly accurate method with straightforward extension to systems with the number of particles $N \geq 5$.

The wave function of an η-nuclear system with orbital momentum $L = 0$ is expanded as a linear combination of correlated Gaussians

*e-mail: m.schafer@ujf.cas.cz

$$\Psi = \sum_k c_k \mathcal{A}\left\{\chi_S^k \xi_{TT_z}^k \exp\left(-\frac{1}{2}\mathbf{x}^T A_k \mathbf{x}\right)\right\}, \tag{1}$$

where $\mathbf{x}$ stands for Jacobi coordinates and χ_S^k ($\xi_{TT_z}^k$) are corresponding spin (isospin) parts of a given spin (isospin) configuration. The matrix A_k is symmetric positive definite and includes $N(N-1)/2$ variational parameters. The SVM optimizes the variational basis step-by-step in a random trial and error procedure (details can be found in Ref. [5]).

SVM calculations of η-nuclear quasi-bound states in p-shell nuclei represent a rather challenging task. First, the computational complexity scales with $N!$, second, the amount of different spin-isospin configurations starts to increase quite rapidly. Preliminary results [6] showed that taking into account only one configuration underestimated binding of the nuclear core ^{6}Li by approximately 1.8 MeV. This led to development of a new high-performance SVM code which was used in the very recent fully self-consistent calculation of η^6Li, taking into account all posible spin-isospin configurations.

In our study of η-nuclear quasi-bound states we use the Minnesota NN central potential [7] which reproduces well properties of the ground states of s-shell and light p-shell nuclei. The interaction of the η meson with nucleons is described by a complex two-body energy dependent effective potential derived from the coupled-channel meson-baryon interaction models GW [8] and CS [9]. The form of ηN potential is taken according to [1] as

$$V_{\eta N}(\delta\sqrt{s}, r) = -\frac{4\pi}{2\mu_{\eta N}} b(\delta\sqrt{s})\rho_\Lambda(r), \quad \rho_\Lambda(r) = \left(\frac{\Lambda}{2\sqrt{\pi}}\right)^3 \exp\left(-\frac{\Lambda^2 r^2}{4}\right), \tag{2}$$

where $\mu_{\eta N}$ stands for the ηN reduced mass, $\delta\sqrt{s} = \sqrt{s} - \sqrt{s_{th}}$ is the energy shift with respect to the ηN threshold, Λ is a scale parameter which is inversely proportional to the range of $V_{\eta N}$, and $b(\delta\sqrt{s})$ is an energy dependent complex amplitude.

The value of Λ is connected to EFT momentum cut-off; its upper bound corresponds to vector-meson exchange $\Lambda \leq 3.9\text{fm}^{-1}$ or more restrictively to $\Lambda \leq 3.0$ fm^{-1} excluding ρN channel from dynamical generation of the $N^\star(1535)$ resonance [3].

For given Λ, $b(\delta\sqrt{s})$ is fitted to the phase shifts derived from subthreshold $\delta\sqrt{s} < 0$ scattering amplitude of the corresponding ηN interaction model. See Ref. [3] for details.

The energy dependence of $V_{\eta N}$ is treated self-consistently: we search for a SVM solution that fulfills $\delta\sqrt{s_{sc}} = \left\langle \delta\sqrt{s_{sc}} \right\rangle$ where $\delta\sqrt{s}$ enters $V_{\eta N}$ and $\left\langle \delta\sqrt{s} \right\rangle$ is obtained from the SVM solution for a given value of $\delta\sqrt{s}$ [3]:

$$\left\langle \delta\sqrt{s} \right\rangle = -\frac{B}{A} - \xi_N \frac{1}{A}\langle T_N \rangle + \frac{A-1}{A} E_\eta - \xi_A \xi_\eta \left(\frac{A-1}{A}\right)^2 \left\langle T_\eta \right\rangle, \tag{3}$$

where B is the total binding energy, T_N (T_η) denotes the kinetic energy of nucleons (η), and A is the number of nucleons. The energy $E_\eta = \langle\psi| H - H_N |\psi\rangle$ where H_N is Hamiltonian of the nuclear core, $\xi_{N(\eta)} = m_{N(\eta)}/(m_N + m_\eta)$, and $\xi_A = Am_N/(Am_N + m_\eta)$.

The imaginary part of $V_{\eta N}$ is significantly smaller than its real part. This allows to calculate the width Γ_η perturbatively [1]. The SVM η-nuclear calculations are thus performed only for the real part of the ηN potential and Γ_η is evaluated using the expression

$$\Gamma_\eta = -2\left\langle \Psi_{g.s.} \middle| \,\mathrm{Im} V_{\eta N} \middle| \Psi_{g.s.} \right\rangle, \tag{4}$$

where $\left|\Psi_{g.s.}\right\rangle$ is the SVM solution for the η-nuclear ground state corresponding to Re$V_{\eta N}$. Another possible way how to calculate Γ_η is to solve a generalized eigenvalue problem for complex Hamiltonian (including Im$V_{\eta N}$) using variationally determined SVM basis states for Re$V_{\eta N}$. This approach, already used in SVM calculations of kaonic nuclei [10], yields complex eigenenergy of the ground state E = Re(E) + iIm(E) and consequently the width as $\Gamma_\eta = -2\mathrm{Im}(E)$. This method takes into account the effect of the non-zero imaginary part of $V_{\eta N}$ on the η binding energy. Namely, Im$V_{\eta N}$ acts as repulsion and thus makes the η meson less bound in the nucleus.

3 Results

Results of our SVM calculations of the η binding energies B_η and widths Γ_η in η^3He, η^4He, and η^6Li are summarized in Fig. 1. The calculations were performed using the GW and CS models and the parameter Λ = 2 and 4 fm^{-1}. In the GW model, η^6Li is rather comfortably bound for both values of Λ. On the other hand, the CS model yields η-nuclear quasi-bound state only for Λ = 4 fm^{-1}, with B_η = 0.68 MeV.

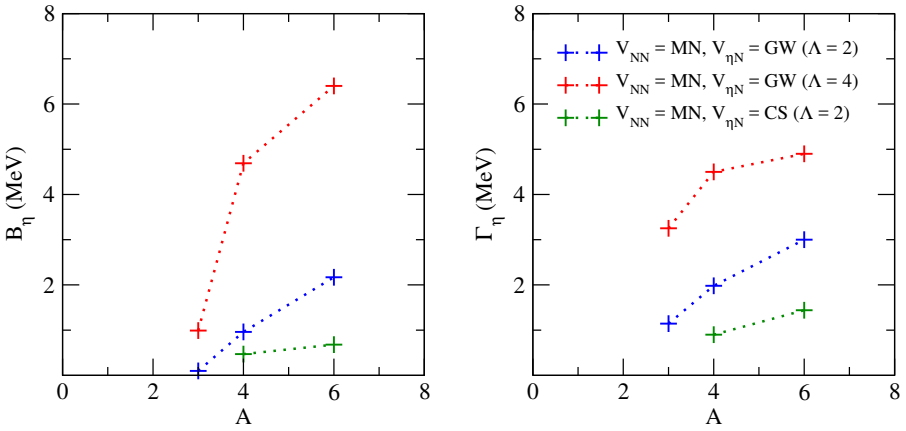

Figure 1. SVM calculations of the binding energy B_η and width Γ_η in η^3He, η^4He, and η^6Li using the Minnesota NN potential with Coulomb force included and two ηN interaction models - GW and CS.

Table 1. Comparison of self-consistent SVM calculations using two different width Γ_η evaluations - the mean-value approximation (Eq. 4) and the complex eigenvalue problem (cmplx) approach. Calculations were performed for the Minnesota NN potential with Coulomb force and the GW model. The η binding energy B_η and self-consistent energy $\delta\sqrt{s_{sc}}$ are shown as well.

η^3He		B$_\eta$ [MeV]	Γ_η [MeV]	$\delta\sqrt{s_{sc}}$ [MeV]
Λ = 2 fm^{-1}	(Eq. 4)	0.11	1.37	−9.23
	(cmplx)	−0.25	1.32	−8.87
Λ = 4 fm^{-1}	(Eq. 4)	1.01	3.32	−13.18
	(cmplx)	0.36	3.44	−12.72
η^4He		B$_\eta$ [MeV]	Γ_η [MeV]	$\delta\sqrt{s_{sc}}$ [MeV]
Λ = 2 fm^{-1}	(Eq. 4)	0.97	2.17	−19.64
	(cmplx)	0.77	2.22	−19.50
Λ = 4 fm^{-1}	(Eq. 4)	4.62	4.38	−29.73
	(cmplx)	4.40	4.41	−29.60

In Table 1, we compare two approaches to evaluation of the width Γ_η introduced in the previous section: the mean-value approach (Eq. 4) and the complex eigenvalue problem (cmplx) approach. Calculations of η^3He and η^4He were performed within the GW model with $\Lambda = 2$ and 4 fm^{-1}. It is apparent that the effect of the imaginary part of $V_{\eta N}$ on B_η, which is included in the cmplx approach, is quite significant in η^3He (with $\delta\sqrt{s}$ close to threshold) and decreases in η^4He with larger energy shift with respect to threshold. For the CS model (not shown in the table) the η^3He is not bound while in η^4He the effect of Im$V_{\eta N}$ is smaller (few tens of keV) due to the lower value of Im$V_{\eta N}$ than in the GW model. Table 1 illustrates that the size of the changes of B_η caused by Im$V_{\eta N}$ decreases with the magnitude of the subthreshold energy shift $\delta\sqrt{s}$. Namely, the strength of Im$V_{\eta N}$ has for both CS and GW interaction models maximum close to threshold and decreases with $\sqrt{s}$, as shown in Figure 2 of Ref. [3]. Moreover, the cmplx method confirms the estimate of Γ_η within the mean-value approach (Eq. 4), giving practically the same widths in all considered cases.

4 Summary

We performed few-body calculations of η-nuclear quasi-bound states in s-shell nuclei as well as in the p-shell nucleus ^{6}Li within our newly developed high-performance SVM code. We considered the Minnesota NN potential and two ηN interaction models - GW and CS. Calculations of η^6Li within the GW model yield the binding energy B_η and corresponding width consistent with previous RMF calculations [11]. The CS model gives quasi-bound state only for $\Lambda = 4$ fm^{-1}. This suggests that to bind η^6Li, the real part of the ηN scattering length should be greater than Re$a_{\eta N} = 0.67$ fm, predicted by the CS model.

Next, we repeated our previous study of the onset of η-nuclear binding in He isotopes taking into account the effect of Im$V_{\eta N}$ on the binding energy B_η. We observed considerable decrease of B_η in ${}^3_\eta$He and rather negligible effects in ${}^4_\eta$He as well as in ${}^6_\eta$Li. The η meson is barely bound in ${}^3_\eta$He even for the larger value of the cut-off parameter $\Lambda = 4$ fm^{-1}. This indicates that in order to study the η^3He system, one has to explore the resonance region as well, e.g., using the complex rotation method [12].

M. Schäfer acknowledges financial support from the CTU-SGS Grant No. SGS16/243/OHK4/3T/14 and from the organizers of the MESON2018 conference.

References

[1] N. Barnea, E. Friedman, A. Gal, Phys. Lett. **B 747**, 345 (2015)
[2] N. Barnea, B. Bazak, E. Friedman, A. Gal, Phys. Lett. **B 771**, 297 (2017); Erratum in Phys. Lett. **B 775**, 364 (2017)
[3] N. Barnea, E. Friedman, A. Gal, Nucl. Phys. **A 968**, 35 (2017)
[4] Y. Suzuki, K. Varga, Phys. Rev. **C 52**, 2885 (1995)
[5] Y. Suzuki, K. Varga, *Stochastic Variational Approach to Quantum-Mechanical Few-Body Problems* (Springer, Heidelberg, 1998)
[6] A. Cieplý, et al., PoS Hadron2017, 203 (2017)
[7] D. R. Thompson, M. LeMere, Y. C. Tang, Nucl. Phys. **A 286**, 53 (1977)
[8] A. M. Green, S. Wycech, Phys. Rev. **C 71**, 014001 (2005)
[9] A. Cieplý, J. Smejkal, Nucl. Phys. **A 919**, 334 (2013)
[10] S. Ohnishi *et al.*, Phys. Rev. **C 95**, 065202 (2017)
[11] A. Cieplý, E. Friedman, A. Gal, J. Mareš, Nucl. Phys. **A 925**, 126 (2014)
[12] J. Nutall, H. L. Cohen, Phys. Rev. **188**, 1542 (1969)

Physics Letters B 785 (2018) 90–94

Contents lists available at ScienceDirect

Physics Letters B

www.elsevier.com/locate/physletb

$\Lambda^*(1405)$-matter: Stable or unstable?

J. Hrtánková [a,b], N. Barnea [c], E. Friedman [c], A. Gal [c,*], J. Mareš [a], M. Schäfer [a,b]

[a] Nuclear Physics Institute, 25068 Řež, Czech Republic
[b] Faculty of Nuclear Sciences and Physical Engineering, Czech Technical University in Prague, 115 19 Prague 1, Czech Republic
[c] Racah Institute of Physics, The Hebrew University, 91904 Jerusalem, Israel

ARTICLE INFO

Article history:
Received 29 May 2018
Received in revised form 20 July 2018
Accepted 2 August 2018
Available online 24 August 2018
Editor: J. Hisano

Keywords:
Strange matter
$\Lambda^*(1405)$ resonance
Kaonic atoms
RMF

ABSTRACT

A recent suggestion by Akaishi and Yamazaki (2017) [3] that purely-$\Lambda^*(1405)$ nuclei provide the absolute minimum energy in charge-neutral baryon matter for baryon-number $A \gtrsim 8$, is tested within RMF calculations. A broad range of Λ^* interaction strengths, commensurate with $(\bar{K}\bar{K}NN)_{I=0}$ binding energy assumed to be of order 100 MeV, is scanned. It is found that the binding energy per Λ^*, B/A, saturates for $A \gtrsim 120$ with values of B/A considerably below 100 MeV, implying that $\Lambda^*(1405)$ matter is highly unstable against strong decay to Λ and Σ hyperon aggregates. The central density of Λ^* matter is found to saturate as well, at roughly twice nuclear matter density. Moreover, it is shown that the underlying very strong $\bar{K}N$ potentials, fitted for isospin $I = 0$ to the mass and width values of $\Lambda^*(1405)$, fail to reproduce values of single-nucleon absorption fractions deduced across the periodic table from K^- capture-at-rest bubble chamber experiments.

1. Introduction

Strangeness ($\mathcal{S}$) provides for extension of standard nuclear matter to strange matter in which SU(3)-octet hyperons (Λ, Σ, Ξ) may prove as abundant as nucleons [1]. Particularly interesting at present is the role of hyperons in the composition of the neutron star interior, the so called 'hyperon puzzle' [2]. Little is known about the possible role of higher-mass hyperons in hadronic matter. However, it was recently suggested by Akaishi and Yamazaki (AY) [3] that purely-$\Lambda^*(1405)$ aggregates become increasingly bound with the number $A = -\mathcal{S}$ of Λ^* constituents, reaching absolute stability for $A \gtrsim 8$. This suggestion for which we found no documented supporting calculations beyond $A = 2$ follows a similar conjecture made already in 2004 [4]. It is worth recalling that solving the A-body Schrödinger equation for purely attractive $\Lambda^*\Lambda^*$ interactions will necessarily lead to collapse, with the binding energy per Λ^*, B/A, and the central Λ^* density $\rho(r \approx 0)$ diverging as A increases. This immediately raises the question whether AY perhaps just overlooked this basic many-body aspect of the Schrödinger equation in asserting that purely-Λ^* matter becomes absolutely stable for some given value of A. Therefore the issue of stability has to be checked within calculational schemes that avoid many-body collapse. A commonly used approach in nuclear and hadronic physics that avoids collapse and provides sufficiently faithful reproduction of nuclear binding energies and densities is the Relativistic Mean Field (RMF) approach [5] which is used here.

In this Letter, we show within RMF calculations in which strongly attractive $\Lambda^*\Lambda^*$ interactions are generated through scalar meson (σ) and vector meson (ω) exchanges that both B/A, the Λ^*-matter binding energy per baryon, and the central density $\rho(r \approx 0)$ saturate for values of A of order $A \sim 100$. For the case considered here, B/A saturates at values between roughly 30 to 80 MeV, depending on details of the RMF modeling, and the associated central densities saturate at values about twice nuclear-matter density. This leaves Λ^* aggregates highly unstable against strong interaction decay governed by two-body conversion reactions such as $\Lambda^*\Lambda^* \to \Lambda\Lambda, \Sigma\Sigma$.

The plan of this note is as follows. In Sect. 2 we briefly review several few-body calculations of $\bar{K}$ nuclear quasibound states, including those based on energy independent strongly attractive $\bar{K}N$ potentials as advocated by AY, in order to introduce plausible input values for the $\Lambda^*\Lambda^*$ binding energy ($B_{\Lambda^*\Lambda^*}$) used to determine the strength of the scalar and vector meson-exchange couplings applied in our subsequent RMF calculations. In Sect. 3 we question the validity of such energy independent strongly attractive $\bar{K}N$ interactions by checking their ability to reproduce the single-nucleon absorption fractions deduced from K^- capture observations in bubble chamber experiments. RMF calculations of purely-Λ^* nuclei are reported in Sect. 4, showing clearly how B/A

* Corresponding author.
E-mail address: avragal@savion.huji.ac.il (A. Gal).

https://doi.org/10.1016/j.physletb.2018.08.031

Table 1
$(\bar{K}N)_{I=0}$, $(\bar{K}NN)_{I=1/2}$ and $(\bar{K}\bar{K}NN)_{I=0}$ binding energies B (in MeV) calculated using energy dependent (E-dep.) [9] and energy independent (E-indep.) [10] $\bar{K}N$ potentials. $(\bar{K}\bar{K}NN)_{I=0}$ binding energies are transformed in the last row to $B_{\Lambda^*\Lambda^*}$ values.

$\bar{K}$ nuclei	(E-dep.)	$(\text{E-indep.})_a$	$(\text{E-indep.})_b$
$(\bar{K}N)_{I=0}$	11.4	26.6	64.2
$(\bar{K}NN)_{I=1/2}$	15.7	51.5	102
$(\bar{K}\bar{K}NN)_{I=0}$	32.1	93	190
$\Lambda^*\Lambda^*$	9.3	40	62

and ρ saturate as a function of A, thereby leaving Λ^* matter highly unstable. A brief Conclusion section summarizes our results with some added discussion.

2. $\bar{K}$ nuclear quasibound states

The $I = 0$ antikaon–nucleon $(\bar{K}N)$ interaction near threshold is attractive and sufficiently strong to form a quasibound state. Using a single-channel energy independent $\bar{K}N$ potential this quasibound state has been identified by AY, e.g. in Refs. [6,7], with the $J^P = (1/2)^-$ $\Lambda^*(1405)$ resonance about 27 MeV below the K^-p threshold. In contrast, in effective field theory (EFT) approaches where the $\bar{K}N$ effective single-channel potential comes out energy dependent, reflecting the coupling to the lower-energy $\pi\Sigma$ channel, this $\bar{K}N$ quasibound state is bound only by about 10 MeV [8]. The difference between $\bar{K}N$ binding energies gets compounded in multi-$\bar{K}N$ quasibound states predicted in these two approaches, as demonstrated for $(\bar{K}\bar{K}NN)_{I=0}$ in Table 1 by comparing binding energies B listed in the (E-dep.) column with those listed in the (E-indep.) columns. Regarding these two columns, we note that the binding energies listed in column $(\text{E-indep.})_b$ arise by fitting the $(\bar{K}N)_{I=0}$ potential strength such that it reproduces the value $B(\bar{K}NN)_{I=1/2} = 102$ MeV derived from the DISTO experiment [11]. This derivation was challenged subsequently by the HADES Collaboration [12]. The most recent J-PARC E15 [13] dedicated experiment derives a value of $B(\bar{K}NN)_{I=1/2} = 47 \pm 3^{+3}_{-6}$ MeV. Therefore, when studying energy independent $\bar{K}N$ potentials, we will keep to the $(\text{E-indep.})_a$ scenario that also identifies the $(\bar{K}N)_{I=0}$ quasibound state with the $\Lambda^*(1405)$ resonance observed 27 MeV below threshold. This identification plays an essential role in the earlier Akaishi and Yamazaki works, Refs. [6,7]. It is worth noting that the more refined state-of-the-art chiral EFT approaches, with low-energy constants fitted to *all* existing K^-p low-energy data, produce two $(\bar{K}N)_{I=0}$ quasibound states [14], the narrower and least bound of which is consistent with the (E-dep.) column of Table 1.

3. Kaonic atoms test

Here we confront the $(\text{E-indep.})_a$ scenario of the last section with the broad data base of kaonic atoms which are known to provide a sensitive test of $\bar{K}N$ interaction models near threshold [15]. In the last decade several chiral EFT models of the $\bar{K}N$ interaction provided K^-N scattering amplitudes based on fits to low energy K^-p data, including kaonic hydrogen from the SIDDHARTA experiment [16,17]. Kaonic atom potentials based on such single-nucleon amplitudes within a sub-threshold kinematics approach are generally unable to fit the kaonic atom data unless an additional phenomenological density dependent amplitude representing multi-nucleon processes is introduced. In a recent work [18] this procedure was applied to several chiral EFT $\bar{K}N$ model amplitudes. Good fits to the data were reached with χ^2 values of 110 to 120 for 65 data points. Considering that the data come

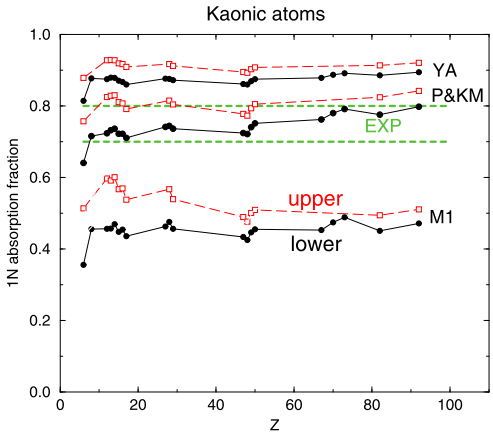

Fig. 1. K^- single-nucleon absorption fractions calculated using K^-N amplitudes from the chiral EFT models M1, P and KM, see Ref. [18], and as generated from Eq. (1) (here marked YA). The range of experimentally deduced fractions, 0.70–0.80, is marked by horizontal dashed lines; see Ref. [18] for a comment on carbon (lowest Z points).

from four different laboratories, covering the whole of the periodic table, these χ^2 values are quite satisfactory. This procedure was extended to include also $\bar{K}N$ amplitudes generated from the energy independent $\bar{K}N$ potentials used by Yamazaki and Akaishi (YA) [7] (in MeV),

$$V^{I=0}_{\bar{K}N}(r) = (-595 - \text{i}83)\exp[-(r/0.66\ \text{fm})^2],$$
$$V^{I=1}_{\bar{K}N}(r) = (-175 - \text{i}105)\exp[-(r/0.66\ \text{fm})^2]. \quad (1)$$

These potentials approximate reasonably the $(\text{E-indep.})_a$ scenario of the last section. The corresponding $\bar{K}N$ amplitudes are shown in Fig. 15 of Ref. [19].[1] Like other models, also this model fails to fit kaonic atoms data on its own. Adding a phenomenological density dependent amplitude produces fits with χ^2 of 150 for the 65 data points, which is significantly inferior to fits obtained for the chiral EFT models considered in Ref. [18].

It was shown in Ref. [18] that one could distinguish between different $\bar{K}N$ models by testing their ability to reproduce experimentally deduced values of single-nucleon absorption fractions at threshold across the periodic table. Fig. 1 shows such fractions as calculated for four models of the $\bar{K}N$ interaction, including that of Eq. (1). Results of calculated absorptions from the so-called lower state and whenever provided by measured yields also from the upper state are shown for each kaonic atom. Experiments [20–22] do not distinguish directly between the two types of absorption.

As shown in the figure the $\bar{K}N$ interaction model of Eq. (1) (marked by YA) leads to far too large single-nucleon fractions whereas, for example, the Murcia (M1) model leads to too small ratios. The Kyoto–Munich (KM) model and the Prague (P) model, which yield predictions indistinguishable from each other, provide a very good agreement with experiment. The bottom line for the present discussion is that the $\bar{K}N$ interaction model of Eq. (1) does not reproduce the experimental absorption fractions.

4. RMF calculations of purely-Λ^* nuclei

Bound systems of Λ^* hyperons are treated here in a similar way as applied to nuclei [5] and also to hypernuclei, e.g. in Ref. [23], within the RMF framework. In our calculations of Λ^* nuclei, we employed the linear RMF model HS [24], taking into account the

[1] We thank Tetsuo Hyodo for providing us with tables of these amplitudes.

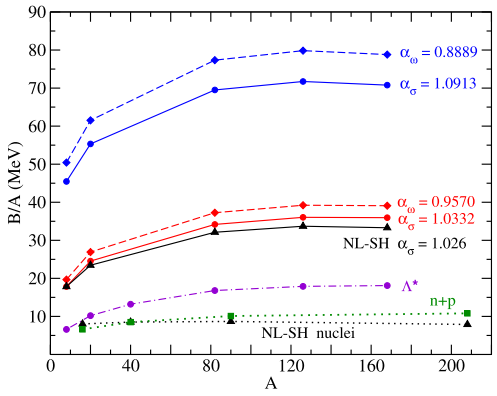

Fig. 2. Binding energy of Λ^* nuclei per Λ^*, B/A as a function of mass number A, calculated within the HS and NL-SH RMF models for various strengths of scalar and vector fields (see text for details). The binding energy per nucleon in atomic nuclei is shown for comparison ($n+p$: HS without Coulomb and ρ meson field, NL-SH nuclei: including these terms).

coupling of Λ^* baryons to isoscalar–scalar σ and isoscalar–vector ω meson fields. Other fields considered in ordinary nuclei, such as isovector–vector $\vec{\rho}$ or Coulomb fields were disregarded since the Λ^* is a neutral $I=0$ baryon. The resulting RMF model Lagrangian density for Λ^* nuclei is of the form ($\hbar = c = 1$ from now on):

$$\mathcal{L} = \bar{\Lambda}^* \left[\mathrm{i}\gamma^\mu D_\mu - (M_{\Lambda^*} - g_{\sigma\Lambda^*}\sigma) \right] \Lambda^* + (\sigma, \omega_\mu \text{ free-field terms}), \tag{2}$$

where the covariant derivative $D_\mu = \partial_\mu + \mathrm{i}\, g_{\omega\Lambda^*}\omega_\mu$ couples the vector meson field ω to the Λ^* baryon fields. Here we disregard the $\omega\Lambda^*$ tensor coupling term $f_{\omega\Lambda^*}\sigma_{\mu\nu}\omega_\nu$ which, while affecting spin–orbit splittings of single-particle levels, has little effect on the total binding energies of closed-shell nuclear systems (or Λ^* nuclei).

To start with, we used the HS linear model for atomic nuclei [24] with scalar and vector meson masses m_i ($i = \sigma, \omega$) and coupling constants g_{iN} given by

$$m_\sigma = 520\ \text{MeV},\quad m_\omega = 783\ \text{MeV},\quad g_{\sigma N} = 10.47,\quad g_{\omega N} = 13.80. \tag{3}$$

Modifying these coupling constants in ways described below, we explored Λ^* nuclei with closed shells by solving self-consistently the coupled system of the Klein–Gordon equations for meson fields and the Dirac equation for Λ^*.

In Fig. 2 we show binding energy values per baryon, B/A, calculated as a function of A for atomic nuclei (lowest two lines) and for purely Λ^* nuclei using mostly the linear HS model. It is clear that B/A saturates in all shown cases for $A \gtrsim 120$, to a value of order 10 MeV for nucleons when using parameters specified in Eq. (3), and to a somewhat higher value in the case of Λ^* nuclei (marked by Λ^*) upon using the same parameters. The increased B/A values in this case with respect to atomic nuclei is due to the higher Λ^* mass which reduces its kinetic energy. This is not yet the Λ^* matter calculation we should pursue since when extrapolated to $A=2$ it gives a $B_{\Lambda^*\Lambda^*}$ value of only a few MeV, whereas the calculation pursued here assumes a considerably stronger $\Lambda^*\Lambda^*$ binding corresponding to $B(\bar{K}\bar{K}NN)_{I=0} - 2B(\bar{K}N)_{I=0} \approx 40$ MeV from column (E-indep.)$_a$ in Table 1.[2] To renormalize the Λ^* RMF calculation to such a high value of $B_{\Lambda^*\Lambda^*}$ we need to increase $g_{\sigma N}$ or decrease $g_{\omega N}$ from the values listed in Eq. (3). This is how the other B/A lines marked by scaling factors α_σ or α_ω in Fig. 2 are obtained. The appropriate values of α_σ and α_ω are determined as follows.

[2] We note for comparison that the scalar and vector Λ^* couplings estimated in the microscopic calculations of Ref. [28] within a chiral EFT model do not produce a bound $\Lambda^*\Lambda^*$ state.

Table 2
Values of the scaling parameters α_σ and α_ω for σ and ω fields, respectively, each yielding $B_{\Lambda^*\Lambda^*} = 40$ MeV.

$V_{\Lambda^*\Lambda^*}$	α_σ	α_ω
Dover–Gal (4)	1.0332	0.9750
Machleidt (5)	1.0913	0.8889

The RMF underlying attractive scalar (σ) exchange and repulsive vector (ω) exchange baryon–baryon (BB) spin-singlet $S=0$ potentials are given to lowest order in $(m/M)^2$ recoil corrections, disregarding tensor couplings, by:

$$V_{BB}(r) = g^2_{\omega B}\,(1 - \frac{3}{8}\frac{m^2_\omega}{M^2_B})\,Y_\omega(r) - g^2_{\sigma B}\,(1 - \frac{1}{8}\frac{m^2_\sigma}{M^2_B})\,Y_\sigma(r) \tag{4}$$

according to Dover–Gal [26], or

$$V_{BB}(r) = g^2_{\omega B}\,Y_\omega(r) - g^2_{\sigma B}\,(1 - \frac{1}{4}\frac{m^2_\sigma}{M^2_B})\,Y_\sigma(r) \tag{5}$$

according to Machleidt [27]. Here $Y_i(r) = \exp(-m_i r)/(4\pi r)$ is the Yukawa form for meson exchange. The difference in the $(m/M)^2$ recoil terms in these two forms arises from a total neglect of nonlocal contributions in Dover–Gal, while partially retaining them by Machleidt. Using these BB $= \Lambda^*\Lambda^*$ potentials, with $M_{B=\Lambda^*} = 1405$ MeV, $\Lambda^*\Lambda^*$ binding energies were calculated by solving a two-body Schrödinger equation, scaling either $g_{\sigma N}$ or $g_{\omega M}$ according to $g_{\sigma N} \to g_{\sigma\Lambda^*} = \alpha_\sigma g_{\sigma N}$ and $g_{\omega N} \to g_{\omega\Lambda^*} = \alpha_\omega g_{\omega N}$ so as to get $B_{\Lambda^*\Lambda^*} = 40$ MeV while retaining the other coupling constant fixed. The resulting scaling parameters are listed in Table 2.

We then performed RMF calculations of Λ^* nuclei using the renormalized coupling constants as marked to the right of each line in Fig. 2. Saturation is robust in all versions for $A \gtrsim 120$, but the saturation value depends on which potential version is used, Dover–Gal (4) or Machleidt (5). Scaling the ω meson coupling results in larger values of Λ^* binding energies than by scaling the σ meson coupling. Calculations were also performed using the nonlinear RMF model NL-SH [25] for comparison. The corresponding scaling parameter $\alpha_\sigma = 1.026$ was fitted to yield the binding energy of the $8\Lambda^*$ system calculated within the HS model for $\alpha_\sigma = 1.0332$. The resulting NL-SH calculation yields similar binding energies per Λ^* to those produced in the linear HS model. Fig. 2 clearly demonstrates that B/A does not exceed 100 MeV in any of the versions studied here. The calculated values are without exception considerably lower than the ≈ 290 MeV required to reduce the $\Lambda^*(1405)$ mass in the medium below that of the lightest hyperon $\Lambda(1116)$. This conclusion remains valid when Λ^* absorption is introduced in the present RMF calculations, say by considering the two-body conversion processes $\Lambda^*\Lambda^* \to YY$ ($Y = \Lambda,\ \Sigma$). Absorption normally translates into effective repulsion in bound state problems, thereby reducing the total binding energy and hence also the associated B/A values in Λ^* nuclei.

Having shown that B/A values saturate in Λ^* nuclei to values less than 100 MeV, we illustrate in Fig. 3 that the central density $\rho(r \approx 0)$ also saturates as a function of the mass number A. This is demonstrated in the left panel for the NL-SH model and $\alpha_\sigma = 1.026$. The central densities $\rho(0)$ shown in the figure vary in the range of 0.3–0.45 fm^{-3}, which is about twice nuclear matter density. Expressing the r.m.s. radius of the Λ^* nuclear density distribution ρ as $r_{\rm rms} = r_0 A^{\frac{1}{3}}$, the variation of the radius parameter r_0 with A is shown in the right panel of the figure for selected

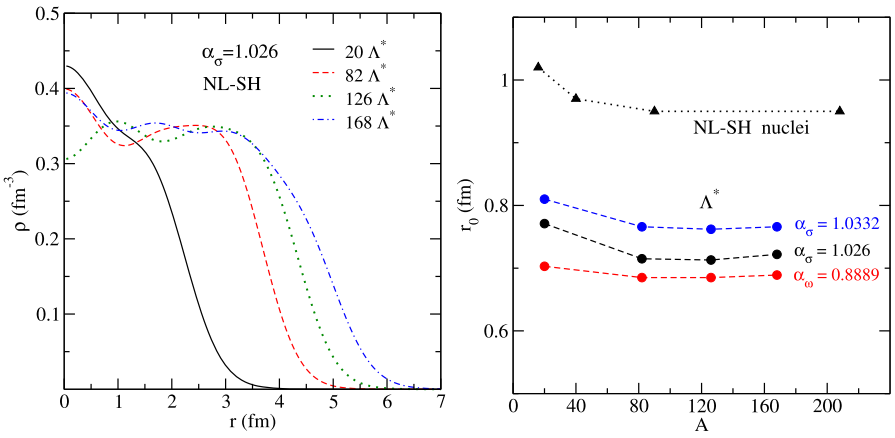

Fig. 3. Left: Λ^* density distribution in systems composed of 20, 82, 126 and 168 Λ^* baryons, calculated within the NL-SH RMF model for $\alpha_\sigma = 1.026$. Right: values of the r.m.s. radius parameter r_0 in Λ^* nuclei (see text) for three of the RMF models and interaction strengths giving rise to B/A lines in Fig. 2. Values of r_0 in atomic nuclei (marked 'NL-SH nuclei') calculated within the NL-SH model are shown for comparison.

$\Lambda^*\Lambda^*$ potential versions. Again, the radii r_0 saturate with values about 0.7–0.8 fm, indicating that Λ^* nuclei are more compressed than atomic nuclei in which r_0 is typically 0.9–1.0 fm, as shown by the upper line. The approximate constancy of r_0 with A is consistent with approximately uniform Λ^* matter density.

5. Conclusion

It was shown within a straightforward RMF calculation that the $\Lambda^*(1405)$ stable-matter scenario promoted by AY [3] is unlikely to be substantiated in standard many-body schemes. The decisive role of Lorentz covariance to produce saturation in the RMF calculations of binding energies and sizes reported in Sect. 4 is worth noting. Lorentz covariance introduces two types of baryon density, a scalar $\rho_S = \bar{B}B$ associated with the attractive σ meson field and a vector $\rho_V = \bar{B}\gamma_0 B$ associated with the repulsive ω meson field. Whereas ρ_V coincides with the conserved baryon density $B^\dagger B$ (denoted simply ρ on the l.h.s. of Fig. 3), ρ_S shrinks with respect to ρ_V in dense matter by a multiplicative factor $M^*/E^* < 1$, where $M^* = M - g_{\sigma B}\langle\sigma\rangle < M$ is the baryon density-dependent effective mass, thereby damping the attraction from the scalar σ meson field [5]. Saturation in the RMF model is thus entirely a relativistic phenomenon. Calculations within the non-relativistic approach with static potentials such as (4) or (5) would lead to collapse of systems composed of sufficiently large number of Λ^* baryons, as it also holds for nucleons [29].

Doubts were also raised in the present work on the validity of using a very strong and energy-independent $\bar{K}N$ $I = 0$ dominated potential fitted directly to the position and width of the $\Lambda^*(1405)$ resonance. Similar potentials have been used by AY over the years to promote the case for strongly bound $\bar{K}$ nuclear clusters, see Table 1 here, and thereby also to suggest strongly attractive $\Lambda^*\Lambda^*$ interactions that would according to them lead to absolutely stable Λ^* matter. It was shown in Sect. 3 here that such strong and energy-independent $\bar{K}N$ potentials do not pass the test of kaonic atoms, hence casting doubts on their applicability in describing higher density kaonic features. Having said it, we concede that a proper description of high density hadronic matter, considerably beyond the $\rho \approx 2\rho_0$ density regime reached in our own calculations, may require the introduction of additional, new interaction mechanisms such as proposed recently in Ref. [30].

Finally, we recall related RMF calculations of multi-$\bar{K}$ nuclei [31] in which, for a given core nucleus, the resulting $\bar{K}$ separation energy $B_{\bar{K}}$, as well as the associated nuclear and $\bar{K}$-meson densities, were found to saturate with the number of $\bar{K}$ mesons ($\gtrsim 10$). Saturation appeared in that study robust against a wide range of variations, including the RMF nuclear model used and the type of boson fields mediating the strong interactions. In particular strange systems made of protons and K^- mesons, as similar as possible to aggregates of $\Lambda^*(1405)$ baryons, were found in that work to be less bound than other strange-matter configurations. Our findings are in good qualitative agreement with the conclusion reached there that the SU(3) octet hyperons (Λ, Σ, Ξ) provide, together with nucleons, for the lowest energy strange hadronic matter configurations [1].

Acknowledgements

J.H. and M.S. acknowledge financial support from the CTU-SGS Grant No. SGS16/243/OHK4/3T/14. The work of N.B. is supported by the Pazy Foundation and by the Israel Science Foundation grant No. 1308/16.

References

[1] J. Schaffner, C.B. Dover, A. Gal, C. Greiner, H. Stöcker, Phys. Rev. Lett. 71 (1993) 1328;
J. Schaffner, C.B. Dover, A. Gal, C. Greiner, D.J. Millener, H. Stöcker, Ann. Phys. 235 (1994) 35;
J. Schaffner-Bielich, A. Gal, Phys. Rev. C 62 (2000) 034311.
[2] D. Chatterjee, I. Vidaña, Eur. Phys. J. A 52 (2016) 29.
[3] Y. Akaishi, T. Yamazaki, Phys. Lett. B 774 (2017) 522.
[4] T. Yamazaki, Y. Akaishi, A. Doté, Phys. Lett. B 587 (2004) 167.
[5] B.D. Serot, J.D. Walecka, Adv. Nucl. Phys. 16 (1986) 1, preceded by a more compact and accessible form in Phys. Lett. B 87 (1979) 172.
[6] Y. Akaishi, T. Yamazaki, Phys. Rev. C 65 (2002) 044005.
[7] T. Yamazaki, Y. Akaishi, Phys. Rev. C 76 (2007) 045201.
[8] T. Hyodo, D. Jido, Prog. Part. Nucl. Phys. 67 (2012) 55.
[9] N. Barnea, A. Gal, E.Z. Liverts, Phys. Lett. B 712 (2012) 132.
[10] S. Maeda, Y. Akaishi, T. Yamazaki, Proc. Jpn. Acad. Ser. B 89 (2013) 418.
[11] T. Yamazaki, et al., Phys. Rev. Lett. 104 (2010) 132502.
[12] G. Agakishiev, et al., Phys. Lett. B 742 (2015) 242.
[13] S. Ajimura, et al., arXiv:1805.12275 [nucl-ex], submitted for publication to Phys. Rev. Lett.
[14] U.-G. Meißner, T. Hyodo, Pole structure of the Λ(1405) region, a PDG18 Review in M. Tanabashi, et al., Phys. Rev. D 98 (2018) 030001.
[15] E. Friedman, A. Gal, Phys. Rep. 452 (2007) 89.
[16] M. Bazzi, et al., SIDDHARTA Collaboration, Phys. Lett. B 704 (2011) 113.
[17] M. Bazzi, et al., SIDDHARTA Collaboration, Nucl. Phys. A 881 (2012) 88.
[18] E. Friedman, A. Gal, Nucl. Phys. A 959 (2017) 66.
[19] T. Hyodo, W. Weise, Phys. Rev. C 77 (2008) 035204.
[20] H. Davis, et al., Nuovo Cimento A 53 (1968) 313.
[21] J.W. Moulder, et al., Nucl. Phys. B 35 (1971) 332.
[22] C. Vander Velde-Wilquet, et al., Nuovo Cimento A 39 (1977) 538.
[23] J. Mareš, B.K. Jennings, Phys. Rev. C 49 (1994) 2472.
[24] C.J. Horowitz, B.D. Serot, Nucl. Phys. A 368 (1981) 503.

[25] M.M. Sharma, M.A. Nagarajan, P. Ring, Phys. Lett. B 312 (1993) 377.
[26] C.B. Dover, A. Gal, Prog. Part. Nucl. Phys. 12 (1984) 171.
[27] R. Machleidt, Adv. Nucl. Phys. 19 (1989) 189.
[28] T. Uchino, T. Hyodo, M. Oka, Nucl. Phys. A 868–869 (2011) 53.
[29] M. Schäfer, et al., work in preparation.
[30] W. Paeng, M. Rho, Phys. Rev. C 91 (2015) 015801.
[31] D. Gazda, E. Friedman, A. Gal, J. Mareš, Phys. Rev. C 77 (2008) 045206.

Λ^* matter and its stability

J. Hrtánková[a,*], M. Schäfer[a,b], and J. Mareš[a]

[a] *Nuclear Physics Institute CAS, 250 68 Rez,Czech Republic*
[*] *E-mail: hrtankova@ujf.cas.cz*
[b] *Faculty of Nuclear Sciences and Physical Engineering, Czech Technical University in Prague, 115 19 Prague 1, Czech Republic*

A. Gal, E. Friedman, and N. Barnea

Racah Institute of Physics, The Hebrew University, 91904 Jerusalem, Israel

We performed calculations of nuclear systems composed solely of Λ^* hyperons, aiming at exploring the possibility of existence of absolutely stable Λ^* matter. We considered Λ^* interaction strengths compatible with the $\Lambda^*\Lambda^*$ binding energy $B_{\Lambda^*\Lambda^*}$ given by the $\bar{K}N$ interaction model by Yamazaki and Akaishi [1]. We found that the binding energy per Λ^* saturates at values well below 100 MeV for mass number $A \geq 120$. The Λ^* matter is thus highly unstable against strong interaction decay.

Keywords: Strange matter; Λ^* resonance; SVM; RMF.

1. Introduction

This contribution concerns our recent study of Λ^* nuclei [2], which was stirred up by a conjecture about absolutely stable charge-neutral baryonic matter composed solely of $\Lambda(1405)$ (Λ^*) hyperons [3].

We calculated Λ^* few-body systems within the Stochastic Variational Method (SVM) [4], as well as Λ^* many-body systems within the Relativistic Mean Field (RMF) approach [5]. The meson-exchange Λ^* potentials applied in our work were fitted to reproduce the $\Lambda^*\Lambda^*$ binding energy $B_{\Lambda^*\Lambda^*} = 40$ MeV, given by the phenomenological $\bar{K}N$ interaction model [1]. We recall that the $\bar{K}N$ potentials used by Akaishi and Yamazaki [1,3], fitted for $I = 0$ to the mass and width of the $\Lambda(1405)$ resonance, fail to reproduce K^- single-nucleon absorption fractions deduced from K^- capture bubble chamber experiments [6]. Nevertheless, we employed these very strong potentials in order to demonstrate that while solving the A-body Schrödinger equation for purely attractive $\Lambda^*\Lambda^*$ interactions will inevitable lead to collapse, with the binding energy per particle diverging as A increases, this

scenario promoted in ref.[3] is unlikely in standard many-body approaches. In the following sections, we discuss only briefly our main results; more details can be found in ref.[2].

2. Λ^* Few-Body Systems

We started our study of Λ^* nuclei by calculations of few-body systems within the Stochastic Variational Method[4] for the meson-exchange potentials of the Dover-Gal form[7]:

$$V_{\Lambda^*\Lambda^*}(r) = g^2_{\omega\Lambda^*}\,(1+\tfrac{1}{8}\tfrac{m^2_\omega}{M^2_{\Lambda^*}})\,Y_\omega(r) - g^2_{\sigma\Lambda^*}\,(1-\tfrac{1}{8}\tfrac{m^2_\sigma}{M^2_{\Lambda^*}})\,Y_\sigma(r) + g^2_{\omega\Lambda^*}\tfrac{1}{6}\tfrac{m^2_\omega}{M^2_{\Lambda^*}}\,Y_\omega(r)(\vec{\sigma}_1\cdot\vec{\sigma}_2)\ , \quad (1)$$

or the Machleidt form[8]:

$$V_{\Lambda^*\Lambda^*}(r) = g^2_{\omega\Lambda^*}(1+\tfrac{1}{2}\tfrac{m^2_\omega}{M^2_{\Lambda^*}})\,Y_\omega(r) - g^2_{\sigma\Lambda^*}\,(1-\tfrac{1}{4}\tfrac{m^2_\sigma}{M^2_{\Lambda^*}})\,Y_\sigma(r) + g^2_{\omega\Lambda^*}\tfrac{1}{6}\tfrac{m^2_\omega}{M^2_{\Lambda^*}}\,Y_\omega(r)(\vec{\sigma}_1\cdot\vec{\sigma}_2)\ , \quad (2)$$

where $M_{\Lambda^*} = 1405$ MeV, m_i are the meson masses, $g_{i\Lambda^*} = \alpha_i g_{iN}$ are the corresponding coupling constants with g_{iN} taken from the HS model[9], and $Y_{i=\sigma,\omega}(r) = \exp(-m_i r)/(4\pi r)$. In the above expressions, the mass correction factors ($\sim m_i^2/M^2_{\Lambda^*}$) as well as the spin-spin interaction terms ($\sim(\vec{\sigma}_1\cdot\vec{\sigma}_2)$) are included.

In the calculations we fit either the value of α_σ and kept α_ω fixed to 1 or vice versa in order to get the binding energy of the $\Lambda^*\Lambda^*$ system $B_{\Lambda^*\Lambda^*} = 40$ MeV. We present here only selected results for $\alpha_\sigma \neq 1$.

In Fig. 1, left panel, we show the binding energy per Λ^*, B/A, as a function of mass number in few-body Λ^* nuclei, calculated within the SVM approach for the Machleidt potential (1). When the spin-spin interaction is omitted, the binding energy per particle is rapidly increasing with A, reaching $B/A \approx 130$ MeV for A=6. The mass corrections have almost no effect on the calculated values of B/A. On the other hand, when the spin-spin interaction is taken into account, the increase of B/A is considerably less steep. The corresponding rms radius of the considered Λ^* nuclei is presented in the right panel. The rms radius is extremely small, hardly exceeding the value 0.8 fm even if the spin-spin interaction is included.

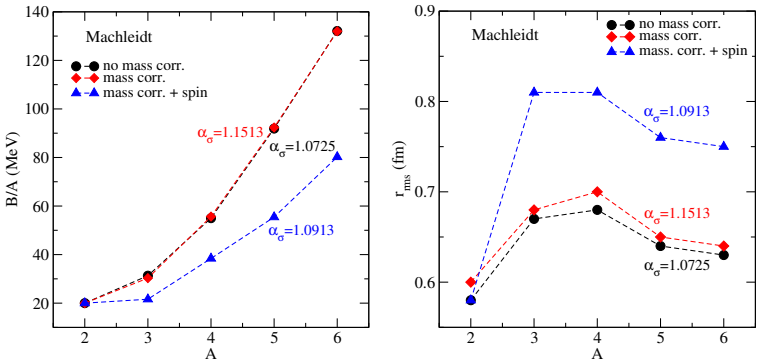

Fig. 1. Binding energy of Λ^* nuclei per particle, B/A (left panel) and rms radius (right panel) of few-body Λ^* systems as a function of mass number A, calculated using the Machleidt potential with and without mass corrections, as well as including spin-spin interaction.

3. Λ^* Many-Body Systems

As the next step, we explored many-body systems composed solely of Λ^* hyperons within the RMF framework[5], where the interaction among Λ^*'s is mediated by the exchange of the scalar σ and vector ω meson fields. The underlying Lagrangian density is of the form

$$\mathcal{L} = \bar{\Lambda}^* \left[\mathrm{i}\gamma^\mu D_\mu - (M_{\Lambda^*} - g_{\sigma\Lambda^*}\sigma) \right] \Lambda^* + (\sigma, \omega_\mu \,\text{free-field terms}) \ , \quad (3)$$

where $D_\mu = \partial_\mu + \mathrm{i}\, g_{\omega\Lambda^*}\, \omega_\mu$. It is to be noted that the isovector-vector $\vec{\rho}$ and Coulomb fields were not taken into account since the Λ^* is a neutral $I = 0$ baryon. First calculations were perfomed using the linear HS model[9] with the coupling constants scaled by α_{i}, $g_{i\Lambda^*} = \alpha_i g_{iN}$, determined by fitting $B_{\Lambda^*\Lambda^*}$ (see previous section). For comparison, we performed also calculations using the nonlinear NL-SH model[10]. The corresponding scaling parameter α_σ was fitted to yield the binding energy of the $8\Lambda^*$ system calculated within the HS model. We explored Λ^* nuclei with closed shells and solved self-consistently the coupled system of the Klein-Gordon equations for meson fields and the Dirac equation for Λ^*.

The results of our RMF calculations are summarized in Fig. 2. In the left panel, the binding energy per particle, B/A, is plotted as a function of mass number A, calculated within the RMF HS model with the properly rescaled σ meson coupling constant corresponding to the Λ^* potentials (1) and (2). For comparison, B/A calculated within the RMF NL-SH model in

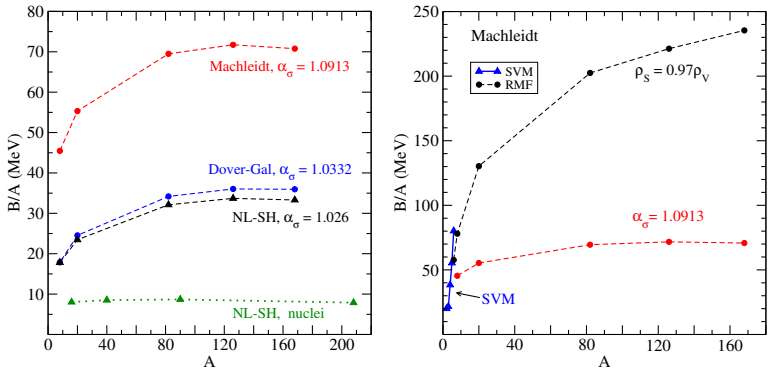

Fig. 2. Left panel: Binding energy of Λ^* nuclei per particle, B/A as a function of mass number A, calculated within the HS and NL-SH models; B/A in atomic nuclei ('nuclei') is shown for comparison. Right panel: Comparison of B/A calculated in Λ^* nuclei within the HS model for the Machleidt potential (red line) with a similar calculation using $\rho_s = 0.97\rho_v$ (black line); B/A in few body systems, calculated within the SVM is shown for comparison. See text for details.

Λ^* nuclei as well as in ordinary nuclei is shown as well. The binding energy per Λ^* saturates with the number of constituents for $A \geq 120$ in all versions considered and reaches tens of MeV depending on the potential used. Calculations with the rescaled ω coupling constant yield similar saturation curves for B/A in Λ^* nuclei.

The observed saturation originates from the Lorentz covariance which introduces two types of baryon densities — the scalar density ρ_s associated with the attractive σ field and the vector (baryon) density ρ_v associated with the repulsive ω field. In dense matter, the scalar density decreases with respect to the vector density since $\rho_s \sim M^*/E^*\rho_v$ where $\frac{M^*}{E^*} < 1$, and $M^* = M - g_{\sigma B}\langle\sigma\rangle$ is baryon effective mass. As a consequence, the attraction from the scalar field is reduced considerably at higher densities. This is illustrated in Fig. 2 (right panel), where we present the RMF calculation of B/A in Λ^* nuclei, in which we replaced the scalar density ρ_s by a density equal to $0.97\rho_v$ (this corresponds to ρ_s/ρ_v in ^{16}O). The binding energy per Λ^* (denoted '$\rho_s = 0.97\rho_v$') is rapidly increasing in this case, similar to the SVM calculations (also shown for comparison), and does not seem to saturate within the explored mass range, unlike B/A evaluated using the 'dynamical' scalar density ρ_s (denoted '$\alpha_\sigma = 1.0913$'). It is to be noted that the central density of calculated Λ^* nuclei saturates as a

function of A as well, reaching about twice nuclear matter density.

Finally, we introduced the Λ^* absorption and explored how the Λ^* decay width changes in the medium. We considered the two-body decay $\Lambda^*\Lambda^* \to \Lambda\Lambda$ in the $1s$ state, described by the imaginary part of an optical potential in a '$t\rho$' form with the amplitude fitted to assumed width $\Gamma_{\Lambda^*\Lambda^*} = 100$ MeV at threshold, taking into account phase space suppression. We found that the conversion widths, despite being suppressed to some extent in the Λ^* nuclei (by 28% in A=8 systems and by less than 1% in A=168 systems), remain considerable and the $\Lambda^*\Lambda^*$ pairs will thus inevitably decay.

4. Summary

We performed calculations of Λ^* nuclei with various Λ^* interaction strengths compatible with the value $B_{\Lambda^*\Lambda^*} = 40$ MeV of the YA model[1] in order to demonstrate that the Λ^* stable-matter scenario[3] is not supported by standard many-body approaches. We found that the binding energy per Λ^* in many-body systems saturates in all cases for $A \geq 120$ at values far below ≈ 290 MeV, which is the energy required to reduce the $\Lambda(1405)$ mass in the medium below the mass of the lightest hyperon $\Lambda(1116)$. The Λ^* matter is thus highly unstable against strong interaction decay.

Acknowledgment

This work was partly supported by the Czech Science Foundation GACR grant 19-19640S.

References

1. T. Yamazaki and Y. Akaishi, Phys. Rev. **C 76**, 045201 (2007).
2. J. Hrtánková, N. Barnea, E. Friedman, A. Gal, J. Mareš and M. Schäfer, Phys. Lett. **B 785**, 90 (2018).
3. Y. Akaishi and T. Yamazaki, Phys. Lett. **B 774**, 552 (2017).
4. K. Varga and Y. Suzuki, *Stochastic Variational Approach to Quantum-Mechanical Few-Body Problems* (Springer 1998).
5. B. D. Serot and J. D. Walecka, Adv. Nucl. Phys. **16**, 1 (1986).
6. E. Friedman and A. Gal, Nucl. Phys. **A 959**, 66 (2017).
7. C. B. Dover and A. Gal, Prog. Part. Nucl. Phys. **12**, 171 (1984).
8. R. Machleidt, Adv. Nucl. Phys. **19**, 189 (1989).
9. C. J. Horowitz and B. D. Serot, Nucl. Phys. **A 368**, 503 (1981).
10. M. M. Sharma, M. A. Nagarajan, P. Ring, Phys. Lett. **B 312** (1993) 377.

Physics Letters B 808 (2020) 135614

Contents lists available at ScienceDirect

Physics Letters B

www.elsevier.com/locate/physletb

The continuum spectrum of hypernuclear trios

M. Schäfer [a,b], B. Bazak [c], N. Barnea [c,*], J. Mareš [b]

[a] Czech Technical University in Prague, Faculty of Nuclear Sciences and Physical Engineering, Břehová 7, 11519 Prague 1, Czech Republic
[b] Nuclear Physics Institute of the Czech Academy of Sciences, 25069 Řež, Czech Republic
[c] The Racah Institute of Physics, The Hebrew University, Jerusalem 9190401, Israel

ARTICLE INFO

Article history:
Received 19 March 2020
Received in revised form 5 July 2020
Accepted 8 July 2020
Available online 10 July 2020
Editor: W. Haxton

Keywords:
Hypernuclei
Effective field theory
Hypertriton
Λnn
Resonance

ABSTRACT

The spectrum of hypernuclear trios composed of a Λ baryon and two nucleons is the subject of an ongoing experimental campaign, aiming to study the interaction of the Λ particle with a neutron, and the 3-body Λ-nucleon-nucleon force. In this manuscript we utilize baryonic effective field theory at leading order, constrained to reproduce the available low energy light hypernuclear data, to study the continuum spectrum of such hypernuclear trios. Using the complex scaling method and the inverse analytic continuation in the coupling constant method we find the existence of a virtual state in the Λnp $J^\pi = 3/2^+$ channel, leading to cross-section enhancement near threshold. For the Λnn $J^\pi = 1/2^+$ channel we predict a resonance state. Depending, however, on the value of the ΛN scattering length, the resonance pole moves from the physical to the unphysical complex energy sheet within the experimental bounds.

1. Introduction

Understanding the interaction between nucleons and a Λ hyperon is the subject of an ongoing experimental and theoretical campaign [1]. In the last few years much effort is dedicated to the study of hypernuclear trios (ΛNN) aiming to determine the unknown Λ-neutron (Λn) interaction, and the ΛNN 3-body force. The latter is known to have a crucial effect in the nuclear equation of state at high density, and therefore on our understanding of neutron stars.

The Λ-nucleon interaction is not strong enough to bind a ΛN pair, making the hypertriton ${}^3_\Lambda\mathrm{H}(I=0,\, J^\pi = 1/2^+)$ the lightest hypernuclei. It is weakly bound with a Λ separation energy $B_\Lambda = 0.13 \pm 0.05$ MeV [2]. The experimental search for other bound hypernuclear trios has found no evidence for the hypertriton state ${}^3_\Lambda\mathrm{H}^*$, ${}^3_\Lambda\mathrm{H}(I=0,\, J^\pi = 3/2^+)$, indicating that the singlet $s=0$ ΛN interaction is somewhat stronger than the triplet $s=1$ interaction.

Recently, the HypHI collaboration [3] has claimed evidence for a bound Λnn state, ${}^3_\Lambda n(I=1,\, J^\pi = 1/2^+)$. However, this observation contradicts theoretical analyses demonstrating that such a bound state cannot exist. Since the first calculation by Dalitz and Downs [4], numerous theoretical studies of $I = 0, 1$ and $J = 1/2, 3/2$ ΛNN states have been performed, confirming the observation that no bound Λnn and ${}^3_\Lambda\mathrm{H}(I=0,\, J^\pi = 3/2^+)$ exist within Faddeev calculations for separable potentials [5,6], chiral constituent quark model of YN interactions [7,8] or the Nijmegen hyperon-nucleon potentials [9]. The same conclusion was drawn in [10] within variational calculations using YN model, simulating the realistic Nijmegen interaction. The Λnn system was also studied within a baryonic (pionless) effective field theory ($\not\pi$EFT) [11,12], however, due to uncertainty in fixing the three-body Λnn force no firm predictions of its stability could be made.

In spite of the theoretical consensus regarding a bound Λnn, the nature of hypernuclear ΛNN trios remains a subject of an ongoing discussion [13]. Specifically, the search for the Λnn system is a goal of the JLab E12-17-003 experiment [14], and the study of the ${}^3_\Lambda\mathrm{H}(I=0,\, J^\pi = 3/2^+)$ state is part of the JLab proposal P12-19-002 [15].

Regardless the apparent interest, the possible existence of Λnn and ${}^3_\Lambda\mathrm{H}^*$ hypernuclear continuum states has been directly addressed in only few theoretical works. Calculating zeros of the three-body Jost function, Belyaev et al. found a very wide, near-threshold, Λnn resonance [16]. Afnan and Gibson [17] using Faddeev calculation and separable potentials, fitted to reproduce ΛN and NN scattering length and effective range, concluded that the Λnn state exists as a sub-threshold resonance. They also found that a small increase of the ΛN interaction strength shifts the resonance position above threshold and thus yields an observable resonance. We are not aware of any direct calculation of the ${}^3_\Lambda\mathrm{H}^*$ continuum state, however, as Garcilazo et al. concluded, there is a

* Corresponding author.
E-mail addresses: m.schafer@ujf.cas.cz (M. Schäfer), betzalel.bazak@mail.huji.ac.il (B. Bazak), nir@phys.huji.ac.il (N. Barnea), mares@ujf.cas.cz (J. Mareš).

https://doi.org/10.1016/j.physletb.2020.135614

hint of near-threshold pole which gives rise to large Λd scattering length in $J^\pi = 3/2^+$ channel [7].

The aforementioned continuum studies [7,8,16,17] were limited to $A = 3$ systems. Therefore, the predictive power of their interaction models was not verified against the available experimental B_Λ data in e.g. 4-body or 5-body s-shell hypernuclei. In fact, applying a gaussian potential mimicking the low energy behavior of the separable potential of [17] we find substantial overbinding in these systems. Given the relatively poorly known ΛN scattering parameters, and the precise B_Λ data, such comprehensive study is called for.

Motivated by the debate regarding the nature of the hypernuclear 3-body states, and the soon to be published JLab E12-17-003 Λnn results [14], in the present work we report on precise few-body calculations of the hypernuclear ΛNN bound and continuum spectrum, using Hamiltonians constructed at leading order (LO) in $\not\pi$EFT [18]. This $\not\pi$EFT is an extension, including Λ hyperons, of the n, p nuclear $\not\pi$EFT Hamiltonian, first reported in [19,20] and more recently used to study lattice-nuclei in [21–24]. At LO $\not\pi$EFT contains both 2-body and 3-body contact interactions. The theory's parameters, i.e. the 2- and 3-body low-energy constants (LECs), were fitted to reproduce the $\Lambda N, NN$ scattering lengths, ^{3}H binding energy, and the available 3,4-body B_Λ data [18]. The predictive power of the theory was tested against the measured $^5_\Lambda$He separation energy [18,41]. The $\not\pi$EFT breakup scale can be associated with 2-pion exchange $2m_\pi$, or the threshold value for exciting ΣN pair. These two values are remarkably close. Assuming a typical energy scale E_Λ of about 1 MeV, the momentum scale $Q \approx \sqrt{2M_\Lambda E_\Lambda} = 47$ MeV/c, suggesting a $\not\pi$EFT expansion parameter $(Q/2m_\pi) \approx 0.2$. This implies a $\not\pi$EFT LO accuracy of order $(Q/2m_\pi)^2 \approx 4\%$.

The 3-body calculations were performed with the Stochastic Variational Method (SVM) expanding the wave function on a correlated gaussian basis [25,26], the continuum states were located using the Complex Scaling Method (CSM) [32], or the Inverse Analytic Continuation in the Coupling Constant (IACCC) Method [40].

Our main findings are: (a) The possible existence of a bound Λnn, or $^3_\Lambda$H* state is ruled out, confirming findings of previous theoretical studies [4–10,16,17]. (b) The excited state of hypertriton, $^3_\Lambda$H$^*(J^\pi = 3/2^+)$, is a virtual state. (c) The Λnn state is a resonance pole near the three-body threshold in a complex energy plane. The position of this pole depends on the value of the ΛN scattering length. Within the current bounds on the ΛN scattering length it can either be a real resonance or a sub-threshold resonance.

2. Calculational details

2.1. Hypernuclear $\not\pi$EFT at LO

At LO the $\not\pi$EFT of neutrons, protons and Λ-hyperons is given by the Lagrangian density

$$\mathcal{L} = N^\dagger\Big(i\partial_0 + \frac{\nabla^2}{2M_N}\Big)N + \Lambda^\dagger\Big(i\partial_0 + \frac{\nabla^2}{2M_\Lambda}\Big)\Lambda + \mathcal{L}_{2B} + \mathcal{L}_{3B} \quad (1)$$

where N and Λ are nucleon and Λ-hyperon fields, respectively, and $\mathcal{L}_{2B}, \mathcal{L}_{3B}$ are 2-body, and 3-body, s-wave contact interactions, with no derivatives. These contact interactions are regularized by introducing a local gaussian regulator with momentum cutoff λ, see e.g. [27],

$$\delta_\lambda(\boldsymbol{r}) = \left(\frac{\lambda}{2\sqrt{\pi}}\right)^3 \exp\left(-\frac{\lambda^2}{4}\boldsymbol{r}^2\right) \quad (2)$$

that smears the Dirac delta appearing in the contact terms over distances $\sim \lambda^{-1}$. This procedure yields Hamiltonian containing two-body V_2 and three-body V_3 interactions

Table 1
Input spin-singlet $a_0^{\Lambda N}$ and spin-triplet $a_1^{\Lambda N}$ scattering lengths (in fm), used to fit the hypernuclear 2-body LECs. Also shown is the spin-independent combination of ΛN scattering lengths $\bar{a}^{\Lambda N} = (3a_1^{\Lambda N} + a_0^{\Lambda N})/4$.

model	Reference	$a_0^{\Lambda N}$	$a_1^{\Lambda N}$	$\bar{a}^{\Lambda N}$
Alexander B	[28]	-1.80	-1.60	-1.65
NSC97f	[29]	-2.60	-1.71	-1.93
χEFT(LO)	[30]	-1.91	-1.23	-1.40
χEFT(NLO)	[31]	-2.91	-1.54	-1.88

$$V_2 = \sum_{I,S} C_\lambda^{I,S} \sum_{i<j} \mathcal{P}_{ij}^{I,S} \delta_\lambda(r_{ij})$$
$$V_3 = \sum_{I,S} D_\lambda^{I,S} \sum_{i<j<k} Q_{ijk}^{I,S} \sum_{cyc} \delta_\lambda(r_{ij})\delta_\lambda(r_{jk}), \quad (3)$$

where $\mathcal{P}_{ij}^{I,S}$ and $Q_{ijk}^{I,S}$ are the 2- and 3-body projection operators into an s-wave isospin-spin (I, S) channels. The cutoff λ dependent parameters $C_\lambda^{I,S}$, and $D_\lambda^{I,S}$ are the 2- and 3-body LECs, fixed for each λ by the appropriate renormalization condition. For λ higher than the breakup scale of the theory ($\lambda > 2m_\pi$), observables posses residual cutoff dependence, at LO $O(Q/\lambda)$, suppressed with λ approaching the renormalization group invariant limit $\lambda \to \infty$ [18].

In total there are 4 two-body (NN, ΛN), and 4 three-body (NNN, ΛNN) LECs. The nuclear LECs $C_\lambda^{I=0,S=1}$, $C_\lambda^{I=1,S=0}$, and $D_\lambda^{I=1/2,S=1/2}$ are fitted to the deuteron binding energy, NN spin-singlet scattering length a_0^{NN}, and to the triton binding energy, respectively. The hypernuclear two-body LECs $C_\lambda^{I=1/2,S=0}$ and $C_\lambda^{I=1/2,S=1}$ are fixed by the ΛN < spin-singlet $a_0^{\Lambda N}$ and spin-triplet $a_1^{\Lambda N}$ scattering lengths. The three-body hypernuclear LECs $D_\lambda^{I=0,S=1/2}$, $D_\lambda^{I=1,S=1/2}$, and $D_\lambda^{I=0,S=3/2}$ are fitted to the experimental Λ separation energies $B_\Lambda(^3_\Lambda\text{H})$, $B_\Lambda(^4_\Lambda\text{H})$, and the excitation energy $E_{\rm exc}(^4_\Lambda\text{H}^*)$.

Since $a_0^{\Lambda N}$ and $a_1^{\Lambda N}$ are not well constrained by experiment, we consider different values both as given by direct analysis of experimental data [28], or as predicted by several ΛN interaction models [29–31], see Table 1. For the particular values of the LECs see [18].

2.2. The stochastic variational method

The A-body Schrödinger equation is solved expanding the wave function Ψ in correlated gaussians basis [25]

$$\Psi = \sum_i c_i\, \psi_i = \sum_i c_i\, \hat{\mathcal{A}}\left\{\exp\left(-\frac{1}{2}\mathbf{x}^T A_i \mathbf{x}\right)\chi^i_{SM_S}\xi^i_{IM_I}\right\}, \quad (4)$$

where $\hat{\mathcal{A}}$ stands for the antisymmetrization operator over nucleons, $\mathbf{x} = (\mathbf{x}_1, ..., \mathbf{x}_{A-1})$ denotes a set of Jacobi vectors, and $\chi^i_{SM_S}$ ($\xi^i_{IM_I}$) is the spin (isospin) part. The information about interparticle correlations is contained in the $(A-1)$ dimensional positive-definite symmetric matrix A_i. Once we fix all basis functions ψ_i, both energies and coefficients c_i are obtained through diagonalization of the Hamiltonian matrix. The $A(A-1)/2$ nonlinear variational parameters contained in each A_i matrix are determined using the Stochastic Variational Method (SVM) [25,26].

Unlike bound states, continuum wave functions are not square-integrable. Therefore, resonances or virtual states can not be directly described using an L^2 basis set of correlated gaussians. Techniques such as CSM or IACCC have to be used to study such states with a correlated gaussians. Below we discuss in some detail the techniques we applied in our study.

2.3. The complex scaling method

The CSM [32] is a reliable tool to study few-body resonances [33]. The basic idea in the CSM is to locate resonances introducing complex rotation of coordinates and momenta

$$U(\theta)\mathbf{r} = \mathbf{r}e^{\mathrm{i}\theta}, \quad U(\theta)\mathbf{k} = \mathbf{k}e^{-\mathrm{i}\theta}, \tag{5}$$

that transforms the continuum states into integrable L^2 states. This transformation rotate continuum state energies by 2θ uncovering a section of the second energy plane between the real axis and a ray defined by $|\arg E| = 2\theta$, exposing resonances with argument $\theta_r = \arctan(\Gamma/2E_r)/2$ smaller than θ. Here, $E_r = \mathrm{Re}(E)$ is the resonance energy and $\Gamma = -2\mathrm{Im}(E)$ is the width. Using gaussian regulator (3) the rotation angle is restricted to be $\theta < \frac{\pi}{4}$, to prevent divergence of the rotated gaussian, limiting the scope of the CSM.

The SVM method uses the variational principle as a tool to optimize the nonlinear basis parameters A_i (4), minimizing the basis size. This does not apply to resonance states, making it a highly non trivial problem to choose the appropriate basis. Here, we present a new efficient procedure to determine the basis set for an accurate description of resonance states. To optimize the basis, we supplement the Hamiltonian H with an additional harmonic oscillator (HO) trap

$$H^{\mathrm{trap}}(b) = H + V^{\mathrm{HO}}(b), \quad V^{\mathrm{HO}}(b) = \frac{\hbar^2}{2mb^4}\sum_{j<k} r_{jk}^2, \tag{6}$$

where m is an arbitrary mass scale, and b is the HO trap length. The potential $V^{\mathrm{HO}}(b)$ gives rise to a HO spectrum of the ground and excited states which is affected by the presence of a resonance in the Hamiltonian H [34]. For a given trap length b we select basis states ψ_i (4) using the SVM, optimizing the variational parameters for the ground state energy and then subsequently for excited states energies up to $E_{\max} > E_r + \Gamma/2$. The SVM procedure prefers basis states which promote interparticle distances r_{jk} in a specific region given by the trap length b. Increasing b we enlarge the typical radius of the correlated gaussians ψ_i. For large enough b, the CSM resonance solution for the Hamiltonian H starts to stabilize and both the short range and the suppressed long range asymptotic parts of a resonance wave function are described sufficiently well. In order to further enhance the accuracy of our CSM solution, we use a grid $\{b_k\}$, of a HO trap lengths, and for each grid point we independently select correlated gaussians basis. Then we merge basis states determined for each b_k into a larger basis while ensuring linear independence and numerical stability of the overlap matrix. We have found that this procedure works well for both narrow, and broad resonances.

2.4. Inverse analytic continuation in the coupling constant method

The Analytic Continuation in the Coupling Constant (ACCC) method [35] has been successfully applied in various calculations of few-body resonances and virtual states [36,37]. Moreover, it was pointed out that the ACCC method provides rather convenient way how to extend applicability of the SVM into the continuum region [36,38]. We consider a few-body Hamiltonian consisting of the physical part H and an auxiliary attractive potential V^{aux}

$$H^{\mathrm{IACCC}} = H + \alpha\, V^{\mathrm{aux}}, \tag{7}$$

which introduces a bound state for a certain value of α, but ensures that the physical dissociation thresholds for the various subsystems remain unaffected. By decreasing the strength α the bound state moves closer to the threshold and for a certain α_0 it turns into a resonance or virtual state. It has been demonstrated for a two-body system that in the vicinity of the branching point α_0 the square root of an energy $k = \sqrt{E}$ behaves as $k \approx (\alpha - \alpha_0)$ for s-wave ($l = 0$) and $k \approx \sqrt{\alpha - \alpha_0}$ for $l > 0$ [35]. Defining new variable $x = \sqrt{\alpha - \alpha_0}$ one obtains two branches $k(x)$ and $k(-x)$ where the former one describes motion of the S-matrix pole assigned to a bound state on a positive imaginary k-axis to the third quadrant of a k-plane. Using analyticity of the function $k(x)$ one can continue from a bound region $\alpha > \alpha_0$ to a resonance region $\alpha < \alpha_0$. In practice this is done by constructing a Padé approximant

$$k(x) \approx \mathrm{i}\frac{\sum_{j=0}^{M} c_j x^j}{1 + \sum_{j=1}^{N} d_j x^j} \tag{8}$$

for the function $k(x)$ using $M + N + 1$ bound state solutions $\{(x_j, k_j);\, j = 1, \ldots, M + N + 1\}$ for different values of $\alpha > \alpha_0$. The evaluation of the Padé approximant (8) at $x = \sqrt{-\alpha_0}$ yields complex k which is assigned to the physical resonance solution $k^2 = E_r - \mathrm{i}\Gamma/2$ corresponding to the Hamiltonian H. For more details regarding the ACCC method see [39].

The ACCC method suffers from two drawbacks which are predominantly of numerical nature. The first issue is high sensitivity of the numerical solution to precise determination of the branching point value α_0 [35]. The second obstacle appears with increasing orders M and N of the Padé approximant (8) when the numerical solution starts to deteriorate.

Rather recently Horáček et al. [40] have introduced a modified version of the ACCC method called the Inverse Analytic Continuation in the Coupling Constant (IACCC) method which provides more robust numerical stability. Starting in the same manner as in the ACCC case, we consider the Hamiltonian (7) and calculate series of bound states for different values of $\alpha > \alpha_0$. Next, we construct a Padé approximant of a function $\alpha(\kappa)$, where $\kappa = -\mathrm{i}k$, using a relevant set of bound state solutions

$$\alpha(\kappa) \approx \frac{P_M(\kappa)}{Q_N(\kappa)} = \frac{\sum_{j=0}^{M} c_j \kappa^j}{1 + \sum_{j=1}^{N} d_j \kappa^j}. \tag{9}$$

The parameters of the physical resonance or virtual state pole are then readily obtained by setting $\alpha = 0$ as the physical root of a simple polynomial equation $P_M(\kappa) = 0$.

To ensure that the properties of the 2-body part of the Hamiltonian, such as scattering lengths or deuteron binding energy, remain unaffected, we choose the auxiliary potential to be an attractive 3-body force. The natural choice is to select it to have the same form as the $\not\pi$EFT 3-body potential (3),

$$V_3^{\mathrm{IACCC}} = d_\lambda^{I,S} \sum_{i<j<k} Q_{ijk}^{I,S} \sum_{\mathrm{cyc}} e^{-\frac{\lambda^2}{4}\left(r_{ij}^2 + r_{jk}^2\right)}, \tag{10}$$

where the amplitude $d_\lambda^{I,S}$ defines its strength, corresponding to the parameter α in Eq. (7), and is negative for an attractive auxiliary potential.

The accuracy of our IACCC resonance solutions in the fourth quadrant of the complex energy plane, $\mathrm{Re}(E) > 0$, $\mathrm{Im}(E) < 0$, are better than $\approx 10^{-3}$ MeV. These results compare very well with the CSM calculations in their region of applicability $\theta < \pi/4$.

3. Results

Using $\not\pi$EFT at LO with the LECs fitted to the available data as described earlier [18], we find no bound Λnn or ${}^{3}_{\Lambda}\mathrm{H}^*$ states. Further examining the hypothetical existence of these states, we found that they are incompatible with the well measured $A = 4, 5$ hypernuclear spectrum.

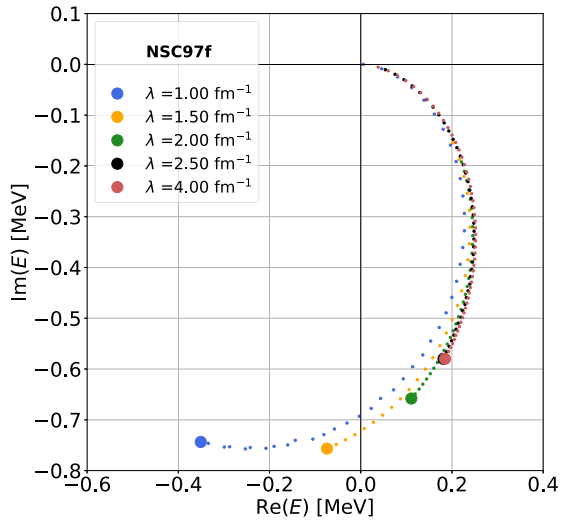

Fig. 1. Trajectories of the Λnn resonance pole in the complex energy plane determined by a decreasing attractive strength of the auxiliary three-body force $d_\lambda^{I=1,S=1/2}$ for several cutoffs λ and the NSC97f set of ΛN scattering lengths. Small dots mark IACCC solutions for different $d_\lambda^{I=1,S=1/2}$, larger symbols stand for the physical position of the Λnn pole ($d_\lambda^{I=1,S=1/2}=0$). Notice the almost overlapping trajectories for $\lambda=2.50$ fm^{-1} and $\lambda=4.00$ fm^{-1}.

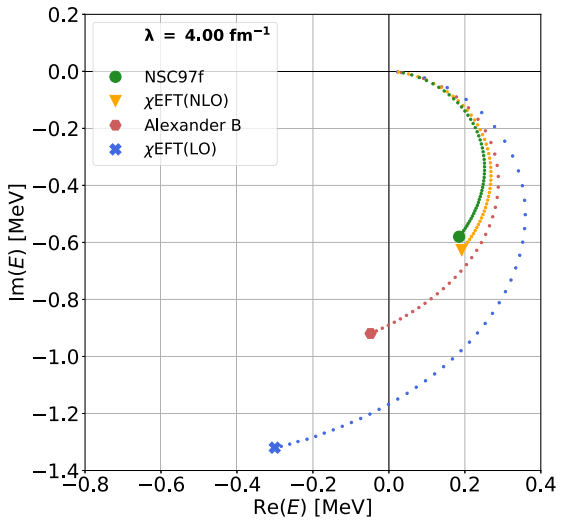

Fig. 2. Trajectories of the Λnn resonance pole in the complex energy plane determined by a decreasing attractive strength $d_\lambda^{I=1,S=1/2}$ for selected sets of ΛN scattering length, calculated at $\lambda=4.00$ fm^{-1}. Larger symbols stand for the physical position of the Λnn pole ($d_\lambda^{I=1,S=1/2}=0$).

As we have already pointed out, the possible existence of bound Λnn and ${}^3_\Lambda\mathrm{H}^*$ states has been quite convincingly ruled out in several theoretical studies [4–10]. Our $\not\pi$EFT findings support their conclusions.

3.1. A Λnn resonance?

We start our study of three-body hypernuclear continuum states with the Λnn system. To understand the cutoff dependence of our theory we present, in Fig. 1, the trajectories $E_{\Lambda nn}(d_\lambda^{I=1,S=1/2},\lambda)$ of the Λnn resonance pole, calculated using the IACCC method for different values of cutoff λ, and for a representative set of $a_s^{\Lambda N}$ - NSC97f. With decreasing attraction of V_3^{IACCC}, the resonance poles move along a circular trajectory in the complex energy plane starting from the $\Lambda+n+n$ threshold to the physical end point where $d_\lambda^{I=1,S=1/2}=0$. The figure suggests that the trajectories $E_{\Lambda nn}(d_\lambda^{I=1,S=1/2},\lambda)$ and the physical end points converge with increasing cutoff, and already at $\lambda=2.5$ fm^{-1} we approach stabilized results.

Repeating the same calculations for all sets of scattering lengths given in Table 1, we find that regardless the cutoff value, the imaginary part of the physical solution $\mathrm{Im}(E^\lambda_{\Lambda nn})$ lies in the interval $-1.32\le\mathrm{Im}(E^\lambda_{\Lambda nn})\le-0.58$ MeV for all $a_s^{\Lambda N}$ sets. In contrast, the real part $\mathrm{Re}(E^\lambda_{\Lambda nn})$ exhibits large cutoff dependence. As shown in Fig. 1 for the NSC97f case, the pole moves with increasing λ from the unphysical part of the Riemann sheet ($\mathrm{Re}(E)<0$, $\mathrm{Im}(E)<0$; third quadrant) towards the physical one ($\mathrm{Re}(E)>0$, $\mathrm{Im}(E)<0$; fourth quadrant).

In Fig. 2 we compare the trajectories $E_{\Lambda nn}(d_\lambda^{I=1,S=1/2},\lambda)$ for the different values of ΛN scattering lengths, Table 1, at cutoff $\lambda=4$ fm^{-1}. From the figure, we can deduce that the existence of a physically observable Λnn resonance is very sensitive to the ΛN interaction. The latter must be strong enough to ensure the pole's location in the fourth quadrant of a complex energy plane. The figure and Table 1 show that with increasing size of the spin-averaged scattering length $\bar a^{\Lambda N}=3/4a_1^{\Lambda N}+1/4a_0^{\Lambda N}$ the Λnn pole trajectories move closer to the $\Lambda+n+n$ threshold. Moreover, by increasing the cutoff λ the physical Λnn pole is shifted closer to or into the fourth quadrant. In this sense the pole position in the renormalization group invariant limit $\lambda\to\infty$ could be considered as the most favorable to the existence of an observable resonance. Nevertheless, in the $\lambda\to\infty$ limit only two sets of $a_s^{\Lambda N}$ - NSC97f and χEFT(NLO) undoubtedly predict a physical resonance. From the results shown in Fig. 2 we can roughly estimate that $\bar a^{\Lambda N}\approx1.7$ fm^{-1} is the minimal value for the Λnn pole to enter the fourth quadrant, becoming a physical resonance. It should be noted that though the size of $\bar a^{\Lambda N}$ plays a dominant role, one should take into account also the effect of the three-body force which might introduce more complicated dependence on $a_0^{\Lambda N}$ and $a_1^{\Lambda N}$.

3.2. The hypertriton excited state ${}^3_\Lambda H^*(J^\pi=3/2^+)$

The excited state of the hypertriton ${}^3_\Lambda\mathrm{H}^*(J^\pi=3/2^+)$ might be considered as a good candidate for a near-threshold resonance. Indeed, several works demonstrated an emergence of a bound state by increasing rather moderately the ΛN interaction strength. Applying the IACCC method we follow the pole trajectory given by the amplitude of auxiliary 3-body force $d_\lambda^{I=0,S=3/2}$ from a bound region to its physical position in a Λ+deuteron ($\Lambda+d$) continuum. In Fig. 3 we show the ${}^3_\Lambda\mathrm{H}^*$ pole momentum $k=\sqrt{2\mu_{\Lambda d}[E({}^3_\Lambda\mathrm{H}^*)-E_B({}^2\mathrm{H})]}$, $\mu_{\Lambda d}=m_d m_\Lambda/(m_d+m_\Lambda)$, as a function of $d_\lambda^{I=0,S=3/2}$ for Alexander B ΛN scattering lengths and $\lambda=6$ fm^{-1}. We observe that with a decreasing auxiliary attraction the imaginary part of the momentum $\mathrm{Im}(k)$ decreases from positive value (bound state) to a negative value (unbound state) whereas the real part $\mathrm{Re}(k)$ remains equal to zero. This behavior is regarded as definition of a virtual state [42].

Repeating the calculations for various cutoffs and different ΛN scattering lengths, Table 1, we find ${}^3_\Lambda\mathrm{H}^*$ to be a virtual state in all considered cases. As we have seen in the Λnn calculations, the energy of the virtual state E_v is stabilized at cutoffs $\lambda\ge4$ fm^{-1}.

The existence of the ${}^3_\Lambda\mathrm{H}^*$ virtual state is further confirmed by the CSM. We do not see any sign of resonance for all sets of ΛN scattering lengths, cutoffs, or auxiliary 3-body force values $d_\lambda^{I=0,S=3/2}$. Odsuren et al. [43] have showed that the rotated discretized CSM continuum spectra reflect phenomena such as near-threshold virtual states, although one would naively assume that virtual states having $|\arg E|=\pi/2$ are beyond the reach of the CSM. From continuum level density they have extracted the scat-

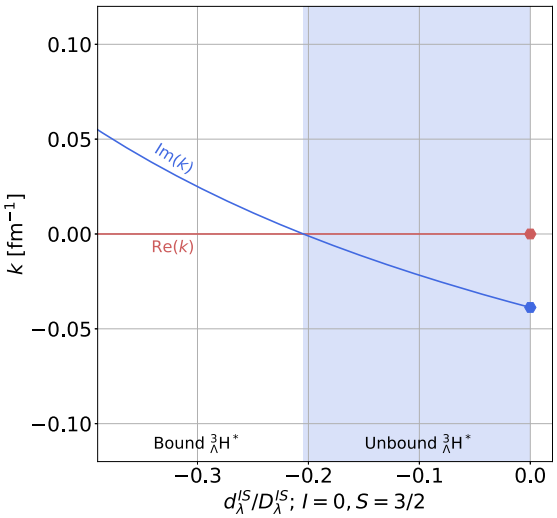

Fig. 3. Imaginary (blue) and real (red) parts of the ${}^3_\Lambda$H* pole momentum k as a function of $d_\lambda^{I=0,S=3/2}$, normalized to the physical three-body LEC $D_\lambda^{I=0,S=3/2}$. Unbound region is determined through the IACCC method. Dots mark the physical solution with for $d_\lambda^{I=0,S=3/2}=0$.

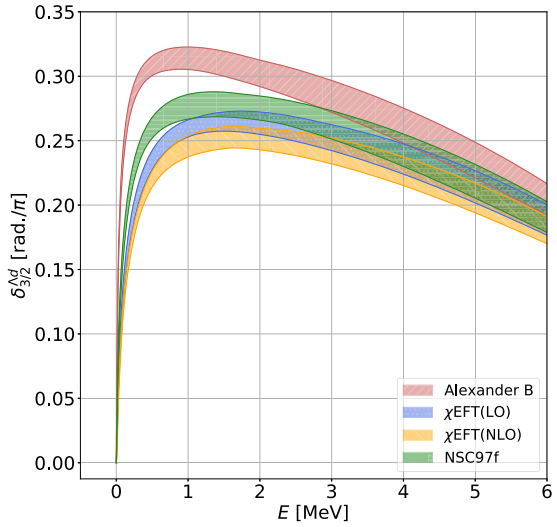

Fig. 4. S-wave Λd phase shifts in the $J^\pi=3/2^+$ channel $\delta_{3/2}^{\Lambda d}$ as a function of energy E above the $\Lambda+d$ threshold, extracted from the continuum level density of the rotated CSM spectra. The phase-shifts are calculated for cut-off $\lambda=6$ fm^{-1} and several ΛN interaction strengths. Shaded areas mark uncertainty introduced by the rotation angle θ within interval $15^\circ<\theta<20^\circ$.

tering phase shifts which revealed enhancement due to the vicinity of the pole [43,44]. Following this approach we calculated the Λd s-wave phase shifts $\delta_{3/2}^{\Lambda d}$ for the $J^\pi=3/2^+$ channel. The calculated phase shifts, presented in Fig. 4, exhibit clear enhancement close to threshold implying proximity of a pole. The shaded areas in the figure reflect the phase shift dependence on rotation angle θ, which we checked for a rather broad interval $15^\circ<\theta<20^\circ$.

The scattering length $a_{3/2}^{\Lambda d}$ and effective range $r_{3/2}^{\Lambda d}$ extracted from the Λd phase shifts reveal through their sign, negative $a_{3/2}^{\Lambda d}$ and positive $r_{3/2}^{\Lambda d}$, the existence of a virtual state [45]. Using $a_{3/2}^{\Lambda d}, r_{3/2}^{\Lambda d}$ the virtual state binding momentum $k_v=\sqrt{2\mu_{\Lambda d}E_v}$ can be approximated by

$$k_v=\frac{i}{r_{3/2}^{\Lambda d}}\left(1-\sqrt{1-\frac{2\,r_{3/2}^{\Lambda d}}{a_{3/2}^{\Lambda d}}}\right). \tag{11}$$

Table 2
Calculated Λd scattering lengths $a_{3/2}^{\Lambda d}$, effective ranges $r_{3/2}^{\Lambda d}$, and virtual state energies E_v in $J^\pi=3/2^+$ channel for several ΛN interaction strengths and cutoff $\lambda=6$ fm^{-1}. Results of two different methods are presented - the continuum level density of rotated CSM spectra and the IACCC method. For the CSM we obtain E_v using relation (11), for the IACCC using the relation $a_{3/2}^{\Lambda d}=-i/\sqrt{2\mu_{\Lambda d}E_v}$. The scattering length and effective range are given in fm, E_v in MeV.

	CSM			IACCC	
	$a_{3/2}^{\Lambda d}$	$r_{3/2}^{\Lambda d}$	E_v	$a_{3/2}^{\Lambda d}$	E_v
Alexander B	-17.3	3.6	-0.08	-25.7	-0.042
NSC97f	-10.8	3.8	-0.18	-16.1	-0.108
χEFT(LO)	-8.5	3.5	-0.28	-12.8	-0.169
χEFT(NLO)	-7.6	3.6	-0.34	-11.7	-0.205

In Table 2 we present the IACCC results for E_v, and an estimate $a_{3/2}^{\Lambda d}=-i/\sqrt{2\mu_{\Lambda d}E_v}$ for the scattering length, together with the scattering parameters $a_{3/2}^{\Lambda d}$ and $r_{3/2}^{\Lambda d}$ extracted from the CSM calculations and the resulting estimate for E_v, Eq. (11). Inspecting the table, one might naively expect clear monotonic dependence of E_v on the spin-triplet scattering length $a_1^{\Lambda N}$. However, the dominance of $a_1^{\Lambda N}$ is undermined by the 3-body force in the $(I,S)=(0,3/2)$ channel, fixed by $B_\Lambda({}^4_\Lambda\mathrm{H}^*)$. Comparing the IACCC and CSM results, one clearly sees that both approaches are in mutual agreement, they exhibit the same dependence on the ΛN interaction strength, though, the CSM yields larger estimates for $|E_v|$. It is a well known drawback of the CSM that eigenvalues in a vicinity of the threshold start to be affected by inaccuracies caused by complex arithmetic.

Concluding this section, we see that at LO $\not\pi$EFT firmly predicts the excited state of hypertriton ${}^3_\Lambda$H*($J^\pi=3/2^+$) to be a virtual state in the vicinity of the $\Lambda-d$ threshold. This result has important implications for prospective experimental search of this state. Experimental observation of ${}^3_\Lambda$H* as a resonance state seems to be highly unlikely. Instead, there is a near-threshold virtual state which should be seen through the enhancement of s-wave Λd phase shifts in the $J^\pi=3/2^+$ channel as demonstrated in Fig. 4.

4. Conclusions

In this work we have presented the first comprehensive $\not\pi$EFT study of continuum hypernuclear ΛNN trios. The underlying nucleon and hyperon interactions were described within a $\not\pi$EFT at LO, with the LECs fixed by 2-body low energy observables and experimental input from 3- and 4-body s-shell systems. The Λnn and ${}^3_\Lambda$H* energies were then obtained as predictions of the theory. In view of poor low energy ΛN scattering data we considered several sets of ΛN scattering lengths, whereas the NN interaction remained constrained by experiment [18].

Few-body wave functions were described within a correlated gaussians basis. Bound state solutions were obtained using the SVM. The continuum region was studied employing two independent methods - the IACCC method and CSM.

The $\not\pi$EFT predicts that both Λnn and ${}^3_\Lambda$H* are unbound. Tuning the 3-body LECs to put the Λnn or ${}^3_\Lambda$H* binding energy on threshold, yielded considerable discrepancy between the calculated and measured B_Λ in the $A=4,5$ hypernuclei. Our findings further strengthen the conclusions of previous theoretical studies that both states are unbound [4–10,16,17].

Our LO $\not\pi$EFT calculations predict Λnn and ${}^3_\Lambda$H* to be near-threshold continuum states. We thus anticipate that the EFT truncation error is small due to low characteristic momenta and thus higher order corrections would not change our results qualitatively. We conclude that position of the Λnn pole depends strongly on the spin independent scattering length $\bar{a}^{\Lambda N}$. For $\bar{a}^{\Lambda N}\gtrsim 1.7$ fm^{-1} the Λnn pole becomes a physical resonance close to threshold

with $E_r \leq 0.3$ MeV, and a large width most likely in the range $1.16 \leq \Gamma \leq 2.00$ MeV. If observed, the position of the Λnn resonance can yield tight constraints on the ΛN scattering length. We note, however, that the exact position of the Λnn depends both on $a_0^{\Lambda N}$ and $a_1^{\Lambda N}$, and also on subleading $\not\pi$EFT terms neglected here. The excited state of hypertriton ${}^{3}_{\Lambda}\mathrm{H}^{*}$ was firmly predicted to be a near-threshold virtual state regardless of the value of $a_s^{\Lambda N}$. We have demonstrated that this virtual state has a strong effect on the Λd s-wave phase shifts in $J^{\pi} = 3/2^{+}$ channel.

Declaration of competing interest

The authors declare that they have no known competing financial interests or personal relationships that could have appeared to influence the work reported in this paper.

Acknowledgements

We are grateful to Avraham Gal for valuable discussions and careful reading of the manuscript. This work was partly supported by the Czech Science Foundation GACR grant 19-19640S. The work of NB was supported by the PAZY Foundation and by the Israel Science Foundation grant 1308/16.

References

[1] A. Gal, E.V. Hungerford, D.J. Millener, Rev. Mod. Phys. 88 (2016) 035004.
[2] D.H. Davis, Nucl. Phys. A 754 (2005) 3c.
[3] C. Rappold, et al., HypHI Collaboration, Phys. Rev. C 88 (2013) 041001(R).
[4] B.W. Downs, R.H. Dalitz, Phys. Rev. 114 (1959) 593.
[5] H. Garcilazo, J. Phys. G 13 (1987) 63.
[6] A. Gal, H. Garcilazo, Phys. Lett. B 736 (2014) 93.
[7] H. Garcilazo, T. Fernández-Caramés, A. Valcarce, Phys. Rev. C 75 (2007) 034002; H. Garcilazo, T. Fernández-Caramés, A. Valcarce, Phys. Rev. C 76 (2007) 034001.
[8] H. Garcilazo, A. Valcarce, Phys. Rev. C 89 (2014) 057001.
[9] K. Miyagawa, H. Kamada, W. Glöckle, V. Stoks, Phys. Rev. C 51 (1995) 2905.
[10] E. Hiyama, S. Ohnishi, B.F. Gibson, Th.A. Rijken, Phys. Rev. C 89 (2014) 061302(R).
[11] S.-I. Ando, U. Raha, Y. Oh, Phys. Rev. C 92 (2015) 024325.
[12] F. Hildenbrand, H.-W. Hammer, Phys. Rev. C 100 (2019) 034002.
[13] S. Bleser, M. Bölting, T. Gaitanos, J. Pochodzalla, F. Schupp, M. Steinen, AIP Conf. Proc. 2130 (2019) 030001.
[14] JLab, E12-17-003, https://misportal.jlab.org/mis/physics/experiments/viewProposal.cfm?paperId=917, 2020.
[15] JLab proposal P12-19-002, https://www.jlab.org/exp_prog/proposals/19/PR12-19-002.pdf, 2020.
[16] V.B. Belyaev, S.A. Rakityansky, W. Sandhas, Nucl. Phys. A 803 (2008) 210.
[17] I.R. Afnan, B.F. Gibson, Phys. Rev. C 92 (2015) 054608.
[18] L. Contessi, N. Barnea, A. Gal, Phys. Rev. Lett. 121 (2018) 102502.
[19] U. van Kolck, Nucl. Phys. A 645 (1999) 273.
[20] P.F. Bedaque, H.-W. Hammer, U. van Kolck, Nucl. Phys. A 676 (2000) 357.
[21] N. Barnea, L. Contessi, D. Gazit, F. Pederiva, U. van Kolck, Phys. Rev. Lett. 114 (2015) 052501.
[22] J. Kirscher, N. Barnea, D. Gazit, F. Pederiva, U. van Kolck, Phys. Rev. C 92 (2015) 054002.
[23] L. Contessi, A. Lovato, F. Pederiva, A. Roggero, J. Kirscher, U. van Kolck, Phys. Lett. B 772 (2017) 839.
[24] J. Kirscher, E. Pazy, J. Drachman, N. Barnea, Phys. Rev. C 96 (2017) 024001.
[25] K. Varga, Y. Suzuki, Phys. Rev. C 52 (1995) 2885.
[26] Y. Suzuki, K. Varga, Stochastic Variational Approach to Quantum-Mechanical Few-Body Problems, Springer, 1998.
[27] B. Bazak, M. Eliyahu, U. van Kolck, Phys. Rev. A 94 (2016) 052502.
[28] G. Alexander, U. Karshon, A. Shapira, et al., Phys. Rev. 173 (1968) 1452.
[29] Th.A. Rijken, V.G.J. Stoks, Y. Yamamoto, Phys. Rev. C 59 (1999) 21.
[30] H. Polinder, J. Haidenbauer, U.-G. Meißner, Nucl. Phys. A 779 (2006) 244.
[31] J. Haidenbauer, S. Petschauer, N. Kaiser, U.-G. Meißner, A. Nogga, W. Weise, Nucl. Phys. A 915 (2013) 24.
[32] J. Augilar, J.M. Combes, Commun. Math. Phys. 22 (1971) 269; E. Balslev, J.M. Combes, Commun. Math. Phys. 22 (1971) 280.
[33] S. Aoyama, T. Myo, K. Katō, K. Ikeda, Prog. Theor. Phys. 116 (2006) 1.
[34] T.D. Fedorov, et al., Few-Body Syst. 45 (2009) 191.
[35] V.M. Kukulin, V.M. Krasnopol'sky, J. Phys. A 10 (1977) 33; V.M. Krasnopol'sky, V.I. Kukulin, Phys. Lett. A 69 (1978) 251; V.I. Kukulin, V.M. Krasnopol'sky, M. Miselkhi, Sov. J. Nucl. Phys. 29 (1979) 421.
[36] N. Tanaka, Y. Suzuki, K. Varga, R.G. Lovas, Phys. Rev. C 59 (1999) 1391.
[37] R. Lazauskas, E. Hiyama, J. Carbonell, Phys. Lett. B 791 (2019) 335, and references therein.
[38] N. Tanaka, Y. Suzuki, K. Varga, Phys. Rev. C 56 (1997) 562.
[39] V.I. Kukulin, V.M. Krasnopol'sky, J. Horáček, Theory of Resonances, Principles and Applications, Kluwer Academic Publishers, 1989.
[40] J. Horáček, L. Pichl, Commun. Comput. Phys. 21 (2017) 1154.
[41] L. Contessi, N. Barnea, A. Gal, AIP Conf. Proc. 2130 (2019) 040012.
[42] J.R. Taylor, Scattering Theory: Quantum Theory on Nonrelativistic Collisions, 99 edition, Willey, 1972.
[43] M. Odsuren, Y. Kikuchi, T. Myo, G. Khuukhenkhuu, H. Masui, K. Katō, Phys. Rev. C 95 (2017) 064305.
[44] M. Odsuren, K. Katō, M. Aikawa, T. Myo, Phys. Rev. C 89 (2014) 034322.
[45] T. Hyodo, Phys. Rev. Lett. 111 (2013) 132002.

Nature of the Λnn $(J^\pi = 1/2^+, I = 1)$ and ${}^3_\Lambda\mathrm{H}^*(J^\pi = 3/2^+, I = 0)$ states

M. Schäfer*
Czech Technical University in Prague, Faculty of Nuclear Sciences and Physical Engineering, Břehová 7, 11519 Prague 1, Czech Republic and
Nuclear Physics Institute of the Czech Academy of Sciences, 25069 Řež, Czech Republic

B. Bazak† and N. Barnea‡
Racah Institute of Physics,The Hebrew University, Jerusalem 91904, Israel

J. Mareš§
Nuclear Physics Institute of the Czech Academy of Sciences, 25069 Řež, Czech Republic
(Dated: July 24, 2020)

The nature of the Λnn and ${}^3_\Lambda\mathrm{H}^*(J^\pi = 3/2^+,\ I = 0)$ states is investigated within a pionless effective field theory at leading order, constrained by the low energy ΛN scattering data and hypernuclear 3- and 4-body data. Bound state solutions are obtained using the stochastic variational method, the continuum region is studied by employing two independent methods - the inverse analytic continuation in the coupling constant method and the complex scaling method. Our calculations yield both the Λnn and ${}^3_\Lambda\mathrm{H}^*$ states unbound. We conclude that the excited state ${}^3_\Lambda\mathrm{H}^*$ is a virtual state and the Λnn pole located close to the three-body threshold in a complex energy plane could convert to a true resonance with $\mathrm{Re}(E) > 0$ for some considered ΛN interactions. Finally, the stability of resonance solutions is discussed and limits of the accuracy of performed calculations are assessed.

I. INTRODUCTION

The s-shell Λ hypernuclei play an important role in the study of baryon-baryon interactions in the strangeness sector. In view of scarce hyperon-nucleon scattering data they provide a unique test ground for the underlying interaction models thanks to reliable few-body techniques. In particular, experimental values of the Λ separation energies in $A = 3,\ 4$ Λ hypernuclei including their known spin and parity assignments, as well as the ${}^4_\Lambda\mathrm{H}^*$ and ${}^4_\Lambda\mathrm{He}^*$ excitation energies represent quite stringent constraints (see [1] and references therein).

The hypertriton ${}^3_\Lambda\mathrm{H}$ $(J^\pi = 1/2^+,\ I = 0)$ is the lightest known hypernucleus, with the Λ separation energy $B_\Lambda = 0.13 \pm 0.05$ MeV [2]. In view of the small value of B_Λ in the hypertriton ground state, it is likely that the excited state ${}^3_\Lambda\mathrm{H}^*$ $(J^\pi = 3/2^+,\ I = 0)$ is located just above the $\Lambda + d$ threshold, however, its physical nature is not yet known. Moreover, since the isospin-triplet NN state is unbound, it is highly unlikely that there exists a bound state in the $I = 1$ Λnn system. A thorough study of the $A = 3$ hypernuclear systems with different spin and isospin, addressing the question whether they are bound or continuum states, provides invaluable information about the spin and isospin dependence of the ΛN interaction, as well as dynamical effects in these few-body systems caused by a Λ hyperon. Moreover, the issue of the Λnn and also $\Lambda\Lambda nn$ states as possible candidates for widely discussed bound neutral nuclear systems has attracted increased attention recently in connection with the experimental evidence for the bound Λnn state reported by the HypHI collaboration [3].

The first variational calculation demonstrating that the Λnn system is unbound was performed by Dalitz and Downs more than 50 years ago [4]. Later, this conclusion was further supported by Garcilazo using Faddeev approach with separable potentials [5]. Following, more detailed, studies of both Λnn and ${}^3_\Lambda\mathrm{H}^*$ systems within Faddeev approach using either Nijmegen YN potential [6] or chiral constituent quark model of YN interactions [7, 8] confirmed that both systems are indeed unbound. In addition, these calculations revealed that with increasing YN attraction the binding of ${}^3_\Lambda\mathrm{H}^*$ comes first. The investigation of the Λd scattering length in $J^\pi = 3/2^+$ channel indicated existence of a pole in the vicinity of the $\Lambda + d$ threshold. Continuum calculations of the unbound Λnn system were performed by Belyaev et al. using a phenomenological ΛN potential [9]. This neutral hypernuclear system was found to form a very wide, near-threshold resonance.

In view of the above theoretical calculations, the claimed evidence of the Λnn reported by HypHI Collaboration was quite surprising and it stimulated renewed interest in the nature of the 3-body hypernuclear states. The HypHI conclusions were seriously challenged by succeeding calculations [10, 11], demonstrating inconsistency of the existence of the Λnn bound state with ΛN scattering as well as 3- and 4-body hypernuclear data. Furthermore, the renewed analysis of the BNL-AGS-E906 experiment [12] led to conclusion that the formation of a bound Λnn nucleus is highly unlikely. In addition, rather recently Gal and Garzilazo [13] made a

* m.schafer@ujf.cas.cz
† betzalel.bazak@mail.huji.ac.il
‡ nir@phys.huji.ac.il
§ mares@ujf.cas.cz

rough but solid estimate of Λnn lifetime which, if bound, is considerably longer than the one of free Λ hyperon τ_Λ. This result is in disagreement with the shorter Λnn lifetime with respect to τ_Λ extracted from the HypHI events assigned to this system. The Λnn was also explored within pionless effective field theory ($\not\pi$EFT) [14, 15].

In spite of the apparent interest the Λnn and ${}^{3}_{\Lambda}\mathrm{H}^{*}$ continuum states have been investigated in only few theoretical works[9, 16, 17]. Afnan and Gibson [16] performed Faddeev calculations of Λnn using two-body separable potentials fitted to reproduce NN and ΛN scattering lengths and effective ranges. They pointed out that while Λnn pole appears in the subthreshold region ($\mathrm{Re}(E)<0$), only small increase of the ΛN interaction strength produces a Λnn resonance ($\mathrm{Re}(E)>0$). This work encouraged the search for the Λnn system in the JLab E12-17-003 experiment [18].

In this work, we performed few-body calculations of the Λnn and ${}^{3}_{\Lambda}\mathrm{H}^{*}$ hypernuclear systems within LO $\not\pi$EFT , both in the bound and continuous region, exploring thoroughly their nature. The first selected results have been reported in Ref. [17]. As demonstrated in that work the virtual state ${}^{3}_{\Lambda}\mathrm{H}^{*}$ pole position close to the $\Lambda+d$ threshold strongly affects the Λd s-wave phase shifts in $J^\pi = 3/2^+$ channel. The calculated Λd scattering lengths and effective ranges from this work were further employed by Haidenbauer in the study of Λd correlation functions within the Lednicky-Lyuboshits formalism [19]. It is to be noted that the nature of the ${}^{3}_{\Lambda}\mathrm{H}^{*}$ state is a subject of the JLab proposal P12-19-002 [20].

The $\not\pi$EFT approach was applied to s-shell Λ hypernuclei and, among others, the experimental value of the Λ separation energy B_Λ in ${}^{5}_{\Lambda}\mathrm{He}$ was successfully reproduced [21]. The $\not\pi$EFT was further extended to $S=-2$ sector with the aim to study the onset of binding in $\Lambda\Lambda$ hypernuclei [22]. Finally, in the present work the $\not\pi$EFT is applied to the study of continuum states in 3-body hypernuclear systems. Bound state calculations are performed using the Stochastic Variational Method (SVM), the continuum states are described within the Inverse Analytic Continuation in the Coupling Constant (IACCC) Method and the Complex Scaling Method (CSM). The IACCC calculations are benchmarked against the CSM and the stability of resonance solutions is discussed. The CSM is in addition used to set limits of the accuracy of performed calculations.

The paper is organized as follows: In Section II, we first give a brief description of the $\not\pi$EFT approach and the SVM method applied in the calculations of few-body hypernuclear systems. Then, we introduce the CSM and IACCC method used to describe continuum states and pole movement in a complex energy plane. In Section III, we present results of our study of the Λnn and ${}^{3}_{\Lambda}\mathrm{H}^{*}$ systems. We discuss in more detail the relation between the applied LO $\not\pi$EFT approach and phenomenological models and, in particular, the stability and numerical accuracy of our $\not\pi$EFT calculations. Finally, we summarize our findings in Section V.

II. MODEL AND METHODOLOGY

Hypernuclear systems studied in this work are described within the $\not\pi$EFT at LO which was introduced in detail in [21]. In this section we present only basic ingredients of the theory. The LO $\not\pi$EFT contains 2- and 3-body s-wave contact interaction terms, each of them associated with corresponding isospin-spin channel. The contact terms are then regularized by applying a Gaussian regulator with momentum cutoff λ. This procedure yields two-body V_2 and three-body V_3 potentials which together with the kinetic energy T_k enter the total Hamiltonian H :

$$H = T_\mathrm{k} + V_2 + V_3, \tag{1}$$

where

$$V_2 = \sum_{I,S} C_\lambda^{I,S} \sum_{i<j} \mathcal{P}_{ij}^{I,S} \mathrm{e}^{-\frac{\lambda^2}{4} r_{ij}^2} \tag{2}$$

and

$$V_3 = \sum_{I,S} D_\lambda^{I,S} \sum_{i<j<k} \mathcal{Q}_{ijk}^{I,S} \sum_{\mathrm{cyc}} \mathrm{e}^{-\frac{\lambda^2}{4}\left(r_{ij}^2 + r_{jk}^2\right)}. \tag{3}$$

Here, $\mathcal{P}_{ij}^{I,S}$ and $\mathcal{Q}_{ijk}^{I,S}$ are the projection operators to 2- and 3-body s-wave isospin-spin (I,S) channels and the 2- and 3-body low energy constants (LECs) $C_\lambda^{I,S}$ and $D_\lambda^{I,S}$ are fixed for each λ by experimental data. The momentum cutoff λ might be understood as a scale parameter with respect to a typical momentum Q. Calculated observables exhibit residual cutoff dependence $\mathcal{O}(Q/\lambda)$ suppressed with λ approaching the renormalization group invariant limit $\lambda \to \infty$ [21].

There are in total 4 two-body (NN, ΛN) and 4 three-body (NNN, ΛNN) LECs. Nuclear LECs $C_\lambda^{I=0,S=1}$, $C_\lambda^{I=1,S=0}$, and $D_\lambda^{I=1/2,S=1/2}$ are fitted to the deuteron binding energy, NN spin-singlet scattering length a_0^{NN}, and to the triton binding energy, respectively. Hypernuclear two-body LECs $C_\lambda^{I=1/2,S=0}$ and $C_\lambda^{I=1/2,S=1}$ are fixed by the ΛN scattering length in a spin-singlet $a_0^{\Lambda N}$ and spin-triplet $a_1^{\Lambda N}$ channel. Three-body hypernuclear LECs $D_\lambda^{I=0,S=1/2}$, $D_\lambda^{I=1,S=1/2}$, and $D_\lambda^{I=0,S=3/2}$ are fitted to the experimental values of Λ separation energies $B_\Lambda({}^{3}_{\Lambda}\mathrm{H})$, $B_\Lambda({}^{4}_{\Lambda}\mathrm{H})$ and the excitation energy $E_\mathrm{exc}({}^{4}_{\Lambda}\mathrm{H}^{*})$.

Since $a_0^{\Lambda N}$ and $a_1^{\Lambda N}$ are not constrained sufficiently well by experiment, we use their values given by direct analysis of scattering data [23] or predicted by several models of ΛN interaction [24–26]. Considered $a_0^{\Lambda N}$ and $a_1^{\Lambda N}$ together with the data used to fix NN spin-singlet ${}^1S_0$ and spin-triplet ${}^3S_1$ LECs are given in Table. I. The $\not\pi$EFT approach was applied to s-shell Λ hypernuclei and, among others, the experimental value of the Λ separation energy B_Λ in ${}^{5}_{\Lambda}\mathrm{He}$ was successfully reproduced [21] as demonstrated in the last column of Table I.

The calculation of $A = 3, 4, 5$ -body s-shell Λ hypernuclear systems are performed within finite basis set of

TABLE I. Values of spin-singlet $a_0^{\Lambda N}$ and spin-triplet $a_1^{\Lambda N}$ scattering lengths[a] used to fit hypernuclear 2-body LECs together with effective ranges $r_0^{\Lambda N}$ and $r_1^{\Lambda N}$ (in fm). Corresponding Λ separation energies $B_\Lambda({}^5_\Lambda\mathrm{He};\infty)$ (in MeV), predicted within $\not\pi$EFT for $\lambda\to\infty$ [21] are to be compared with the experimental value $B_\Lambda({}^5_\Lambda\mathrm{He}) = 3.12(2)$ MeV [2].

	$a_0^{\Lambda N}$	$r_0^{\Lambda N}$	$a_1^{\Lambda N}$	$r_1^{\Lambda N}$	$B_\Lambda({}^5_\Lambda\mathrm{He};\infty)$
Alexander B [23]	-1.80	2.80	-1.60	3.30	3.01(10)
NSC97f [24]	-2.60	3.05	-1.71	3.33	2.74(11)
χEFT(LO) [25]	-1.91	1.40	-1.23	2.20	3.96(08)
χEFT(NLO) [26]	-2.91	2.78	-1.54	2.27	3.01(06)
NN [27, 28]	-18.63	2.75	$E_\mathrm{B}({}^2\mathrm{H}) = -2.22457$ MeV		

[a] We use the effective range expansion sign convention defined as $k\mathrm{cotg}(\delta) = -\frac{1}{a_s} + \frac{1}{2}r_s k^2 + \cdots$.

correlated Gaussians [29]

$$\psi_i = \hat{\mathcal{A}}\,\exp\left(-\frac{1}{2}\mathbf{x}^T A_i \mathbf{x}\right)\chi^i_{SM_S}\xi^i_{IM_I}, \qquad (4)$$

where the operator $\hat{\mathcal{A}}$ ensures antisymmetrization between nucleons, $\mathbf{x}^T = (\mathbf{x}_1,\ldots,\mathbf{x}_{A-1})$ is a set of Jacobi coordinates, and $\chi^i_{SM_S}$ and $\xi^i_{IM_I}$ stand for corresponding spin and isospin parts, respectively. Each ψ_i includes $A(A-1)/2$ nonlinear parameters which are placed in the $(A-1)$ dimensional positive-definite symmetric matrix A_i plus 2 discreet parameters which represent different spin and isospin configuration in $\chi^i_{SM_S}$ and $\xi^i_{IM_I}$, respectively.

In order to choose ψ_i with the most appropriate nonlinear parameters we use the Stochastic Variational Method (SVM) [30] which was proved to provide systematic procedure to optimize the finite basis set, thus reaching highly accurate bound state description.

Resonances and virtual states, predominantly interpreted as poles of S-matrix [31, 32], can not be addressed directly using the SVM with the finite basis set. Consequently, in order to study hypernuclear continuum we apply the Inverse Analytic Continuation in the Coupling Constant (IACCC) method [33] which was proposed as numerically more stable alternative to the Analytic Continuation in the Coupling Constant [34].

Following the spirit of analytical continuation techniques we supplement the Hamiltonian H (1) by an auxiliary 3-body attractive potential

$$V_3^{\mathrm{IACCC}} = d_\lambda^{I,S}\sum_{i<j<k}\mathcal{Q}^{I,S}_{ijk}\sum_{\mathrm{cyc}}\mathrm{e}^{-\frac{\lambda^2}{4}\left(r_{ij}^2+r_{jk}^2\right)}, \qquad (5)$$

where the amplitude $d_\lambda^{I,S}$ defines its strength and is negative for attraction. The projection operator $\mathcal{Q}^{I,S}_{ijk}$ ensures that the potential affects only a particular (I,S) three-body channel - $(1,\frac{1}{2})$ for Λnn or $(0,\frac{3}{2})$ for ${}^3_\Lambda\mathrm{H}^*$. If not explicitly mentioned λ in V_3^{IACCC} is equal to the $\not\pi$EFT cutoff λ. In principle one can use a rather large class of 2- or 3-body attractive auxiliary potentials which fulfill certain criteria imposed by analytic continuation [32]. Using V_3^{IACCC} (5) ensures that the properties of 2-body part of the $\not\pi$EFT Hamiltonian (1) such as scattering lengths or deuteron binding energy remain unaffected. Its form is selected to be the same as of the $\not\pi$EFT 3-body potential (1).

With increasing attractive strength of $d_\lambda^{I,S}$ the resonance or virtual state S-matrix pole described by H starts to move towards the bound state region and at certain $d_{0,\,\lambda}^{I,S}$ becomes a bound state. The other way around, studying bound state energy E_B as a function of $d_\lambda^{I,S} < d_{0,\,\lambda}^{I,S}$ we can perform an analytic continuation of the pole position from the bound region back into the continuum ($d_\lambda^{I,S} > d_{0,\,\lambda}^{I,S}$) up to the point of its physical position with no auxiliary force ($d_\lambda^{I,S} = 0$).

In practice, we apply the SVM to calculate a set of $M+N+1$ bound state energies for different values of the coupling constant $\{E^i_\mathrm{B}(d_i)\ ;\ d_i < d_0\ ;\ i = 1,\ldots,M+N+1\}$, where $d_i = d_{i,\,\lambda}^{I,S}$. Next, using this set we construct the Padé approximant of degree (M,N) $\mathcal{P}^{(M,N)}$ of function $d(\kappa)$

$$\mathcal{P}^{(M,N)}(\kappa) = \frac{\sum_{j=0}^{M} b_j\kappa^j}{1+\sum_{j=1}^{N} c_j\kappa^j} \approx d(\kappa), \qquad (6)$$

where b_j and c_j are real parameters of the $\mathcal{P}^{(M,N)}$. The κ is defined as $\kappa = -\mathrm{i}k = -\mathrm{i}\sqrt{E}$ with E standing for a bound state energy with respect to the nearest dissociation threshold. The position of the S-matrix pole corresponding to H is calculated setting $d = 0$ in Eq. (6) which leads to the the simple polynomial equation

$$\sum_{j=0}^{M} b_j\kappa^j = 0. \qquad (7)$$

The resonance or virtual state energy with respect to the nearest threshold is then obtained as $E = (\mathrm{i}\kappa)^2$, where κ now corresponds to the physical root of Eq. (7). Here, for complex resonance energy, we use the notation $E = E_r - \mathrm{i}\Gamma/2$, where $E_r = \mathrm{Re}(E)$ is the position of the resonance and $\Gamma = -2\ \mathrm{Im}(E)$ stands for the resonance width.

Using the IACCC method we study the whole pole trajectory $E(d)$ in the continuum region $d \in \langle d_0; 0\rangle$ (see Fig. 4). For a given set of bound state energies $\{E^i_\mathrm{B}(d_i)\ ;\ d_i < d_0\ ;\ i = 1,\ldots,M+N+1\}$, we shift $d_i \to d - d_i$ in the $E^i_\mathrm{B}(d_i)$ set, construct new Padé approximant (6), and obtain $E(d)$ as a corresponding root of Eq. (7).

The specific choice of V_3^{IACCC} (5) provides clear physical interpretation for any $d_\lambda^{I,S}$ solution. By varying $d_\lambda^{I,S}$ the Λnn or ${}^3_\Lambda\mathrm{H}^*$ pole moves along its trajectory $E(d_\lambda^{I,S},\lambda)$ which is defined purely by the underlying 2-body interactions and cutoff λ. Supplementing the physical Hamiltonian (1) by V_3^{IACCC} might be understood as a shift of

the three-body LEC constant $D_\lambda^{I,S} \to D_\lambda^{I,S} + d_\lambda^{I,S}$. Since $D_\lambda^{I=1,S=1/2}$ and $D_\lambda^{I=0,S=3/2}$ have been fitted for each λ to the experimental value of $B_\Lambda({}^4_\Lambda\mathrm{H})$ and $E_{\mathrm{exc}}({}^4_\Lambda\mathrm{H}^*)$, respectively [21], one could assign the parts of trajectories for $d_\lambda^{I,S} < 0$ to an overbound 4-body system. In other words, for a given set of $a_0^{\Lambda N}$ and cutoff λ the trajectory $E(d_\lambda^{I=1,S=1/2}, \lambda)$ of Λnn pole positions corresponds to different values of $B_\Lambda({}^4_\Lambda\mathrm{H})$ and similarly the trajectory $E(d_\lambda^{I=0,S=3/2}, \lambda)$ of ${}^3_\Lambda\mathrm{H}^*$ pole positions corresponds to different values of $E_{\mathrm{exc}}({}^4_\Lambda\mathrm{H}^*)$.

For each IACCC resonance calculation we benchmark part of the corresponding pole trajectory against the Complex Scaling Method (CSM) [35]. The main ingredient of the CSM is a transformation $U(\theta)$ of relative coordinates $\mathbf{r}$ and their conjugate momenta $\mathbf{k}$

$$U(\theta)\mathbf{r} = \mathbf{r}e^{\mathrm{i}\theta}, \quad U(\theta)\mathbf{k} = \mathbf{k}e^{-\mathrm{i}\theta}, \tag{8}$$

where θ is a real positive scaling angle. Applying this transformation to the Schrödinger equation one obtains its complex scaled version

$$H(\theta)\Psi(\theta) = E(\theta)\Psi(\theta), \tag{9}$$

where $H(\theta) = U(\theta)HU^{-1}(\theta)$ is the complex scaled Hamiltonian and $\Psi(\theta) = U(\theta)\Psi$ is the corresponding wave function. For large enough θ, the divergent asymptotic part of the resonance wave function is suppressed and $\Psi(\theta)$ is normalizable - possible resonant states can then be obtained as discrete solutions of Eq. (9) [36]. In order to prevent divergence of the complex scaled Gaussian potential (1) the scaling angle is limited to $\theta < \frac{\pi}{4}$.

A mathematically rigorous formulation of the CSM for a two-body system results in the ABC theorem [35] which provides description of the behavior of a complex scaled energy $E(\theta)$ with respect to θ : (i) Bound state energies remain unaffected (ii) The continuum spectrum rotates clockwise in a complex energy plane by angle 2θ from the real axis with its center of rotation at the corresponding threshold (iii) For $\theta > \theta_r = \frac{1}{2}\arctan\left(\frac{\Gamma}{2E_r}\right)$ corresponding to the resonance energy E_r and width Γ, the resonance is described by a square-integrable function and its energy and width are given by a complex energy $E(\theta) = E_r - \mathrm{i}\Gamma/2$ which does not change further with increasing θ.

In this work, we expand $\Psi(\theta)$ in a finite basis of correlated Gaussians (4)

$$\Psi(\theta) = \sum_{i=1}^{N} c_i(\theta)\ \psi_i. \tag{10}$$

Both resonance energies $E(\theta)$ and corresponding coefficients $c_i(\theta)$ are then obtained using the c-variational principle [37] as a solution of generalized eigenvalue problem

$$\sum_{j=1}^{N} (\psi_i|H(\theta)|\psi_j)\, c_j^\alpha(\theta) = E^\alpha(\theta) \sum_{j=1}^{N} (\psi_i|\psi_j)\, c_j^\alpha(\theta), \tag{11}$$

where $(|)$ stands for the c-product (bi-orthogonal product) [36, 38]. In the case of real ψ_i, the c-product in Eq. (11) is equivalent to the inner product $< | >$. It was proved that the solutions of Eq. (11) are stationary in the complex variational space, and for $N \to \infty$ they are equal to exact solutions of the complex scaled Schrödinger equation (9) [37]. Nevertheless, with increasing number of basis states the solution stabilizes and there is no upper or lower bound to an exact resonance solution [39].

In fact, due to a finite dimension of the basis set the resonance energy $E(\theta)$ (11) moves with increasing scaling angle along the θ-trajectory even for $\theta > \theta_r$, featuring residual θ dependence [36, 40]. It was demonstrated that following the generalized virial theorem [37, 41] the best estimate of a resonance energy is given by the most stationary point of the θ-trajectory, i.e. such $E(\theta_{\mathrm{opt}})$ for which the residual θ dependence is minimal but not necessarily equal to zero

$$\left|\frac{\mathrm{d}E(\theta)}{\mathrm{d}\theta}\right|_{\theta_{\mathrm{opt}}} \approx 0. \tag{12}$$

A real scaling angle θ is frequently used in finite basis CSM calculations with satisfactory results [40, 42, 43]. However, identifying the resonance energy with $E(\theta_{\mathrm{opt}})$ using the θ-trajectory ($\mathrm{Im}(\theta) = 0$, $\mathrm{Re}(\theta)$ changing) is still approximate. As pointed out by Moiseyev [39] the resonance stationary condition requires exact equality in Eq. (12), which can be achieved in a finite basis set by considering complex θ_{opt}. Consequently, taking θ real introduces certain theoretical error and it is problematic to quantify how much the result obtained using θ-trajectory technique deviates from the true CSM resonance solution (zero derivative in Eq. (12)).

Following Aoyama et al. [36] we use both θ-trajectory and β-trajectories ($\mathrm{Re}(\theta)$ fixed, $\mathrm{Im}(\theta)$ changing) to locate the position of the true CSM solution. In the above work it was numerically demonstrated that for certain $\mathrm{Re}(\theta_{\mathrm{opt}})$ the θ-trajectory approaches the stationary point and then starts to move away. On the other hand, the β-trajectories are roughly circles with decreasing radius as the corresponding $\mathrm{Re}(\theta)$ approaches $\mathrm{Re}(\theta_{\mathrm{opt}})$. In view of orthogonality of the θ- and β-trajectories at given scaling angle θ, the true CSM solution is then located inside an area given by circular β-trajectories. More specifically, it is identified as the center of the circular β-trajectory with the smallest radius where the CSM error is given by the size of this radius [36].

Another non-trivial task is to determine an appropriate yet not excessively large correlated Gaussian basis which yields stable CSM resonance solution. In this work, we apply the HO trap technique [17] which introduces systematic algorithm how to select such basis. First, we place a resonant system described by the Hamiltonian H into a harmonic oscillator (HO) trap

$$H^{\mathrm{trap}}(b) = H + V^{\mathrm{HO}}(b), \quad V^{\mathrm{HO}}(b) = \frac{\hbar^2}{2mb^4} \sum_{j<k} r_{jk}^2, \tag{13}$$

where b is the HO trap length and m is an arbitrary mass scale. Next, for given b we apply the SVM to determine basis set which yields accurate description of the ground as well as excited states of $H^{\rm trap}(b)$. The potential $V^{\rm HO}(b)$ plays a role analogous to a box boundary condition (though not so stringent) – the SVM procedure promotes basis states with their typical radius given by the trap length b. By increasing b we enlarge the typical radius of the correlated Gaussians ψ_i. For large enough b, the CSM resonance solution for the Hamiltonian H starts to stabilize and both the short range and suppressed long range asymptotic parts of a resonance wave function are described sufficiently well.

For $\theta \geq \theta_r$ the CSM resonant wave function $\Psi(\theta)$ is localized at certain interaction region whereas its asymptotic part is suppressed by the CSM transformation (8). Consequently, we use the HO trap technique in order to build the CSM basis which describes physically relevant interaction region of $\Psi(\theta)$ up to certain large enough $R_{\rm max}$ beyond which the asymptotic part does not contribute significantly to the CSM solution .

In practice, for each CSM calculation, we apply the HO trap technique to independently select basis sets for a grid of increasing trap lengths $\{b_i; b_i \leq b_{\rm max}\}$. Next, merging these sets into a larger CSM basis we calculate the resonance θ-trajectory solving Eq. (11). In the last step we study stabilization of the θ-trajectory with increasing $b_{\rm max}$ considered in the merged basis set. For more details and an example see Subsection III A.

III. RESULTS

We applied the LO $\not\pi$EFT approach with 2- and 3-body regulated contact terms defined in Eq. (1) to the study of the s-shell Λ hypernuclei, the Λnn and ${}^3_\Lambda{\rm H}^*(J^\pi = 3/2^+,\ I = 0)$ systems in particular. In this section, we present results of the calculations and provide comparison of the results obtained within our LO $\not\pi$EFT approach and phenomenological models. In a separate subsection, we discuss in detail stability and numerical accuracy of the presented SVM and IACCC resonance solutions.

The additional auxiliary 3-body potential $V_3^{\rm IACCC}$ (5) introduced to study continuum states allows us to vary the amount of attraction and thus explore different scenarios, as demonstrated in Fig. 1. Here, the Λnn and ${}^3_\Lambda{\rm H}^*$ bound state energies $E_{\rm B}$ are plotted as a function of the strength $d_\lambda^{I,S}$ of the auxiliary force normalized to the strength $D_\lambda^{I,S}$ of the 3-body ΛNN potential of the $\not\pi$EFT . In the limiting case $d_\lambda^{I,S}/D_\lambda^{I,S} = -1$, the 3-body repulsion is completely canceled and the systems undergo Thomas collapse [44] in the limit of $\lambda \to \infty$. For suitably chosen values of $d_\lambda^{I,S}/D_\lambda^{I,S}$ between -1 and 0, both Λnn and ${}^3_\Lambda{\rm H}^*$ are bound and one can study implications for the 4- and 5-body s-shell hypernuclei as will be shown below where we tune $d_\lambda^{I,S}$ to get either Λnn or ${}^3_\Lambda{\rm H}^*$ just bound by 0.001 MeV. Finally, for the zero auxiliary force $d_\lambda^{I,S}/D_\lambda^{I,S} = 0$ one gets physical solutions, namely continuum states of Λnn and ${}^3_\Lambda{\rm H}^*$ (either resonant or virtual states). The figure suggests that the value of $d_\lambda^{I,S}/D_\lambda^{I,S}$ considerably closer to 0, i.e. much less additional attraction, is needed to get ${}^3_\Lambda{\rm H}^*$ bound then in the case of Λnn.

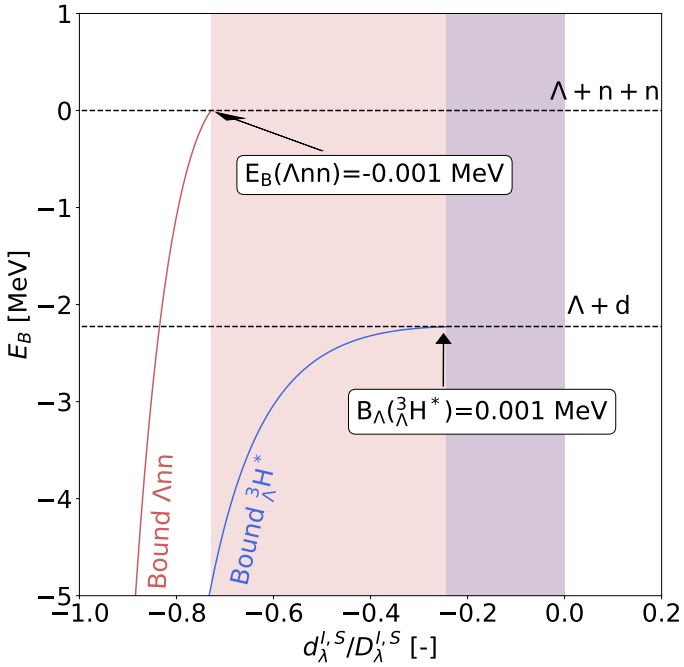

FIG. 1. The Λnn and ${}^3_\Lambda{\rm H}^*$ bound state energies $E_{\rm B}$ as a function of $d_\lambda^{I,S}$ normalized to $D_\lambda^{I,S}$ for $I = 1, S = 1/2$ and $I = 0, S = 3/2$, respectively. The calculation is performed for the Alexander B set of ΛN scattering lengths and $\lambda = 6$ fm^{-1}.

We will now demonstrate that such Λ interactions tuned to bind Λnn and/or ${}^3_\Lambda{\rm H}^*$ are inconsistent with Λ separation energies in $A = 4$ and 5 hypernuclei. We keep 2- and 3-body LECs fixed and fit the attractive strength of the auxiliary 3-body force, either $d_\lambda^{I=0,S=3/2}$ to Λ separation energy $B_\Lambda({}^3_\Lambda{\rm H}^*) = 0.001$ MeV or $d_\lambda^{I=1,S=1/2}$ to bound state energy $E_B(\Lambda nn) = -0.001$ MeV.

Consequences of such tuning are illustrated in Fig. 2. Here, we present Λ separation energies B_Λ in s-shell hypernuclei, calculated for selected ΛN scattering lengths and cutoff $\lambda = 6$ fm^{-1} which already exhibits partial renormalization group invariance. Variations of $d_\lambda^{I=0,S=3/2}$ or $d_\lambda^{I=1,S=1/2}$ do not affect the $I, S = \left(0, \frac{1}{2}\right)$ three-body channel, consequently, the Λ separation energy of the hypertriton ground state remains unaffected and is not shown in the figure. In order to get the ${}^3_\Lambda{\rm H}^*$ system just bound (left panel), the amount of repulsion in the $\left(0, \frac{3}{2}\right)$ three-body channel must decrease, which leads in return to overbinding of both the ${}^4_\Lambda{\rm H}^*$ excited state and the ${}^5_\Lambda$He hypernucleus. The wave function of the ${}^4_\Lambda$H ground state does not include the $\left(0, \frac{3}{2}\right)$ component and thus its B_Λ remains intact. As was already noted and demonstrated in Fig. 1, the

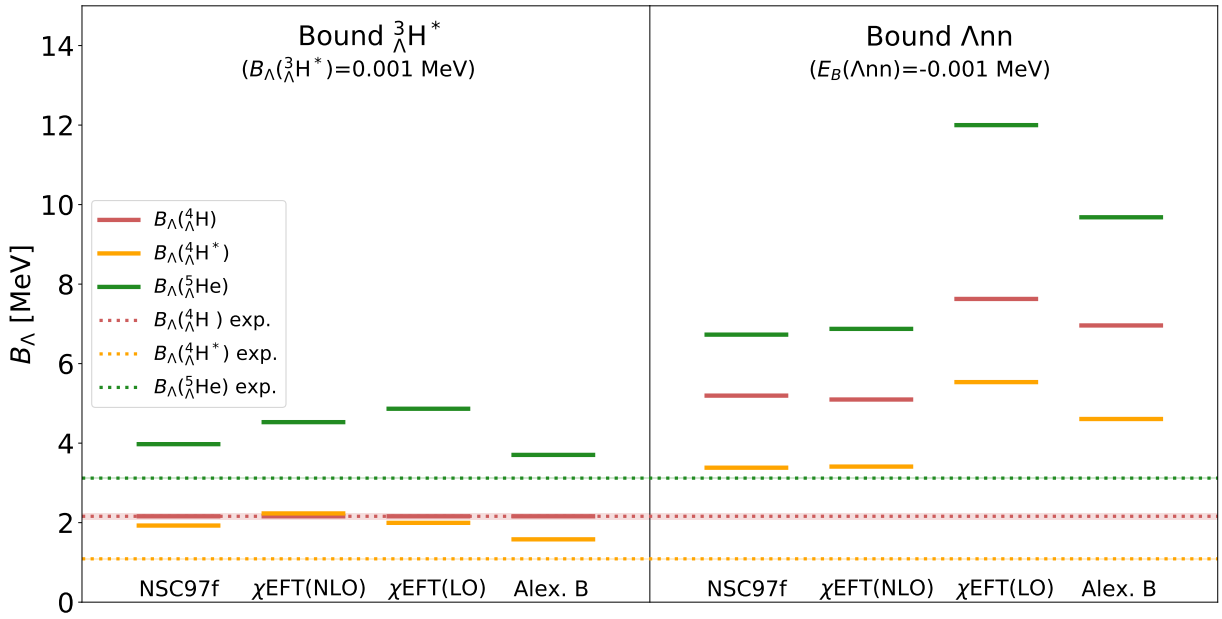

FIG. 2. Λ separation energies B_Λ from SVM calculations using cutoff $\lambda = 6$ fm^{-1} and several sets of ΛN scattering lengths for two cases - just bound ${}^{3}_{\Lambda}\mathrm{H}^{*}$ (left) and just bound Λnn (right). Horizontal dotted lines mark experimental values of B_Λ.

binding of the Λnn system requires a larger change in the corresponding auxiliary three-body force. Indeed, decreasing amount of repulsion in the $\left(1, \frac{1}{2}\right)$ three-body channel induces even more severe overbinding than in the ${}^{3}_{\Lambda}\mathrm{H}^{*}$ case - B_Λs are more than twice larger than experimental values (right panel). We might deduce that by varying the strength of Λ interactions, it is harder to get Λnn bound - the bound ${}^{3}_{\Lambda}\mathrm{H}^{*}$ state appears more likely first. This result is in agreement with previous works [6–8].

In Fig. 3 we show the physical solutions (with no auxiliary force) corresponding to the ∉EFT Hamiltonian H (1). Here, the real Re(E) and imaginary Im(E) parts of the Λnn resonance energy (left panel) and the energy E_v of the virtual state ${}^{3}_{\Lambda}\mathrm{H}^{*}$ (right panel) are plotted as a function of the cutoff λ for the ΛN scattering length versions listed in Table I. The calculated energies in the both hypernuclear systems depend strongly on the input ΛN interaction strength. In the case of ${}^{3}_{\Lambda}\mathrm{H}^{*}$, we obtain for all considered ΛN scattering lengths a virtual state solution. Namely, in accord with the definition of a virtual state [31], the imaginary part of the ${}^{3}_{\Lambda}\mathrm{H}^{*}$ pole momentum Im(k) decreases from a positive value (bound state) to a negative value (unbound state) with a decreasing auxiliary attraction whereas the real part Re(k) remains equal to zero [31] (as was demonstrated in ref. [17]). On the other hand, in the case of the Λnn system the ∉EFT predicts a resonant state. Moreover, only the NSC97f and χEFT(NLO) yield ΛN interaction strong enough to ensure for $\lambda \geq 2$ fm^{-1} the Λnn pole position in the fourth quadrant of a complex energy plane (Re(E) > 0, Im(E) < 0), i.e. predict a physical Λnn resonance.

In Fig. 3 we also demonstrate stability of the solutions with respect to the cutoff λ. The calculated energies vary smoothly beyond the value $\lambda = 2$ fm^{-1} and already at $\lambda = 4$ fm^{-1} they stabilize within extrapolation uncertainties at an asymptotic value corresponding to the renormalization scale invariance limit $\lambda \to \infty$. This is illustrated in the right panel, where we present for the Alexander B case the extrapolation function and the asymptotic value including the extrapolation error for the energy E_v of the ${}^{3}_{\Lambda}\mathrm{H}^{*}$ virtual state. It is to be noted that one might naively expect clear dependence on the strength of the ΛN spin-triplet interaction which solely enters the ${}^{3}_{\Lambda}\mathrm{H}^{*}$ hypernuclear part on a two-body level. However, the dominance of the spin-triplet interaction is undermined by 3-body force in the $\left(0, \frac{3}{2}\right)$ channel compensating the size of the spin-singlet scattering length $a_0^{\Lambda N}$, being fixed by the $B_\Lambda({}^{4}_{\Lambda}\mathrm{H}^{*})$ experimental value.

One could argue that considering different values of $a_s^{\Lambda N}$, ΛNN three-body forces or an effect of non-zero effective range r_s would open a possibility to locate the Λnn resonance in the fourth quadrant closer to the real axis and thus decrease its width Γ. This would certainly facilitate its experimental observation. However, ΛNN forces are fixed by experimental B_Λs of 3- and 4-body hypernuclear systems. Considering unusually large values of $a_s^{\Lambda N}$ would allow Λnn pole position closer to the threshold but ΛN interactions would have to be reconciled again with remaining s-shell systems. At LO ∉EFT we would be constrained by a possibility of bound ${}^{3}_{\Lambda}\mathrm{H}^{*}$ and by the experimental value of $B_\Lambda({}^{5}_{\Lambda}\mathrm{He})$.

Incorporation of a non-zero effective range for $\lambda \to \infty$ is restricted by the Wigner bound [45] and leads to per-

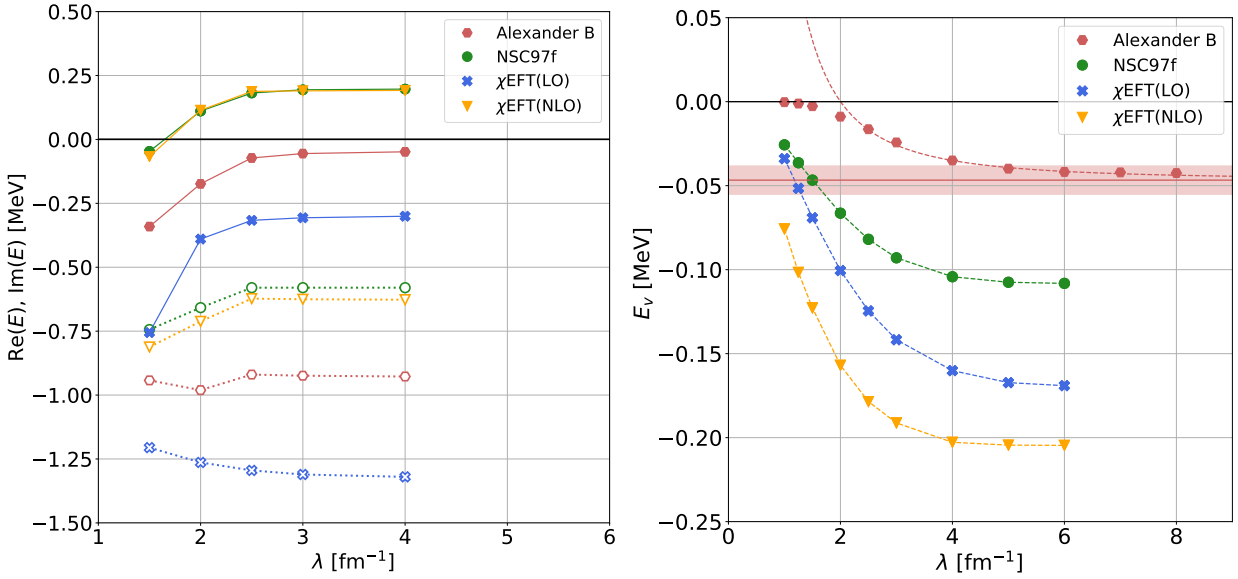

FIG. 3. Real Re(E) (full symbols) and imaginary Im(E) (empty symbols) parts of the Λnn resonance energy (left) and energy $E_{\rm v}$ of the ${}^{3}_{\Lambda}{\rm H}^{*}$ virtual state (right) as a function of cutoff λ calculated using the IACCC method for several ΛN interaction strengths. For ${}^{3}_{\Lambda}{\rm H}^{*}$ virtual state (right) and Alexander B we perform extrapolation for $\lambda \to \infty$. The red dashed line is the extrapolation function, the solid red line and shaded area mark the contact limit and the extrapolation error.

turbative inclusion of NLO term [46]. Assuming that the total energy of the Λnn resonance is below 1 MeV one might estimate maximal Λ (N) typical momentum as $p_\Lambda \approx \sqrt{2M_\Lambda E} = 47$ MeV ($p_N \approx \sqrt{2M_N E} = 43$ MeV) which yields truncation error of of the LO $\not\pi$EFT of order $(\frac{Q}{2m_\pi})^2 \approx 3\%$ ($(\frac{Q}{m_\pi})^2 \approx 10\%$) for hypernuclear (nuclear) part. Consequently, NLO effects are not expected to qualitatively change the LO results.

Our work represents the first EFT study of the Λnn and ${}^{3}_{\Lambda}{\rm H}^{*}$ hypernuclear systems in a continuum. Therefore, we find it appropriate to discuss difference of our approach with respect to the previous calculations of the Λnn resonance performed by Afnan and Gibson using a phenomenological approach [16]. Following their work we neglect three-body force but instead of separable nonlocal two-body potentials we employ one range Gaussians

$$V(r) = \sum_{I,S} \hat{\mathcal{P}}_{I,S}\; C_{I,S}\; \exp\left(-\frac{\lambda_{I,S}^2}{4} r^2\right) \qquad (14)$$

to describe s-wave interaction in nuclear $I,S = (0,1)$, $(1,0)$ and hypernuclear $I,S = (1/2,1)$, $(1/2,0)$ two-body channels. Here, $\hat{\mathcal{P}}_{I,S}$ is the projection operator. The parameters $C_{I,S}$ and $\lambda_{I,S}$ are fitted to the values of a_s and r_s listed in [16]. Moreover, we took into account $a_s^{\Lambda N}$ and $r_s^{\Lambda N}$ related to Alexander B and χEFT(LO) given in Table I.

The calculated Λnn pole trajectories for the Phen-2B potential (14) are presented in Fig. 4, left panel. The auxiliary interaction is in a form of three-body force (5) with cutoff $\lambda = 1$ fm^{-1}. We observe that calculated physical pole positions (filled larger symbols) are in good agreement with those presented in [16] (empty symbols). Indeed, as might be expected the position of the near-threshold Λnn resonance is predominantly given by low-momentum characteristics of an interaction - a_s and r_s which are the same in both cases.

In order to reveal the relation between the LO $\not\pi$EFT and phenomenological approaches discussed above, one can consider the finite cutoff λ_s which gives roughly the same values of r_s as used in the above phenomenological calculations. Such a value, $\lambda_s \approx 1.25$ fm^{-1} for NSC97f and χEFT(NLO), yields in addition $B_\Lambda({}^{5}_{\Lambda}{\rm He})$ remarkably close to experiment [47]. As explained by the authors one might understand that λ_s absorbs into LECs NLO contributions of the theory which are likely to increase its precision, however, success of this procedure is not in general guaranteed for all systems. Indeed, higher orders above NLO which behave as powers of (Q/λ) are induced as well and are not suppressed by $\lambda \to \infty$. In Fig. 4, right panel, we present Λnn pole trajectories calculated using the $\not\pi$EFT for this specific λ_s value and several ΛN interaction strengths. One notices very close positions of the Λnn resonance calculated for χEFT(NLO) and NSC97f using the Phen-2B potential (left panel) and the $\not\pi$EFT (right panel). The LO $\not\pi$EFT for $\lambda = 1.25$ fm^{-1} could thus be considered as a suitable phenomenological model which yields good predictions for 4- and 5- body hypernuclei and hypertriton [21, 47].

In addition, in both panels of Fig. 4 we compare the Λnn pole positions calculated within the CSM and IACCC method for the same values of $d_\lambda^{I=1,S=1/2}$ located in the area reachable by the CSM. We might see remarkable agreement between IACCC (dots) and CSM

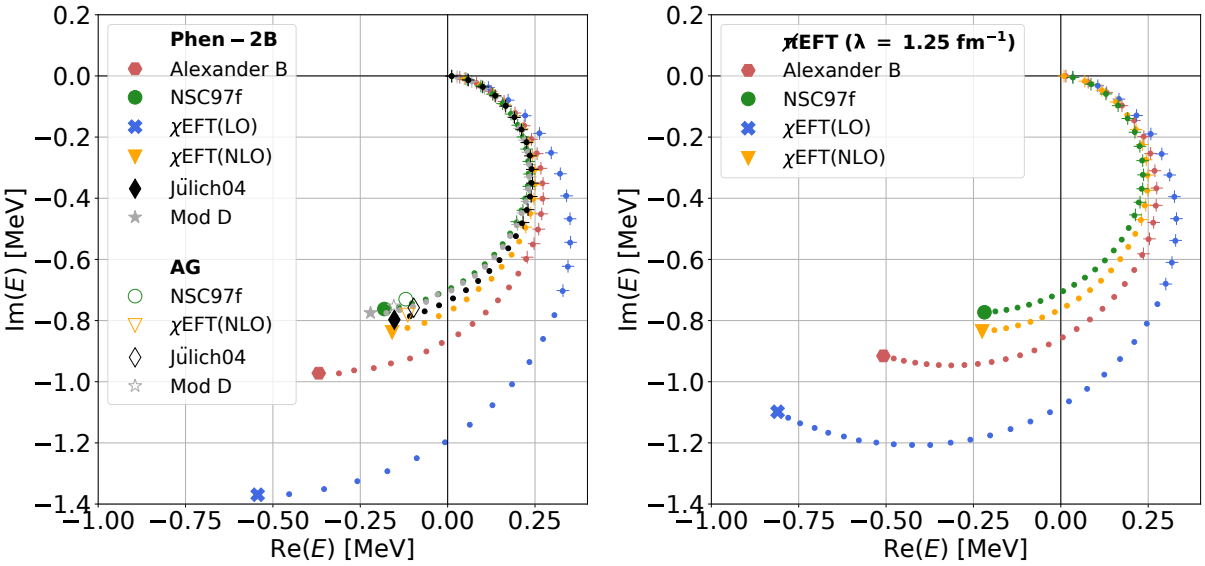

FIG. 4. Trajectories of the Λnn resonance pole in a complex energy plane determined by a decreasing attractive strength $d_\lambda^{I=1,S=1/2}$ for several ΛN interaction strengths. Left panel: Calculations using ΛN and NN phenomenological potential Phen-2B (14). Larger full symbols stand for the physical position of the Λnn pole ($d_\lambda^{I=1,S=1/2}=0$), empty symbols (left panel) mark corresponding solutions obtained by Afnan and Gibson (AG) [16] for the same scattering lengths and effective ranges used to fix potential Phen-2B (14). Right panel: $\not\pi$EFT calculations for cut-off $\lambda = 1.25$ fm^{-1}. In a region accessible by the CSM we also show for each IACCC solution (dots) the one obtained by the CSM (crosses) for the same amplitude of the auxiliary three-body force.

(crosses) solutions, which provides benchmark of the calculations and demonstrates high precision of our results.

In Fig. 5, we show B_Λ of remaining s-shell hypernuclear systems, calculated using the Phen-2B potential (14). The hypertriton ground state ${}^3_\Lambda$H is in most cases overbound, calculated $B_\Lambda({}^3_\Lambda\mathrm{H})$ are consistent with those obtained by Afnan and Gibson using separable non-local potentials fitted to the same ΛN interaction strengths [16]. The excited state of hypertriton ${}^3_\Lambda$H* turns to be bound, which is in disagreement with previous theoretical calculations [6, 11]. Heavier s-shell systems are considerably overbound as well, regardless of which specific set of $a_s^{\Lambda N}$ and $r_s^{\Lambda N}$ is fitted. Overbinding of s-shell hypernuclear systems brought about by the Phen-2B interaction (14) clearly indicates a missing piece which would introduce necessary repulsion. This could be provided by introducing a ΛNN three-body force. In fact, Afnan and Gibson stated that more detailed study of the Λnn resonance including three-body forces should be considered [16]. In $\not\pi$EFT additional repulsion is included right through the ΛNN force fitted for each cutoff λ to experimental values of B_Λ in 3- and 4-body hypernuclei. As a result, though both the Phen-2B (as well as AG) interaction and the $\not\pi$EFT for $\lambda = 1.25$ fm^{-1} yield close positions of the Λnn resonance (see Fig. 4), the interplay between three-body forces in the $\not\pi$EFT exhibits large effect which completely removes overbinding presented for the Phen-2B interaction in Fig. 5, yielding correct $B_\Lambda({}^5_\Lambda\mathrm{He})$, exact $B_\Lambda({}^3_\Lambda\mathrm{H})$, $B_\Lambda({}^4_\Lambda\mathrm{H})$, and $E_{\mathrm{exc}}({}^4_\Lambda\mathrm{H}^*)$ plus unbound ${}^3_\Lambda$H* as presented in Fig. 3. This suggests that the sensitivity of the Λnn system to the three-body ΛNN force seems to be relatively small.

A. Stability and error of continuum solutions

In this subsection, we demonstrate stability and accuracy of our CSM and IACCC resonance solutions for a particular point of the Λnn pole trajectory. More precisely, we use the χEFT(LO) $\not\pi$EFT interaction with $\lambda = 1.25$ fm^{-1} and the strength of auxiliary three-body interaction $d_\lambda^{I=1,S=1/2} = -24$ MeV. This specific choice was motivated by large $\theta_r = \arctan(E/2\Gamma)/2$ angle of the corresponding Λnn resonance energy since it can be already challenging to describe such a pole position accurately within the CSM (see the last χEFT(LO) CSM solution in the right panel of Fig. 4).

Using the CSM in a finite basis we make sure that our resonant solution is stable and does not change with an increasing number of basis states. Here, we apply the harmonic oscillator (HO) trap technique [17] with mass scale $m = 939$ MeV (13) which provides us with an efficient algorithm to select an appropriate, yet not excessively large CSM basis. For a chosen HO trap length b (13), this procedure yields stochastically optimized basis of correlated Gaussians with a maximal typical radius R_{max} which gets larger as the trap becomes more broad. We choose a grid of increasing trap lengths b_i ranging from 20 fm to 80 fm with 2 fm step and using HO trap technique for each b_i, we prepare 31 different

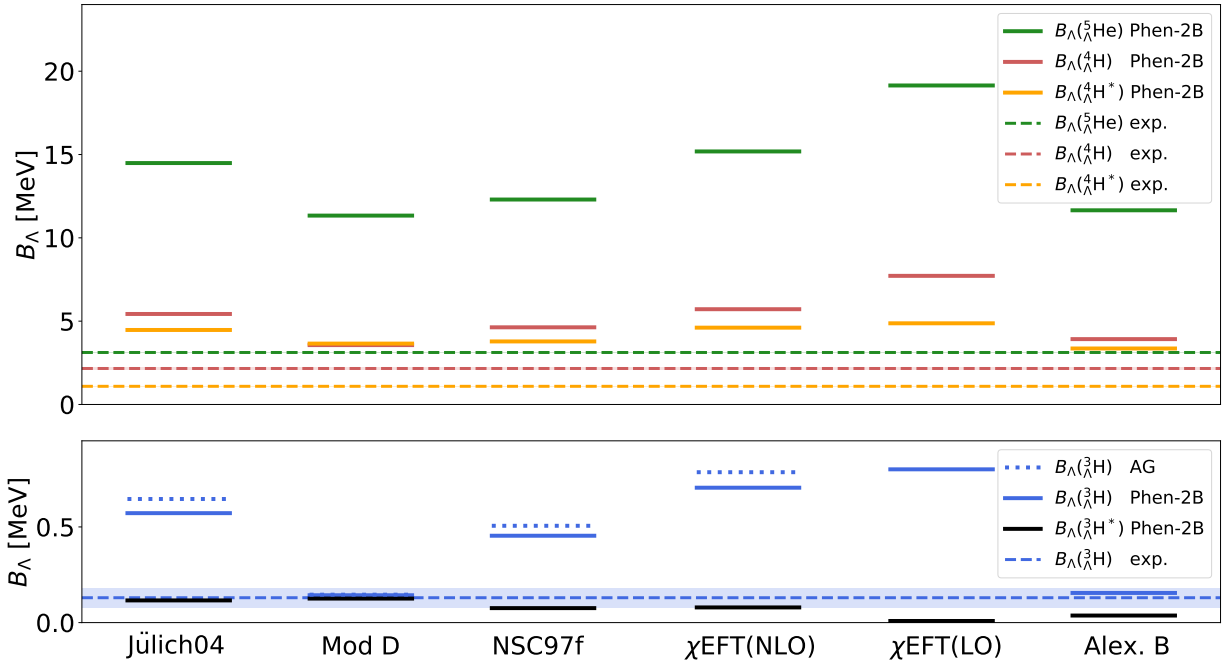

FIG. 5. Λ separation energies B_Λ from SVM calculations using various ΛN interaction strengths of the Phen-2B interaction (14). The nuclear part is given by the same form of a phenomenological potential. Experimental values of B_Λ are marked by dashed horizontal lines.

basis sets. In the next step, we build the CSM basis for our resonance calculation in the following way : First, we fix correlated Gaussian states obtained for the lowest $b_0 = 20$ fm trap length. Second, we take the basis states for $b_1 = 22$ fm leaving out the states which are nearly linear dependent to any of already fixed b_0 correlated Gaussians and we merge b_0 and b_1 basis sets. Next, in the same way, we add correlated Gaussians from the $b_2 = 24$ fm basis set to already fixed b_0 and b_1 states. We continue this procedure for all b_i up to certain $b_{\max}$ and construct our final CSM basis set.

The stability of the CSM solution with respect to HO trap length b is illustrated in Fig. 6. Here, we present calculated real and imaginary parts of the Λnn resonance energy using different CSM bases obtained combining HO trap sets up to a certain $b_{\max}$. Black dots stand for the most stationary point of the resonance θ-trajectory $E^{\mathrm{CSM}}_{\Lambda nn}(\theta_{\mathrm{opt}})$ for which $\left|\frac{\mathrm{d}E}{\mathrm{d}\theta}\right|_{\theta_{\mathrm{opt}}}$ is minimal. Shaded areas then show the spread of resonance energy $E^{\mathrm{CSM}}_{\Lambda nn}(\theta)$ within the $\theta_{\mathrm{opt}} \pm 1^\circ$ range (darker shaded area) and the $\theta_{\mathrm{opt}} \pm 4^\circ$ range (lighter shaded area) thus indicating the level of the CSM resonance energy dependence on the scaling angle θ (8). Calculated Λnn resonance energy stabilizes already using the CSM basis constructed for $b_{\max} = 36$ fm. It is clearly visible that considering higher $b_{\max}$ and thus including more basis states does not affect the CSM solution.

In Fig. 7 we show the calculated θ-trajectory and several β-trajectories for two different CSM bases which were obtained for $b_{\max} = 24$ fm (left panel) and for $b_{\max} = 80$ fm (right panel). For $b_{\max} = 24$ fm we can

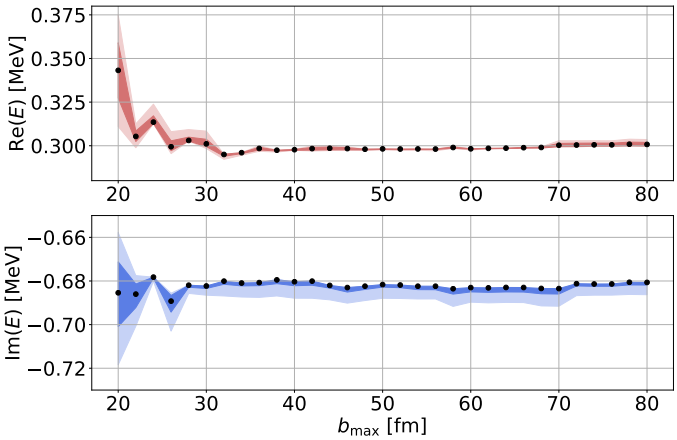

FIG. 6. Stability of the Λnn CSM resonant solution $E(\theta) = \mathrm{Re}(E(\theta)) + \mathrm{iIm}(E(\theta))$ as a function of increasing HO trap length $b_{\max}$. Black dots show the most stationary point of the θ-trajectory $E(\theta_{\mathrm{opt}})$. Darker shaded area shows uncertainty of $E(\theta)$ within $\theta_{\mathrm{opt}} \pm 1^\circ$ range, lighter shaded area shows the same within $\theta_{\mathrm{opt}} \pm 4^\circ$ range. The particular pole position was calculated for $\not\pi$EFT interaction with χEFT(LO) ΛN scattering lengths and $\lambda = 1.25$ fm^{-1}, strength of auxiliary three-body force was set to $a_\lambda^{I=1,S=1/2} = -24$ MeV.

clearly see that β-trajectories are not circular and manifest highly unstable behaviour due to poor quality of the employed basis set. In fact, we have already pointed out in Fig. 6 that the Λnn resonance solution stabilizes at least for $b_{\max} = 36$ fm. Using the CSM basis for

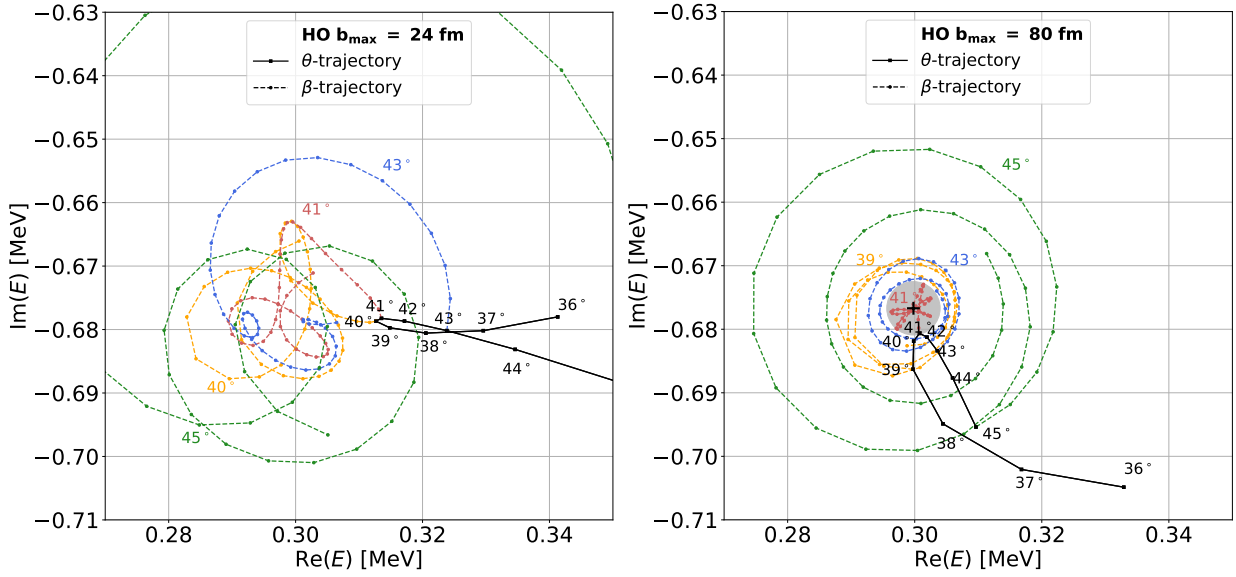

FIG. 7. Λnn resonance θ-trajectory (Im(θ)=0; black solid line) and β-trajectories (colored dotted lines) showing movement of corresponding $E(\theta)$ as a function of θ in the complex energy plane. Trajectories are calculated for two different CSM basis sets which were obtained combining HO trap sets up to $b_{\max}$ = 24 fm (left panel) and up to $b_{\max}$ = 80 fm (right panel). β-trajectories are presented for several different Re(θ) changing Im(θ) from 0 to 0.44 radians with 0.01 step. Black cross in the left panel indicates estimated Λnn resonance position of the true CSM solution satisfying Eq. (12). Shaded gray area then shows corresponding CSM error. Λnn calculation is performed using the same interaction as in Fig. 6

.

$b_{\max}$ = 80 fm (right panel) our results are stable showing almost circular β-trajectories characterised by their decreasing radius as the corresponding Re(θ) approaches Re($\theta_{\rm opt}$) $\approx 41°$. The β-trajectory for Re(θ) = 41° exhibits oscillatory behaviour within a small region around the true CSM solution. We assume that this effect is related to a finite dimension of our CSM basis set and corresponding circular trajectory would be recovered by considering more basis states. The most probable Λnn resonance energy $E^{\rm CSM}_{\Lambda nn}$ is in the center of the grey shaded circle while its radius defines the error of our true CSM solution. In this particular case, the Λnn resonance energy is $E^{\rm CSM}_{\Lambda nn} = 0.2998(42) - {\rm i}\, 0.6767(42)$ MeV.

The stability of the IACCC solution is demonstrated in Table II where we present Λnn resonance energies $E^{\rm IACCC}_{\Lambda nn}$ using different degrees (M, N) of the Padé approximant $\mathcal{P}^{(M,N)}$ (6). As expected, calculated $E^{\rm IACCC}_{\Lambda{\rm nn}}$ start to stabilize with increasing (M, N). The IACCC solution saturates already for (7,7) and does not improve dramatically with further increase of (M, N). This is predominantly explained by finite precision of our SVM bound state energies which are used to fix the parameters of $\mathcal{P}^{(M,N)}$ and by numerical instabilities which slowly start to affect our IACCC solution at higher degrees of the approximant. Comparing saturated IACCC solution obtained with different (M, N) ranging from (7,7) up to (13,13) we estimate for this specific example the $E^{\rm IACCC}_{\Lambda nn}$ accuracy $\sim 3 \times 10^{-3}$ MeV. Despite considerable difference between IACCC and CSM, both approaches predict remarkably consistent Λnn resonance energies. In fact, all presented IACCC energies starting from the Padé approximant of degree (7,7) and higher lie within the errors of the corresponding CSM prediction.

Dependence of our IACCC calculations of the ${}^{3}_{\Lambda}{\rm H}^{*}$ virtual state energy $E^{\rm IACCC}_{{\rm v},\,{}^{3}_{\Lambda}{\rm H}^{*}}$ on different degrees of the Padé approximant is demonstrated in Table II as well. In this particular case we use as an example the $\not\pi$EFT interaction with the χEFT(LO) ΛN scattering lengths, cut-off λ = 1.25 fm^{-1}, and no auxiliary interaction. We see that the ${}^{3}_{\Lambda}{\rm H}^{*}$ solution starts to stabilize already for $\mathcal{P}^{(4,4)}$ and it is approximately by two orders more accurate than the solutions for the Λnn resonance. The reason is that the ${}^{3}_{\Lambda}{\rm H}^{*}$ virtual state lies in the vicinity of the $\Lambda + d$ threshold, analytical continuation from the bound region is thus not performed far into the continuum, which enhances the IACCC precision.

The uncertainty of our IACCC resonance solutions in the fourth quadrant of a complex energy plane (Re(E) > 0, Im(E) < 0) does not exceed $\approx 4 \times 10^{-3}$ MeV. All IACCC results are crosschecked by the CSM in a region of its applicability determined by the maximal resonance angle $\theta_r \approx 35°$ for which our complex scaling results are still reliable. Up to this point the CSM solution possesses the same minimal accuracy as the IACCC solution, however, for higher θ_r approaching the limiting value 45° the CSM solution quickly starts to deteriorate due to numerical instabilities.

Subthreshold resonance positions are calculated within the IACCC method. For poles residing deeper in this region of a complex energy plane (Re(E) < 0, Im(E) < 0)

TABLE II. Stability of the Λnn resonance energy $E^{\rm IACCC}_{\Lambda nn}$ and ${}^{3}_{\Lambda}{\rm H}^{*}$ virtual state energy with respect to the $\Lambda + d$ threshold $E^{\rm IACCC}_{{\rm v},\ {}^{3}_{\Lambda}{\rm H}^{*}}$ calculated within the IACCC for increasing degree (M, N) of the Padé approximant. Λnn calculation is performed using the same interaction as in Fig. 6. Position of the ${}^{3}_{\Lambda}{\rm H}^{*}$ virtual state is determined for $\not\pi$EFT interaction with χEFT(LO) ΛN scattering lengths and $\lambda = 1.25$ fm^{-1} with no auxiliary three-body force, i.e. $d^{I=0,S=3/2}_{\lambda} = 0$ MeV. $E_{\rm diff}$ stands for the difference between absolute values of IACCC solution calculated for two neighbouring Padé approximants $E^{(M,N)}_{\rm diff} = |E^{(M,N)}| - |E^{(M-1,N-1)}|$. All energies are given in MeV.

(M,N)	$E^{\rm IACCC}_{\Lambda nn}$	$\lvert E^{\rm IACCC}_{\Lambda nn}\rvert$	$E_{\rm diff}(\Lambda nn)$	$E^{\rm IACCC}_{{\rm v},\ {}^{3}_{\Lambda}{\rm H}^{*}}$	$E_{\rm diff}({}^{3}_{\Lambda}{\rm H}^{*})$
(3,3)	-0.0588 - i0.5605	0.5636		-0.04216	
(4,4)	0.3367 - i0.7041	0.7805	0.2169	-0.05192	0.00976
(5,5)	0.2965 - i0.6559	0.7198	-0.0652	-0.05154	-0.00038
(6,6)	0.2941 - i0.6770	0.7381	0.0183	-0.05161	0.00007
(7,7)	0.3003 - i0.6796	0.7430	0.0050	-0.05160	-0.00001
(8,8)	0.2997 - i0.6796	0.7427	-0.0003	-0.05160	$< 10^{-5}$
(9,9)	0.3001 - i0.6796	0.7429	0.0002	-0.05156	-0.00004
(10,10)	0.3014 - i0.6791	0.7430	0.0001	-0.05159	0.00003
(11,11)	0.3012 - i0.6795	0.7433	0.0003	0.05160	0.00001
(12,12)	0.3020 - i0.6757	0.7401	-0.0032	-0.05160	$< 10^{-5}$
(13,13)	0.3026 - i0.6765	0.7411	0.0010	-0.05161	0.00001

the precision of our results, predominantly of the imaginary part ${\rm Im}(E)$, decreases. For ${\rm Re}(E) \in (-0.25, 0)$ MeV the maximal error of ${\rm Im}(E)$ is $\approx 5 \times 10^{-3}$ MeV, for ${\rm Re}(E) \in (-0.5, -0.25)$ MeV it is ≈ 0.03 MeV, and for ${\rm Re}(E) \in (-1.0, -0.5)$ MeV it is ≈ 0.1 MeV. Since we are primarily interested in a possible experimental observation, i.e. resonance solutions close to or in the fourth quadrant, we deem such accuracy satisfactory, not affecting our conclusions.

The IACCC method proved to be highly precise in the study of near-threshold virtual state positions. Here, we reach accuracy up to $\approx 10^{-4}$ MeV in all considered cases.

IV. CONCLUSIONS

In the present work, we have studied few-body hypernuclear systems Λnn and ${}^{3}_{\Lambda}{\rm H}^{*}(J^{\pi} = 3/2^{+},\ I = 0)$ within a LO $\not\pi$EFT with 2- and 3-body regulated contact terms. The ΛN LECs were associated with ΛN scattering lengths given by various interaction models and the ΛNN LECs were fitted to known Λ separation energies B_{Λ} in $A \leq 4$ hypernuclei and the excitation energy $E_{\rm exc}({}^{4}_{\Lambda}H^{*})$. Few-body wave functions were described within a correlated Gaussians basis. Bound state solutions were obtained using the SVM. The continuum region was studied by employing two independent methods - the IACCC and CSM. Our LO $\not\pi$EFT approach, which accounts for known s-shell hypernuclear data, represents a unique tool to describe within a unified interaction model 3-, 4-, 5- and 6-body hypernuclar systems – single- and double-Λ hypernuclei including continuum states. In that it differs from other similar studies which focused solely on few particular hypernuclei. Moreover, the $\not\pi$EFT approach allows us to develop systematically higher orders corrections, assess reliably precision of calculations and evaluate errors of their solutions.

The additional auxiliary 3-body potential introduced to study Λnn and ${}^{3}_{\Lambda}{\rm H}^{*}$ continuum states allows us to explore different scenarios. Fixing the attractive strength of the auxiliary force in order to get these systems just bound yields considerable discrepancy between calculated and experimental B_{Λ}s of 4- and 5-body s-shell hypernuclei. Our conclusions thus ruled out the possibility for the existence of bound Λnn and ${}^{3}_{\Lambda}{\rm H}^{*}$ states, which is in accord with conclusions of previous theoretical studies [4–8, 10, 11]. Moreover, we found that by increasing the strength of the Λ attraction, the onset of the ${}^{3}_{\Lambda}{\rm H}^{*}$ comes before the Λnn binding. The experimental evidence for the bound Λnn state reported by the HypHI collaboration [3] would thus imply existence of the bound state ${}^{3}_{\Lambda}{\rm H}^{*}$.

On the basis of our $\not\pi$EFT calculations with the auxiliary force set to zero, we firmly conclude that the excited state ${}^{3}_{\Lambda}{\rm H}^{*}$ is a virtual state. On the other hand, the Λnn pole located close to the three-body threshold in a complex energy plane could convert to a true resonance with ${\rm Re}(E) > 0$ for some considered ΛN interactions [e.g., for NSC97f and χEFT(NLO)] but most likely does not exceed $E_r \approx 0.3$ MeV. However, its width Γ is rather large – $1.16 \leq \Gamma \leq 2.00$ MeV. Even larger width would be obtained for a rather weak ΛN interaction strength but it does not yield experimentally observable Λnn pole. On the contrary, the observation of a sharp resonance would definitely attract considerable attention since it would signal that the ΛN interaction at low-momenta is stronger than most ΛN interaction models suggest.

Besides the model dependence of our calculations we

explored the stability of solutions with respect to the cutoff parameter λ. We demonstrated that already for $\lambda = 4$ fm^{-1} the calculated energies stabilize close to the asymptotic value corresponding to the renormalization scale invariance limit $\lambda \to \infty$. We anticipate that the truncation error, describing effects of higher order corrections, is small due to low typical momenta and does not change our results qualitatively. In a region accessible by the CSM we performed comparison of the CSM with IACCC method, which yielded highly consistent solutions, hence proving reliability of our results. Moreover, we verified that our CSM solutions for Λnn are stable with respect to the considered number of basis states. Exploring both the θ and β trajectories of the Λnn pole for one particular case we set the true CSM solution including its error. The stability of the IACCC method with respect to the degree of the employed Padé approximant was investigated and the uncertainty of the calculations was assessed.

A rather different situation occurs when we consider just 2-body phenomenological interactions fitted to NN and ΛN scattering lengths and effective ranges. We then obtain subthreshold Λnn pole positions close to those of Afnan and Gibson [16]. However, these interactions fail to describe other few-body Λ hypernuclei. The predicted overbinding of the s-shell hypernuclei induced by these phenomenological 2-body interactions indicates a missing repulsive part of the Λ interaction. In the $\not$EFT , it is provided by an additional ΛNN 3-body force. A comparison with our LO $\not$EFT calculations revealed that the results of Afnan and Gibson could be reproduced for the finite cutoff value $\lambda_s \approx 1.25$ fm^{-1}. However, thanks to the repulsive ΛNN force the s-shell hypernuclear data are now described successfully. The LO $\not$EFT with $\lambda_s \approx 1.25$ fm^{-1} could thus be considered as a suitable phenomenological model.

Our method presented here can be directly applied to the double-Λ hypernuclear continuum using the recently introduced $\Lambda\Lambda$ extension of a LO $\not$EFT [22]. It is highly desirable to explore possible resonances in the neutral $\Lambda\Lambda n$ and $\Lambda\Lambda nn$ systems or in the ${}^{4}_{\Lambda\Lambda}$H hypernucleus, where a consistent theoretical continuum study has not been performed yet. Indeed, an example of its importance is the continuing ambiguity in interpretation of the AGS-E906 experiment [48] referred to as the E906 puzzle. It was firstly interpreted as the bound ${}^{4}_{\Lambda\Lambda}$H system [48], however, more recent analyses suggested that the decay of the ${}^{7}_{\Lambda\Lambda}$He [49] or $\Lambda\Lambda nn$ [12] hypernucleus might provide more plausible interpretation.

This clearly demonstrates the growing importance of precise few-body continuum studies which, although being difficult to conduct, significantly contribute to the complete picture of a stability of hypernuclear systems. In fact, the applicability of our few-body approach is rather broad in principle – it might be used not only to calculations of hypernuclear systems but also η or K^- mesic nuclei, or even atoms.

ACKNOWLEDGMENTS

We are grateful to Avraham Gal for valuable discussions and careful reading of the manuscript. This work was partly supported by the Czech Science Foundation GACR grant 19-19640S. The work of NB was supported by the Pazy Foundation and by the Israel Science Foundation grant 1308/16.

[1] A. Gal, E. V. Hungerford, D. J. Millener, Rev. Mod. Phys. **88**, 035004 (2016).
[2] D. H. Davis, Nucl. Phys. A **754**, 3c (2005).
[3] C. Rappold, E. Kim, T. R. Saito, O. Bertini, S. Bianchin, and V. Bozkurt et al. (HypHI Collaboration), Phys. Rev. C **88**, 041001(R) (2013).
[4] B. W. Downs and R. H. Dalitz, Phys. Rev. **114**, 593 (1959).
[5] H. Garcilazo, J. Phys. G **13**, 63 (1987).
[6] K. Miyagawa, H. Kamada, W. Glöckle, and V. Stoks, Phys. Rev. C **51**, 2905 (1995).
[7] H. Garcilazo, T. Fernández-Caramés, and A. Valcarce, Phys. Rev. C **75**, 034002 (2007).
[8] H. Garcilazo, A. Valcarce, and T. Fernández-Caramés, Phys. Rev. C **76**, 034001 (2007).
[9] V. B. Belyaev, S. A. Rakityansky, W. Sandhas, Nucl. Phys. A **803**, 210 (2008).
[10] A. Gal, H. Garcilazo, Phys. Lett. B **736**, 93 (2014).
[11] E. Hiyama, S. Ohnishi, B. F. Gibson, and Th. A. Rijken, Phys. Rev. C **89**, 061302(R) (2014).
[12] S. Blesser, M. Bölting, T. Gaitanos, J. Pochodzalla, F. Schupp, and M. Steinen, Phys. Lett. B **790**, 502 (2019).
[13] A. Gal, H. Garcilazo, Phys. Lett. B **791**, 48 (2019).
[14] S.-I. Ando, U. Raha, and Y. Oh, Phys. Rev. C **92**, 024325 (2015).
[15] F. Hildenbrand and H.-W. Hammer, Phys. Rev. C **100**, 034002 (2019).
[16] I. R. Afnan and B. F. Gibson, Phys. Rev. C **92**, 054608 (2015).
[17] M. Schäfer, B. Bazak, N. Barnea, and J. Mareš, Phys. Lett. B **808**, 135614 (2020).
[18] JLab, E12-17-003, https://www.jlab.org/exp_prog/proposals/17/PR12-17-003.pdf, 19.5.2020.
[19] J. Haidenbauer, arXiv:2005.05012 (2020).
[20] JLab proposal P12-19-002, https://www.jlab.org/exp_prog/proposals/19/PR12-19-002.pdf, 19.5.2020.
[21] L. Contessi, N. Barnea, and A. Gal, Phys. Rev. Lett. **121**, 102502 (2018).
[22] L. Contessi, M. Schäfer, N. Barnea, A. Gal, and J. Mareš, Phys. Lett. B **797**, 134893 (2019).
[23] G. Alexander, U. Karshon, A. Shapira, et al., Phys. Rev. **173**, 1452 (1968).
[24] Th.A. Rijken, V.G.J. Stoks, and Y. Yamamoto, Phys.Rev. C **59**, 21 (1999).
[25] H. Polinder, J. Haidenbauer, and U.-G. Meißner, Nucl.Phys. A **779**, 244 (2006).

[26] J. Haidenbauer, S. Petschauer, N. Kaiser, U.-G. Meißner, A. Nogga, and W. Weise, Nucl. Phys. A **915**, 24 (2013).

[27] G.A. Miller, M.K. Nefkens, I. Slaus, Phys. Rep. **1**, 194 (1990).

[28] C. Van Der Leun, C. Alderliesten, Nucl. Phys. A **380**, 261 (1982).

[29] K. Varga and Y. Suzuki, Phys. Rev. C **52**, 2885 (1995).

[30] Y. Suzuki, K. Varga, Stochastic Variational Approach to Quantum-Mechanical Few-Body Problems, Springer (1998).

[31] J. R. Taylor, Scattering Theory: Quantum Theory on Nonrelativistic Collisions, Willey, 99 edition (1972).

[32] V. I. Kukulin, V. M. Krasnopol'sky, and J. Horáček, Theory of resonances, Principles and Applications, Kluwer Academic Publishers (1989).

[33] J. Horáček and L. Pichl, Commun. Comput. Phys. **21**, 1154, (2017).

[34] V. M. Kukulin and V. M. Krasnopol'sky, J. Phys. A **10**, 33 (1977); V. M. Krasnopol'sky, and V. I. Kukulin, Phys. Lett. A **69**, 251 (1978); V. I. Kukulin, V. M. Krasnopol'sky, and M. Miselkhi, Sov. J. Nucl. Phys. **29**, 421 (1979).

[35] J. Augilar and J. M. Combes, Commun. Math. Phys. **22**, 269 (1971); E. Balslev and J.M. Combes, Commun. Math. Phys. **22**, 280 (1971).

[36] S. Aoyama, T. Myo, K. Kat, K. Ikeda, Prog. Theor. Phys **116**, 1 (2006).

[37] N. Moiseyev, P.R. Certain, F. Weinhold, Mol. Phys. **36**, 1613 (1978).

[38] N. Moiseyev, Non-Hermitian Quantum Mechanics, Cambridge University Press, (2011).

[39] N. Moiseyev, Phys. Rep. **302**, 212 (1998).

[40] J. Zs. Mezei, A. T. Kruppa, K. Varga, Few Body Syst. **41**, 233 (2007).

[41] R. Yaris, P. Winkler, J. Phys. B**11**, 1475 (1978).

[42] D. V. Fedorov, E. Garrido, and A. S. Jensen, Few-Body Syst. **33**, 153 (2003).

[43] E. Hiyama, M. Isaka, M. Kamimura, T. Myo, and T. Motoba, Phys. Rev. C **91**, 054316 (2015).

[44] L. H. Thomas, Phys. Rev. **47**, 903 (1935).

[45] E. P. Wigner, Phys. Rev. **98**, 145 (1955).

[46] U. van Kolck, Nucl. Phys. A **645**, 273 (1999).

[47] L. Contessi, N. Barnea, and A. Gal, AIP Conf. Proc. **2130**, 040012 (2019).

[48] J. K. Ahn, S. Ajimura, H. Akikawa, B. Bassalleck, A. Berdoz, and D. Carman et al., Phys. Rev. Lett. **87**, 132504 (2001).

[49] S. D. Randeniya and E. V. Hungerford, Phys. Rev. C **76**, 064308 (2007).

Physics Letters B 797 (2019) 134893

Contents lists available at ScienceDirect

Physics Letters B

www.elsevier.com/locate/physletb

The onset of $\Lambda\Lambda$ hypernuclear binding

L. Contessi [a], M. Schäfer [b,c], N. Barnea [a], A. Gal [a,*], J. Mareš [c]

[a] Racah Institute of Physics, The Hebrew University, Jerusalem 91904, Israel
[b] Czech Technical University in Prague, Faculty of Nuclear Sciences and Physical Engineering, Břehová 7, 11519 Prague 1, Czech Republic
[c] Nuclear Physics Institute, Academy of Sciences of Czech Republic, 250 69 Řež, Czech Republic

ARTICLE INFO

Article history:
Received 24 July 2019
Received in revised form 13 August 2019
Accepted 21 August 2019
Available online 28 August 2019
Editor: W. Haxton

Keywords:
Light $\Lambda\Lambda$ hypernuclei
LO $\not\pi$EFT
SVM calculations

ABSTRACT

Binding energies of light, $A \leq 6$, $\Lambda\Lambda$ hypernuclei are calculated using the stochastic variational method in a pionless effective field theory ($\not\pi$EFT) approach at leading order with the purpose of assessing critically the onset of binding in the strangeness $\mathcal{S} = -2$ hadronic sector. The $\not\pi$EFT input in this sector consists of (i) a $\Lambda\Lambda$ contact term constrained by the $\Lambda\Lambda$ scattering length $a_{\Lambda\Lambda}$, using a range of values compatible with $\Lambda\Lambda$ correlations observed in relativistic heavy ion collisions, and (ii) a $\Lambda\Lambda N$ contact term constrained by the only available $A \leq 6$ $\Lambda\Lambda$ hypernucler binding energy datum of ${}^{\;\;6}_{\Lambda\Lambda}$He. The recently debated neutral three-body and four-body systems ${}^{\;\;3}_{\Lambda\Lambda}$n and ${}^{\;\;4}_{\Lambda\Lambda}$n are found unbound by a wide margin. A relatively large value of $|a_{\Lambda\Lambda}| \gtrsim 1.5$ fm is needed to bind ${}^{\;\;4}_{\Lambda\Lambda}$H, thereby questioning its particle stability. In contrast, the particle stability of the $A = 5$ $\Lambda\Lambda$ hypernuclear isodoublet ${}^{\;\;5}_{\Lambda\Lambda}$H–${}^{\;\;5}_{\Lambda\Lambda}$He is robust, with Λ separation energy of order 1 MeV.

1. Introduction

Single-Λ and double-Λ ($\Lambda\Lambda$) hypernuclei provide a unique extension of nuclear physics into strange hadronic matter [1]. Whereas the behavior of a single Λ hyperon in atomic nuclei has been deduced quantitatively by studying Λ hypernuclei (${}^{\;\;A}_{\Lambda}$Z) from $A = 3$ to 208 [2], only three $\Lambda\Lambda$ hypernuclei (${}^{\;\;A}_{\Lambda\Lambda}$Z) are firmly established: the lightest known ${}^{\;\;6}_{\Lambda\Lambda}$He Nagara event [3] and two heavier ones, ${}^{\;\;10}_{\Lambda\Lambda}$Be and ${}^{\;\;13}_{\Lambda\Lambda}$B [4]. Remarkably, their binding energies come out consistently in shell-model calculations [5]. Few ambiguous emulsion events from KEK [6] and J-PARC [7] have also been reported. However, and perhaps more significant is the absence of any good data on the onset of $\Lambda\Lambda$ hypernuclear binding for $A < 6$. In distinction from the heavier species, these very light s-shell species, if bound, could be more affected by microscopic strangeness $\mathcal{S} = -2$ dynamics. An obvious issue is the effect of a possible ΞN dominated H dibaryon resonance some 20–30 MeV above the $\Lambda\Lambda$ threshold [8,9] on $\Lambda\Lambda$ hypernuclear binding in general.

Several calculations of light $A < 6$ s-shell $\Lambda\Lambda$ hypernuclei using $\Lambda\Lambda$ interactions fitted to ${}^{\;\;6}_{\Lambda\Lambda}$He suggest a fairly weak $\Lambda\Lambda$ interaction, with the onset of $\Lambda\Lambda$ hypernuclear binding deferred to $A = 4$. Indeed, a slightly bound $I = 0$ ${}^{\;\;4}_{\Lambda\Lambda}H(1^+)$ was found in $\Lambda\Lambda pn$ four-body calculations by Nemura et al. [10,11] but not in a four-body calculation by Filikhin and Gal [12] who nonetheless got it bound as a $\Lambda\Lambda d$ cluster. Unfortunately, the AGS-E906 counter experiment [13] searching for light $\Lambda\Lambda$ hypernuclei failed to provide conclusive evidence for the particle stability of ${}^{\;\;4}_{\Lambda\Lambda}$H [14,15]. Interestingly, the neutral four-body system ${}^{\;\;4}_{\Lambda\Lambda}$n has been assigned in Ref. [15] to the main yet unexplained signal observed by AGS-E906. Recent few-body calculations of ${}^{\;\;4}_{\Lambda\Lambda}$n [16,17] diverge on its particle stability, but since none was constrained by the ${}^{\;\;6}_{\Lambda\Lambda}$He binding energy datum, no firm conclusion can be drawn yet.

In the present work we study the light $A \leq 6$ s-shell $\Lambda\Lambda$ hypernuclei together with their nuclear and Λ hypernuclear cores at leading-order (LO) $\not\pi$EFT. The $\not\pi$EFT approach was first applied to few-nucleon atomic nuclei in Refs. [18,19] and recently also in lattice calculations of nuclei [20–23] and to s-shell single-Λ hypernuclei [24]. Focusing on $\not\pi$EFT applications to $\mathcal{S} = -2$ light systems, we note Λ-Λ-core LO calculations done for $A = 4$ [25] and separately for $A = 6$ [26], which therefore limits their predictive power. Among past non-EFT studies, the only work that covers *all* s-shell $\Lambda\Lambda$ hypernuclei is by Nemura et al. [11] who used simulated forms of outdated hard-core YN and YY Nijmegen potentials [27]. No chiral EFT (χEFT) calculations of $\Lambda\Lambda$ hypernuclei have been reported, although χEFT representations of the $\Lambda\Lambda$ interaction at LO [28] and NLO [29] do exist. Hence, the present LO $\not\pi$EFT work is the first comprehensive EFT application to light

* Corresponding author.
E-mail address: avragal@savion.huji.ac.il (A. Gal).

https://doi.org/10.1016/j.physletb.2019.134893

$\Lambda\Lambda$ hypernuclei, and could be generalized in principle to study multi-Λ hypernuclei and strange hadronic matter.

The $\not\pi$EFT baryonic Lagrangian governing multi-Λ hypernuclei requires, at LO, one $\Lambda\Lambda$ and one $\Lambda\Lambda N$ interaction terms beyond the interaction terms involved in the description of single-Λ hypernuclei. We fit the new $\Lambda\Lambda$ contact term to a $\Lambda\Lambda$ scattering length value spanning a range of values, -0.5 fm to -1.9 fm, suggested by analyses of the $\Lambda\Lambda$ invariant mass spectrum [30] measured in the ^{12}C(K^-, K^+) reaction at the KEK-PS [31] and of $\Lambda\Lambda$ correlations [32] extracted from ultra-relativistic Au+Au collisions at the RHIC-STAR experiment [33]. The corresponding $\Lambda\Lambda$ interactions are weakly attractive, far from producing a $\Lambda\Lambda$ bound state. Recent analyses of LHC-ALICE experiments reach similar conclusions, but leave room also for a $\Lambda\Lambda$ bound state [34]. For each choice of $\Lambda\Lambda$ contact term we determine a $\Lambda\Lambda N$ three-body contact term, promoted to LO, by fitting to $\Delta B_{\Lambda\Lambda}({}^{\;\;6}_{\Lambda\Lambda}\mathrm{He}) = B_{\Lambda\Lambda}({}^{\;\;6}_{\Lambda\Lambda}\mathrm{He}) - 2B_{\Lambda}({}^{5}_{\Lambda}\mathrm{He}) = 0.67 \pm 0.17$ MeV. With such $\Lambda\Lambda$ and $\Lambda\Lambda N$ contact-term input our $\not\pi$EFT scheme exhibits renormalization scale invariance in the limit of point-like interactions, demonstrating that no $N \geq 4$ N-body contact term is required at LO, as first shown by Platter et al. [35] for a four-nucleon system. Applying this scheme to explore $A = 3, 4, 5$ $\Lambda\Lambda$ hypernuclei, we find that unless $|a_{\Lambda\Lambda}| \gtrsim 1.5$ fm, ${}^{\;\;4}_{\Lambda\Lambda}$H is unlikely to be particle stable. The neutral systems ${}^{\;\;3}_{\Lambda\Lambda}$n and ${}^{\;\;4}_{\Lambda\Lambda}$n are found unstable by a wide margin. A robust particle stability is established for the ${}^{\;\;5}_{\Lambda\Lambda}$H–${}^{\;\;5}_{\Lambda\Lambda}$He $A = 5$ isodoublet, with Λ separation energy of order 1 MeV, providing further support for a recent J-PARC proposal P75 [36] to produce ${}^{\;\;5}_{\Lambda\Lambda}$H. Possible extensions of our work are briefly discussed in the concluding section.

2. Application of $\not\pi$EFT to $\Lambda\Lambda$ hypernuclei

With $\Lambda\Lambda$ one-pion exchange forbidden by isospin invariance, the lowest mass pseudoscalar meson exchange is provided by a short range η exchange ($\approx$0.4 fm) which is rather weak in SU(3) flavor. Pions appear in the $\Lambda\Lambda$ dynamics through excitation to fairly high-lying $\Sigma\Sigma$ intermediate states. Therefore, a reasonable choice of a $\not\pi$EFT breakup scale is $2m_\pi$, same as argued for in our recent work on Λ hypernuclei [24]. Excitation from $\Lambda\Lambda$ states to the considerably lower mass ΞN intermediate states requires a shorter range K meson exchange which, together with other short-range exchanges, is accounted for implicitly by the chosen $\not\pi$EFT contact interactions. To provide a meaningful $\not\pi$EFT expansion parameter we note that since $\Delta B_{\Lambda\Lambda}({}^{\;\;6}_{\Lambda\Lambda}\mathrm{He})$ is less than 1 MeV, considerably smaller than $B_\Lambda({}^{5}_{\Lambda}\mathrm{He})$, a Λ momentum scale Q in ${}^{\;\;6}_{\Lambda\Lambda}$He may be approximated by that in ${}^{5}_{\Lambda}$He [24], namely $p_\Lambda \approx \sqrt{2M_\Lambda B_\Lambda} = 83$ MeV/c, yielding a $\not\pi$EFT expansion parameter $(Q/2m_\pi) \approx 0.3$ and LO accuracy of order $(Q/2m_\pi)^2 \approx 0.09$.

To construct the appropriate $\not\pi$EFT Lagrangian density at LO we follow our previous work on single-Λ hypernuclei [24]:

$$\mathcal{L}^{(\mathrm{LO})} = \sum_B B^\dagger (i\partial_0 + \frac{\nabla^2}{2M_B}) B - \mathcal{V}_2 - \mathcal{V}_3, \tag{1}$$

where $B = (N, \Lambda)$ and $\mathcal{V}_2, \mathcal{V}_3$ consist of two-body and three-body s-wave contact interaction terms, each of which is associated with its own low-energy constant (LEC). These contact terms are shown diagrammatically in Fig. 1 and the corresponding LECs are listed alongside. Going from single-Λ hypernuclei to multi-Λ hypernuclei brings in one new $\Lambda\Lambda$ two-body LEC, C_5, and one new $\Lambda\Lambda N$ three-body LEC, D_5, each one labeled by the total Pauli-spin and isospin involved. This completes the set of LECs required to describe single-, double- and in general multi-Λ hypernuclei at LO. Further contact terms, such as a three-body $\Lambda\Lambda\Lambda$ term, appear only at subleading orders.

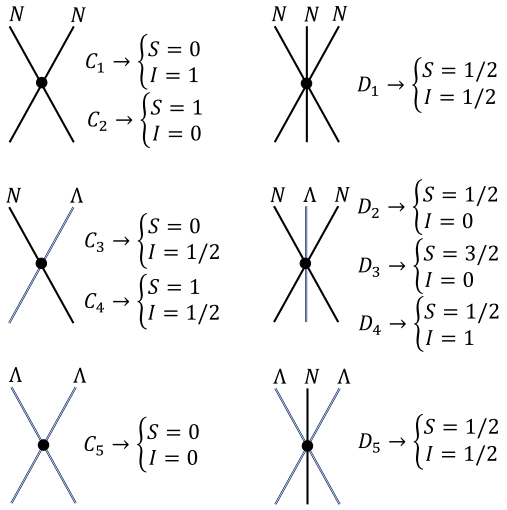

Fig. 1. Diagrammatic presentation of two-body (left) and three-body (right) contact terms, and their associated LEC input $(C_1, \ldots, C_5)$ and $(D_1, \ldots, D_5)$ to a LO $\not\pi$EFT calculation of light nuclei (upper) Λ hypernuclei (middle) and $\Lambda\Lambda$ hypernuclei (lower), with values of spin S and isospin I corresponding to s-wave configurations.

Following the procedure applied in Ref. [18], the two-body contact interaction term $\mathcal{V}_2$ gives rise to a two-body potential

$$V_2 = \sum_{IS} C_\lambda^{IS} \sum_{i<j} \mathcal{P}_{IS}(ij)\delta_\lambda(\boldsymbol{r}_{ij}), \tag{2}$$

where $\mathcal{P}_{IS}$ are projection operators on s-wave $NN, \Lambda N, \Lambda\Lambda$ pairs with isospin I and spin S values associated in Fig. 1 with two-body LECs. These LECs are fitted to low-energy two-body observables, e.g., to the corresponding $NN, \Lambda N, \Lambda\Lambda$ scattering lengths. The subscript λ attached to C^{IS} in Eq. (2) stands for a momentum cutoff introduced in a Gaussian form to regularize the zero-range contact terms:

$$\delta_\lambda(\boldsymbol{r}) = \left(\frac{\lambda}{2\sqrt{\pi}}\right)^3 \exp\left(-\frac{\lambda^2}{4}\boldsymbol{r}^2\right), \tag{3}$$

thereby smearing a zero-range (in the limit $\lambda \to \infty$) Dirac $\delta^{(3)}(\boldsymbol{r})$ contact term over distances $\sim \lambda^{-1}$. The cutoff parameter λ may be viewed as a scale parameter with respect to typical values of momenta Q. To make observables cutoff independent, the LECs must be properly renormalized. Truncating $\not\pi$EFT at LO and using values of λ higher than the breakup scale of the theory (here $\approx 2m_\pi$), observables acquire a residual dependence $O(Q/\lambda)$ which diminishes with increasing λ.

The three-body contact interaction, promoted to LO, gives rise to a three-body potential

$$V_3 = \sum_{\alpha IS} D_{\alpha\lambda}^{IS} \sum_{i<j<k} \mathcal{Q}_{IS}(ijk) \left(\sum_{\mathrm{cyc}} \delta_\lambda(\boldsymbol{r}_{ij})\delta_\lambda(\boldsymbol{r}_{jk})\right), \tag{4}$$

where $\mathcal{Q}_{IS}$ projects on NNN, $NN\Lambda$ and $\Lambda\Lambda N$ s-wave triplets with isospin I and spin S values associated in Fig. 1 with three-body LECs which are fitted to given binding energies. The subscript α distinguishes between the two $IS = \frac{1}{2}\frac{1}{2}$ NNN and $\Lambda\Lambda N$ triplets marked in the figure.

Using two-body V_2 and three-body V_3 regularized contact interaction terms as described above, we solved the A-body Schrödinger equation variationally by expanding the wave function Ψ in a correlated Gaussian basis using the SVM. For a comprehensive review of this method, see Ref. [38]. For a specific calculation of the three-body interaction matrix elements, see Ref. [39].

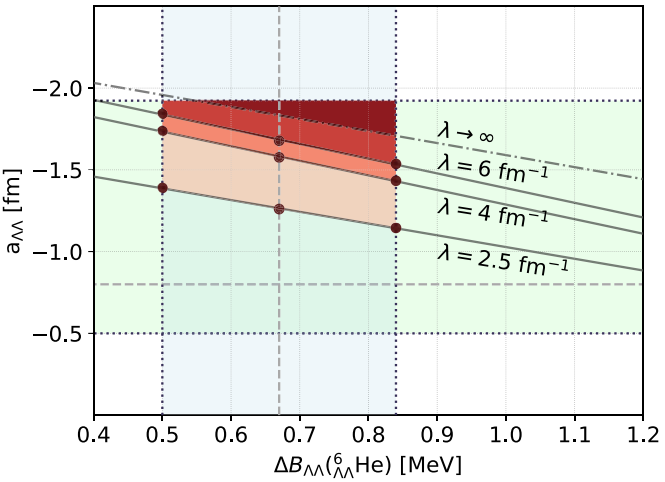

Fig. 2. Minimum values of $|a_{\Lambda\Lambda}|$ for which ${}^{4}_{\Lambda\Lambda}\mathrm{H}$ becomes bound are plotted, for several values of cutoff λ, as a function of $\Delta B_{\Lambda\Lambda}({}^{6}_{\Lambda\Lambda}\mathrm{He})$ using the Alexander[B] ΛN interaction model [24]. The vertical dotted lines mark the experimental uncertainty of $\Delta B_{\Lambda\Lambda}$. Horizontal lines mark the range of $a_{\Lambda\Lambda}$ values $[-0.5, -1.9]$ fm suggested by studies of $\Lambda\Lambda$ correlations [30,32], with a representative value of $a_{\Lambda\Lambda} = -0.8$ fm marked by a dashed line. The $\lambda \to \infty$ limit is reached assuming a Q/λ asymptotic behavior, similar to the discussion around Eq. (5) below.

Table 1
Λ separation energies $B_{\Lambda}({}^{A}_{\Lambda\Lambda}\mathrm{Z})$ for $A = 3$–6, calculated using $a_{\Lambda\Lambda} = -0.8$ fm, cutoff $\lambda = 4$ fm^{-1} and the Alexander[B] ΛN interaction model [24]. In each row a $\Lambda\Lambda N$ LEC was fitted to the underlined binding energy constraint.

Constraint (MeV)	${}^{3}_{\Lambda\Lambda}\mathrm{n}$	${}^{4}_{\Lambda\Lambda}\mathrm{n}$	${}^{4}_{\Lambda\Lambda}\mathrm{H}$	${}^{5}_{\Lambda\Lambda}\mathrm{H}$	${}^{6}_{\Lambda\Lambda}\mathrm{He}$
$\Delta B_{\Lambda\Lambda}({}^{6}_{\Lambda\Lambda}\mathrm{He}) = \underline{0.67}$	–	–	–	1.21	3.28
$B_{\Lambda}({}^{4}_{\Lambda\Lambda}\mathrm{H}) = \underline{0.05}$	–	–	0.05	2.28	4.76
$B({}^{4}_{\Lambda\Lambda}\mathrm{n}) = \underline{0.10}$	–	0.10	0.86	4.89	7.89
$B({}^{3}_{\Lambda\Lambda}\mathrm{n}) = \underline{0.10}$	0.10	15.15	18.40	22.13	25.66

3. Results and discussion

We first discuss the case of ${}^{4}_{\Lambda\Lambda}\mathrm{H}$, with $I = 0$ and $J^{\pi} = 1^{+}$, which following the brief discussion in the Introduction could signal the onset of $\Lambda\Lambda$ hypernuclear binding. For each of several given cutoff values λ we searched for minimum values of $|a_{\Lambda\Lambda}|$, as a function of $\Delta B_{\Lambda\Lambda}({}^{6}_{\Lambda\Lambda}\mathrm{He})$, that would make ${}^{4}_{\Lambda\Lambda}\mathrm{H}$ particle stable. The choice of a specific value for this $\Delta B_{\Lambda\Lambda}$ determines the $\Lambda\Lambda N$ LEC necessary for the ${}^{4}_{\Lambda\Lambda}\mathrm{H}$ calculation, in addition to the $\Lambda\Lambda$ LEC determined by $a_{\Lambda\Lambda}$. The resulting values of $|a_{\Lambda\Lambda}|$ above which ${}^{4}_{\Lambda\Lambda}\mathrm{H}$ is particle stable are plotted in Fig. 2 as a function of $\Delta B_{\Lambda\Lambda}({}^{6}_{\Lambda\Lambda}\mathrm{He})$. Choosing sufficiently large values of the cutoff λ, say $\lambda \gtrsim 4$ fm^{-1}, for which convergence to the renormalization scale invariance limit $\lambda \to \infty$ is seen explicitly in the figure, one concludes that $|a_{\Lambda\Lambda}|$ needs to be larger than $\approx$1.5 fm to bind ${}^{4}_{\Lambda\Lambda}\mathrm{H}$. A $\Lambda\Lambda$ scattering length of such size would make the $\Lambda\Lambda$ interaction almost as strong as the ΛN interaction, whereas most theoretical constructions, e.g. recent Nijmegen models, suggest that it is considerably weaker, say $|a_{\Lambda\Lambda}| \approx 0.8$ fm [40]. For this reason we argue that ${}^{4}_{\Lambda\Lambda}\mathrm{H}$ is unlikely to be particle stable.

Using representative values $a_{\Lambda\Lambda} = -0.8$ fm and cutoff $\lambda = 4$ fm^{-1}, values for which according to Fig. 2 ${}^{4}_{\Lambda\Lambda}\mathrm{H}$ is particle unstable, one may reduce the repulsive $\Lambda\Lambda N$ LEC in order to make it particle stable. According to the first two rows in Table 1, this will overbind ${}^{6}_{\Lambda\Lambda}\mathrm{He}$ by $\approx$1.5 MeV. Reducing further the $\Lambda\Lambda N$ LEC one binds the neutral systems, first ${}^{4}_{\Lambda\Lambda}\mathrm{n}$ (third row) and then ${}^{3}_{\Lambda\Lambda}\mathrm{n}$ (fourth row), at a price of overbinding further ${}^{6}_{\Lambda\Lambda}\mathrm{He}$. In fact, the particle stability of these $A = 3, 4$ neutral $\Lambda\Lambda$ systems is incompatible with the ${}^{6}_{\Lambda\Lambda}\mathrm{He}$ Nagara event binding energy datum for all

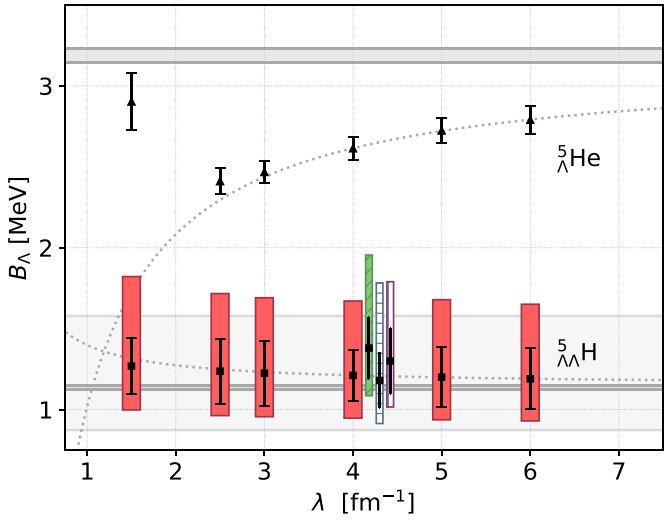

Fig. 3. Λ separation energies $B_{\Lambda}({}^{5}_{\Lambda\Lambda}\mathrm{H})$ and $B_{\Lambda}({}^{5}_{\Lambda}\mathrm{He})$ from SVM calculations that use $\not\pi$EFT LO two-body (2) and three-body (4) regularized contact interactions, constrained by requiring $\Delta B_{\Lambda\Lambda}({}^{6}_{\Lambda\Lambda}\mathrm{He}) = 0.67 \pm 0.17$ MeV, are plotted as a function of the cutoff λ. Error bars (in black) reflect the experimental uncertainty inherent in the ${}^{3}_{\Lambda}\mathrm{H}$, ${}^{4}_{\Lambda}\mathrm{H}$, ${}^{4}_{\Lambda}\mathrm{H}^{*}$ and ${}^{6}_{\Lambda\Lambda}\mathrm{He}$ binding-energy input data, and (red) rectangles include also varying $a_{\Lambda\Lambda}$ between -0.5 to -1.9 fm. The ΛN interaction model used is Alexander[B] [24], with results for models χLO, χNLO and NSC97f shown from left to right in this order for $\lambda = 4$ fm^{-1}. Dotted lines show extrapolations, as $\lambda \to \infty$, to the respective scale renormalization invariance limits marked by gray horizontal bands. The wider ${}^{5}_{\Lambda\Lambda}\mathrm{H}$ band accounts for uncertainties in the experimental values of binding energies used in extrapolating to $\lambda \to \infty$.

values of cutoff λ and scattering length $a_{\Lambda\Lambda}$ tested in Fig. 2. These results suggest quantitatively that the $A = 3, 4$ light neutral $\Lambda\Lambda$ hypernuclei are unbound within a large margin.

Calculated values of the Λ separation energy $B_{\Lambda}({}^{5}_{\Lambda\Lambda}\mathrm{H})$ are shown in Fig. 3. Several representative values of the $\Lambda\Lambda$ scattering length were used: $a_{\Lambda\Lambda} = -0.5, -0.8, -1.9$ fm, spanning a broad range of values suggested in $\Lambda\Lambda$ correlation studies [30, 32] of experimental spectra mentioned in the Introduction. Again, the choice of $a_{\Lambda\Lambda}$ determines the one $\Lambda\Lambda$ LEC required at LO, while the $\Lambda\Lambda N$ LEC was fitted to the $\Delta B_{\Lambda\Lambda}({}^{6}_{\Lambda\Lambda}\mathrm{He}) = 0.67 \pm 0.17$ MeV datum. For the ΛN interaction terms we generally used the Alexander[B] ΛN model [24], with its ΛN C_3 and C_4 LECs (see Fig. 1) corresponding to the scattering lengths $a_s = -1.8$ fm and $a_t = -1.6$ fm, respectively, from [41]. For cutoff $\lambda = 4$ fm^{-1} we also used three other ΛN interaction models from Ref. [24]: χLO [42], χNLO [43] and NSC97f [44], demonstrating that the ΛN model dependence is rather weak when it comes to Λ separation energies in double-Λ hypernuclei, provided B_{Λ} values of single-Λ hypernuclei for $A < 5$ are fitted to generate the necessary ΛNN LECs.[1] Calculated values of $B_{\Lambda}({}^{5}_{\Lambda}\mathrm{He})$, compatible with those from Ref. [24] are also shown in the figure, demonstrating the suitability of the input ΛN model. One observes that ${}^{5}_{\Lambda\Lambda}\mathrm{H}$ comes out particle stable over a broad range of finite cutoff values used in the calculations. This is not the case for ${}^{4}_{\Lambda\Lambda}\mathrm{H}$ which, as discussed above, is unbound with respect to ${}^{3}_{\Lambda}\mathrm{H}$ for most of the permissible parameter space.

The calculated B_{Λ} values shown in Fig. 3 exhibit renormalization scale invariance in the limit of $\lambda \to \infty$. To figure out the associated $B_{\Lambda}(\lambda \to \infty)$ values, we extrapolated $B_{\Lambda}(\lambda)$ for $\lambda \geq 4$ fm^{-1} using a power series in the small parameter Q/λ:

[1] This is reminiscent of the weak dependence of Λ separation energies in single-Λ hypernuclei on the input NN interaction, found in few-body calculations by Nogga et al. [45].

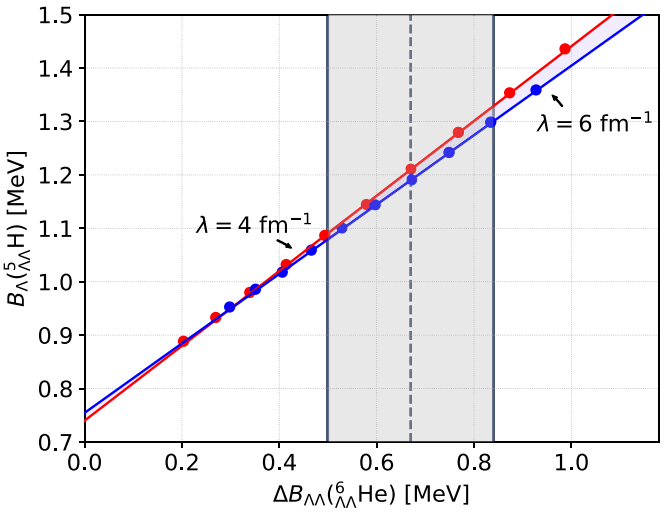

Fig. 4. Hypernuclear Tjon lines: calculated Λ separation energies $B_\Lambda(^5_{\Lambda\Lambda}\mathrm{H})$ are plotted as a function of the constrained value assumed for $\Delta B_{\Lambda\Lambda}(^6_{\Lambda\Lambda}\mathrm{He})$ for two cutoff values, using $a_{\Lambda\Lambda} = -0.8$ fm. The shaded vertical area marks the observed value $\Delta B_{\Lambda\Lambda}(^6_{\Lambda\Lambda}\mathrm{He}) = 0.67 \pm 0.17$ MeV. The ΛN interaction model used is Alexander[B] [24].

$$\frac{B_\Lambda(\lambda)}{B_\Lambda(\infty)} = \left[1 + \alpha\frac{Q}{\lambda} + \beta\left(\frac{Q}{\lambda}\right)^2 + \ldots\right]. \tag{5}$$

The corresponding extrapolation curves are shown by dotted lines in Fig. 3, converging at asymptotic values $B_\Lambda(\infty)$ given with their extrapolated uncertainties by the gray horizontal bands in the figure. $^5_{\Lambda\Lambda}$H remains particle stable in this limit with Λ separation energy $B_\Lambda(\infty) = 1.14 \pm 0.01^{+0.44}_{-0.26}$ MeV, where the first uncertainty is due to extrapolating by use of Eq. (5) and the second one is due to the $a_{\Lambda\Lambda}$ and B_Λ uncertainties.

The Λ separation energies $B_\Lambda(^5_{\Lambda\Lambda}\mathrm{H})$ studied above are correlated with those of $^6_{\Lambda\Lambda}$He in a way reminiscent of the Tjon line correlation between binding energies calculated for ^{3}H and ^{4}He [46]. This is shown in Fig. 4 by the linear dependence of $B_\Lambda(^5_{\Lambda\Lambda}\mathrm{H})$, for two given values of the cutoff λ, on the value assumed for $\Delta B_{\Lambda\Lambda}(^6_{\Lambda\Lambda}\mathrm{He})$, which was varied for this purpose around the 'physical' value 0.67±0.17 MeV. We note that the cutoff dependence of this correlation is very weak. The hypernuclear correlation noted here is generated by variation of the $\Lambda\Lambda N$ LEC which is derived from $\Delta B_{\Lambda\Lambda}(^6_{\Lambda\Lambda}\mathrm{He})$. This is similar to the origin and realization of Tjon-line correlations in nuclear physics, where many-body contact interaction terms beyond three-body terms do not appear at LO [35]. However unlike other physics applications where Tjon lines were shown to hold, its appearance here does not require proximity to the unitary limit.

We note that $a_{\Lambda\Lambda}$ includes implicitly the coupling of the $\Lambda\Lambda$ channel to the higher mass $I = S = 0$ ΞN and $\Sigma\Sigma$ channels. However, beginning with $^6_{\Lambda\Lambda}$He the coupling to the relatively low-lying ΞN channel is partially Pauli blocked (with the formed nucleon excluded from the s shell). It could be argued then that the reference value of $\Delta B_{\Lambda\Lambda}(^6_{\Lambda\Lambda}\mathrm{He})$ used in this work has to be somewhat increased in order to account for the blocked states which are included effectively in the present LO application of $\not\pi$EFT to $\Lambda\Lambda$ hypernuclei. The coupled-channel calculations by Vidaña et al. [50] suggest an increase of ≈0.25 MeV which according to Fig. 4 would increase $B_\Lambda(^5_{\Lambda\Lambda}\mathrm{H})$ by roughly 0.15 MeV and $^4_{\Lambda\Lambda}$H, had it been bound, by no more than 0.03 MeV. Interestingly, recent HAL QCD Collaboration studies based on LQCD find a vanishingly small $I = 0$ $^1S_0$ $\Lambda\Lambda - \Xi N$ coupling potential for $r \gtrsim 0.6$ fm [51]. Consequences of this extremely weak coupling, as well as the one derived at NLO within χEFT [29], on few-body $\Lambda\Lambda$ hypernuclei should be studied in future NLO calculations.

4. Summary and outlook

The focus in this first comprehensive $\not\pi$EFT application to light $\Lambda\Lambda$ hypernuclei was to study the onset of binding in the $\mathcal{S} = -2$ hadronic sector by constraining $\Delta B_{\Lambda\Lambda}(^6_{\Lambda\Lambda}\mathrm{He})$ to the most recent value 0.67±0.17 MeV [4] assigned to the Nagara event [3]. We varied the value assumed for the $\Lambda\Lambda$ scattering length $a_{\Lambda\Lambda}$ over a range of values suggested in Refs. [30,32] by analyzing $\Lambda\Lambda$ correlations observed in several high-energy production reactions, but barring an unlikely $\Lambda\Lambda$ bound state [8,9,52]. Our results suggest with little model dependence that both members of the $A = 5$ isodoublet pair, $^5_{\Lambda\Lambda}$H and $^5_{\Lambda\Lambda}$He, are particle stable. Of the $A = 4$ $\Lambda\Lambda$ hypernuclei, the particle stability of the $I = 0$ $^4_{\Lambda\Lambda}\mathrm{H}(1^+)$ requires values of $|a_{\Lambda\Lambda}| \gtrsim 1.5$ fm, which are unlikely in our opinion. The $I = 1$ excited state $^4_{\Lambda\Lambda}\mathrm{H}(0^+)$, or its isospin analog state $^4_{\Lambda\Lambda}$n are far from being bound; if any of these were established experimentally, the soundness of the Nagara event would suffer a serious setback.

Extensions of the present LO work should consider explicit $\Lambda\Lambda$-ΞN-$\Sigma\Sigma$ coupling in the $^1S_0$ channel or, at least, address momentum dependent $\Lambda\Lambda$ interaction components generated in NLO EFT through effective-range ($r_{\Lambda\Lambda}$) contributions. We note that no conclusive determination of $r_{\Lambda\Lambda}$ exists yet because of the scarce and inaccurate hyperon-hyperon (mostly $\Xi^- p$) scattering and reaction data available in the ≈25 MeV interval between the $\Lambda\Lambda$ and ΞN thresholds. For example, small values of $r_{\Lambda\Lambda}$ between 0.3 to 0.8 fm were derived from such data in the LO χEFT work of the Jülich-Bonn group [28] using values of $a_{\Lambda\Lambda}$ about −1.5 fm. In contrast, large values of $r_{\Lambda\Lambda}$ between 5 to 7 fm were derived from the same data in the NLO χEFT work of the Jülich-Bonn-Munich group [29] using values of $a_{\Lambda\Lambda}$ about −0.65 fm. This dichotomy is apparent also for the Nijmegen soft core potentials listed in Table I of Ref. [30] and would have to be considered in future studies of $\Lambda\Lambda$ hypernuclei.

Acknowledgements

The work of L.C. and N.B. was supported by the PAZY Foundation and by the Israel Science Foundation Grant No. 1308/16. The work of M.S. and J.M. was supported by the Czech Science Foundation GACR Grant No. 19-19640S.

References

[1] J. Schaffner-Bielich, A. Gal, Phys. Rev. C 62 (2000) 034311, and references therein.
[2] A. Gal, E.V. Hungerford, D.J. Millener, Rev. Mod. Phys. 88 (2016) 035004.
[3] H. Takahashi, et al., Phys. Rev. Lett. 87 (2001) 212502.
[4] E. Hiyama, K. Nakazawa, Annu. Rev. Nucl. Part. Sci. 68 (2018) 131.
[5] A. Gal, D.J. Millener, Phys. Lett. B 701 (2011) 342, Hyperfine Interact. 210 (2012) 77.
[6] A. Aoki, et al., KEK E176 Collaboration, Nucl. Phys. A 828 (2009) 191; K. Nakazawa, for KEK E176 and E373 Collaborations, Nucl. Phys. A 835 (2010) 207.
[7] H. Ekawa, et al., J-PARC E07 Collaboration, Prog. Theor. Exp. Phys. 2019 (2019) 021D02.
[8] T. Inoue, et al., HAL QCD Collaboration, Nucl. Phys. A 881 (2012) 28.
[9] J. Haidenbauer, U.-G. Meißner, Nucl. Phys. A 881 (2012) 44.
[10] H. Nemura, Y. Akaishi, K.S. Myint, Phys. Rev. C 67 (2003) 051001(R).
[11] H. Nemura, S. Shinmura, Y. Akaishi, K.S. Myint, Phys. Rev. Lett. 94 (2005) 202502. Note that $^4_{\Lambda\Lambda}$H which is bound in this work by as little as $B_\Lambda = 2$ keV would become particle unstable upon revising $\Delta B_{\Lambda\Lambda}(^6_{\Lambda\Lambda}\mathrm{He})$ from 1.01±0.20 MeV [3], a value used there to calibrate the strength of the $\Lambda\Lambda$ interaction, to the latest value 0.67±0.17 MeV [4].
[12] I.N. Filikhin, A. Gal, Phys. Rev. Lett. 89 (2002) 172502.
[13] J.K. Ahn, et al., Phys. Rev. Lett. 87 (2001) 132504.

[14] S.D. Randeniya, E.V. Hungerford, Phys. Rev. C 76 (2007) 064308.
[15] S. Bleser, M. Bölting, T. Gaitanos, J. Pochodzalla, F. Schupp, M. Steinen, Phys. Lett. B 790 (2019) 502.
[16] J.M. Richard, Q. Wang, Q. Zhao, Phys. Rev. C 91 (2015) 014003.
[17] H. Garcilazo, A. Valcarce, J. Vijande, Chin. Phys. C 41 (2017) 074102.
[18] U. van Kolck, Nucl. Phys. A 645 (1999) 273.
[19] P.F. Bedaque, H.-W. Hammer, U. van Kolck, Nucl. Phys. A 676 (2000) 357.
[20] N. Barnea, L. Contessi, D. Gazit, F. Pederiva, U. van Kolck, Phys. Rev. Lett. 114 (2015) 052501.
[21] J. Kirscher, N. Barnea, D. Gazit, F. Pederiva, U. van Kolck, Phys. Rev. C 92 (2015) 054002.
[22] L. Contessi, A. Lovato, F. Pederiva, A. Roggero, J. Kirscher, U. van Kolck, Phys. Lett. B 772 (2017) 839.
[23] J. Kirscher, E. Pazy, J. Drachman, N. Barnea, Phys. Rev. C 96 (2017) 024001.
[24] L. Contessi, N. Barnea, A. Gal, Phys. Rev. Lett. 121 (2018) 102502.
[25] S.-I. Ando, G.-S. Yang, Y. Oh, Phys. Rev. C 89 (2014) 014318.
[26] S.-I. Ando, Y. Oh, Phys. Rev. C 90 (2014) 037301.
[27] M.M. Nagels, T.A. Rijken, J.J. de Swart, Phys. Rev. D 15 (1977) 2547, Phys. Rev. D 20 (1979) 1633.
[28] H. Polinder, J. Haidenbauer, U.-G. Meißner, Phys. Lett. B 653 (2007) 29.
[29] J. Haidenbauer, U.-G. Meißner, S. Petschauer, Nucl. Phys. A 954 (2016) 273.
[30] A.M. Gasparyan, J. Haidenbauer, C. Hanhart, Phys. Rev. C 85 (2012) 015204.
[31] C.J. Yoon, et al., KEK-PS E522 Collaboration, Phys. Rev. C 75 (2007) 022201(R).
[32] K. Morita, T. Furumoto, A. Ohnishi, Phys. Rev. C 91 (2015) 024916;
A. Ohnishi, K. Morita, K. Miyahara, T. Hyodo, Nucl. Phys. A 954 (2016) 294.
[33] L. Adamczyk, et al., STAR Collaboration, Phys. Rev. Lett. 114 (2015) 022301.
[34] S. Acharya, et al., ALICE Collaboration, Phys. Rev. C 99 (2019) 024001;
See also S. Acharya, et al., ALICE Collaboration, Phys. Lett. B 797 (2019) 134822.
[35] L. Platter, H.-W. Hammer, U.-G. Meißner, Phys. Lett. B 607 (2005) 254.
[36] H. Fujioka, T. Fukuda, E. Hiyama, T. Motoba, T. Nagae, S. Nagao, T. Takahashi, in: AIP Conf. Proc., vol. 2130, 2019, p. 040002. The case for particle stability of ${}^{5}_{\Lambda\Lambda}$H, in relation to the ${}^{6}_{\Lambda\Lambda}$He Nagara event, was made in Ref. [37] and confirmed since then by several other calculations reviewed in Ref. [2].
[37] I.N. Filikhin, A. Gal, Nucl. Phys. A 707 (2002) 491.
[38] Y. Suzuki, K. Varga, Stochastic Variational Approach to Quantum Mechanical Few-Body Problems, Springer-Verlag, Berlin, 1998.
[39] B. Bazak, M. Eliyahu, U. van Kolck, Phys. Rev. A 94 (2016) 052502.
[40] E. Hiyama, T. Motoba, T.A. Rijken, Y. Yamamoto, Prog. Theor. Phys. Suppl. 185 (2010) 1.
[41] G. Alexander, U. Karshon, A. Shapira, et al., Phys. Rev. 173 (1968) 1452.
[42] H. Polinder, J. Haidenbauer, U.-G. Meißner, Nucl. Phys. A 779 (2006) 244.
[43] J. Haidenbauer, S. Petschauer, N. Kaiser, U.-G. Meißner, A. Nogga, W. Weise, Nucl. Phys. A 915 (2013) 24.
[44] Th.A. Rijken, V.G.J. Stoks, Y. Yamamoto, Phys. Rev. C 59 (1999) 21.
[45] A. Nogga, H. Kamada, W. Glöckle, Phys. Rev. Lett. 88 (2002) 172501.
[46] J.A. Tjon, Phys. Lett. B 56 (1975) 217. Tjon line correlations in hypernuclear physics were noted between calculated values of $\Delta B_{\Lambda\Lambda}({}^{6}_{\Lambda\Lambda}\mathrm{He})$ and $\Delta B_{\Lambda\Lambda}({}^{10}_{\Lambda\Lambda}\mathrm{Be})$ [47–49] and also for $\Delta B_{\Lambda\Lambda}({}^{5}_{\Lambda\Lambda}\mathrm{H})$ and $\Delta B_{\Lambda\Lambda}({}^{6}_{\Lambda\Lambda}\mathrm{He})$ [37].
[47] A.R. Bodmer, Q.N. Usmani, J. Carlson, Nucl. Phys. A 422 (1984) 510.
[48] X.C. Wang, H. Takaki, H. Bando, Prog. Theor. Phys. 76 (1986) 865.
[49] I.N. Filikhin, A. Gal, Phys. Rev. C 65 (2002) 041001(R).
[50] I. Vidaña, A. Ramos, A. Polls, Phys. Rev. C 70 (2004) 024306.
[51] K. Sasaki, et al., HAL QCD Collaboration, EPJ Web Conf. 175 (2018) 05010.
[52] A. Gal, Phys. Rev. Lett. 110 (2013) 179201.

Stability of fermionic states with contact theories

M. Schäfer,[1,2,*] L. Contessi,[3,4,†] and J. Kirscher[5]

[1] *Nuclear Physics Institute of the Czech Academy of Sciences, 25069 Řež, Czech Republic*
[2] *Czech Technical University in Prague, Faculty of Nuclear Sciences and Physical Engineering, Břehová 7, 11519 Prague 1, Czech Republic*
[3] *Racah Institute of Physics, The Hebrew University, 91904 Jerusalem, Israel*
[4] *AESNT, CEA, IRFU, Département de Physique Nucléaire, Université de Paris Saclay, F-91191 Gif-sur-Yvette*
[5] *Theoretical Physics Division, School of Physics and Astronomy, The University of Manchester, Manchester, M13 9PL, United Kingdom*

(Dated: March 24, 2020)

We analyze the stability of systems composed of isomassive fermions in which the number of particles is larger than the number fermionic flavours. To this end, the leading order of a momentum- and flavour-independent contact effective field theory is renormalized to shallow dimer and trimer states. The regulator dependence of the stability is assessed as a function of particle number and of the proximity of the two-body interaction to unitarity. The systems become unstable with respect to decays into spatially symmetric fragments if the regulator-induced effective ranges are below a certain threshold. This critical range decreases when the number of particles is increased down to a minimum range which is significantly smaller than the dimer scale. The closer the system is to unitarity, the more particles are needed to attain the minimum. At unitarity, the critical range tends to zero parabolically with the particle number.

We elaborate on the consequences of these results for the systematic description of any system close to unitarity. For nuclei in particular, the usefulness of the pionless theory for the description of P-wave stable systems such as ^{6}Li and ^{7}Li effectively is considered.

Introduction If each particle of a set of A isomassive fermions can be distinguished by an internal degree of freedom, the dynamics changes significantly with this number A exceeding the dimension d of the flavour space. For $A \leq d$, the system can realize bose-like behaviour in a totally symmetric spatial state while mixed symmetry is demanded if $A > d$. If the mutual interaction is flavour independent, this change is solely a consequence of the statistical properties of the particles. As such, the difference between fermionic and bose-like few-body phenomena can be studied in a universal approach, which does not depend on the short-distance structure of the particle-particle interaction, namely, with a resonant contact interaction [1]. The ideal resonant system, *viz.* at unitarity, has a two-body bound state exactly at the threshold with a corresponding scattering length $a = \pm\infty$. Physical systems typically deviate from this ideal. However, if their two-body correlation/scattering length is much larger than any other relevant length scale of the problem, as a three-body extension, they still share universal few-body phenomena, *e.g.* , the three-body Efimov effect [2], the Tjon [3] and Phillips [4] correlations, and the spectrum of the multi-boson system [5]. Certain mesons, nuclei, and atoms (see, *e.g.* , Refs. [3, 4, 6–9]) are prominent members of this universality class which exhibit structure at widely different scales.

With interactions of this type, three- and four-body systems driven by fermionic substructures were also found in form of the absence of shallow resonant [10] and bound states [11] in isomassive two-flavour three- and four-body systems, respectively. It thus appears that the description of fermionic systems which exhibit such peculiar structure, *e.g.* , a hypothetical three-neutron (^3n) resonance, needs to consider an additional scale which relaxes unitarity. Multiple mechanisms could, in principle, generate such a scale: a specific realization of the discrete scale invariance in the three-boson [12] system with a S-wave three-body contact; finite two-body scales beyond the scattering length; the difference between particle number and flavour-space dimension $(A - d)$; the absolute numbers of A, and d, respectively.

Here, we explore these possibilities with an effective field theory (EFT) applied to a variety of few-body problems. This entails renormalization as a systematic way to trace the effect of short-distance scales in a range of A-body observables for various flavour-space dimensions.

Theory The minimal EFT for non-relativistic point particles exhibiting two- and three-body shallow states has been studied extensively (*e.g.* Refs.[12–17]). The theory is defined as a perturbative series and can be refined systematically to attain a desired accuracy. Its Hamiltonian formulation at leading order (LO) comprises zero-range two- and three-body vertices which depend on the renormalization parameter Λ:

$$H = -\sum_{i<j} \frac{\hbar^2}{2m} \boldsymbol{\nabla}_{ij}^2 + C^\Lambda \sum_{i<j} \delta_\Lambda(\boldsymbol{r}_i - \boldsymbol{r}_j) + D^\Lambda \sum_{\substack{i<j<k \\ \text{cyc}}} \delta_\Lambda(\boldsymbol{r}_i - \boldsymbol{r}_j)\delta_\Lambda(\boldsymbol{r}_i - \boldsymbol{r}_k). \quad (1)$$

In the expansion of any resultant amplitude, the LO is represented by all Born terms depending solely on the coupling constants C^Λ and D^Λ. Parameters representing the aforementioned refinements enter perturbatively at the order given naïvely by their mass dimension. In this work, a Gaussian regulator $\delta_\Lambda(\boldsymbol{x}) \propto \Lambda^3 e^{-\frac{\Lambda^2}{4}\boldsymbol{x}^2}$ is used. It induces a Λ dependence in C^Λ and D^Λ which was calibrated to the energy of a single bound state in the two- ($B(2)$) and three-body ($B(3)$) system, respectively. Whether or not the Λ convergence of another amplitude depends on the specific choice for $B(2)$ and $B(3)$ classifies the corresponding observable as universal or emergent. The few-body problem is thereby specified with five parameters: the particle's mass (here, $m = 938$ MeV), the number of particles (A) and flavours (d), and the dimer and trimer binding energies.

We use this structure to consider a class of few-body systems with $A \oplus 1$ statistics [31] as they approach the unitarity limit by increasing the ratio $\upsilon := B(3)/B(2)$. We choose the combinations $B(2) = 1$ MeV with $B(3) \in \{1.5$ [32], 3, $4\}$ MeV; and $B(2) = 0^+$ with $B(3) = 3$ MeV. Finally, the nuclear pionless EFT (EFT($\not\pi$)) is renormalized to yield the deuteron and triton binding energies of $B(2) = 2.22$ MeV and $B(3) = 8.48$ MeV, respectively. The necessary fits for D^Λ employ Stochastic-Variational (SVM, [18]) and Resonating-Group (RGM, [19]) variational diagonalizations. C^Λ is determined via a Numerov-type integration of the appropriate one-dimensional radial Schrödinger equation.

Results The bose-like ground states of a theory with Hamiltonian of type (1) have been analysed in detail numerically (see *e.g.* Refs.[20–24]). The SVM-predicted bose-like ground state energies for $A < 7$ are shown in fig. 1. We find convergent behaviour as $\Lambda \to \infty$ (renormalization-group (RG) invariance). At unitarity, we find the ratio $B(4)/B(3)$ consistent with Refs. [25, 26]. In addition, we find $B(A)/B(3)\Big|_{\upsilon=3} < B(A)/B(3)\Big|_{\upsilon=4}$ which implies that the universal ratios $B(A)/B(3)$ are approached from below when taking the unitarity limit.

Now, we extend the analysis to $A \oplus 1$ systems. In those, our SVM calculations with anti-symmetric wave function and total orbital angular momentum $L_{\text{total}} = 0$ yield no stable states, which confirms the intuitive demand for mixed spatial symmetry. Even if expected due to Pauli repulsion, this result is non-trivial because of the numerous angular couplings between particles in many-fermion systems.

When projecting the spatial component of the variational basis onto $L_{\text{total}} = 1$, we find $A \oplus 1$ systems for A between 2 and 6 to sustain stable states ($B(A \oplus 1) > B(A)$) for $\Lambda \approx 0.1\,\text{fm}^{-1}$. In order to assess the universal character of these bound states, we vary the cutoff ($1.2\ a^{-1} < \Lambda < 60\ a^{-1}$) for all considered $\upsilon < \infty$. Increasing the cutoff, *i.e.* , decreasing the interaction range while approaching the contact limit, unbinds the $A \oplus 1$ systems at some critical value Λ_c (fig. 1). The interaction range at which an $A \oplus 1$ system disintegrates decreases with the number of particles $A = d$ comprising its spatially symmetric core. For small systems, this relation is almost linear, $\Lambda_c \propto A < 7$. To assess the dependence for $A > 6$, we employ a single-channel effective two-fragments resonating-group local approximation (to be detailed in upcoming communication in extension of Refs. [19, 27]). This approximation turns the few-body into a two-body problem between a "frozen" core and the one residual particle which is forced out of the Pauli shell. The halo character of the problem motivates a one-parameter representation of the bose core as a product of harmonic oscillator ground states because of the increasingly large gap between $B(A)$ and $B(A-1)$ which does not allow for its excitation by the out-of-shell particle. For $A < 7$, the parameter is fitted to the SVM results for the rms radius of the core. For larger A, we match the core wave function with the drop model formula $r_{\text{rms}} \propto A^{1/3}$ as successfully employed in Ref. [5]. Thereby, we find Λ_c to increase up to a maximum number of particles A^*. Both, A^* and the associated $\Lambda_c(A^*)$ increase with υ (compare maxima of the two curves in fig. 2) and we observe $\lim_{\upsilon\to\infty} A^* > 100$. The existence of A^* thus appears to be an artifact of the deviation from unitarity. As a finite Λ_c indicates a drastic change of the system's behaviour, its magnitude being of the order of or even above a conceivable breakdown scale would exclude this behaviour from the range of applicability of the theory. For systems with breakdown scales below Λ_c, our results expose the instability of $A \oplus 1$ system as universal.

To substantiate the conjecture of such a universal instability for nuclei and a more generic Pauli-shell structure, we fit the experimental deuteron and triton binding energies, $B(2) = 2.22$ MeV and $B(3) = 8.48$ MeV, respectively, thereby realizing a $SU(4)$-symmetric version of EFT($\not\pi$) [28]. For $A \leq 4$, we observe an instability pattern qualitatively identical to those found earlier (compare fig. 1 with fig. 3). Hence, the three-parameter theory predicts correctly

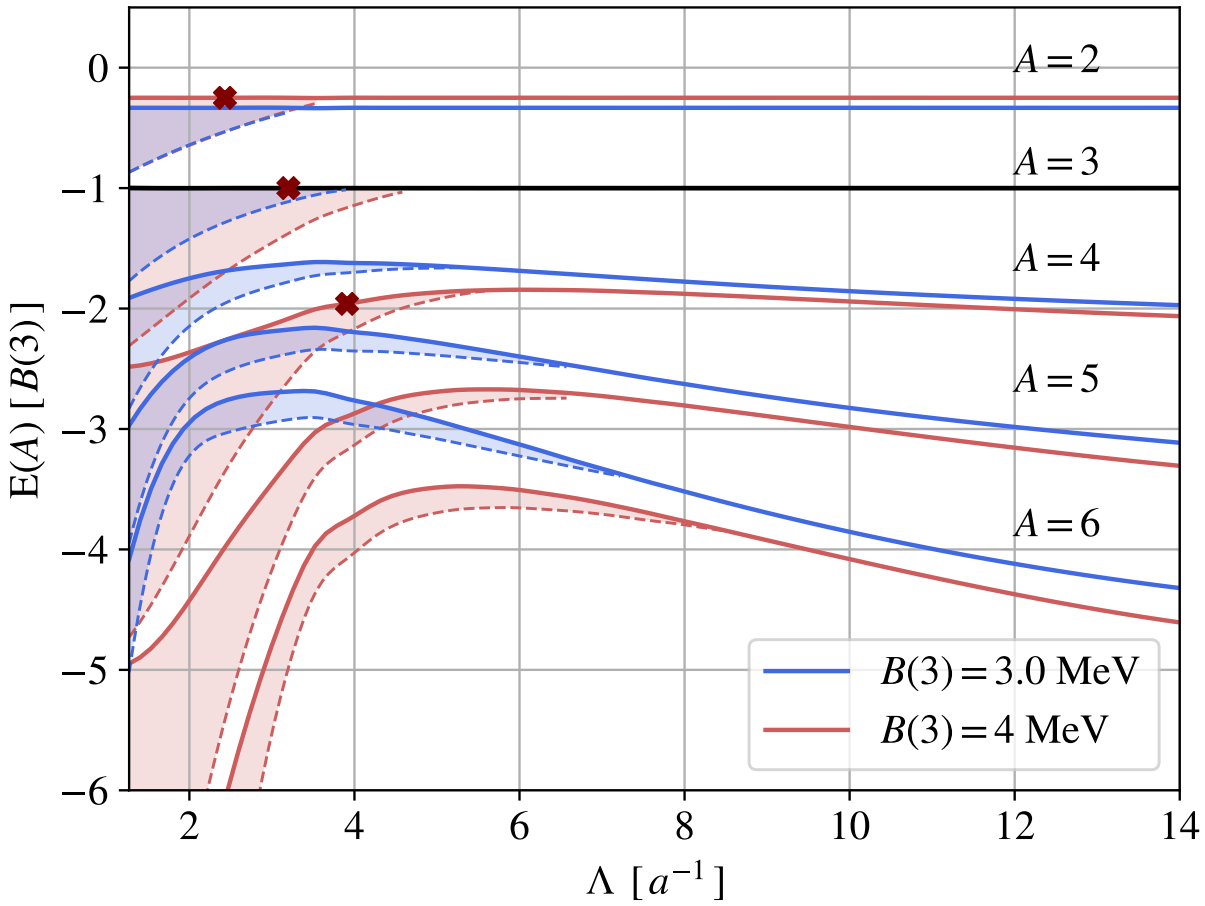

FIG. 1: (Color online) LO Cutoff dependence of ground-state energies of A bosons (solid) and $A \oplus 1$ mixed-symmetry systems (dashed) obtained with $B(2) = 1$ MeV and $B(3) = 3$ and 4 MeV (blue and red) from (1). With scattering volume set to zero, the $A \oplus 1$ systems destabilize at smaller Λ_c (red crosses, $B(3) = 4$ MeV).

the experimentally established instability of nuclei in the ${}^3\mathrm{H}(\frac{3}{2}^-)$, ${}^3n$, ${}^4\mathrm{H}$, ${}^{3,4}\mathrm{Li}$, and ${}^5\mathrm{He}$ channels. In contrast, the isotopes ${}^{6,7}\mathrm{Li}$ with $J^\pi = 1^+$ and $\frac{3}{2}^-$,respectively, are known to sustain bound states. In these channels, we find particle-stable systems ($4 \oplus 2$ and $4 \oplus 3$) only below critical cutoffs $\Lambda_c \approx 2\,\mathrm{fm}^{-1}$ and $1\,\mathrm{fm}^{-1}$. For larger Λ, the systems break into an α-particle and a deuteron or triton, respectively. Furthermore, we find ${}^8\mathrm{Be}$ ($4^2 \oplus 0$, $J^\pi = 0^+$), which is considered to be stable without Coulomb repulsion [29, 30], to α-decay at a $\Lambda_c \approx 0.7\,\mathrm{fm}^{-1} \approx \mathcal{O}(m_\pi)$. Λ_c being of the same order as the nuclear breakdown scale renders the stability as a cutoff artifact. We explain the loss of stability with increasing number of particles in different Pauli shells heuristically with the smaller spatial extent of the pertinent nuclear fragments, *i.e.* , the α particle, the triton, and the deuteron. The larger is the rms radius of the fragment, the larger is its overlap with the symmetric α core, which increases the attraction between the two. Furthermore, our three-parameter calculations at $\Lambda < \Lambda_c$, *i.e.* , when a stable ground state is realized, postdict the ordering of states in the rotational spectrum in ${}^8\mathrm{Be}$ - 0^+, 2^+, and 4^+ correctly. More specifically, these states emerge in form of bound excited states for $\Lambda < 0.4$ fm^{-1}.

The study of the trajectories of the bound-state poles through the respective $\alpha - \mathrm{n}$, $\alpha - {}^2\mathrm{H}$, $\alpha - {}^3\mathrm{H}$, and $\alpha - \alpha$ thresholds at $\Lambda > \Lambda_c$ is crucial for the usefulness of EFT($\not\pi$) for the description of these nuclear channels. This will tell whether a perturbative insertion of subleading order must move a shallow scattering pole to a stable one, or if a non-perturbative mechanism has to account for the creation of the pole anew. At unitarity, a shallow $2 \oplus 1$ pole cannot be fixed to a specific energy. In this limit, *i.e.* , without any scale, the resonance can only converge to threshold or diverge to infinity for $\Lambda \to \infty$ [33]. In the first case, three-body unitarity would be a universal consequence of

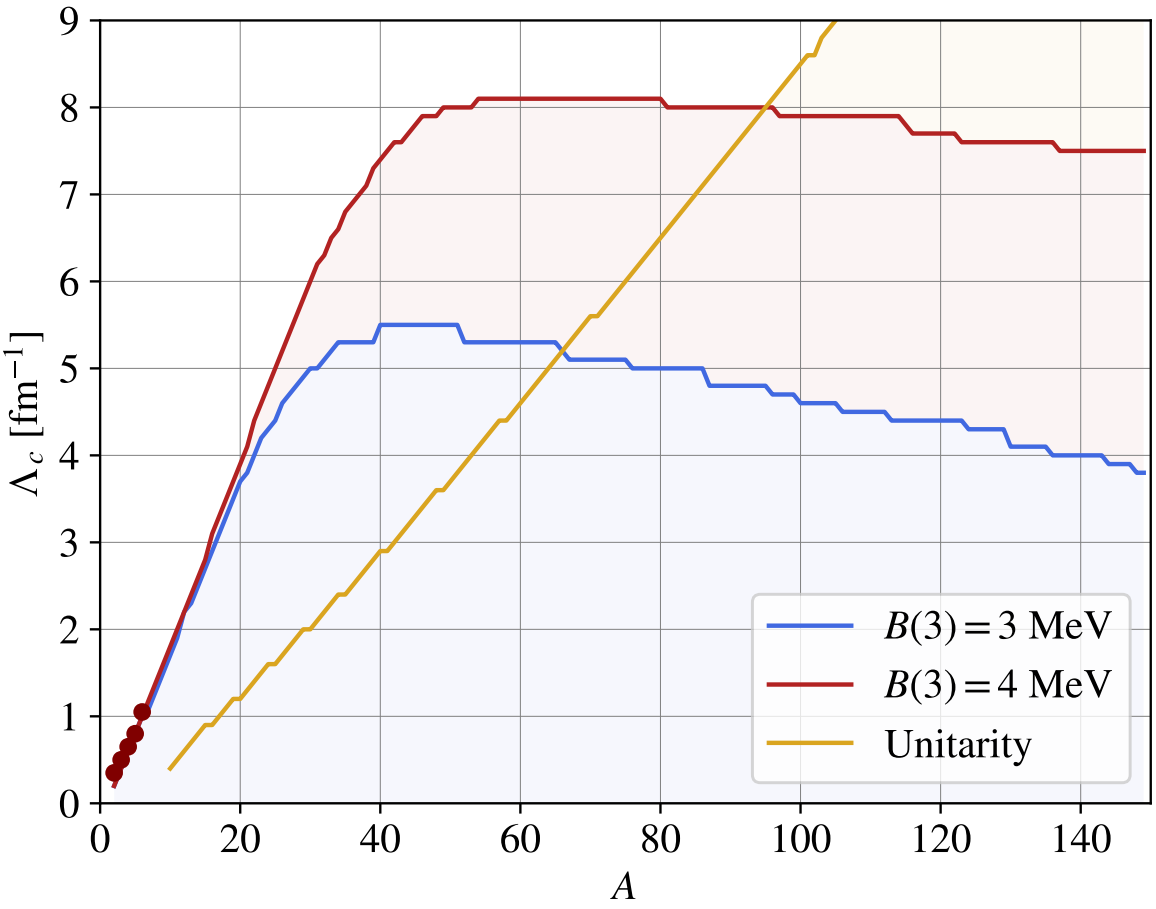

FIG. 2: (Color online) Dependence of the critical cutoff Λ_c on the number of core particles A. SVM few-body results are shown for $A < 7$ (dots, $B(3) = 4$ MeV) along with single-channel resonating-group approximations for $A < 150$ (lines). The unitarity limit (yellow) was realized with $B(2) \to 0^+$ and $B(3) = 3$ MeV and deviations from it with $B(2) = 1$ MeV and $B(3) \in \{3, 4\}$ MeV (blue, red). In the shaded regions, the respective theories do sustain bound $A \oplus 1$ states, while systems above the lines are unstable. The step-like change in the curves results from a numerical criterion for the onset of binding and can be removed systematically.

the resonant two-body interaction. In the second case, the pole is an unphysical artifact which disappears with the regulator. In contrast, for $d > 2$, scale invariance is broken, and the associated emergence of a scale could pin the resonance to a finite energy. As of now, such a study has not been done.

For the conception of an extension of the EFT($\not\pi$) which predicts also the particle-stable character of ^{6,7}Li and ^{8}Be in the zero-range limit, we analyze the mechanism behind the stability of these systems for $\Lambda < \Lambda_c$. Of all artifacts introduced by the finite range of the regulated contact interaction, the finite effective range in the two-body S-wave channel and a non-zero attractive two-body P-wave interaction are expected to dominate. Both contribute to the attraction in the $A \oplus 1$ system but their relative significance in this role is obscure. In other words, the finite-range interaction does not only describe a finite but large S-wave scattering length but also other finite parameters of the effective-range expansion of the S-wave amplitude like the effective range r_0. Furthermore, the scattering volume a_1 of the two-nucleon P-wave amplitude is non-zero as well. To shed light on their relative importance, we project the two-body interaction in an asymmetric internal state. This forces two interacting particles into an even spatial state ($L = 0, 2, ..$) removing any spatially asymmetric contributions. In effect, a reduction of Λ_c^A by about 50% is observed (crosses in fig. 1). Hence, the finite r_0 and a_1 seem to be of similar significance for the stability of the corresponding nuclear systems.

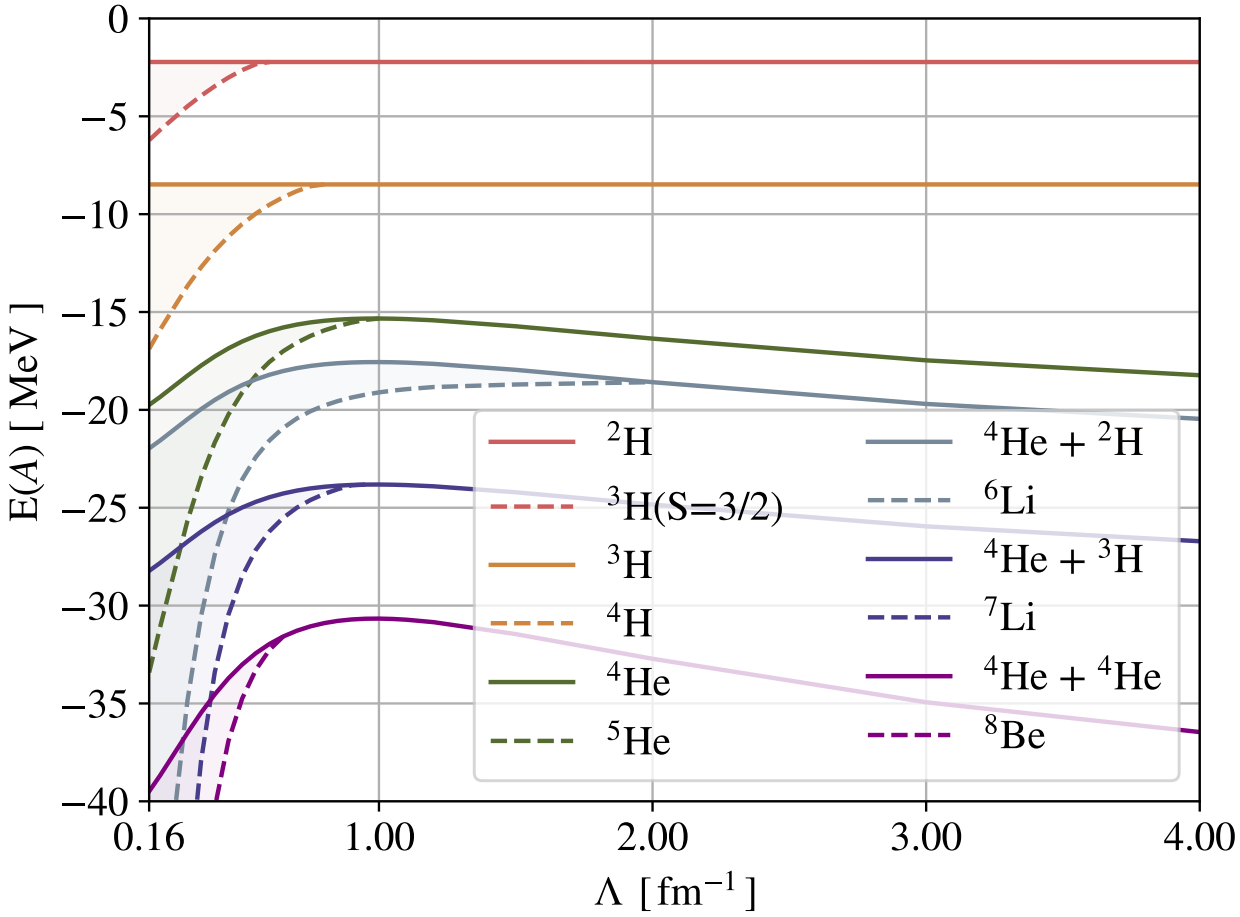

FIG. 3: (Color online) Cutoff dependence of nuclear ground-state energies obtained in LO EFT($\not\pi$). For $A < 5$, solid lines represent nuclei with spatially symmetric ground-state wave functions. For $A > 4$, solid lines mark the lowest decay threshold into two bose-like fragments.

Conclusion We find that a non-relativistic system of $d+1$ particles with identical masses and a d-dimensional internal flavour space cannot sustain a stable state if its dynamics is constrained by representations of two- and three-body momentum-independent contact interactions which are renormalized to yield a resonant two-body state and a single bound three-body state and whose residual finite-range is below a critical value. If the range of the regulated contact interactions, however, surpasses the critical range, the $L_{\text{total}} = 1$ ground state of the $d+1$ particles is stable with respect to breakup into a spatially symmetric d-body ground state and a single free particle. This critical range decreases with the system's particle number increasing as $A = d+1$. For a set of interactions close to unitarity, the critical range reaches a minimum at a certain number of particles. At unitarity, we observe that the critical range keeps decreasing up to $d \sim 100$ particles. Similarly, with the pionless EFT at leading order, we find the nuclear systems ^{6,7}Li, and ^{8}Be unstable, contrary to expectations.

We investigate the finite effective-range and scattering volume of two bodies as the dominant parameters affecting stability. Both were found of similar importance to bind the studied systems at small cut-off. With the vanishing of these parameters in the contact limit, the result questions the capability of such theories for the description of P-wave-stable states and asks for a study of the renormalization-group running of hypothetical shallow scattering poles. Only RG-stable poles might be stabilized with insertions of sub-leading operators, while in their absence they would have to be created anew. The latter result would have fundamental consequences for the effective-field-theory formulation.

Acknowledgments We thank N. Barnea, M. Birse, U. van Kolck, J. Mareš, N. Walet for insightful discussions. M.S. was supported by the Czech Science Foundation GACR Grant No.19-19640S. L.C. and J.K. acknowledge support from "Espace de Structure et de réactions Nucléaire Théorique" (ESNT, http://esnt.cea.fr) at CEA-Saclay, where this work was partially carried out. L.C. was also supported by the Pazy Foundation and by the Israel Science Foundation Grant No. 1308/16.

* m.schafer@ujf.cas.cz
† lorenzo.contessi@cea.fr

[1] H. Bethe and R. Peierls, "Quantum Theory of the Diplon," *Proceedings of the Royal Society of London Series A*, vol. 148, pp. 146–156, Jan. 1935.
[2] V. Efimov, "Energy levels arising form the resonant two-body forces in a three-body system," *Phys. Lett.*, vol. 33B, pp. 563–564, 1970.
[3] J. A. Tjon, "Bound states of 4 He with local interactions," *Phys. Lett.*, vol. 56B, pp. 217–220, 1975.
[4] A. C. Phillips, "Consistency of the low-energy three-nucleon observables and the separable interaction model," *Nucl. Phys.*, vol. A107, pp. 209–216, 1968.
[5] J. Carlson, S. Gandolfi, U. van Kolck, and S. A. Vitiello, "Ground-state properties of unitary bosons: From clusters to matter," *Phys. Rev. Lett.*, vol. 119, p. 223002, Nov 2017.
[6] N. A. Tornqvist, "Possible large deuteron - like meson meson states bound by pions," *Phys. Rev. Lett.*, vol. 67, pp. 556–559, 1991.
[7] M. B. Voloshin, "Interference and binding effects in decays of possible molecular component of X(3872)," *Phys. Lett.*, vol. B579, pp. 316–320, 2004.
[8] E. Braaten and M. Kusunoki, "Low-energy universality and the new charmonium resonance at 3870-MeV," *Phys. Rev.*, vol. D69, p. 074005, 2004.
[9] P. Courteille, R. S. Freeland, D. J. Heinzen, F. A. van Abeelen, and B. J. Verhaar, "Observation of a feshbach resonance in cold atom scattering," *Phys. Rev. Lett.*, vol. 81, pp. 69–72, Jul 1998.
[10] O. I. Kartavtsev and A. V. Malykh, "Low-energy three-body dynamics in binary quantum gases," *Journal of Physics B: Atomic, Molecular and Optical Physics*, vol. 40, pp. 1429–1441, mar 2007.
[11] D. S. Petrov, C. Salomon, and G. V. Shlyapnikov, "Scattering properties of weakly bound dimers of fermionic atoms," *Phys. Rev.*, vol. A71, p. 012708, 2005.
[12] P. F. Bedaque, H. W. Hammer, and U. van Kolck, "Renormalization of the three-body system with short range interactions," *Phys. Rev. Lett.*, vol. 82, pp. 463–467, 1999.
[13] G. P. Lepage, "How to renormalize the Schrodinger equation," in *Nuclear physics. Proceedings, 8th Jorge Andre Swieca Summer School, Sao Jose dos Campos, Campos do Jordao, Brazil, January 26-February 7, 1997*, pp. 135–180, 1997.
[14] U. van Kolck, "Effective field theory of nuclear forces," *Prog. Part. Nucl. Phys.*, vol. 43, pp. 337–418, 1999.
[15] E. Braaten and H. W. Hammer, "Universality in few-body systems with large scattering length," *Phys. Rept.*, vol. 428, pp. 259–390, 2006.
[16] H. W. Hammer, C. Ji, and D. R. Phillips, "Effective field theory description of halo nuclei," *J. Phys.*, vol. G44, no. 10, p. 103002, 2017.
[17] H. W. Hammer, S. König, and U. van Kolck, "Nuclear effective field theory: status and perspectives," 2019.
[18] Y. Suzuki and K. Varga, *Stochastic variational approach to quantum-mechanical few-body problems*. Lecture Notes in Physics Monographs, Berlin: Springer, 1998.
[19] J. A. Wheeler, "Molecular viewpoints in nuclear structure," *Phys. Rev.*, vol. 52, pp. 1083–1106, Dec 1937.
[20] B. Bazak, M. Eliyahu, and U. van Kolck, "Effective Field Theory for Few-Boson Systems," *Phys. Rev.*, vol. A94, no. 5, p. 052502, 2016.
[21] Y. Yan and D. Blume, "Energy and structural properties of N -boson clusters attached to three-body Efimov states: Two-body zero-range interactions and the role of the three-body regulator," *Phys. Rev.*, vol. A92, p. 033626, Sep 2015.
[22] M. Gattobigio, A. Kievsky, and M. Viviani, "Energy spectra of small bosonic clusters having a large two-body scattering length," *Phys. Rev.*, vol. A86, p. 042513, 2012.
[23] J. von Stecher, "Universal Five- and Six-Body Droplets Tied to an Efimov Trimer," *Phys. Rev. Lett.*, vol. 107, p. 200402, 2011.
[24] M. Gattobigio, A. Kievsky, and M. Viviani, "Spectra of helium clusters with up to six atoms using soft core potentials," *Phys. Rev.*, vol. A84, p. 052503, 2011.
[25] H. W. Hammer and L. Platter, "Universal Properties of the Four-Body System with Large Scattering Length," *Eur. Phys. J.*, vol. A32, pp. 113–120, 2007.
[26] J. von Stecher, J. P. D'Incao, and C. H. Greene, "Signatures of universal four-body phenomena and their relation to the Efimov effect," *Nature Physics*, vol. 5, pp. 417–421, Jun 2009.
[27] P. Naidon, S. Endo, and A. M. García-García, "Scattering of universal fermionic clusters in the resonating group method," *Journal of Physics B: Atomic, Molecular and Optical Physics*, vol. 49, p. 034002, jan 2016.
[28] S. König, H. W. Grießhammer, H. W. Hammer, and U. van Kolck, "Nuclear Physics Around the Unitarity Limit," *Phys. Rev. Lett.*, vol. 118, no. 20, p. 202501, 2017.

[29] S. A. AFZAL, A. A. Z. AHMAD, and S. ALI, "Systematic Survey of the alpha-alpha Interaction," *Rev. Mod. Phys.*, vol. 41, pp. 247–273, 1969.
[30] R. Higa, H. W. Hammer, and U. van Kolck, "alpha alpha Scattering in Halo Effective Field Theory," *Nucl. Phys.*, vol. A809, pp. 171–188, 2008.
[31] We refer to a system of A d-flavour fermions with $A > d$ as $d^p \oplus b$ with p d-uplets of fermions which can share the same spatial quantum states, and $b < d$ are the residual particles which are not enough to fill the flavour degeneracy of the states. This notation exposes the number of particles not on-shell for the Pauli interaction. For example, in this notation the nuclear ^{6}Li is denoted $4 \oplus 2$; a hypothetical system of 33 atoms of Helium-3 (spin 1/2 fermions), $2^{16} \oplus 1$;
[32] This constraint changes the threshold structure significantly. Consequently, the ground states of $A \oplus 1$ systems are not expected in the same $L_{\text{total}} = 1$ channels. Consistently, our SVM calculations do not yield bound states for this choice of $B(3)$.
[33] We thank U. van Kolck for clarifying discussions on this issue.